Flow behaviour of solid-liquid suspensions in horizontal pipes and stirred vessels: insights from positron emission particle tracking and data-driven Lagrangian modelling

by

Hamzah Ahmed Sheikh

A thesis submitted to the University of Birmingham for the degree of

DOCTOR OF PHILOSOPHY



UNIVERSITY OF BIRMINGHAM

School of Chemical Engineering

College of Engineering and Physical Sciences

University of Birmingham

December 2022

UNIVERSITY OF
BIRMINGHAM

University of Birmingham Research Archive

e-theses repository

This unpublished thesis/dissertation is copyright of the author and/or third parties. The intellectual property rights of the author or third parties in respect of this work are as defined by The Copyright Designs and Patents Act 1988 or as modified by any successor legislation.

Any use made of information contained in this thesis/dissertation must be in accordance with that legislation and must be properly acknowledged. Further distribution or reproduction in any format is prohibited without the permission of the copyright holder.

Abstract

Chemical, pharmaceutical, food, and petroleum industries are just a few of the multitude of sectors that frequently process solid-liquid flows. These slurry mixtures are transported through pipes and often mixed, dispersed, reacted, or involved in heat or mass transfer in stirred vessels.

The motion of solid particles in these flows is an inherently Lagrangian process, and to fully understand the characteristics and behaviours of such systems requires both Lagrangian and Eulerian information of the phases involved. The work described here uses a technique of positron emission particle tracking (PEPT) to capture the Lagrangian information in horizontal transient and turbulent solid-liquid pipe flows. An experimental flow apparatus with nearly-neutrally buoyant particles in a 40 mm ID pipe was used to investigate the effects of particle size, concentration, and Reynolds number on the velocity and occupancy profiles. The effect of solid-liquid particle density difference was also tested. As the particles restricted optical access, the PEPT technique was an excellent method to obtain accurate particle and fluid trajectories particularly for high solid loadings.

This non-intrusive technique has previously been used to obtain flow information of solid-liquid mixtures in stirred vessels. Here, the Lagrangian information from solid-liquid stirred vessel PEPT experiments was used to construct and develop three data-driven models; unique computationally-efficient methods with the aim

of extending experimental and computational (obtained from Euler-Lagrange CFD) particle trajectories. These novel implementations of relatively simple calculations were successful in capturing the flow characteristics of both the liquid and solid phases in a range of stirred vessel experiments, using as little as 1 min Lagrangian experimental information to construct long-term trajectories of tracer particles.

Acknowledgements

I am extremely grateful to Professor Mostafa Barigou for his invaluable support and guidance throughout my PhD journey. It has been a privilege to work under his supervision, and I sincerely thank him for his valuable advice, encouragement, and patience.

My work would also not have been possible without the help of my colleague and friends; Dr. Ananda Jadhav, Dr. Chiya Savari, Dr. Kun Li and Zhuangjian "Jack" Yang.

Finally I want to express my utmost gratitude to my loving family for all their patience and support throughout this experience.

Contents

List of Figures viii

List of Tables xvii

1 Introduction 1

1.1 Objectives 3

1.2 Thesis layout 4

1.3 Publications arising from thesis 6

I Solid-liquid flow in horizontal pipes using positron emission particle tracking 8

2 Solid-liquid flow in horizontal pipes using positron emission particle tracking 9

2.1 Literature review 9

2.1.1 Introduction 9

2.1.2 Experimental studies 11

2.2 Theory 14

2.2.1 Flow regimes 14

2.2.2 Forces on spherical particles in Newtonian fluids 15

2.3 Positron emission particle tracking 16

2.3.1 ADAC Forte Positron Camera 18

2.3.2 Location algorithms 20

3 Investigation on solid-liquid pipe flow using PEPT 30

3.1 Introduction 30

3.2 Experimental methodology 31

3.2.1 Solid-liquid flow apparatus 31

3.2.2 Alginate particle preparation 33

3.2.3 Positron emission particle tracking 34

3.3 Experimental protocol 35

3.4 Analysis procedure 36

3.4.1 Axial velocity profiles 39

3.4.2 Axially-averaged Eulerian maps 39

3.5 Experimental results and discussion 40

3.5.1 Effect of solid concentration and particle size 40

3.5.2 Transient and turbulent flow 43

3.5.3 Effect of solid-liquid density difference 44

3.6 Conclusions 45

II Modelling of three-dimensional solid-liquid flow in stirred vessels using novel Lagrangian methods 48

4 Solid-liquid flow in mixing vessels 49

4.1 Literature review 49

4.1.1 Introduction 49

4.1.2 Experimental studies 51

4.1.3 Computational studies 53

4.2 Experimental methodology 56

5 Lagrangian stochastic modelling of liquid flow in a mechanically agitated vessel 61

5.1 Introduction 62
5.2 Experimental 65
5.2.1 Mixing vessel apparatus 65
5.2.2 Positron emission particle tracking 66
5.3 Lagrangian stochastic modelling 67
5.3.1 Input velocity field 68
5.3.2 Model equations 71
5.3.3 Boundary collision 74
5.4 Results and discussion 77
5.4.1 Predicting long-term trajectories from short-term LSM driver trajectories 78
5.4.2 Model validation 79
5.4.3 Effects of impeller configuration 83
5.4.4 Prediction of flow conditions outside range of experimental measurements 85
5.5 Conclusion 87

6 A data-driven stochastic model for particle-liquid flow and phase distribution in a stirred vessel 94

6.1 Introduction 95
6.2 Experimental 97
6.2.1 Mixing vessel apparatus 97
6.2.2 Positron emission particle tracking 99
6.3 Lagrangian stochastic modelling 99
6.3.1 Model equations 100
6.3.2 Model parameters 102
6.4 Model testing and validation 105
6.4.1 Velocity profiles 106
6.4.2 Spatial particle distribution 111

6.4.3 Prediction of flow conditions outside range of experimental measurements . . . 114

6.5 Conclusion . . . 117

7 Machine learning framework for construction of Lagrangian turbulent flow field in multiphase stirred vessels 124

7.1 Introduction . . . 125

7.2 Theory . . . 128

7.2.1 Analysis of Lagrangian trajectory . . . 128

7.2.2 K-nearest neighbours regressor . . . 131

7.2.3 Lagrangian trajectory construction using ML . . . 133

7.3 Experimental . . . 138

7.3.1 Stirred vessels . . . 138

7.3.2 Positron emission particle tracking . . . 138

7.4 Results and discussion . . . 139

7.4.1 Framework validation and evaluation . . . 140

7.4.2 Prediction of particle-liquid flows . . . 147

7.5 Conclusions . . . 151

7.6 Supplementary material . . . 153

8 Predicting three-dimensional flow in stirred vessels using neural networks 164

8.1 Introduction . . . 164

8.1.1 Recurrent networks . . . 167

8.1.2 Long short-term memory networks . . . 168

8.2 Neural network theory . . . 171

8.2.1 Data pre-processing . . . 175

8.2.2 Activation functions . . . 176

8.2.3 Hyperparameters . . . 180

8.2.4 Data propagation . . . 182

8.2.5 Network training and optimisers . . . 183
8.3 Experimental . . . 186
8.3.1 Mixing vessel . . . 186
8.3.2 Positron emission particle tracking . . . 186
8.4 Network setup . . . 187
8.4.1 Data preparation . . . 187
8.4.2 Network architecture . . . 188
8.5 Results and discussion . . . 191
8.5.1 Evaluation method . . . 191
8.5.2 Velocity profiles . . . 192
8.5.3 Occupancy . . . 195
8.5.4 Predicting flow for conditions outside of training data . . . 198
8.6 Conclusion . . . 201

9 General conclusions and recommendations 206

9.1 PEPT . . . 206
9.2 Solid-liquid pipe flow . . . 207
9.3 Modelling of solid-liquid flow in mixing vessels . . . 209

List of Figures

2.1 ADAC Forte camera system at the University of Birmingham. 19

3.1 Solid-liquid flow apparatus (not to scale), showing overall setup (a) and axial view of test section (b). 32

3.2 Apparatus images 33

3.3 A sample of 2 mm spherical calcium alginate particles 34

3.4 An image of alginate particles flowing in the perspex pipe (2 mm particles, 10 wt%) 37

3.5 Effect of solid concentration on axial liquid flow velocity, $Re = 3500$. 40

3.6 Effect of solid concentration on axial solid flow velocity, $Re = 3500$ . . 41

3.7 Effect of concentration of 2 mm alginate beads on solid flow distribution, $Re = 3500$ 42

3.8 Effect of Reynolds number on liquid and solid velocity profiles 44

3.9 Effect of particle density on solid velocity profiles, 30 wt% loading of 4 mm particles, $Re = 3500$ 45

3.10 Effect of Reynolds number on liquid and solid flow, concentration = 30 wt% 47

4.1 Mixing vessel dimensions 57

5.1 Schematic of experimental setup: (a) mixing vessel and PEPT γ-ray detectors; (b) computational grid consisting of N_r cells in the r-direction, N_z cells in the z-direction and N_θ cells in the θ-direction; (c) method of calculation of local time-averaged velocity v_{cell} in the ith cell. 66

5.2 Flowchart of LSM algorithm: showing collision model (CM) and random particle injection (RPI) methods of re-inserting model particles into the domain. 68

5.3 Effect of grid mesh density on number of detected positions in each cell: Sample results shown are based on 5 min-long experimental PEPT trajectories for one layer of cells in the θ-direction ($N_\theta = 12$); white cells have no detected positions; agitation speed = 300 rpm, PBTD configuration. 70

5.4 Histograms of PEPT particle tracer-wall collision factor, C_f, for experiments using PBTD configuration at 100 and 500 rpm: (a) $C_f = v_2/v_1$; (b) $C_f = \frac{1}{tan(\phi)}$ 76

5.5 Sensitivity analysis of LSM-predicted time-averaged velocity profiles in cells adjacent to the vessel wall to the value of Cf adopted: experimental and modelling data shown are for 40 min trajectory obtained at 300 rpm with PBTD configuration: (a) $C_f = v_2/v_1$; (b) $C_f = \frac{1}{tan(\phi)}$. 77

5.6 Effects of length of LSM driver trajectory on azimuthally averaged profiles of total velocity predicted: PEPT and ^1LSM compared at 300 rpm with PBTD configuration. 79

5.7 Azimuthally averaged profiles of local θ-velocity component: PEPT, ^1LSM and ^2LSM compared at 300 rpm with PBTD configuration. . 81

5.8 Azimuthally averaged profiles of local z-velocity component: PEPT, ^1LSM and ^2LSM compared at 300 rpm with PBTD configuration. . 82

5.9 Azimuthally averaged profiles of local r-velocity component: PEPT, ^1LSM and ^2LSM compared at 300 rpm with PBTD configuration. . 83

5.10 Azimuthally averaged plots of (a) radially-averaged and (b) axially-averaged occupancy: PEPT, ^1LSM and ^2LSM compared at 300 rpm with PBTD configuration. 84

5.11 Azimuthally averaged profiles of total velocity: PEPT, ^1LSM and ^2LSM compared at 300 rpm with PBTU configuration. 85

5.12 Azimuthally averaged profiles of total velocity: PEPT, ^1LSM and ^2LSM compared at 300 rpm with RDT configuration. 86

5.13 Azimuthally averaged profiles of total velocity for 500 rpm PBTD predicted on the basis of 5 min initial data from 100 rpm PBTD experiment: PEPT and 1LSM. 87

6.1 Experimental setup: (a) mixing vessel and PEPT γ-ray detectors; (b) 5 s sample of PEPT Lagrangian trajectory; (c) computational grid consisting of N_r cells in the r-direction, N_z cells in the z-direction and N_θ cells in the θ-direction; (d) method of calculation of local time-averaged velocity v_{cell} in the ith cell. 98

6.2 Histograms of PEPT particle-wall collision factor for experiments containing 20 wt/wt% of 3 mm glass beads: (a) $C_{f,a} = \frac{|v_r|}{|v_i|}$; (b) $C_{f,b} = \frac{1}{tan(\phi)}$; and (c) analysis of sensitivity to the definition and value of C_f adopted of LSM-predicted time-averaged velocity profiles in cells adjacent to the vessel wall. 104

6.3 Azimuthally averaged profiles of total liquid velocity: PEPT, ^1LSM and ^2LSM compared for 40 wt% of particles. 106

6.4 Azimuthally averaged axial and radial profiles of local solid r-velocity component: ^1LSM, ^2LSM predictions and PEPT measurements compared for 40 wt% of particles. 107

6.5 Azimuthally averaged axial and radial profiles of local solid z-velocity component: ^1LSM, ^2LSM predictions and PEPT measurements compared for 40 wt% of particles. 108

6.6 Azimuthally averaged axial and radial profiles of local solid θ-velocity component: ${}^1LSM$, ${}^2LSM$ predictions and PEPT measurements compared for 40 wt% of particles. 109

6.7 Azimuthally averaged profiles of total solid velocity: PEPT, ${}^1LSM$ and ${}^2LSM$ compared for 5 wt% of particles. 110

6.8 Azimuthally averaged profiles of total solid velocity: PEPT, ${}^1LSM$ and ${}^2LSM$ compared for 5, 10, 20, 40 wt% of particles. 111

6.9 Azimuthally averaged profiles of local particle concentration: PEPT, ${}^1LSM$ and ${}^2LSM$ compared for 40 wt% of particles. 113

6.10 Azimuthally averaged profiles of local solid concentration: PEPT, ${}^1LSM$ and ${}^2LSM$ compared for 5, 10, 20, 40 wt% of particles. 114

6.11 Azimuthally averaged profiles of total solid velocity: PEPT and ${}^2LSM$ compared for 20 wt% of particles at $1.25N_{js}$, where ${}^2LSM$ is driven by 5 min of velocity data at N_{js} and 20 wt% of particles. 115

6.12 Azimuthally averaged profiles of total solid velocity: PEPT and ${}^2LSM$ compared for 40 wt% of particles at N_{js}, where ${}^2LSM$ is driven by 5 min of velocity data at N_{js} and 20 wt% of particles. 116

6.13 Azimuthally averaged profiles of total solid concentration: PEPT and ${}^2LSM$ compared for 40 wt% of particles at N_{js}, where ${}^2LSM$ is driven by 5 min of velocity data at N_{js} and 20 wt% of particles. 117

7.1 Experimental set up and grid for Lagrangian data analysis: (a) stirred vessel inside the field of view of PEPT camera; (b) 30 s sample of PEPT Lagrangian trajectory; (c) grid of equal-volume cells used for Lagrangian data analysis; (d) local velocity calculation in each cell. . 129

7.2 Typical distribution of global fluctuating velocity components in single-phase flow: (a) radial, (b) axial and (c) tangential directions; PBTD; $N = 500$ rpm. 130

7.3 Concept of KNN regression. 131

7.4 Workflow of ML framework for Lagrangian trajectory construction in a stirred vessel. 133

7.5 Flowchart of KNN model training. 135

7.6 Illustration of wall collision model. 137

7.7 Effects of number of neighbours and weight function type on (a) root mean square error (RMSE), and (b) determination coefficient for a 2 min PEPT trajectory (23706 training samples) of single-phase flow: PBTD; $N = 500$ rpm. 141

7.8 Effects of training dataset size on azimuthally-averaged vertical and horizontal profiles of r-velocity component PEPT and ML compared in single-phase liquid flow: PBTD; $N = 500$ rpm. 142

7.9 Effects of training dataset size on azimuthally-averaged vertical and horizontal profiles of z-velocity component PEPT and ML compared in single-phase liquid flow: PBTD; $N = 500$ rpm. 143

7.10 Effects of training dataset size on azimuthally-averaged vertical and horizontal profiles of θ-velocity component PEPT and ML compared in single-phase liquid flow: PBTD; $N = 500$ rpm. 144

7.11 Effects of training dataset size on azimuthally-averaged vertical and horizontal profiles of total velocity PEPT and ML compared in single-phase liquid flow: PBTD; $N = 500$ rpm. 145

7.12 Probability distributions of (a) circulation time, (b) circulation trajectory length, (c) residence time and (d) Lagrangian total velocity PEPT and ML compared in single-phase liquid flow: PBTD; $N = 500$ rpm. 146

7.13 Azimuthally-averaged vertical and horizontal profiles of total liquid velocity PEPT and ML compared in 20 wt% particle-liquid flow: PBTD; $N_{js} = 490$ rpm. 148

7.14 Azimuthally-averaged vertical and horizontal profiles of total particle velocity PEPT and ML compared in 20 wt% particle-liquid flow: PBTD; $N_{js} = 490$ rpm. 149

7.15 Azimuthally-averaged vertical and horizontal profiles of solid phase distribution PEPT and ML compared in 20 wt% particle-liquid flow: PBTD; $N_{js} = 490$ rpm. 150

7.16 Effects of training dataset size on azimuthally-averaged vertical and horizontal profiles of total velocity PEPT and ML compared in single-phase liquid flow: PBTU; $N = 330$ rpm. 153

7.17 Effects of training dataset size on azimuthally-averaged vertical and horizontal profiles of total velocity PEPT and ML compared in single-phase liquid flow: PBTD; $N = 100$ rpm. 154

7.18 Azimuthally-averaged vertical and horizontal profiles of total liquid velocity PEPT and ML compared in 40 wt% particle-liquid flow: PBTD; $N_{js} = 590$ rpm. 154

7.19 Azimuthally-averaged vertical and horizontal profiles of total particle velocity PEPT and ML compared in 40 wt% particle-liquid flow: PBTD; $N_{js} = 590$ rpm. 155

7.20 Azimuthally-averaged vertical and horizontal profiles of solid phase distribution PEPT and ML compared in 40 wt% particle-liquid flow: PBTD; $N_{js} = 590$ rpm. 155

8.1 Diagram of a neural network. 171

8.2 Velocity magnitude profiles comparing FFN predictions with experimental data at 100 RPM 193

8.3 Velocity magnitude profiles comparing FFN predictions with experimental data at 500 RPM 194

8.4 Velocity magnitude profiles comparing RNN predictions with experimental data at 500 RPM 195

8.5 Velocity magnitude profiles comparing LSTM predictions with experimental data at 500 RPM 196

8.6 Velocity magnitude profiles comparing FFN, RNN and LSTM predictions with experimental data at 500 RPM 197

8.8 Azimuthally averaged occupancy comparison for FFN, RNN and LSTM predictions with experimental data 197

8.9 Probability density functions for FFN B, RNN B and LSTM B compared to 500 RPM experimental data 198

8.10 Velocity and occupancy errors for predictions outside of training conditions 199

8.11 Effect of training data length on LSTM B predictions for 500 RPM . 200

8.7 Azimuthally averaged velocity magnitude comparison for FFN, RNN and LSTM predictions with experimental data at 500 RPM 205

List of Tables

3.1 Solid-liquid flow experiments 36

4.1 Experimental flow conditions. 57

5.1 Velocity and acceleration decorrelation times for minute intervals of experimental at 500 rpm PBTD PEPT data. 72

7.1 Experimental flow conditions. 139

7.2 Experimental and ML-predicted phase flow numbers for particle-liquid flows. 151

8.1 Neural network architectures 190

Chapter 1

Introduction

The transport and mixing of solid particles within liquid media play a crucial role in various industrial processes, ranging from chemical and pharmaceutical production to mining and wastewater treatment. The dynamics of solid-liquid flows in both pipes and stirred vessels are complex and multifaceted, necessitating a comprehensive understanding to optimise process efficiency, product quality, and equipment design.

Solid-liquid flows involve the movement of discrete solid particles suspended within a liquid phase. These particles can vary widely in size, shape, density, and concentration, influencing the behaviour of the overall mixture. The interactions between solid particles and the surrounding liquid give rise to intricate phenomena such as particle settling, suspension stability, erosion, and particle-particle interactions. These dynamics can be further influenced by the geometry of the conduits they flow through, whether it be pipelines or stirred vessels.

In pipelines, the movement of solid-liquid mixtures introduces challenges related to pressure drop, particle deposition, and wear, all of which impact the flow rate and

system efficiency. Proper understanding and management of these factors are crucial to prevent blockages, enhance the transport of valuable products, and minimise equipment maintenance.

In stirred vessels, the agitation of solid-liquid suspensions is a pivotal aspect of many processes. The mixing intensity, impeller design, and vessel geometry profoundly influence the distribution and dispersion of solid particles within the liquid. Achieving uniform mixing and preventing particle settling are paramount to ensuring consistent product quality, minimising batch-to-batch variations, and maintaining efficient heat and mass transfer rates.

An in-depth understanding of these flows is essential for enhancing process efficiency, reducing operational costs, and ensuring the quality and safety of end products across a wide array of industries. As we delve into the complexities of these systems, we embark on a journey toward more effective and sustainable industrial practices.

To comprehend the intricacies of solid-liquid flows in pipes and stirred vessels, various theoretical and experimental approaches are employed. Computational fluid dynamics (CFD) simulations provide insights into flow patterns, residence time distributions, and shear forces, aiding in the optimisation of process parameters and equipment design. Experimental techniques, such as particle image velocimetry (PIV) and laser-induced fluorescence (PLIF), offer real-time visualisation and quantification of particle movement, aiding validation of theoretical models. Difficulties in CFD and experimentation arise when dealing with dense suspensions, where computational expense in the former and optical access in the latter play major roles in the ability to analyse flow.

In recent years, the advent of sophisticated instrumentation, including techniques like positron emission particle tracking (PEPT) and computer-automated radioac-

tive particle tracking (CARPT), has facilitated a more intricate exploration of these opaque systems, allowing for precise assessments of local flow characteristics.

The research reported in this thesis aims to investigate the flow behaviour of solid-liquid suspensions in horizontal pipes and stirred vessels, using the PEPT technique. This was conduced via an experimental pipe flow rig with nearly-neutrally buoyant particles in turbulent flow, with opaque particles in dense suspensions.

Data from previous stirred vessel PEPT experiments was studied using novel Lagrangian modelling techniques, namely Lagrangian stochastic modelling, a machine learning method using the K-nearest neighbours regressor, and a neural network method using feed-forward and recurrent networks.

1.1 Objectives

This thesis is divided into two parts, the first of which investigates flow of solid-liquid suspensions in pipe flow. The objectives for Part I were to investigate the effect of solid concentration on flow and mixing in a pipe using PEPT and particles of different sizes, and to understand how increasing solid concentration affects the flow profile and velocity of both the liquid and solid phases. The study also aimed to examine the differences in velocity between low and high solid concentrations and how these differences are reflected in axial velocity distributions and occupancy maps. The results of the experiments were intended to provide insights into solid-liquid flow and mixing in pipes and the impact of solids on the flow field.

Part II investigated Lagrangian modelling techniques to predict solid-liquid flow in a stirred vessel. The main objectives of part II were:

- To apply a data-driven Lagrangian stochastic model based on random walk particle tracking to single-phase flow in a mechanically agitated vessel for the first time, and to evaluate its performance under different flow conditions (e.g., different impeller configurations and rotational speeds)

- To use the model to predict two-phase particle-liquid flow in a mechanically agitated vessel, and to evaluate its accuracy in predicting local phase velocity and local particle concentration

- To develop a computationally efficient machine learning (ML) framework for constructing 3D long-term trajectories of single-phase and multiphase turbulent flows in a stirred vessel, and to validate its accuracy using various characteristics of the flow system (e.g., local velocity distributions, Lagrangian statistical analysis, particle concentration distributions, and phase flow numbers)

- To use neural networks to accurately predict the flow patterns in solid-liquid mixing vessels, and to compare the performance of different types of neural networks (e.g., feed-forward, recurrent, and long short-term memory networks)

1.2 Thesis layout

This thesis is separated into two distinct parts, **Part I** investigates flow of solid-liquid suspensions in pipe flow using positron emission particle tracking (PEPT) experiments, and **Part II** investigates novel data-driven Lagrangian modelling techniques to predict solid-liquid flow in a stirred vessel.

Part I:

- **Chapter 2** gives a background literature review and theory on solid-liquid flow in one dimensional pipe flow.

- **Chapter 3** reports the experimental findings from experiments conducted with positron emission particle tracking for solid-liquid flow in pipes.

Part II:

- **Chapter 4** gives a summary on solid-liquid flow in mixing vessels, with a literature review and outline of general experimental methodology

- **Chapter 5** investigates the ability of Lagrangian stochastic modelling for predicting single-phase flow in stirred vessels

- **Chapter 6** expands research from chapter 5 to predictions of solid-liquid flow using Lagrangian stochastic modelling

- **Chapter 7** investigates the ability of using a machine learning framework based on a k-nearest neighbours regressor for the prediction of solid-liquid flow in stirred vessels

- **Chapter 8** investigates the ability of multiple neural networks for the prediction of single-phase flow in stirred vessels

Finally, **Chapter 9** concludes this thesis with general conclusions, recommendations and future work.

1.3 Publications arising from thesis

This research has led to the following publications, and are included in sections 5 and 6 respectively:

- Sheikh, H.A., Savari, C., Barigou, M., 2022. Lagrangian stochastic modelling of liquid flow in a mechanically agitated vessel. *Chemical Engineering Science* 249.
- Sheikh, H.A., Savari, C., Barigou, M., 2022. A data-driven stochastic model for velocity field and phase distribution in stirred particle-liquid suspensions. *Powder Technology* 411.

Work from these research articles were also presented at the following conferences:

- AIChE 2020, Modelling of 3D particle-liquid flows using a data-driven Lagrangian stochastic approach
- FEDSM 2020, A data-driven stochastic model for the analysis of complex two-phase particle-liquid flows
- ChemEng Day UK 2021, Lagrangian stochastic modelling of three-dimensional particle-liquid flows

The author was responsible for supporting conceptualisation, data curating, methodology, formal analysis, and validation for the following article, included in section 7:

- Li, K. Savari, C., Sheikh, H.A., Barigou, M, 2023. Machine learning framework

for construction of Lagrangian turbulent flow field in multiphase stirred vessels. *Physics of Fluids* 35.

The primary author, Dr. Kun Li, was responsible for writing of the original draft.

The author was responsible for data analysis and editing for the following article, not included in this thesis:

- Savari, C., Sheikh, H.A., Barigou, M. 2021. Lagrangian Recurrence Tracking: A Novel Approach for Description of Mixing in Liquid and Particle-Liquid Flows. *Ind. Eng. Chem. Res.* 60, 50.

Part I

Solid-liquid flow in horizontal pipes using positron emission particle tracking

Chapter 2

Solid-liquid flow in horizontal pipes using positron emission particle tracking

2.1 Literature review

2.1.1 Introduction

Particle movement in fluids in pipes is a complex phenomenon that is influenced by a wide range of factors, including the properties of the fluid, the size and shape of the particles, and the flow conditions in the pipe.

One of the key factors that influences particle movement in fluids is the Reynolds number, which is a measure of the relative importance of the inertial forces to the viscous forces in the fluid. At low Reynolds numbers, the viscous forces dominate,

and the particles tend to follow the flow of the fluid, moving in a relatively orderly manner. At high Reynolds numbers, the inertial forces become more dominant, and the particles may tend to move in a more erratic or random fashion (Ojiako et. al, 2006).

The behaviour of solid-liquid flows in pipes is also influenced by the size and shape of the solids, as well as the properties of the fluid. For example, larger particles tend to settle more quickly than smaller ones, and the viscosity of the fluid can affect the rate at which the particles settle. The interaction between the solids and the fluid can also be influenced by the presence of surfactants or other additives, which can alter the surface tension or viscosity of the fluid.

One of the key characteristics of solid-liquid flows in pipes is the concentration of solids, which can range from low concentrations of dispersed particles to high concentrations of densely packed solids. At low concentrations, the solids behave as a suspension in the fluid, with the particles moving independently of each other. As the concentration increases, the solids begin to interact with each other and form clusters, leading to the formation of a packed bed. At even higher concentrations, the solids form a plug flow, in which the particles move together as a single entity.

Overall, the movement of particles in fluids in pipes is a complex and multifaceted process that is influenced by a wide range of factors. A thorough understanding of these factors is essential for the design and operation of systems that involve the transport of particles in fluids.

Solid-liquid transport is typically of two types, homogeneous and heterogeneous flow. The former refers to non-settling slurries, where fine particles are suspended due to Brownian motion; although the definition is often extended to slurries which can be tested viscometrically without settling and have no tendency to form stationary

deposits in pipe flow. Homogeneous slurries are simpler to study and are treated with fluid models to calculate frictional losses. Coarse particles result in heterogeneous flow, due to high settling velocities. Since inertia, gravity and energy dissipation due to particle-wall and particle-particle friction affect the flow, heterogeneous flows are much more challenging to predict and cannot be treated with the same fluid flow models as described for homogeneous slurries.

These heterogeneous flows are present in coal or gravel slurries, and often in solid-liquid food mixtures.

2.1.2 Experimental studies

To research solid-liquid flows, a variety of non-intrusive particle flow methods have been employed. These methods fall into two categories depending on the frame of reference: Eulerian methods, which provide local instantaneous information on the flow field, i.e., time series data at a fixed location, and tracer methods, which offer Lagrangian-type data while the tracer is tracked in space and time.

Many Eulerian optical techniques have been used to measure the residence time or velocity profiles of solid particles in flow. Segré and Silberberg (1962a, 1962b) for instance, determined local concentration by assessing the passages of particles through crossed light beams. Measurement of local velocities and concentrations of very small particles (diameters 0.3–1.8 mm) were obtained by Ohashi et al. using a photographic technique (Ohashi et al., 1979) and later a laser technique (Ohashi et al., 1980), which had good repeatability (standard variation of 5.1%). A video-taping method employed by Dutta and Sastry (1990) measured the average particle velocities of model food particles in tubes resembling those of industrial aseptic processing systems, however were only successful in determining a qualitative math-

ematical model for particle action. In a similar vein, Liu et al. (1993) investigated food flows (carrot-water mixtures) in a flow loop with metal detection, assessing the impact of solids fraction on particle flow velocity, finding stratified flows with solids fractions between 10 and 20% showing the largest variability in particle velocity. Laser-Doppler Velocimetry (LDV) has also been frequently used to measure particle velocities; Kulick et al. (1994) used the technique with copper spherical particles which were smaller than the Kolmogorov length scale for the flow measurement, and therefore responded to some scales of turbulent motion. Following, Averbakh et al. (1997) matched the refractive indices of the carrier fluid and larger particles and applied laser-Doppler velocimetry to measure velocity profiles in a rectangular duct for high concentration of solids (up to 50 vol%).

More recently particle image velocimetry (PIV) has been an effective method for determining velocity and radial position in solid-liquid pipe flows. Lareo et al. (1997a, 1997b) carried out extensive experimentation with vertical upflow for concentrations up to 10%. Using mirrors to the pipe, the radial position of particles could be identified and therefore a detailed velocity profile could be extracted. Three main profiles were identified: partial plug flow in the pipe centre where the particle velocity is independent of radial position, a parabolic profile where particle velocity was dependent on radial position, and a combination of the two.

Although the aforementioned optical techniques are typically straightforward, their applicability are constrained since they require transparent carrier fluids, pipe walls, and low solid concentrations (or refractive index matching). Solid-liquid flows in industry employ substantially higher solid fractions, which are difficult to measure using these techniques due to the limited optical access. To this end, McCarthy et al. (1997) used a magnetic resonance imaging (MRI) technique to investigate residence time curves for two spherical particle sizes (2.5 and 5.0 mm) in a carboxymethyl cellulose (CMC) solution up to 30 wt% solid loading. The method also gave av-

eraged velocity profiles, where the authors discovered flattened velocity profiles in comparison to single-phase flow, with the effect more prominent as solid loading was increased.

Toda et al. (1973) used transparent pipes for measurements in horizontal, vertical, and pipe bends. Radioactive particles with scintillation probes were used to measure the velocities, giving distributions in each tested arrangement. Transparent piping was used for imaging and had no effect on the radioactive measurements. The authors found particle velocities were higher in the vertical arrangement than in the horizontal arrangement. Furthermore, the particle flow in vertical bends with horizontal approaches showed lower velocities than any other bend arrangement.

An efficient flow mapping process for opaque liquids was utilised with the use of an ultrasonic Doppler method, proposed by Takeda (1995). This advance has been effectively utilised to measure velocity profiles as a function of space and time in a multitude of systems such as coal slurries and chocolate transport.

The methods described above however, are intrinsically Eulerian, and cannot track individual particle behaviour independently, rather provided averaged profiles. Positron emission particle tracking (PEPT), is a Lagrangian method which can be used to continuously monitor particles through opaque media, providing space-time data for individually radiolabelled tracers. This method has been effectively investigated by Fairhurst et al. (2001) and Barigou et al. (2003) for pipe flows using 5–10 mm alginate particles at low flows (20–230 mm s^{-1}), presenting a theoretical two-region flow model that predicts accurate residence time distributions for the measured parameters.

2.2 Theory

2.2.1 Flow regimes

There are several different flow regimes that can occur in pipes when transporting solid-liquid mixtures. These regimes are typically characterised by the relative motion between the solids and the liquid and the overall flow behaviour of the mixture. Some common flow regimes include:

- Suspension flow: In this regime, the solids are well-dispersed in the liquid and are suspended in the flow. The solids move along with the liquid, and the overall flow behaviour is similar to that of a single-phase flow. Suspension flow can occur at low solids concentrations and high flow velocities.

- Piston flow: In this regime, the solids form a compact plug in the centre of the pipe, while the liquid flows around the plug. The solids move in a piston-like motion, and the overall flow behaviour is similar to that of a single-phase flow. Piston flow can occur at high solids concentrations and high flow velocities.

- Plug flow: In this regime, the solids form a compact plug in the centre of the pipe, while the liquid flows around the plug. The solids move in a solid-like motion, and the overall flow behaviour is similar to that of a single-phase flow. Plug flow can occur at high solids concentrations and low flow velocities.

- Slurry flow: In this regime, the solids are well-dispersed in the liquid and are suspended in the flow. The solids move along with the liquid, and the overall flow behaviour is similar to that of a single-phase flow. Slurry flow can occur at high solids concentrations and low flow velocities.

- Stratified flow: In this regime, the solids and liquid form distinct layers within the pipe. The solids tend to settle at the bottom of the pipe, while the liquid flows on top. The overall flow behaviour is similar to that of a two-phase flow. Stratified flow can occur at high solids concentrations and low flow velocities.

2.2.2 Forces on spherical particles in Newtonian fluids

There are several forces that can act on spherical solid particles suspended in a Newtonian fluid in a pipe. These forces can influence the motion and behaviour of the particles, as well as the overall flow behaviour of the mixture. Some of the key forces that can act on spherical particles in a Newtonian fluid include:

The **buoyancy force**, which is caused by the difference in density between the particle and the fluid, can be described using the following equation (Crimaldi & Pinsky, 2016):

$$F_b = gV_{particle}\rho_{particle}$$

where F_b is the buoyancy force, g is the acceleration due to gravity, $V_{particle}$ is the volume of the particle, and $\rho_{particle}$ is the density of the particle. The gravitational effect acts in the downward direction and tends to cause the particles to settle towards the bottom of the pipe.

Drag force: The drag force (F_d) acting on a spherical particle moving through a Newtonian fluid is given by the equation:

$$F_d = CdA\rho v^2/2$$

where C_d is the drag coefficient, A is the projected area of the particle, ρ is the

density of the fluid, and v is the velocity of the particle. The drag force acts in the opposite direction to the motion of the particle and tends to cause the particles to slow down.

Lift force: The lift force (F_l) acting on a spherical particle moving through a Newtonian fluid is given by the equation:

$$F_l = C_l A \rho v^2/2$$

where C_l is the lift coefficient. The lift force acts perpendicular to the motion of the particle and can cause the particles to deviate from their original path.

Stokes force: The Stokes force (F_s) acting on a spherical particle moving through a Newtonian fluid is given by the equation:

$$F_s = 6\pi\mu R v$$

where μ is the dynamic viscosity of the fluid, and R is the radius of the particle. The Stokes force acts in the direction of the motion of the particle and tends to cause the particles to speed up.

2.3 Positron emission particle tracking

Positron Emission Tomography (PET), which has been used in medicine extensively, has become one of the most potent and effective imaging modalities. In order to detect functional abnormalities or the development of malignancies, it is used to map the distribution of metabolic fluids, whose molecules have been radiolabelled using positron-emitter radionuclides. The distribution of the metabolic fluid can be

mapped by simultaneously detecting the pair of back-to-back gamma rays produced when a positron annihilates with an electron and by detecting all gamma-ray pairs emerging from various parts of the system and using tomographic image reconstruction techniques. At the University of Birmingham (UK), where the related technique of positron emission particle tracking (PEPT), which allows a single tracer particle to be tracked at high speed within operational equipment, was also developed, the application of PET for engineering processes was pioneered (Parker et al., 1993).

A pair of multiwire detectors were used in the beginning for PEPT, but more recently, a pair of digital gamma camera heads have been used instead. A medical PET/SPECT scanner was purchased by the Positron Imaging Centre in 1999 and reconstructed in a flexible geometry for PEPT investigations (ADAC Laboratories). Fast and precise location of tracer particles that move quickly is now possible.

As previously indicated, the positron camera, a radioactively labelled particle tracer, and a location algorithm are all components of the positron emission particle tracking technique. The apparatus under research is positioned between two position-sensitive detectors used by the positron camera, as shown in fig. 2.1. The positron camera consists of two gamma camera heads that operate simultaneously and are positioned on a motorised gantry that allows them to rotate around a horizontal axis. One sodium iodide crystal is optically connected to a collection of photomultiplier tubes in each detector.

The radioactive tracer that emits positrons is added to the flow. A positron leaves the nucleus and collides with an electron to produce two 511 keV, collinear gamma-rays as a result of their annihilation. The two incident gamma-rays cause scintillations in the crystals inside each detector, which causes the detectors to catch incident gamma-rays throughout a sizable rectangular active region. The corresponding photomultipliers subsequently provide positional signals, which allows the

two 2D centroids to be retrieved.

The position of the positron-emitting particle can be determined at the junction of the photon-trajectories using only a few annihilation events, depending on the location algorithm used (section 2.3.2). The PEPT data is presented as a text file with four columns for the radioactive tracer's three Cartesian coordinates (x, y, and z) and the location time (t). It is also possible to turn this data into an Eulerian description of the flow.

In recent years, flow has been studied using PEPT in a variety of contexts. For instance, Martin et al. (2007) conducted an analysis of the variance in location of a delimited sample of PEPT locations after a given period of time to obtain an indication of phase dispersion in a ribbon bladed mixer. Fangary et al. (2000) used PEPT data to obtain the particle Trajectory Length Distribution in a mechanically agitated non-Newtonian fluid and estimate fluid circulation. The single blade (Laurent and Bridgwater, 2002), high shear (Kuo et al., 2004), ploughshare (Broadbent et al., 1993; Jones and Bridgwater, 1998; Forrest et al., 2003), and planetary (Hiseman et al., 2002) are types of powder mixers where PEPT has produced experimental data.

The method is especially helpful for the study of multiphase flows because it allows one component to be identified and its behaviour to be examined while mapping the flow of fluids and particles (Parker et al., 2002; Barigou, 2004).

2.3.1 ADAC Forte Positron Camera

The PEPT technique relies on the use of gamma cameras to detect the positron events resultant from radioactive tracers. In this study, the camera assembly used was an ADAC Forte consisting of two parallel gamma camera panels on a motorised

gantry. This enabled the gamma camera panels' separation to be controlled between 250–800 mm apart. Furthermore, the gantry enabled a rotation about a horizontal axis.

Each gamma camera panel measures at 590 x 470 mm, with a single sodium iodide crystal optically coupled to an array of 55 photomultiplier tubes. Each photomultiplier is connected to a analogue–to–digital converter to generate a positional signal. A single board computer controls the 55 channels; where a coincidence recording rate of up to 100 kHz can be achieved in the most sensitive region of the camera assembly (Parker et al., 2002). As experiments are conducted, initial coincidence frequencies were between 70–100 kHz, which gradually reduced over time due to the decay of ^{18}F in the tracer until undetectable. This frequency is dependent on the initial activity of the tracer particle and the separation between the gamma ray camera panels.



Figure 2.1: ADAC Forte camera system at the University of Birmingham.

The ADAC Forte system has an intrinsic spatial resolution of 6 mm, however tracer particle positions can be determined with a much higher (sub-millimetre) accuracy

using location algorithms which process information of multiple lines of response to determine the tracer position (section 2.3.2).

The ADAC Forte camera system was used in all experiments discussed in this thesis. In order to achieve the maximum recording frequency and thus highest temporal resolution, the separation of the gamma camera panels was reduced as much as possible. In the case of pipe-flow experiments, this was 300 mm apart.

2.3.2 Location algorithms

Trajectories of tracers during the PEPT measurement are constructed using algorithms which interrogate raw lines of response data generated from the camera system. Although a large number of lines of response are recorded per second, to determine the position of the tracer at any given moment requires triangulation methods which assign multiple lines of response over a short time (e.g., 250 lines of response over 5 ms) to one recorded Lagrangian tracer position. The time stamp assigned to this position is determined by the algorithm used, but is often taken as the average time of the lines of response interrogated. In order to accurately determine the position of the tracer, more lines of response are ideal, however this increases the time of recording and therefore would suffer from a loss of information of a moving tracer. In other words, the spatial and temporal resolution are in competition, resulting in a compromise in the final processed data. A number of distinct algorithms have been developed to maximise both spatial and temporal resolution without losing information and are discussed here.

The Birmingham Method

To track the position of a tracer particle, the Birmingham method (Parker et al., 1993) requires two user parameters; the number of lines of response per time step, N, and the retention fraction, f. As mentioned in the sections above, a high value of N is ideal but will reduce the temporal resolution of the processed data set. The user can interrogate the coincidence frequency of the data, and with a suitable time step for the experimental conditions determine a value of N.

For the first N values in the data, the algorithm determines the minimum distance point between all of the lines of response. Lines furthest from this minimum distance point are then discarded and a new minimum distance point is calculated. The process is repeated until the minimum distance point of fN lines remain, which is given as the tracer position for the first time step. This procedure is repeated for the remaining data, giving a set of Lagrangian particle positions.

As the number of coincidence events for the tracer is determined by chance of radioactive decay and the tracer activity, the time step is not constant for the data set, and is instead given by averaging the N recorded times of the lines of response used for each iteration. Furthermore, as the tracer decays over the duration of the experiment, the coincidence frequency reduces and thereby longer time steps are observed as the experiment continues.

The Birmingham method was also adapted to allow the tracking of multiple particles within the gamma camera field of view at once, but required a significant difference in tracer activity to be successful (Yang et al., 2006). Furthermore, a limitation of this method is the requirement of prior knowledge of how many tracer particles are present in the field of view at any given time, which is not suitable for flow measurements where tracers are entering and exiting the camera field of view

continuously.

The line-density method

The line density method proposed by Bickell et al. (2012) divides the experimental domain into a predefined mesh, of which dimensions are variable considering the camera spatial resolution and computing expense, where the number of lines of response passing through the volumes at any given time (for a short duration) is recorded and analysed. A mesh cell with the most number of lines of response passing through its volume corresponds the the location of the tracer particle for which histograms of the x, y, and z locations are calculated by taking planes of each mesh cell perpendicular to the dimension. Gaussian distributions are fitted to these histograms, determining the position of the tracer within the mesh cell. An advantage of this method is the ability to track multiple tracer particles simultaneously, and has been shown to accurately track up to 8 particles without the requirement of differing tracer activities (Bickell et al., 2012). The algorithm, however, is subject to limitations based on mesh-size dependency which can lead to pixelisation of data.

Wiggins et al. (2017) adopted the line density method, assigning grayscale values to the mesh cells based on the number of line crossings through the cell. This allowed for the use of traditional optical particle tracking methods to be adapted for PEPT data. One such method, known as feature point identification (FPI), uses an iterative cycle with the greyscale mesh data carried out in four stages: smoothing, position estimation, position refinement, and trajectory linking. The FPI method gave accurate results in the study, however poorer spatial resolution compared to alternative G-means clustering methods (described below) were found when tracking one particle. The advantage of FPI is the ability to use fewer lines of response for particle tracking, improving the temporal resolution. The FPI method

also outperformed G-means clustering when dealing with multiple particles.

Clustering methods

A number of data clustering algorithms are widely available, and have been implemented successfully for the use with PEPT data.

Gundogdu (2004) used partitioning around mediods (PAM) clustering with the midpoints of lines of response, where midpoints were defined as the middle of the vector between the closest distance points of two coincidence vectors. Limitations of this method arose when increasing the lines of response, where the clustering method degraded and resulted in discrepancies in position. Given the correct conditions however, the method was capable of tracking up to four particles simultaneously.

Langford et al. (2016) proposed an algorithm combining the Bickell et al. (2012) line density method with a Gaussian clustering (G-means) approach, capable of tracking multiple tracer particles without a prior knowledge of the number of particles or initial particle locations. The study demonstrated successful tracking of 15 particles in a turbulent flow field. As the initiation of the method relies on the line density method, the limitations are therefore similar as the G-means method is subject to mesh-dependency.

Voronoi-based multiple particle tracking

The Voronoi-based multiple particle tracking (VMPT) algorithm proposed by Blakemore et al. (2019) takes advantage of Voronoi tessellations and the ability of cells to become smaller in regions of high data point density. The algorithm consists of a location phase and a tracking phase. The former phase is used to locate individual

particle positions into multiple tracks, and the latter phase is used to combine the track information for simultaneous particle positions.

In the location phase, the lines of response data is split into frames, with each frame containing an equal number of consecutive lines of response. The phase utilises Voronoi tessellations, which divide a volume into nearest-neighbour partitions based on a set of discrete points called seeds. Lines of response are discretised into a set of points separated by a distance equivalent to the particle diameter, and these discrete points are used as seeds for the Voronoi tessellation.

In the tracking phase, a multiple target tracking (MTT) method is used to track data points based only on their positions and velocities. Using a linear least-squares fit, positions on each track are predicted and compared to the points available in a frame, and therefore assigned accordingly depending on a set of conditions.

This method can track at least 20 particles, and requires no prior knowledge of the number or position of tracer particles in the system. Furthermore, tracers entering and exiting the field of view cause no issues with the performance of the algorithm.

Machine learning method

Nicuşan and Windows-Yule (2020) more recently developed a machine learning algorithm to track multiple tracers in a PEPT experiment. The so-called PEPT-ML algorithm, like the VMPT method, requires no prior knowledge of the number or initial position of tracer particles. Similarly, the lines of response data are split into equal frames where cutpoints – the minimum distance point between each pair of lines – are computed. These cutpoints are clustered using a two-pass hierarchical density-based spatial clustering of applications with noise algorithm (HDB-SCAN).

Ultimately a trajectory of every particle is constructed. The algorithm maintains high accuracy with as few as 25 lines of response, and using simulations is capable of tracking up to 128 particles at once.

Currently the PEPT-ML method requires further validation and testing under experimental flow conditions with multiple tracer particles to identify any limitations and required developments.

References

- Averbakh, A., Shauly, A., Nir, A., Semiat, R., 1997. Slow viscous flows of highly concentrated suspensions - part I: laser-doppler velocimetry in rectangular ducts. International Journal of Multiphase Flow 23.

- Barigou, M., Fairhurst, P.G., Fryer, P.J., Pain, J.-P., 2003. Concentric flow regime of solid-liquid food suspensions: theory and experiment. Chemical Engineering Science 58.

- Bickell, M., Buffler, A., Govender, I., Parker, D.J., 2012. A new line density tracking algorithm for PEPT and its application to multiple tracers. Nuclear Instruments and Methods in Physics Research 682, 3641.

- Blakemore, D.M., Govender, I., McBride, A.T., Mainza, A.N., 2019. Multiple particle tracking in PEPT using Voroni tesselations. Chemical Engineering Science 207.

- Broadbent, C.J., Bridgwater, J., Parker, D.J., Keningley, S.T., Knight, P., 1993. A phenomoenological study of a batch mixer using a positron camera. Powder Technology 76.

- Crimaldi, I., & Pinsky, M. (2016). Introduction to Stochastic Flows and the Feynman-Kac Formula. Cambridge University Press.

- Dutta, B., Sastry, S.K., 1990. Velocity distributions of food particle suspensions in holding tube flow: experimental and modeling studies on average particle velocities. Journal of Food Science 55.

- Fairhurst, P.G., Barigou, M., Fryer, P.J., Pain, J.-P., Parker, D.J., 2001. Using positron emission particle tracking (PEPT) to study nearly neutrally buoyant particles in high solid fraction pipe flow. International Journal of Multiphase Flow 27, 18811901.

- Fangary, Y.S., Barigou, M., Seville, J.P.K., Parker, D.J., 2000. Fluid trajectories in a stirred vessel of non-newtonian liquid using positron emission particle tracking. Chemical Engineering Science 55, 59695979.

- Forrest, S., Bridgwater, J., Mort, P.R., Litser, J., Parker, D.J., 2003. Flow patterns in granulating systems. Powder Technology 130.

- Gundogdu, O., 2004. Positron emission tomography particle tracking using cluster analysis. Nuclear Instruments and Methods in Physics Research Section A 534.

- Hiseman, M.J.P., Laurent, B.F.C., Bridgwater, J., Wilson, D.I., Parker, D.J., North, N., Merrifield, D.R., 2002. Granular flow in a planetary mixer. Chemical Engineering Research and Design 80.

- Jones, J.R., Bridgwater, J., 1998. A case study of particle mixing in a ploughshare mixer using positron emission particle tracking. International Journal of Mineral Processing 53.

- Kulick, J.D., Fessler, J.R., Eaton, J.K., 1994. Particle response and turbulence modification in fully developed channel flow. Journal of Fluid Mechanics 277.

- Kuo, H.P., Knight, R.C., Parker, D.J., Adams, M.J., Seville, J.P.K., 2004. Discrete element simulations of a high-shear mixer. Advanced Powder Technology 15.

- Langford, S., Wiggins, C., Tenpenny, D., Ruggles, A., 2016. Positron Emission Particle Tracking (PEPT) for Fluid Flow Measurements. Nuclear Engineering and Design 302, 8189.

- Lareo, C., Branch, C.A., Fryer, P.J., 1997a. Particle velocity profiles for solid-liquid food flows in vertical pipes: I. single particles. Powder Technology 93.

- Lareo, C., Branch, C.A., Fryer, P.J., 1997b. Particle velocity profiles for solid-liquid flows: II. Multiple particles. Powder Technology 93.

- Laurent, B.F.C., Bridgwater, J., 2002. Dispersive granular flow in a horizontal drum stirred by a single blade. AIChE Journal 48.

- Liu, S., Pain, J.-P., Proctor, J., De Alwis, A.A.P., Fryer, P.J., 1993. An experimental study of particle flow velocities in solid-liquid food mixtures. Chemical Engineering Communications 124.

- Martin, T.W., Seville, J.P.K., Parker, D.J., 2007. A general method for quantifying dispersion in multiscale systems using trajectory analysis. Chemical Engineering Science 62.

- McCarthy, K.L., Kerr, W.L., Kauten, R.J., Walton, J.H., 1997. Velocity profiles of fluid/particulate mixtures in pipe flow using MRI. Journal of Food Process Engineering 20.

- Nicuşan, A.L., Windows-Yule, C.R.K., 2020. Positron emission particle tracking using machine learning. Review of Scientific Instruments 91.

- Ohashi, H., Sugawara, T., Kikuchi, K., Henmi, T., 1979. Mass transfer between particles and liquid in solid-liquid two phase up-flow in a vertical tube.

Journal of Chemical Engineering of Japan 12.

- Ohashi, H., Sugawara, T., Kikuchi, K., Ise, M., 1980. Average particle velocity in solid-liquid two-phase flow through vertical and horizontal tubes. Journal of Chemical Engineering of Japan 13.

- Ojiako, U., Fadeyi, O., & Adewumi, M. (2006). Flow of solid-liquid mixtures in pipes. Chemical Engineering Research and Design, 84(A6), 647-658.

- Parker, D.J., Broadbent, C.J., Fowles, P., Hawkesworth, M.R., McNeil, P., 1993. Positron emission particle tracking - a technique for studying flow within engineering equipment. Nuclear Instruments and Methods in Physics Research Section A: Accelerators, Spectrometers, Detectors and Associated Equipment 326, 592607.

- Parker, D.J., Forster, R.N., Fowles, P., Takhar, P.S., 2002. Positron emission particle tracking using the new Birmingham positron camera. Nuclear Instruments and Methods in Physics Research 477, 540545.

- Segré, G., Silberberg, A., 1962a. Behaviour of macroscopic rigid spheres in Poiseuille flow. Part 1. Determination of local concentration by statistical analysis of particle passages through cross light beams. Journal of Fluid Mechanics 14.

- Segré, G., Silberberg, A., 1962b. Behaviour of macroscopic rigid spheres in Poiseuille flow. Part 2. Experimental results and interpretation. Journal of Fluid Mechanics 14.

- Takeda, Y., 1995. Velocity profile measurement by ultrasonic doppler method. Experimental Thermal and Fluid Science 10.

- Toda, M., Ishikawa, T., Saito, S., Maeda, S., 1973. On the particle velocities in solid-liquid two-phase flow through straight pipes and bends. Journal of

Chemical Engineering of Japan 6.

- Wiggins, C., Santos, R., Ruggles, A., 2017. A feature point identification method for positron emission particle tracking with multiple tracers. Nuclear Instruments and Methods in Physics Research Section A: Accelerators, Spectrometers, Detectors and Associated Equipment 843, 2228.

- Yang, Z., Parker, D.J., Fryer, P.J., Bakalis, S., Fan, X., 2006. Multiple-particle trackingan improvement for positron particle tracking. Nuclear Instruments and Methods in Physics Research Section A 564, 332338.

Chapter 3

Investigation on solid-liquid pipe flow using PEPT

3.1 Introduction

Solid-liquid flow in pipes is an important phenomenon that is relevant to a wide range of industries, including chemical, petroleum, and mechanical engineering. Understanding the characteristics and behaviour of solid-liquid flows is essential for the design and operation of pipelines for the transportation of slurries. However, the complexity of solid-liquid flow makes it difficult to accurately predict and model its behaviour. In this experimental study, we aim to investigate the characteristics and behaviour of solid-liquid flow in pipes. Our objective is to determine the effect of key variables, such as the concentration of solids, the size of the particles, and the flow velocity on the behaviour of the flow. To achieve this, we conduced a series of experiments in which one or more of the key variables were varied and measured the resulting flow characteristics using the positron emission particle tracking (PEPT)

technique. The results of these experiments provided valuable insights into the behaviour of solid-liquid flow in pipes and will contribute to the development of more accurate predictive models.

3.2 Experimental methodology

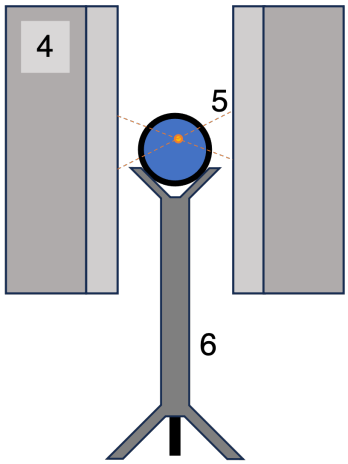
3.2.1 Solid-liquid flow apparatus

In this study, we used a solid-liquid pipe flow rig consisting of a transparent Perspex pipe with an inner diameter of 40 mm and a length of 4 m. The pipe was mounted horizontally on multiple stands, with the inlet end connected to a recessed impeller centrifugal pump and the outlet end connected to a conical vessel containing the solid-liquid mixture. The conical vessel was agitated using a turbine impeller to maintain a homogeneous mixture, with an outlet at the bottom as a feed to the pump, creating a closed loop.

The flow setup was used to observe two systems, the first of which used 36 wt % sugar solution with spherical calcium alginate beads 2 mm 8 mm diameter at weight concentrations ranging from 0 – 30 %. The second configuration used 18 wt% NaCl solution, and the spherical solids 4 mm nylon 66 beads at the same range of weight concentrations. Two carrier fluid systems were chosen to study the effect of Reynolds number, as the sugar solution had a high viscosity (4.5 mPas) in comparison to the NaCl solution which had a viscosity similar to water. Concentrations of each solution were chosen to match the density of solid particles. As alginate particles are porous, a small density difference ($< 4\%$) was unavoidable, hence the particles were nearly neutrally-buoyant. Flow rate was controlled using the pump frequency inverter, and was used to keep a constant Reynolds number between tests as pressure



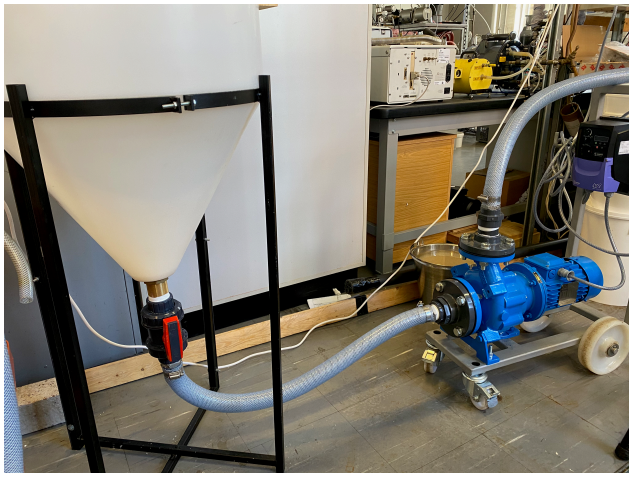
(a) [1]Agitated conical tank, [2]recessed centrifugal pump, [3]pipe test section in ADAC camera



(b) [4]ADAC camera panel, [5]gamma-rays emitted from tracer particle, [6]stand holding pipe section

Figure 3.1: Solid-liquid flow apparatus (not to scale), showing overall setup (a) and axial view of test section (b).

drop changed as solid concentration was increased. The concentration of solids was varied by adding a known mass of beads to the fluid and adjusting the pump frequency to maintain a constant volumetric flow rate. The flow characteristics were measured using a positron emission particle tracking (PEPT) setup, which consisted of measurement area with a length of 350 mm at the outlet end of the straight Perspex pipe. The additional length allowed for flow to steady, negating any entrance effects prior to measurement.



(a) Conical vessel and recessed impeller centrifugal pump with frequency inverter



(b) Test section between ADAC gamma camera panels

Figure 3.2: Apparatus images

3.2.2 Alginate particle preparation

To prepare calcium alginate beads, two 2.5 L solutions were made with 4% (w/w) sodium alginate and 4% (w/w) calcium chloride in pure water, respectively. Using a peristaltic pump, the sodium alginate solution was slowly dripped through a stainless-steel needle into the calcium chloride solution, which was gently stirred. The inner diameter of the needle was varied to produce calcium alginate beads of different sizes (2, 4, 6, and 8 mm). The distance between the needle and the surface of the calcium solution was maintained at 60 cm to control the shape of the beads. Stirring was continued for one hour to ensure complete cross-linking. The calcium alginate beads were then filtered, washed with distilled water, and stored in a concentrated sugar solution in an airtight container one day prior to testing. As the calcium alginate beads are porous structures, consisting of a matrix which traps the surrounding fluid, soaking of the beads prior to testing to allowed the beads to reach an equilibrium density matching the carrier fluid. A minor density difference ($< 4\%$) in the carrier fluid was unavoidable due to the density of the matrix

structure, thereby resulting in nearly neutrally-buoyant beads.

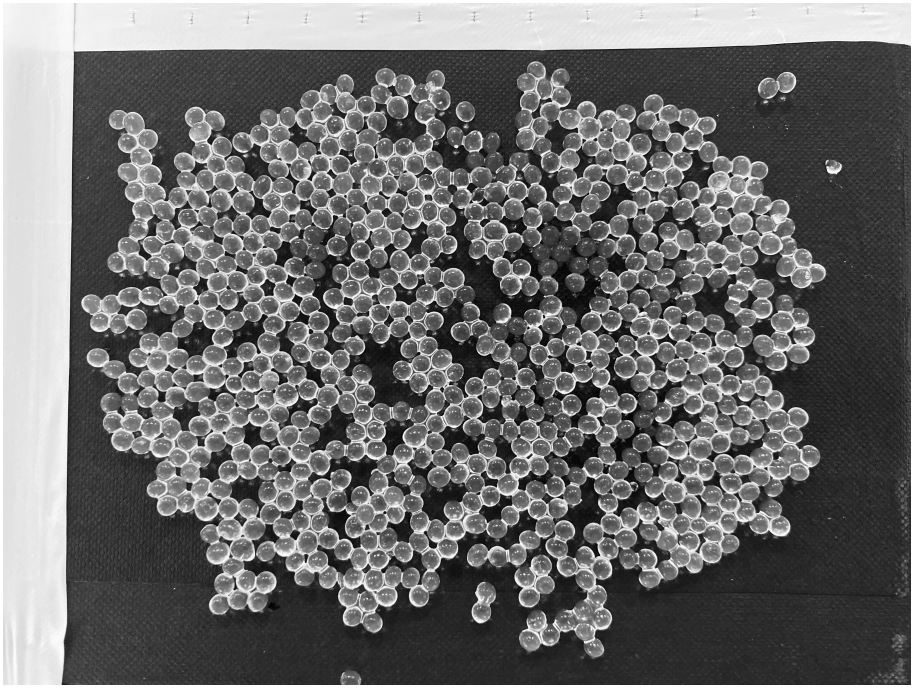


Figure 3.3: A sample of 2 mm spherical calcium alginate particles

3.2.3 Positron emission particle tracking

Flow of the liquid and solid phase were measured using the positron emission particle tracking (PEPT) technique, a non-intrusive method in which a positron emitting tracer particle is accurately tracked within process equipment, providing three-dimensional space and time data for a full Lagrangian trajectory. Details of the PEPT measurement technique, including equipment accuracy can be found in section 2.3. The ADAC Forte camera system was used for experiments, with a spatial resolution of 6 mm. Tracer particle positions could be measured at a much higher accuracy (sub-millimetre) due to the use of multiple lines of response and post-processing PEPT algorithm calculations (see section 2.3.2). Lines of response temporal frequency was between 70–100 kHz, which equated to a tracer position temporal resolution between 3–10 ms. To measure liquid flow, ion exchange resin particles of 300 μm diameter were indirectly labelled with activated water contain-

ing Flourine-18. These activated tracers were then coated with UV-curing resin to prevent leaching of activity into the continuous phase during experiments. Tracers were neutrally buoyant in the study fluids, and up to 8 tracers were added to the flow loop for each test. This allowed for up to 250 tracer passes through the PEPT field of view over a 1.5-hour period, providing positional detections covering the entire pipe cross section for each test resulting in adequate information to describe the flow profiles. Tracers for solid flow were either mixed in sodium alginate solution and dropped into calcium chloride solution to provide encapsulated calcium alginate tracers or inserted into a drilled hole of the solid nylon particles and sealed with UV-curing resin, and a similar number of tracers were added to the flow loop as previously. Solid flow experiments were conducted separately to liquid flow experiments, resulting in two sets of data for each test, one representing liquid flow and the other representing solid flow.

Raw lines of response data from PEPT experiments was processed using the Birmingham algorithm (see section 2.3.2) and post-processed for velocity and occupancy analysis using codes developed in Python 3. Details of the analysis procedure are elaborated in section 3.4.

3.3 Experimental protocol

Experiments conducted resulted in three-dimensional Lagrangian tracer trajectories describing liquid and solid flow. For each test, a number of tracer passes through the field of view were recorded with spatial coordinates at time intervals of around 3–10 ms. Time intervals were irregular due to the nature of the experimental technique. Experiments were conducted to observe the flow effects due to solids concentration, particle size, solid-liquid density difference, and Reynolds number. Table 3.1 shows

the matrix of experiments. Experiments containing solids were tested twice, for

Table 3.1: Solid-liquid flow experiments

Liquid phase	**Dispersed phase**	**Solid concentration (wt %)**	**Particle size (mm)**
Sugar solution (36 wt%)	None	0	-
	Calcium alginate	5	2
			4
			6
			8
		10	2
			4
			6
			8
		20	2
			4
			6
			8
		30	2
			4
			6
			8
	Calcium alginate with 10% silica	5	2
			4
		10	2
			4
		20	2
			4
		30	2
			4
NaCl solution (18%)	None	0	-
	Nylon 66	5	4
		10	4
		20	4
		30	4

independent testing of liquid and solid tracking. For the sugar solution experiments, flow was in the transient regime ($Re \approx 3500$), and for the NaCl solution experiments flow was in the turbulent regime ($Re \approx 15600$). Density of nylon beads matched the density of the NaCl solution providing experiments at neutral buoyancy. Alginate beads without silica were nearly-neutrally buoyant as discussed in section 3.2.2.

3.4 Analysis procedure

The PEPT technique relies on emission of positrons from the tracer colliding with nearby electrons to produce two 511 keV gamma rays emitted 180° to each other.



Figure 3.4: An image of alginate particles flowing in the perspex pipe (2 mm particles, 10 wt%)

The two gamma ray detectors, one placed each side of the test section, are designed to record the time at which a gamma ray detection occurs on both sensor panels, i.e., the time a positron is emitted from the tracer. The position of the gamma ray detection on each panel is also recorded. The result is a table consisting of discrete lines of response defined by a detection time and position on each panel; the columns are time, x_1, y_1, x_2, and y_2, where x and y are the detected gamma ray positions on detector panel 1 and 2 respectively. These lines of response were converted to discrete Lagrangian tracer positions using the Birmingham algorithm, as discussed in section 2.3.2. The resulting Lagrangian data was in the form of a table consisting of discrete tracer detections at a given time, i.e. columns with time, x, y, and z position, and rows for each calculated detection point.

Codes developed in Python 3 were used for post-processing. Firstly, the test section was aligned to the best practical ability to the gamma ray detector panels, however post-processing was used to correct for minute alignment errors. This was achieved by applying a cylindrical mask matching the test section dimensions encapsulating 98% of tracer locations (i.e., ignoring errors in data due to gamma scattering), and calculating the angle of misalignment. The spatial data was multiplied by a rotational matrix of the angle in the opposite direction, giving corrected positions.

Secondly, each tracer pass was separated for residence time calculations. During experiments, tracers would pass through the field of view of the gamma ray detectors, entering on one side, flowing axially, and exiting on the other. The detection system and algorithm used was limited to recording one tracer source in the field of view at once. During the time the tracer was not in the field of view, no presence of gamma rays were detected and therefore no lines of response were recorded. As a new tracer entered the field of view, new lines of response data was recorded, appended to the data already recorded. For residence time calculations, these tracer passes needed to be separated from one another. Multiple tracer particles were used in a staggered entry to the system, to optimise the experimental time as tracer activity reduced over time, limiting the overall length of experiments. This meant, however, time stamp of locations could not be used to distinguish tracer passes as often the stream of data was mostly continuous. Instead, the separation of the tracer passes in the data was achieved by interrogating the axial (flow direction) positions. By computing the difference between the axial position of one detection to the next detected tracer location, the direction of travel of the tracer could be determined. If the difference was positive, this indicated that the tracer location belonged to the same pass through the detector panels. If the difference was negative, however, this indicated that a new tracer had entered the field of view and the subsequent data belonged to a separate pass.

Experimental trajectories required further processing to compare experimental results to one another, as Lagrangian trajectories cannot be directly compared to observe effects between cases. The following analyses were conducted to provide comparisons:

1. Axial velocity profiles in the centre of the pipe

2. Axially-averaged velocity maps depicting distribution across the pipe cross-

section

3. Axially-averaged occupancy maps depicting distribution across the pipe cross-section

3.4.1 Axial velocity profiles

To compute axial velocity profiles for each case, data belonging to a vertical pseudo-plane (2 mm thick) in the centre of the pipe was masked and extracted. This plane was then separated into 11 equal cells with length equal to the axial field of view. Masked tracer detections in each cell had velocities calculated for each position, by taking the differential in position and time to the sequential detected position. Mean velocity for each cell was computed using a time-average; by taking the summation of each velocity multiplied by its respected differential time to the next detection, then dividing by the total time detected in each cell. This mitigated any bias due to non-uniform distribution of detections from cell to cell. As a distribution of velocities were detected for each cell, each figure shown includes error bars which represent one standard deviation below and one standard deviation above the mean value, i.e., representing 68% of the velocities detected in that particular region.

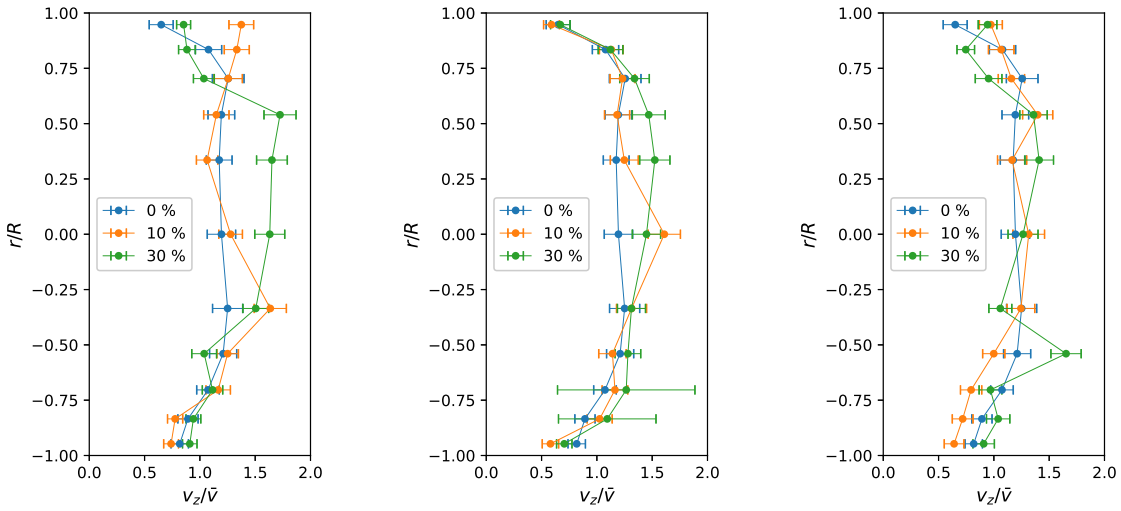
3.4.2 Axially-averaged Eulerian maps

For the Eulerian maps, the pipe cross section was separated into equal volume cells with 15 cells in the r – direction and 30 cells in the θ – direction. Mean velocity in each cell was calculated as mentioned in section 3.4.1. Occupancy for each cell was determined by computing the total time spent by tracers in each cell and dividing by the ergodic time, i.e., summation of tracer detection time divided by the number

of cells (450).

3.5 Experimental results and discussion

3.5.1 Effect of solid concentration and particle size



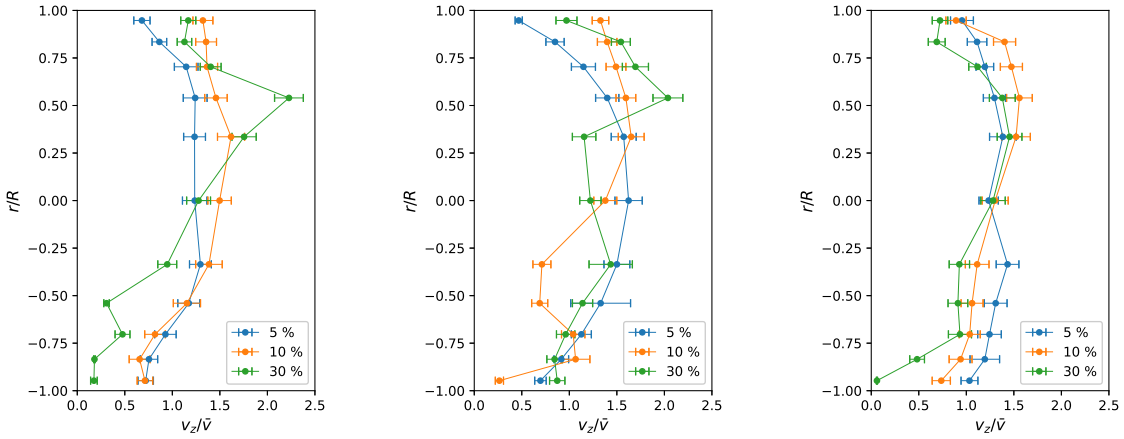
(a) 2 mm calcium alginate beads

(b) 4 mm calcium alginate beads

(c) 6 mm calcium alginate beads

Figure 3.5: Effect of solid concentration on axial liquid flow velocity, $Re = 3500$

Figure 3.5 shows the effect of increasing solid concentration on the liquid flow profile for various sizes of alginate beads. As expected, flow with 0% solids results in a flat velocity profile, describing a turbulent flow field. Increasing the solids concentration has a small effect on the flow profile, with the maximum velocity skewing towards the top of the pipe section. Although the alginate beads are nearly neutrally-buoyant, a small density effect can be seen as liquid flow is faster at the top region, indicating more friction in the lower section of the pipe. This implies the solids are more present in the lower section than the top. These effects are more noticeable with smaller alginate beads, as shown in figure 3.5a.



(a) 2 mm calcium alginate beads

(b) 4 mm calcium alginate beads

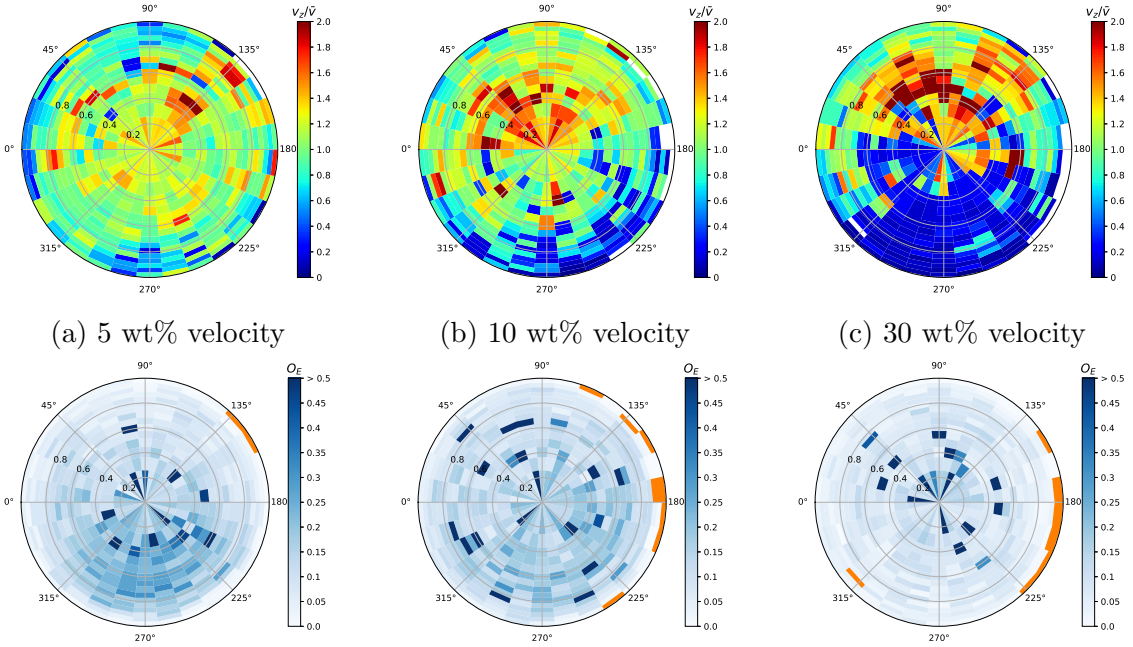
(c) 6 mm calcium alginate beads

Figure 3.6: Effect of solid concentration on axial solid flow velocity, $Re = 3500$

Figure 3.6 shows the effect of increasing solid concentration on the solid flow profiles for various sizes of alginate beads. A trend similar to the liquid flow is found, where increasing solid loading skews the velocity profile such that the maximum velocity is observed higher than the pipe centre. With only 5 wt% of solids loading, the flow profile is mostly similar to a turbulent liquid profile. Increasing the solid concentration results in the velocity in the lower section of the pipe to reduce and the velocity in the higher section of the pipe to increase. Again, this effect is more prominent with smaller alginate beads. The change in velocity profiles is more aggressive for solid flow than the liquid flow, with significant reductions in velocity in the bottom section of the pipe. The small density difference results in more particles present in the lower section, inducing more friction and thereby reducing velocity. Due to conservation of mass, the velocity at the top of the pipe section must increase at a set flow rate. Furthermore, it is clear increasing the concentration of particles results in a more erratic (error-prone) profile, most likely due to the increased chaos due to particle-particle interactions.

Figure 3.7a - 3.7c shows the axial velocity distributions for 2 mm alginate beads at different solid concentrations. The velocity maps show a gradual shift in velocity

distribution, with a mostly turbulent map for 5 wt%, followed reduced velocities in the lower sections for 10 wt%. This effect is increased at 30 wt%. The difference in velocity is further emphasised by the change in contrast; figure 3.7a shows a low variation in colour, whereas the difference in colour is increased as the concentration is increased, i.e., there is more variation in velocity at higher solid concentrations. The area in which velocity is reduced increases as the concentration increases, where more particles are present to result in higher friction and thereby reduced velocity.



(a) 5 wt% velocity (b) 10 wt% velocity (c) 30 wt% velocity

(d) 5 wt% occupancy (e) 10 wt% occupancy (f) 30 wt% occupancy

Figure 3.7: Effect of concentration of 2 mm alginate beads on solid flow distribution, $Re = 3500$

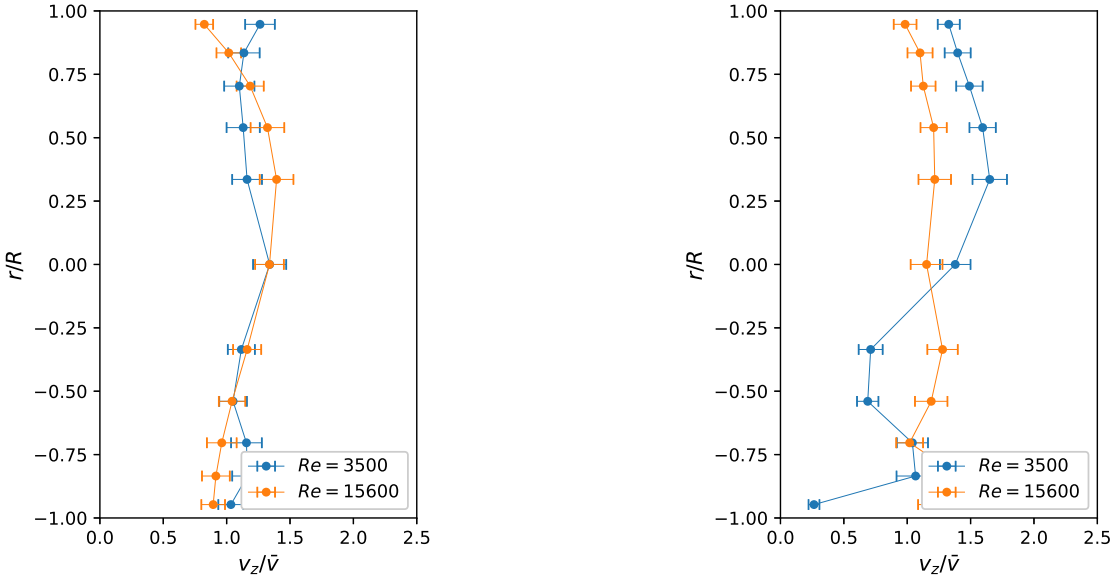
Occupancy maps for the same conditions are shown in figures 3.7d - 3.7f. Occupancy refers to the total time tracers spent in each cell as a fraction of the cell ergodic time, t_E, which is equal to the total experimental time divided by the total number of cells. Zones in dark blue indicate areas which tracers have spent more time than the ergodic time, with orange areas indicating zones with no tracer detections. Figure 3.7d shows that occupancy is higher below the pipe centre line when concentration is low, with the most time spent in regions close to the pipe centre as shown by the dark blue areas. As concentration is increased to 10 wt% (figure 3.7e), occupancy is more

evenly distributed across the pipe section, with highest times more radially dispersed. Increasing the concentration further to 30 wt% results in an even more distributed occupancy map with an almost even map. The occupancy results may seem to contradict findings from velocity profiles discussed above, however can be explained due by taking into consideration a hypothetical 100 wt% experiment would result in a perfectly even distribution of occupancy; in other words increasing concentration should result in more distributed solids.

3.5.2 Transient and turbulent flow

Solid-liquid experiments were also conducted 18 wt% NaCl solution as the liquid phase, resulting in turbulent flow. Figure 3.8 shows the effect of Reynolds number on the liquid and solid velocity profiles. Liquid velocity shows a turbulent profile for both instances, with a mostly uniform velocity across the cross section. For the solid velocities, however, increasing the Reynolds number results in a change in velocity profile. In transient flow, solids in the lower region of the pipe section experience lower velocities, with an increased velocity above the pipe centre line. Increasing the Reynolds number to turbulent flow results in a more uniform velocity profile, indicating particles are suspended in the flow and causing a uniform friction effect in the flow.

Figure 3.10 shows the effect of flow regime on velocity and occupancy maps for solid and liquid flow. Liquid flow displays similar characteristics in both flow regimes, with velocity and occupancy showing mostly uniform distributions. A stark difference can be observed with the solid flow, with a skewed velocity profile at lower Reynolds number (figure 3.10e) in comparison to a uniform velocity as shown in 3.10f. Occupancy for solids also exhibits the same profiles, with high occupancy in the lower half of the pipe section for transient flow (figure 3.10g) in comparison to



(a) Liquid velocity

(b) Solid velocity

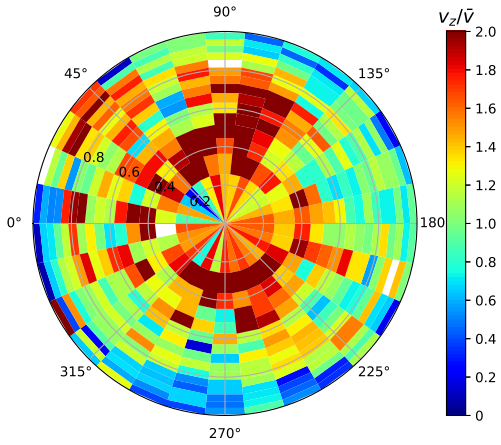
Figure 3.8: Effect of Reynolds number on liquid and solid velocity profiles

uniform occupancy shown in turbulent flow (figure 3.10h). As expected, increased turbulence in the flow results in solids being more suspended in the bulk flow, resulting in more uniform profiles at high solids loading.

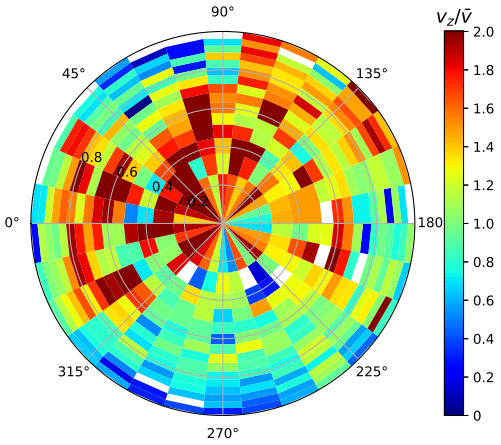
3.5.3 Effect of solid-liquid density difference

Increasing the density difference between the solid phase and liquid phase has some adverse effects on the suspension flow. Figure 3.9 shows the velocity and occupancy profiles for flow containing nearly-neutrally buoyant alginate beads compared to flow with alginate beads containing 10 wt% silica. As expected, maximum velocity for nearly-neutrally buoyant alginate beads is slightly skewed above the pipe centre. This effect is more prominent with the more dense particles, where a larger difference in velocity above and below the pipe centre can be observed. As denser particles are less likely to be entrained in the bulk flow, more of the bottom section of pipe is occupied by particles (figure 3.9d), causing more friction and resulting in lower flow

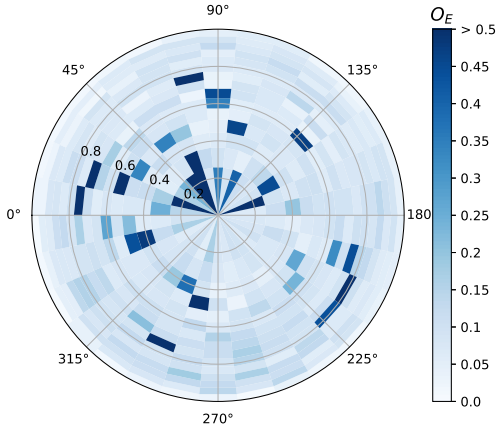
velocities.



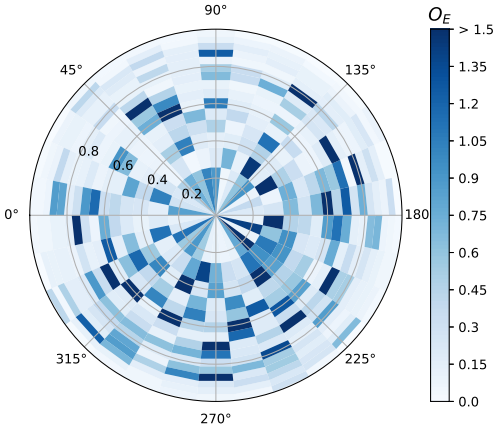
(a) 0% silica, velocity



(b) 10% silica, velocity



(c) 0% silica, occupancy



(d) 10% silica, occupancy

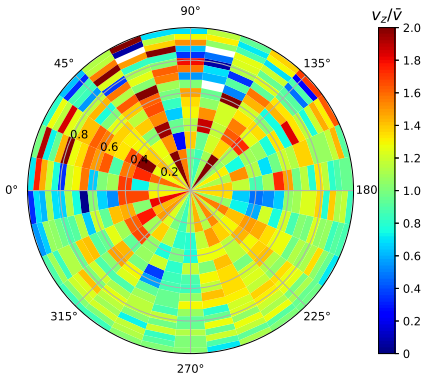
Figure 3.9: Effect of particle density on solid velocity profiles, 30 wt% loading of 4 mm particles, $Re = 3500$

3.6 Conclusions

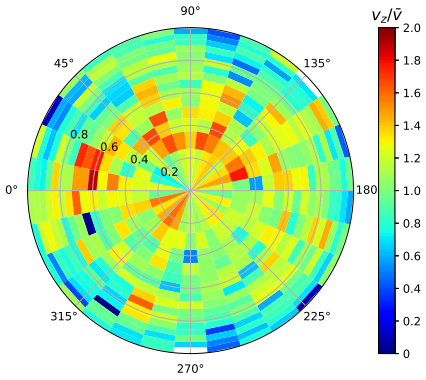
In conclusion, the effect of solid concentration on flow and mixing in a pipe was studied using PEPT and alginate beads of different sizes. Increasing solid concentration had a small effect on the liquid flow profile, with the maximum velocity skewing towards the top of the pipe section. A trend similar to the liquid flow was found for solid flow profiles, where increasing solid loading skewed the velocity profile such

that the maximum velocity was observed higher than the pipe centre. The change in velocity profiles was more prominent for solid flow than the liquid flow, with significant reductions in velocity in the bottom section of the pipe. The difference in velocity between low and high solid concentrations was further emphasised in axial velocity distributions and occupancy maps. The results of these experiments can provide insight into solid-liquid flow and mixing in pipes and the effect of solids on the flow field.

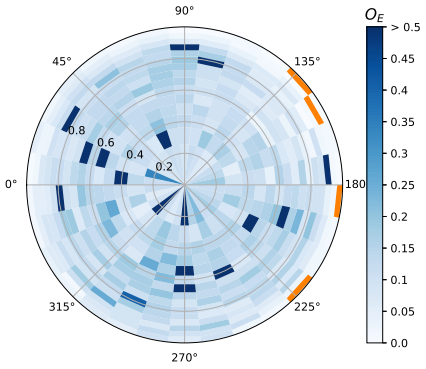
The PEPT technique allowed for the investigation into pipe flow where optical access is not possible due to the solid loading. Insights into the internal flow profiles of both the fluid and solids were measured with small standard deviations, indicating good repeatability. A limitation of the technique, however, is the number of detected positions for each pass of the tracer particle. This is due to the speed at which the tracer was moving, and its radioactivity. A fast moving tracer with a low activity would result in only a few traced locations for averaging, therefore reducing the reliability of measurements taken in that instance. Furthermore, there was no control of the inlet position of the tracer across the cross-section of the pipe, therefore experiments were run for a long time to ensure adequate coverage of detections across the entire profile of the pipe section. Calculations in the analysis (time-averaging & use of ergodic time) aimed to mitigate the effect of this, however one cannot say for certain that the results are free from any spatial bias. Nonetheless, experiments were repeatable and had mostly small deviations, and therefore are likely to show appropriate trends.



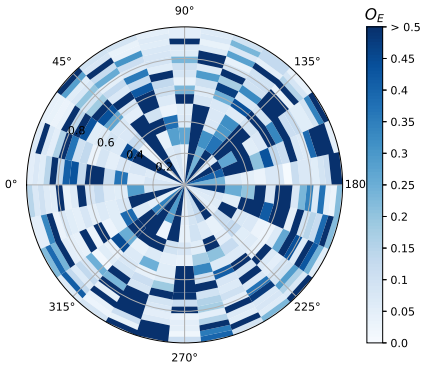
(a) $Re = 3500$, liquid velocity



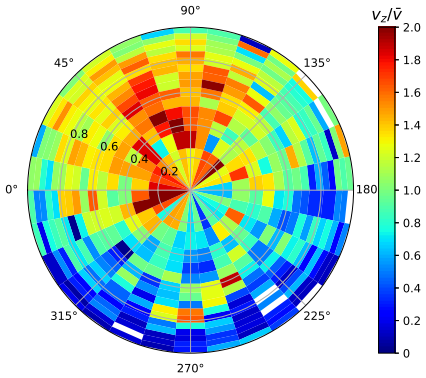
(b) $Re = 15600$, liquid velocity



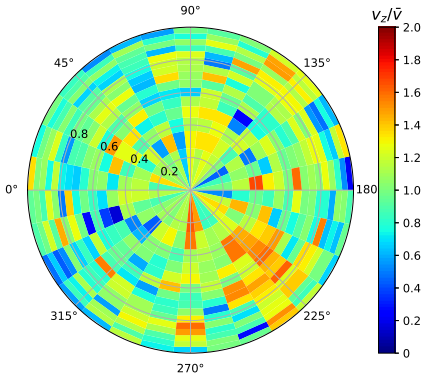
(c) $Re = 3500$, liquid occupancy



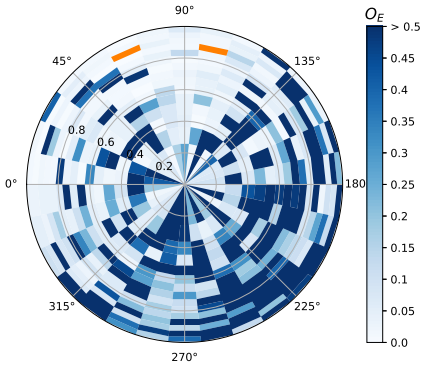
(d) $Re = 15600$, liquid occupancy



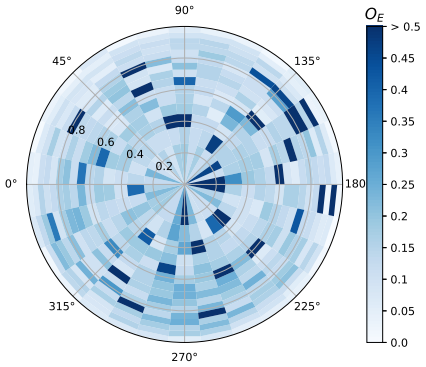
(e) $Re = 3500$, solid velocity



(f) $Re = 15600$, solid velocity



(g) $Re = 3500$, solid occupancy



(h) $Re = 15600$, solid occupancy

Figure 3.10: Effect of Reynolds number on liquid and solid flow, concentration = 30 wt%

Part II

Modelling of three-dimensional solid-liquid flow in stirred vessels using novel Lagrangian methods

Chapter 4

Solid-liquid flow in mixing vessels

4.1 Literature review

4.1.1 Introduction

Mixing is an essential process in many industrial applications, such as chemical processing, food and beverage production, and pharmaceutical manufacturing. In these applications, mixing vessels are commonly used to homogenise different materials and achieve a desired product quality. One important aspect of mixing is the flow of solid-liquid mixtures, which can have a significant impact on the mixing performance and efficiency.

Solid-liquid mixtures can exhibit various flow behaviours, depending on the properties of the solid and liquid phases and the operating conditions of the mixing vessel. For example, the flow of solid-liquid mixtures can be classified as laminar, transitional, or turbulent, depending on the Reynolds number, which is a dimensionless

measure of the flow intensity. Laminar flow occurs at low Reynolds numbers and is characterised by smooth, orderly flow patterns. Transitional flow occurs at intermediate Reynolds numbers and exhibits a mixture of laminar and turbulent flow characteristics. Turbulent flow occurs at high Reynolds numbers and is characterised by chaotic and irregular flow patterns.

The flow behaviour of solid-liquid mixtures can have a significant impact on the mixing performance and efficiency. Laminar flow can lead to slower mixing times and poorer mixing uniformity compared to turbulent flow. On the other hand, turbulent flow can lead to higher energy consumption and the potential for mechanical damage to the mixing equipment. Therefore, it is important to understand and control the flow behaviour of solid-liquid mixtures in mixing vessels in order to optimise the mixing performance and efficiency.

One way to control the flow behaviour of solid-liquid mixtures in mixing vessels is by selecting appropriate mixing impellers and operating conditions. Mixing impellers are mechanical devices that are used to generate flow and mixing in the vessel. Different types of impellers, such as axial flow impellers, radial flow impellers, and tangential flow impellers, can be used to achieve different flow patterns and mixing characteristics. The choice of impeller type and operating conditions, such as impeller speed and vessel geometry, can have a significant impact on the flow behaviour of solid-liquid mixtures.

In addition to impeller selection and operating conditions, the properties of the solid and liquid phases can also influence the flow behaviour of solid-liquid mixtures in mixing vessels. For example, the particle size, shape, and density of the solid phase, as well as the viscosity and surface tension of the liquid phase, can all affect the flow behaviour of the mixture. Understanding the influence of these properties on the flow behaviour can be useful for designing and optimising mixing systems for

specific applications.

In industrial settings, mechanically agitated vessels are frequently used to handle solid-liquid suspensions such as bio-slurries, minerals, food, crystallisation, and catalytic mixes. To provide a fair distribution of all the different phase components and enable an effective interaction between them, excellent mixing is a critical component of this process. A more thorough description of the internal flow structure is required in order to create more logical guidelines for equipment and process design. Traditionally, stirred vessels for solid-liquid mixing have been designed using global methodologies, without the need for understanding of physical intricacies of the flow. An increased effort is being made to better understand the mechanisms behind particle suspension and distribution in these systems as a result of the development of powerful measurement and modelling techniques in recent years (Kagoshima and Mann, 2006; Guha et al., 2007; Unadkat et al., 2009; Tamburini et al., 2009).

4.1.2 Experimental studies

Due to a lack of appropriate measuring techniques capable of probing opaque multiphase systems, comprehensive experimental exploration of these phenomena has remained a significant issue for decades (Barigou, 2004). For examining complex flow fields in optically transparent single-phase systems, laser Doppler velocimetry (LDV) and particle image velocimetry (PIV) have emerged as the most trustworthy flow visualisation approaches (Ducci and Yianneskis, 2006; Chung et al., 2007; Tamburini et al., 2013). However, due to the full failure of these approaches in dense, opaque systems, application to multi-phase investigations has only been limited to diluted suspensions.

A single vertical conductivity or capacitance probe traverse or a withdrawal tech-

nique have been the main methods used to make local measurements in these complex systems, which have primarily been limited to the measurement of mean axial solid-concentration profiles at relatively low concentrations (Barresi and Baldi, 1987; Nasr-El-Din et al., 1996; Brunazzi et al., 2004). Recent experimental experiments using electrical resistance tomography (ERT) have shown, albeit primarily qualitatively, how visualisation of the distribution of gas, solid, or liquid might help to better understand mixing processes (Wang et al., 2000). More recently, Rossi et al. (2022) used acoustic measurements coupled with machine learning algorithms to identify the solid-liquid suspension state, with very high accuracy. None of these techniques, however, is able to thoroughly probe concentrated suspensions in order to get quantitative data on the local flow dynamics of the various phase components or their unique 3-D distributions.

According to a number of mixing studies, changes in particle size have a considerable impact on the fluid dynamics and phase distribution in stirred solid-liquid systems. For instance, LDV experiments by Virdung and Rasmuson (2007) demonstrated that the fluid velocity fluctuations resulting from turbulence in the liquid phase were larger in solid-liquid suspensions than in single phase flow, with an effect that grew with particle size. Altway et al. (2001) demonstrated that the pattern of solid concentration contours for various particle sizes was qualitatively similar, although smaller particles had a more uniform distribution, despite the fact that their simulations encompassed particle sizes less than 0.1 mm. Smaller solid particles provide a more homogenous dispersion, which was experimentally verified by Pidla et al. (2005) using larger particles with 0.1 mm $< d <$0.5 mm. Additionally, their findings demonstrated that when the average solid concentration increased, the homogeneity of the solid-liquid suspension improved.

Based on gamma-ray emissions, Rammohan et al. (2001) created a more complex computer automated radioactive particle tracking (CARPT) method. For some

time, it has been argued that, in cases where such data can be accurately determined, Lagrangian data derived from a single particle trajectory may reveal important mixing information that is not revealed by Eulerian observations (Villermaux, 1996; Wittmer et al., 1998; Doucet et al., 2008; Guida et al., 2009; Barigou et al., 2009; Liu & Barigou, 2015). By utilising a single tiny sub-millimeter positron-emitting particle as a flow tracer, the positron emission particle tracking (PEPT) technology enables non-invasive probing of opaque fluids and within opaque apparatus (Parker and Fan, 2008). PEPT is especially helpful for the study of non-transparent multi-phase or multi-component flows, where one component can be selectively labelled and its behaviour observed, because it can examine flow phenomena in three dimensions in dense opaque systems that could not be observed as effectively by using other techniques (Fangary et al., 2000).

4.1.3 Computational studies

Alongside experimental studies, numerous computational methods have been adopted to provide an in-depth granular understanding of solid-liquid flow in stirred vessels. As discussed above (section 4.1.2), many experimental techniques are hampered due to the requirement of optical access, thereby limiting the study of high solid-loading slurries. Therefore, utilising computational methods (verified with experimental data) is an attractive avenue for understanding the complex flows.

It would be possible to create solid-liquid mixes with logical design and ideal mixing operation with knowledge of local as well as global flow characteristics. Even for relatively straightforward flow scenarios like single-phase flows, computational fluid dynamics (CFD) has so far demonstrated to be a potent and trustworthy method for predicting local fluid dynamics in mixing vessels (Van den Akker, 2006). The highly complicated flow field, which comprises intricate interactions between continuous

and dispersed phase, dispersed phase and flow borders, and amongst dispersed particles, makes it difficult to simulate the hydrodynamics of multiphase stirred vessels. In order to accurately represent all of the complicated flow interactions, it is still unclear how such multiphase flow simulations should be set up and how to choose the best models among those that are now available.

Euler-Euler and Euler-Lagrange are the two primary CFD techniques for multiphase flow modelling. Both continuous and scattered phases are seen as continua that can interact with one another in the Euler-Euler paradigm. The governing equations are developed using averaging techniques based on volume, time, or ensemble averages. Therefore, particles with a specific mass are represented to replicate the momentum exchange at a place. In other words, rather than computing particle attributes, the simulation entails calculating the average solid volume concentration, the average local solid phase velocity, and related factors.

However, the liquid phase is considered as a continuous phase and treated using an Eulerian scheme in the Euler-Lagrange technique, whereas particles are viewed as discrete phases and are tracked individually using force balance analysis. This approach is better able to handle complicated flow phenomena and yields findings that are more accurate representations of the multiphase flow itself. The Euler-Langrage approach has benefits like giving complete information on particle trajectories and local residence time, handling a distribution of particle sizes, and predicting differences in local particle velocities. Particle-particle collisions and particle-wall interactions can also be realistically handled, though at increased computational cost (Farzpourmachiani et al., 2011). Recently, Jadhav & Barigou (2022) implemented the Euler-Lagrange CFD method and directly compared the results with experimental PEPT data, with accurate predictions of 3D phase-velocity components and local particle concentrations.

Another numerical method used for studying flow systems is smoothed particle hydrodynamics (SPH), a purely Lagrangian framework where the physical system (including fluids) is represented by particles reacting to internal interactions and external forces. Integral representation methods are used for the approximation of field fluid functions. The method is attractive as the necessity to solve partial derivative Navier-Stokes equations is eliminated, and replaced with ordinary derivatives of momentum based flow. Very few studies using the SPH method in solid-liquid stirred vessels have been conducted, due to the very high computational cost to spatial accuracy ratio. For high resolution, a large number of particles are required to represent the flow accurately, which significantly impacts the calculation power required. Shamsoddini et al. (2015) applied a weakly compressible SPH method to model micromixing in a 2D cylindrical paddle mixer, and investigated the effects of different types and positions of blades, and hardware limited the resolution for which the system could be studied. This was also the reason for two-dimensional modelling. The SPH method was also adopted by Nikolić % Frawley (2016), who took advantage of CUDA GPU technology in parallelisation of a 3D stirred vessel for modelling batch crystallisation. The authors found the classical grid-based finite volume methods provided more detailed representations of the turbulent flow conditions than the SPH method. SPH gave a good representation of global mean flow, however requires development of turbulence models for its application.

The following chapters investigate the use of computationally efficient data-driven models, with the purpose of extending experimental data or Lagrangian information obtained from costly CFD computations. Furthermore, this approach lends itself to extending experimental Lagrangian data such as those obtained using the PEPT technique, which can be limited by real-world factors such as tracer radioactive decay. These methods were carried out on relatively basic hardware utilised open-source programming (Python 3); more readily available in the industrial environment

where extensive CFD or experimental studies are perhaps more cumbersome tasks.

4.2 Experimental methodology

Chapters 5 - 8 use a common set of experimental data, originally conducted by Dr. Antonio Guida and Dr. Li Liu. Data has been previously verified by the aforementioned authors, and extensively investigated in the field of solid-liquid flow in mixing vessels (Guida et al., 2009; Liu & Barigou, 2015; Jadhav & Barigou, 2022). This section provides an overall summary of the apparatus used.

Figure 4.1 depicts a flat-bottom mixing vessel of diameter $T = 288mm$ was filled with water such that the static fluid height $H = T$. Four baffles of width $B = T/10$ were included in the setup, and the fluid was agitated using an interchangeable impeller of diameter $D = T/2$ and off-bottom clearance of C_{imp}. Three impeller configurations were studied; a 6-blade 45° pitched blade turbine with $C_{imp} = T/4$ in an up-pumping or down-pumping configuration, and a 6-blade Rushton disc turbine (RDT) with $C_{imp} = T/3$. Both impellers had a blade width $W = T/10$. Impeller rotation speeds were varied from 100-500 rpm ($Re_{imp} = 130,000 - 655,000$).

Water was used as the continuous phase, and spherical 3 mm diameter glass beads with specific gravity = 2.5 were added in different solid concentrations ranging from 5.2–40 wt% (2.5–24 vol%).

Tracking of the liquid was achieved by technique of positron emission particle tracking. A $600\mu m$ spherical resin particle was radioactively labelled to emit positrons and added to the fluid. Small quantities of salt were added to the water to maintain a neutral buoyancy. The long-term trajectory of the liquid was observed using cameras sensitive to gamma-rays capable of tracking 3D particle position with millimetre

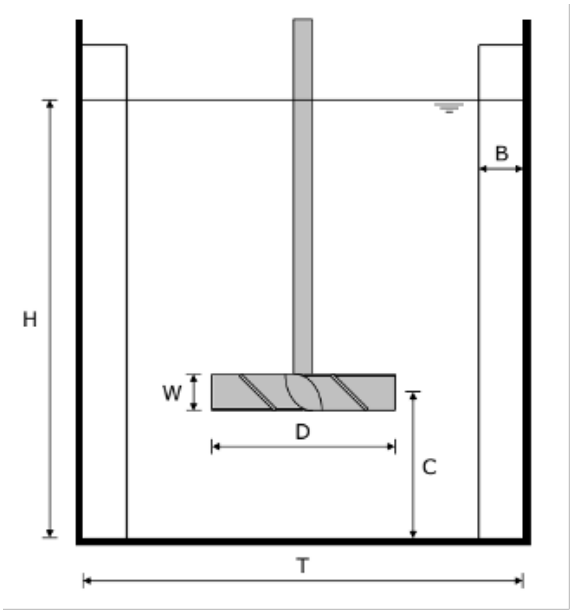


Figure 4.1: Mixing vessel dimensions

Table 4.1: Experimental flow conditions.

Flow system	Solid concentration (wt%)	(vol%)	*N or Njs (s-1)* PBTD	PBTU	Impeller Reynolds number Re_{imp} ($\times 10^5$) PBTD	PBTU
Single-phase	0	0	1.67 (100 rpm)	1.67 (100 rpm)	0.40	0.40
			2.50 (150 rpm)	2.50 (150 rpm)	0.60	0.60
			4.33 (260 rpm)	4.33 (260 rpm)	1.03	1.03
			5.00 (300 rpm)	5.00 (300 rpm)	1.19	1.19
			5.50 (330 rpm)	5.50 (330 rpm)	1.31	1.31
			6.67 (400 rpm)	6.67 (400 rpm)	1.59	1.59
			8.33 (500 rpm)	8.33 (500 rpm)	1.98	1.98
Particle-liquid	5.2	2.5	6.00 (360rpm)	6.25 (375rpm)	1.43	1.49
	10.6	5.2	6.83 (410rpm)	6.75 (405rpm)	1.63	1.61
	20.0	10.4	8.17 (490rpm)	7.83 (470rpm)	1.94	1.87
	40.0	23.6	9.83 (590rpm)	9.67 (580rpm)	2.34	2.31

and millisecond precision. In the cases of solid phase tracking, one glass particle was directly radiolabelled as the tracer and added to the flow.

References

- Altway, A., Setyawan, H., Margono, Winardi, S., 2001. Effect of particle size on simulation of three-dimensional solid dispersion in stirred tank. Chemical Engineering Research and Design 79.

- Barigou, M., 2004. Particle Tracking in Opaque Mixing Systems: An Overview of the Capabilities of PET and PEPT. Chemical Engineering Research and Design 82, 12581267.

- Barresi, A., Baldi, G., 1987. Solid dispersion in an agitated vessel. Chemical Engineering Science 42, 29492956.

- Brunazzi, E., Galletti, C., Paglianti, A., Pintus, S., 2004. An Impedance Probe for the Measurements of Flow Characteristics and Mixing Properties in Stirred Slurry Reactors. Chemical Engineering Research and Design 82, 12501257.

- Chung, K.H.K., Barigou, M., Simmons, M.J.H., 2007. Reconstruction of 3-D flow field inside miniature stirred vessels using a 2-D PIV technique. Chemical Engineering Research and Design 85.

- Chung, K.H.K., Simmons, M.J.H., Barigou, M., 2009. Angle-resolved particle image velocimetry measurements of flow and turbulence fields in small-scale stirred vessels of different mixer configurations. Industrial & Engineering Chemistry Research 48.

- Doucet, J., Bertrand, F., Chaouki, J., 2008. A measure of mixing from Lagrangian tracking and its application to granular and fluid flow systems. Chemical Engineering Research and Design 86.

- Ducci, A., Yianneskis, M., 2006. Turbulence kinetic energy transport processes in the impeller stream of stirred vessels. Chemical Engineering Science 61.

- Fangary, Y.S., Barigou, M., Seville, J.P.K., Parker, D.J., 2000. Fluid trajectories in a stirred vessel of non-newtonian liquid using positron emission particle tracking. Chemical Engineering Science 55, 59695979.

- Guha, D., Ramachandran, P.A., Dudukovic, M.P., 2007. Flow field of suspended solids in a stirred tank reactor by Lagrangian tracking. Chemical

Engineering Science 62, 61436154.

- Guida, A., Nienow, A.W., Barigou, M., 2010. PEPT measurements of solid-liquid flow field and spatial phase distribution in concentrated monodisperse stirred suspensions. Chemical Engineering Science 65, 19051914.

- Jadhav, A.J., Barigou, M., 2022. Eulerian-Lagrangian modelling of turbulent two-phase particle-liquid flow in a stirred vessel: CFD and experiments compared. International Journal of Multiphase Flow 155.

- Kagoshima, M., Mann, R., 2006. Development of a networks-of-zones fluid mixing model for an unbaffled stirred vessel used for precipitation. Chemical Engineering Science 61, 28522863.

- Liu, L., Barigou, M., 2015. Lagrangian particle tracking in mechanically agitated polydisperse suspensions: Multi-component hydrodynamics and spatial distribution. International Journal of Multiphase Flow 73, 8089.

- Nasr-El-Din, H.A., Mac Taggart, R.S., Masliyah, J.H., 1996. Local solids concentration measurement in a slurry mixing tank. Chemical Engineering Science 51.

- Nikolić, D.D., Frawley, P.J., 2016. Application of the Lagrangian meshfree approach to modelling of batch crystallisation: Part I - Modelling of stirred tank hydrodynamics. Chemical Engineering Science 145.

- Rammohan, A.R., Kemoun, A., Al-Dahhan, M.H., Duduković, M.P., 2001. A Lagrangian description of flows in stirred tanks via computer-automated radioactive particle tracking (CARPT). Chemical Engineering Science 56.

- Rossi, A., Alberini, F., Brunazzi, E., 2022. Identification of suspension state using passive acoustic emission and machine learning in a solid-liquid mixing system. Chemical Engineering Research and Design 177.

- Shamsoddini, R., Sefid, M., Fatehi, R., 2015. Lagrangian simulation and analysis of the micromixing phenomena in a cylindrical paddle mixer using a modified weakly compressible smoothed particle hydrodynamics method. Asia-Pacific Journal of Chemical Engineering 10.

- Tamburini, A., Cipollina, A., Micale, G., Brucato, A., 2013. Particle distribution in dilute solid liquid unbaffled tanks via a novel laser sheet and image analysis based technique. Chemical Engineering Science 87.

- Tamburini, A., Cipollina, A., Micale, G., Ciofalo, M., Brucato, A., 2008. Dense solid-liquid off-bottom suspension dynamics: Simulation and experiment. Chemical Engineering Research and Design 87, 587597.

- Unadkat, H., Rielly, C.D., Hargrave, G.K., Nagy, Z.K., 2008. Application of florescent PIV and digital image analysis to measure turbulence properties of solid-liquid stirred suspensions. Chemical Engineering Research and Design 87, 573586.

- Villermaux, J., 1996. Trajectory Length Distribution (TLD), a novel concept to characterize mixing in flow systems. Chemical Engineering Science 51.

- Virdung, T., Rasmuson, A., 2007. Measurements of continuous phase velocities in solid-liquid flow at elevated concentrations in a stirred vessel using LDV. Chemical Engineering Research and Design 85.

- Wang, M., Dorward, A., Vlaev, D., Mann, R., 2000. Measurements of gas-liquid mixing in a stirred vessel using electrical resistance tomography (ERT). Chemical Engineering Journal 77.

- Wittmer, S., Falk, L., Pitot, P., Vivier, H., 1998. Characterisation of stirred vessel hydrodynamics by three dimensional trajectography. The Canadian Journal of Chemical Engineering 76.

Chapter 5

Lagrangian stochastic modelling of liquid flow in a mechanically agitated vessel

Abstract

Deterministic models of complex flows are challenging and computationally expensive. We propose here, for the first time, a computationally efficient data-driven Lagrangian stochastic approach to predict liquid flow inside a mechanically agitated vessel. The model relies on the input of a short driver data set to predict the full flow field. We investigate the capability of zeroth, first and second order models over a wide range of flow conditions including different impeller configurations and rotational speeds. The first and second order models provide good predictions of local flow properties, with the first order model being slightly superior. The technique is also capable of predicting flow well outside the range of experimental conditions.

Keywords: fluid flow, Lagrangian trajectory, mixing, PEPT, stirred vessel, stochastic model.

5.1 Introduction

Numerous process industries depend on the mixing of liquids and particle-liquid mixtures including the manufacture of pharmaceuticals, foods, cosmetics, plastics, minerals, nuclear and petroleum industries. Mixing operations are often conducted in mechanically agitated vessels and understanding of the complex flow dynamics in these processing units is vital for the effective design of products and processes. Various theoretical approaches exist for modelling of mixing flows, including different computational fluid dynamics (CFD) techniques. With the advancement of computing capability, models for describing turbulence are getting increasingly more reliable. In particular, with the aid of high-powered computing, turbulence can be determined using direct numerical simulation (DNS). By using a mesh with elements smaller than the Kolmogorov length scale, DNS solves the Navier-Stokes equations directly without a turbulence model down to the Kolmogorov time scale. This deterministic approach is extremely computationally expensive and is not practical for most engineering applications. As a result, the majority of Eulerian numerical deterministic approaches such as Reynolds averaged Navier-Stokes (RANS) or large eddy simulation (LES) utilise a turbulence model, and include time-averaging or space-filtering (Joshi & Nayak 2019).

Alternatively, turbulence can be handled by using a Lagrangian stochastic model (LSM) in combination with Eulerian methods. In a LSM, the positions are advanced in space over a given time step and are subject to random perturbations, defined by the Wiener process (Gardiner, 2004). These hybrid methods often give

good results whilst reducing computational expense. For example, using a RANS simulation where turbulence velocities were calculated using a LSM, Marshall & Sala (2011) obtained accurate predictions of the growth of algae in photobioreactor flows at a fraction of the computational cost of a DNS simulation. By contrast, a fully Lagrangian method can be used without relying on Eulerian data generated from a RANS or LES simulation. Israelsson et al. (2006) compared three techniques of Lagrangian modelling for environmental applications; forward Gaussian puff tracking (FGPT), backward Gaussian puff tracking (BGPT), and LSM (referred to as random walk particle tracking, RWPT). They showed that out of the three methods, the LSM was applicable to complex velocity or diffusivity fields and produced more accurate results than Eulerian methods, even though it was not the most computationally efficient.

Dehling et al. (2007) used a fully-Lagrangian computational approach to model slug rise in a fluidised bed. Generally, the study showed good agreement with experimental data, especially with a single type of particle. When a second type of particle was introduced, there was more deviation. However, the authors suggested the system would be difficult if not impossible to model using a deterministic approach. The method was later improved by Farzaneh et al. (2011) who used a multigrid approach to model fuel mixing in fluidised beds. The fuel and inert particles having a distinct size and density difference would be difficult to model using Dehling et al.s approach. The multigrid approach yielded good agreement of average trajectories of fuel particles with experimental data under a variety of conditions. Recently, Rezavand et al. (2019) reported a fully-Lagrangian computational model for the integration of mixing and biochemical reactions in anaerobic digestion. The 2D domain was discretised into particles, each containing the information of biologically active compounds. The continuity and momentum equations were discretised using smooth particle hydrodynamics (SPH) along with the Fickian advection-diffusion

equation. The result was a discretised Lagrangian set of equations not involving the Eulerian framework, affording the benefit of direct observation of the impact of mixing on biogas production, information that would otherwise be lost through an Eulerian scheme. Predictions were in good agreement with experimental data.

The RWPT model was also adopted by Nordam et al. (2019) who compared the application of a LSM against Eulerian methods to the vertical transport of buoyant material in a water column. The LSM was capable of capturing the discrete Lagrangian flow behaviour of oil droplets, fish eggs, and microplastics by using a large ensemble of particles to describe the effects of advection and diffusion. Particles were progressed in time with a random perturbation, using a random walk algorithm known as the Visser scheme. Excellent agreement was obtained between the stochastic and deterministic models, due to the importance given to the boundary conditions in the Lagrangian scheme.

An alternative hybrid method also exists, whereby a Eulerian field is already available to impose Lagrangian particles into. This method is often used in environmental studies; see for example Gleicher et al. (2014) and Ferrero & Oettl (2019). The former study used a LSM to model the dispersion of pathogenic spore particles that cause disease in plant canopies, whilst the latter built on the LSM by implementing the Langevin equations proposed by Thomson (1987) to include the effects of concentration-variance dissipation. Results in both cases demonstrated the LSMs high potential to predict the movement of particles in a known velocity field, without the computational cost of a deterministic approach. This approach has also been exploited in engineering applications. Matos et al. (2018) illustrated the ability of a LSM to track particles to describe the front of a fluid in a confined impinging jet reactor, with the aid of a transient Eulerian velocity field from a CFD simulation. The model allowed for the calculation of interfacial area generation, which was found to grow at an exponential rate in chaotic flows and at a linear rate in

steady flows. Therefore, it appears that the LSM strategy in a known velocity field is likely to be suitable for dealing with mixing problems, with the added benefit of low computational cost.

The data-driven LSM technique has not been used to model mixing systems. In this study, we propose a simple yet accurate approach to model turbulent single-phase flow in a mechanically agitated mixing vessel. The Eulerian velocity fields are experimentally determined using a positron emission particle tracking (PEPT) technique. By applying a LSM to these experimental flow fields, a simplified data-driven model is developed to predict flow behaviour.

5.2 Experimental

5.2.1 Mixing vessel apparatus

The flow and mixing of single-phase water was studied in a mixing vessel of diameter $T = 288$ mm and a liquid height $H = T$, as illustrated in Fig. 5.1a. Agitation was achieved using a 6-blade 45^o pitched-blade turbine (PBT) or a 6-blade Rushton disc turbine (RDT) of diameter $D = T/2$, impeller blade width $W = T/10$, baffle width $B = T/10$ and impeller clearance $C_{imp} = T/4$ for PBT and $T/3$ for RDT. The pitched blade turbine was operated in either up-pumping (PBTU) or down-pumping mode (PBTD). A radioactively-labelled resin tracer particle was used to track the flow. The resin particle was made neutrally-buoyant by adding salt to the water to match its density. Experiments were run at different impeller rotational speeds (100-500 rpm) to determine in each case the long-term trajectory of the liquid.

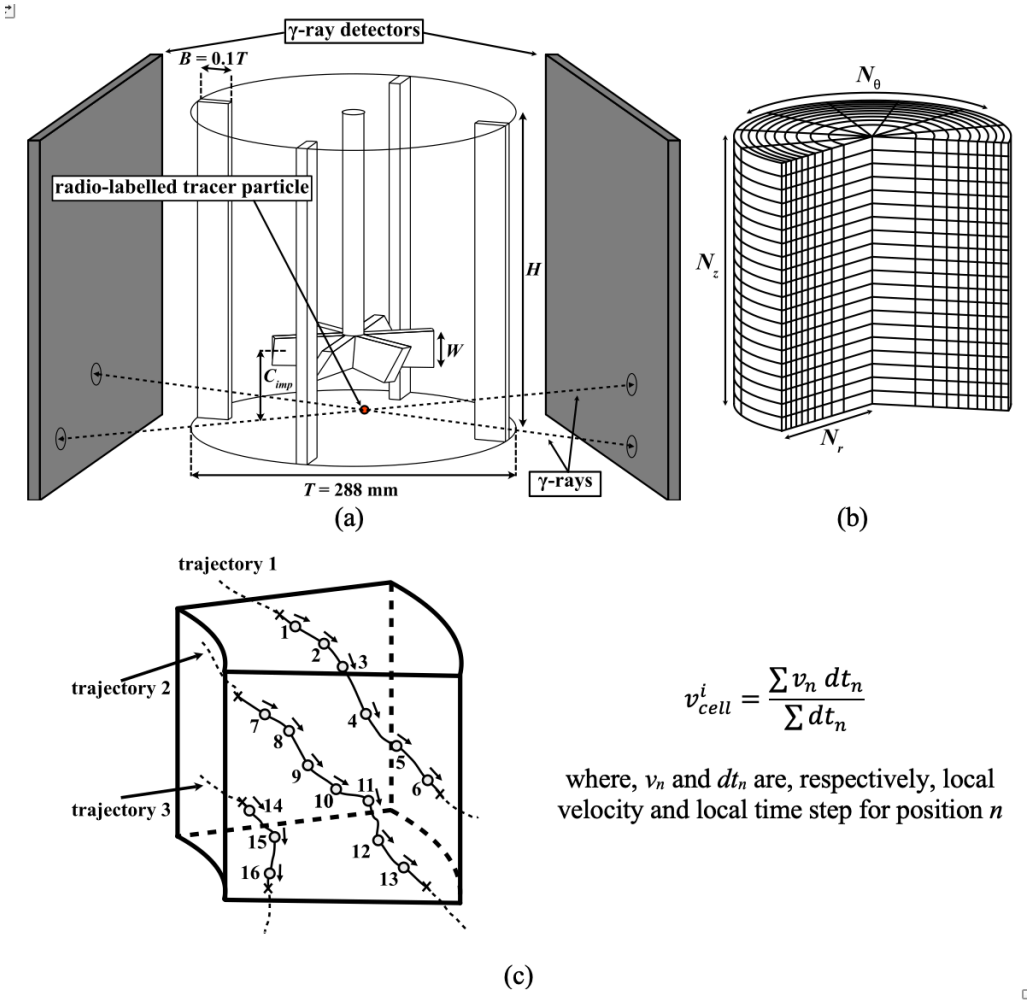


Figure 5.1: Schematic of experimental setup: (a) mixing vessel and PEPT γ-ray detectors; (b) computational grid consisting of N_r cells in the r-direction, N_z cells in the z-direction and N_θ cells in the θ-direction; (c) method of calculation of local time-averaged velocity v_{cell} in the ith cell.

5.2.2 Positron emission particle tracking

PEPT is a non-intrusive method by which a positron emitting tracer particle is accurately tracked within process equipment, providing three-dimensional space and time data for a long-term Lagrangian trajectory (Barigou 2004, Sadrmomtaz et al., 2007). PEPT is able to image flow in opaque fluids and opaque equipment, unlike optical methods such as particle image velocimetry (PIV) and laser Doppler velocimetry (LDV), but with comparable accuracy (Pianko-Oprych et al., 2009). In

PEPT each component in a multiphase flow can be tracked individually to determine its 3D Lagrangian trajectory. PEPT has been extensively used to study flow and mixing in stirred vessels. More details of the technique can be found in our earlier papers (Guida et al., 2010a, 2010b & 2011), and section 2.3.

5.3 Lagrangian stochastic modelling

Stochastic models are used to predict various outcomes of a given system by applying random perturbations to pre-determined variables. As few processes are deterministic, stochastic models can be utilised to give the probability of a certain result. This use of probability can be exploited, for example, to model the Brownian motion of particles or fluid parcels and has previously been used to predict propagation of atmospheric pollutants (Bergin & Milford, 2000), diffusion in oceanography (Ruplo, 2006) and dissipation of odours (Ferrero & Oettl, 2019). Deterministic models for complex flow system are challenging and computationally demanding. Instead, stochastic models adopt a simplified structure, greatly reducing computational cost whilst having the ability to predict complex flow characteristics. In consequence, this approach seems to have potential for modelling fluid flows, in particular inside stirred mixing vessels. In a LSM, fluid parcel positions are advanced in space over a given time step via random perturbations. The basic structure of a LSM algorithm is depicted in Fig. 5.2 and discussed in detail in the section below. Simulation time is similar to the run time of an actual experiment, for example, to compute a one hour trajectory the computational time is around one hour for a first order model.

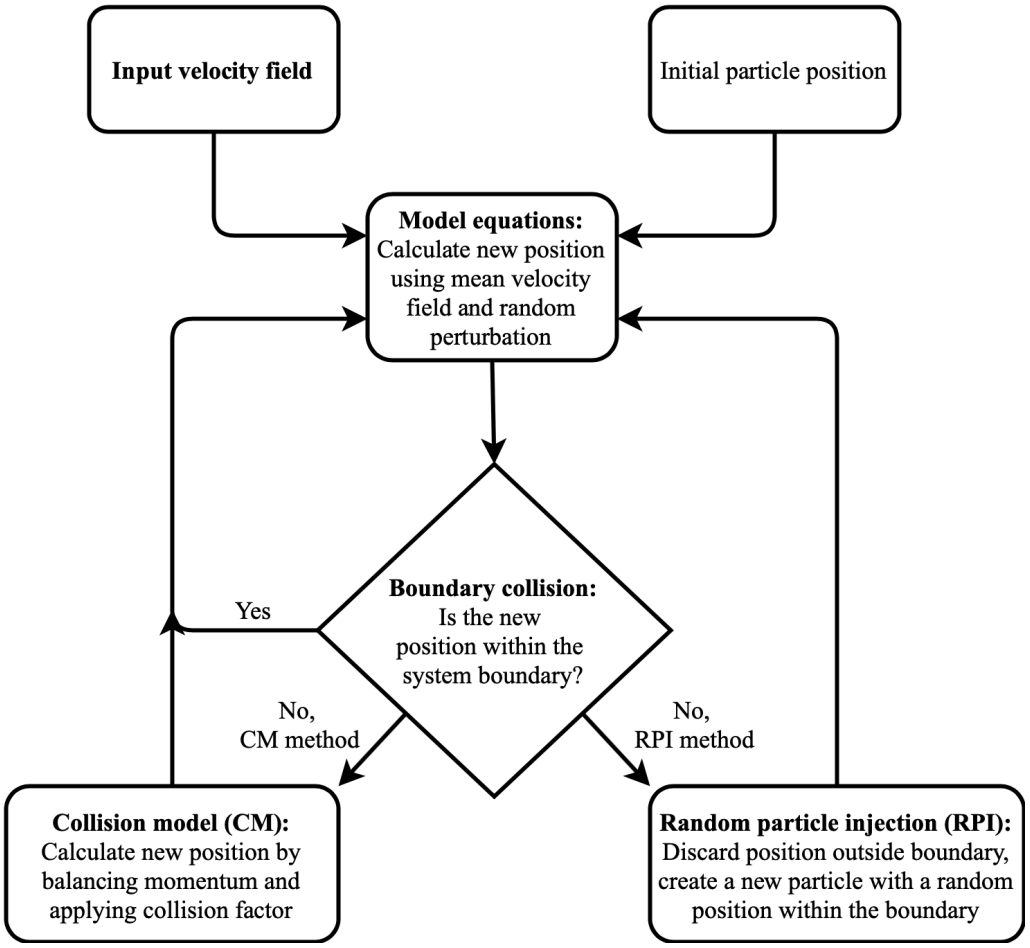


Figure 5.2: Flowchart of LSM algorithm: showing collision model (CM) and random particle injection (RPI) methods of re-inserting model particles into the domain.

5.3.1 Input velocity field

The Lagrangian stochastic model is data driven, i.e., experimental 3D mean velocities from the system form the basis of the operation of the model (Fig. 5.2). An initial particle position is set and is advanced in space over a given time step. Depending on the order of the model, different flow parameters are subjected to random perturbations defined by the Wiener process and described by a Gaussian distribution with unit variance (Gardiner 2004). For the model to yield suitable results, an appropriate experimental velocity field must be used. Here, Lagrangian PEPT velocity data acquired in a stirred vessel were converted to a Eulerian velocity

field. By dividing the vessel volume into a grid of equal volume cells, as shown in Fig. 5.1b, the local time-averaged velocity of each flow component was obtained inside each cell (Fig. 5.1c).

Grid mesh density requires careful selection, given the way LSM re-calculates the position of the particle when it leaves (i.e., collides with) the system boundary. Thus, optimising the cell size near the wall of the vessel is vital for simulations. Too coarse a mesh leads to the cell nearest the wall being too large. The average velocity in such a cell is often directed towards the boundary away from the centre of the tank. If LSM calculates the particle to be in this cell, it is likely to collide with the vessel wall and require re-calculation of position. If a collision model is used, the particle is again likely to enter the same cell due to its size, resulting in a repeating process of the particle colliding with the vessel wall. The opposite case can also pose an issue, as the trajectory data from a PEPT experiment have a finite number of positions and in many cases will not occupy all cells in a mesh if their size is very small. This results in a zero cell; a cell which has no velocity associated with it. If the particle enters a cell with no velocity associated with it, it will remain stationary in the cell for the duration of the simulation, as shown further below (Equations 1-9). Mesh size is dependent on the time step selected for the model and in an ideal scenario, the particle should move into an adjacent cell to prevent any repeating movement especially at the boundary. As the mean temporal resolution of the experimental PEPT data is 5 ms, this value was assigned as the time step for the model and a mesh density study was conducted on sample experimental trajectories to establish a suitable grid for the model.

In general, the aim of LSM is to be able to use a short experimental particle trajectory to predict the long-term trajectory of the particle under similar conditions. In this case, the particle in question is the PEPT tracer particle used to track the liquid motion inside the stirred vessel. A trajectory length of 5 min was selected as an

input to the model as it was sufficient for a particle tracer to visit the majority of the computational grid cells and find a representative velocity field. Fig. 5.3 illustrates the number of detected positions in each mesh cell under different experimental conditions. Mesh size was adjusted in the r and z-directions with a set number of cells in the θ-direction. Once appropriate cell dimensions were determined for the r and z-directions, the number of cells in the θ-direction was adjusted and assessed in the same way.

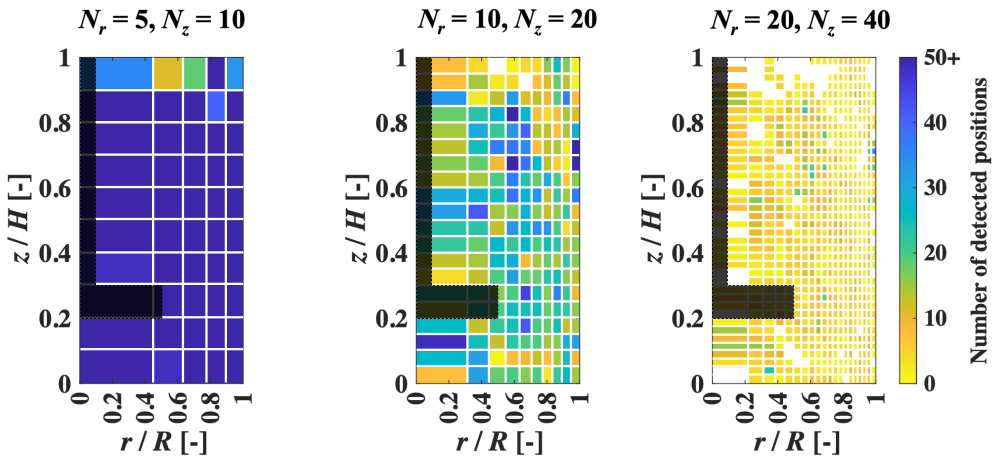


Figure 5.3: Effect of grid mesh density on number of detected positions in each cell: Sample results shown are based on 5 min-long experimental PEPT trajectories for one layer of cells in the θ-direction ($N_\theta = 12$); white cells have no detected positions; agitation speed = 300 rpm, PBTD configuration.

Determining the ideal mesh density is a compromise. Increasing the number of cells improves the fidelity of the velocity field but increases the risk of cells with no detection points and, hence, missing local velocity values. A cell with no detections cannot be used in the model as it results in stalling of the model particle and causes the model to fail. Reducing the number of cells, on the other hand, can also be detrimental as it may reduce resolution to the point where the local velocity field is no longer a true representation of the actual flow. Fig. 5.3 shows the effect of varying the grid mesh density on the number of detected positions in each cell. All cells contain detected positions when $N_r = 5$ and $N_z = 10$. Fewer detections tend to be found near the top of the vessel because liquid agitation is less intense in this

region. Increasing the number of cells in both directions results in fewer detected positions per cell, with increasingly more zero cells appearing near the top and the centre of the vessel ($N_r = 20$, $N_z = 40$). These numerical tests led to an optimised grid of 2400 equal volume cells where $N_\theta = 12$, $N_r = 10$ and $N_z = 20$, which yielded the highest resolution for the velocity field with the fewest cells containing zero detections. To prevent the failure of the model, as pointed out above, where a zero cell is found, the cell is assigned an estimated velocity value using a linear 3D grid interpolation.

5.3.2 Model equations

There are three orders of stochastic model to describe the motion of a particle over time: zeroth, first and second order. The form of these models used in this study, was adopted from the oceanography works of Ruplo (2006) and LaCasce (2008). Along with velocity field information, LSM requires knowledge of decorrelation times when utilising a first or second order model. Velocity and acceleration time signals obtained from the experimental PEPT trajectory were used to estimate these decorrelation times (Guida et al., 2010b). Decorrelation times for velocity and acceleration were calculated in each direction over 1 min intervals along a 5 min trajectory, as summarised in Table 5.1, and an average value taken. LSM uses this information to scale the amount of stochastic noise added to the system, with an inverse relationship. If decorrelation times are short, i.e. the system decorrelates and loses its memory quickly which reflects a high degree of stochasticity, thus the stochastic noise added is large. By contrast, if the time taken to decorrelate is large, the level of turbulence is less and therefore less stochastic noise is added.

The zeroth order model is the simplest variation of LSM, where particle position is

Table 5.1: Velocity and acceleration decorrelation times for minute intervals of experimental at 500 rpm PBTD PEPT data.

	Decorrelation time (ms)					
T (min)	v_x	v_y	v_z	a_x	a_y	a_z
0-1	40	57	24	23	24	23
1-2	38	60	25	23	23	23
2-3	42	69	25	24	24	23
3-4	41	63	25	25	24	23
4-5	42	64	25	24	24	23
average value	**41**	**63**	**25**	**24**	**24**	**23**

progressed using the following set of equations (Ruplo, 2006; LaCasse, 2008):

$$x_i^{t+dt} = x_i^t + dx_i^{dt} \tag{5.1}$$

$$dx_i^{dt} = \bar{U}_i dt + \sqrt{2\bar{U}_i{}^2}(dw^{dt})^2 \tag{5.2}$$

where, x_i and $\bar{U}_i$ are, respectively, the particle position and mean particle velocity in the i-direction, and dw^{dt} is the Wiener process for the time step dt, which is discretised as follows:

$$dw^{dt} \approx \sqrt{dt}N(0,1) \tag{5.3}$$

where, $N(0,1)$ is a normal distribution with a mean of 0 and unit variance.

In the first order model, Eq. 5.2 above is replaced by the following equations:

$$dx_i^{dt} = (u_i^{t+dt} + \bar{U}_i)dt \tag{5.4}$$

$$u_i^{t+dt} = u_i^t + du_i^{dt} \tag{5.5}$$

$$du_i^{dt} = -\frac{u_i^t}{T_{u,i}}dt + \sqrt{\frac{2\bar{U_i}^2}{T_{u,i}}}dw^{dt} \tag{5.6}$$

where, u_i and $T_{u,i}$ are, respectively, the local velocity and the velocity decorrelation time in the i-direction.

In the second order model, Eq. 5.6 above is replaced by the following equations:

$$du_i^{dt} = a_i^{t+dt} - \frac{u_i^t}{T_{u,i}} \tag{5.7}$$

$$a_i^{t+dt} = a_i^t + da_i^{dt} \tag{5.8}$$

$$da_i^{dt} = -\frac{a_i^t}{T_{a,i}}dt + \sqrt{2\bar{U_i}^2\frac{T_{a,i}+T_{u,i}}{T_{a,i}T_{u,i}}}(dw^{dt})^{-1} \tag{5.9}$$

where, a_i and $T_{a,i}$ are, respectively, the local acceleration and the acceleration decorrelation time in the i-direction.

5.3.3 Boundary collision

Due to the nature of LSM, the simulated tracked particle is able to leave the solid boundary of the flow field if not restricted. A check is conducted after each new particle position is computed, as illustrated in the algorithm flowchart (Fig. 5.2). If the particle is outside of the flow domain (in this case the stirred vessel), then there are two possible methods for re-inserting it into the flow:

- Random particle injection (RPI): the particle position outside the boundary is discarded and replaced with a random position within the boundary, and the LSM is re-initiated.

- Collision model (CM): the previous position and current position are used to calculate the particles momentum and, thus, a new particle position inside the flow domain is computed assuming an elastic collision with the vessel wall.

In this case, given the high frequency of boundary collisions with the vessel wall, the RPI method resulted in numerous kinks in the particle trajectory leading to erroneous results. In contrast, the CM method yielded a much more realistic trajectory. Thus, experimental PEPT particle-wall interactions were analysed and results were implemented into the collision model.

Lagrangian data obtained from PEPT experiments are in the form of discrete space-time positions of a tracer particle. Some collisions can be easily identified as a clear interaction with the vessel wall is observed. There are, however, collisions which are hidden in the data as they occur between the recordings of space-time data of the tracer but these cannot be included in collision modelling because of the missing information.

Particle-wall collisions can be compared by analysing the ratio between tracer velocity before and after the collision, using an arbitrary collision factor C_f which can be defined in either of two ways, as follows:

$$C_f = \frac{v_2}{v_1} \tag{5.10}$$

where, v_1 is the total velocity of the particle prior to collision with the vessel wall, and v_2 is the total velocity of the particle after collision with the vessel wall; or alternatively taking into consideration the angle of collision with the vessel wall ϕ:

$$C_f = \frac{1}{tan(\phi)} \tag{5.11}$$

where, ϕ is defined as:

$$tan(\phi) = \frac{\|v_i \times v_r\|}{v_i \cdot v_r} \tag{5.12}$$

where, v_i and v_r are the particle incident and rebound velocity vectors, respectively. A C_f value < 1 indicates a collision angle larger than 45^o, and $C_f > 1$ indicates a collision angle smaller than 45^o.

Typical experimental data are plotted in Fig. 5.4, showing a distribution of Cf values for both definitions of C_f. The mean C_f value in Fig. 5.4(a) is close to 1, indicating perfectly elastic collisions irrespective of the ratio of local values of the shear and normal velocities and the particle-wall contact angles. The data in Fig. 5.4(b) shows a mean C_f value close to 0, i.e. $\phi \approx 90^o$, indicating again almost perfectly elastic collisions. It should be noted that the value of C_f is affected not only by the nature of the collision, but also by the oncoming flow which may impart additional momentum to the bouncing particle. A sensitivity analysis of LSM-predicted time-averaged velocity profiles in cells adjacent to the vessel wall to the

value of C_f adopted is presented in Fig. 5.5. Despite the wide range of C_f values tested, the LSM-predicted velocity field close to the vessel wall was not sensitive to the definition of C_f or the value adopted. Based on this sensitivity analysis, it was clear that either definition C_f could be used with no significant effects on the predicted velocity profiles. Therefore, Eq. 5.10 was adopted in all the calculations as it was less computationally demanding, with an arbitrary value $C_f = 1$.

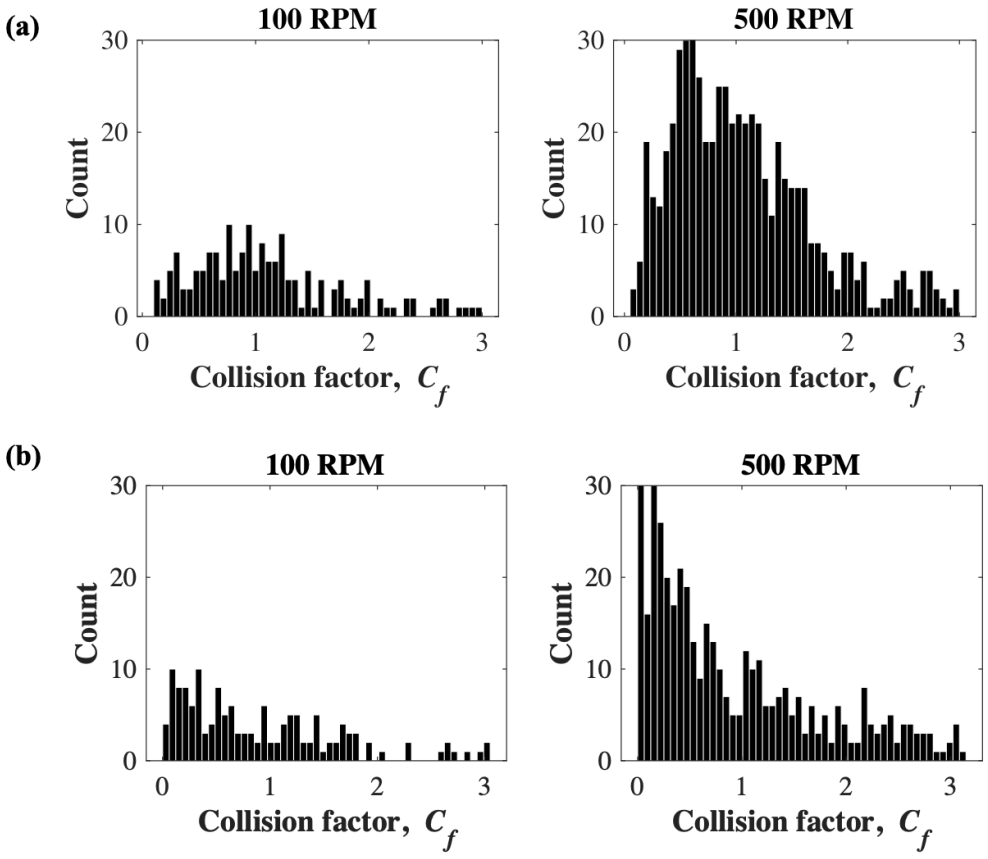


Figure 5.4: Histograms of PEPT particle tracer-wall collision factor, C_f, for experiments using PBTD configuration at 100 and 500 rpm: (a) $C_f = v_2/v_1$; (b) $C_f = \frac{1}{tan(\phi)}$.

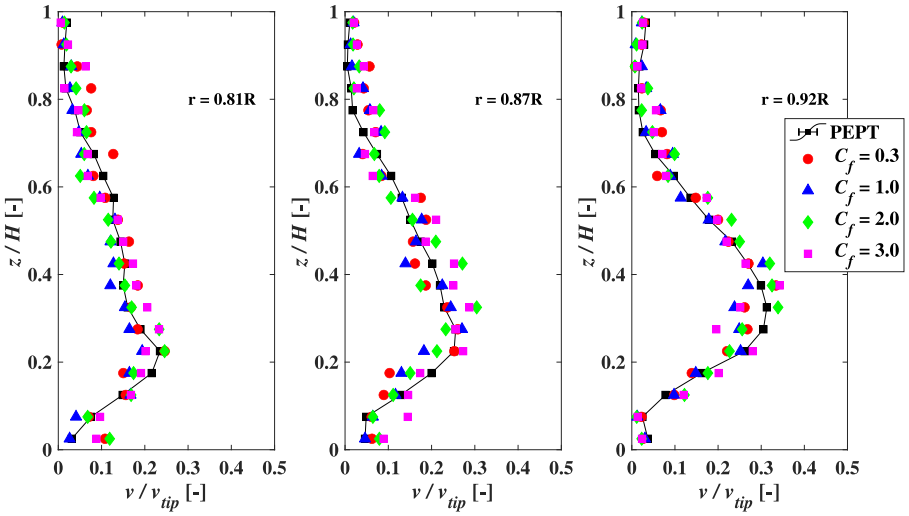


Figure 5.5: Sensitivity analysis of LSM-predicted time-averaged velocity profiles in cells adjacent to the vessel wall to the value of Cf adopted: experimental and modelling data shown are for 40 min trajectory obtained at 300 rpm with PBTD configuration: (a) $C_f = v_2/v_1$; (b) $C_f = \frac{1}{tan(\phi)}$.

5.4 Results and discussion

LSM was used to calculate three-dimensional Lagrangian fluid trajectories in a mixing vessel. The zeroth order model (Eqs. 5.1-5.2) failed to produce sufficiently accurate predictions, thus, detailed analyses are presented here only for the first and second order models, denoted, respectively, by ${}^1LSM$ and ${}^2LSM$. The computations were executed in MATLAB with a time step dt = 5 ms, of the same order as the data acquisition time step achieved in PEPT. The time to compute a 40 min long trajectory via ${}^1LSM$ was ∼30 min, whilst ${}^2LSM$ took nearly twice as long. Such a computational cost is very small in comparison with all known deterministic models.

In order to evaluate the performance of the approach, detailed quantitative comparisons of LSM predictions and PEPT experiments were conducted throughout the stirred vessel. The azimuthally averaged distributions of local velocity were

compared at six different axial and radial planes. Axial (vertical) planes were examined from the tip of the impeller ($r = 0.5R$) to the vicinity of the vessel wall ($r = 0.87R$). Radial (horizontal) planes were examined from the bottom of the vessel ($z = 0.03H$) to the top of the vessel ($z = 0.97H$), including a plane just below the impeller ($z = 0.17H$) and a plane just above the impeller ($z = 0.38H$).

5.4.1 Predicting long-term trajectories from short-term LSM driver trajectories

The potential benefit of using a stochastic model is the ability to use small sets of Lagrangian trajectory data pertaining to specific flow conditions to predict long-term trajectories. Here, we investigate the effects of the size of the initial data set used to drive the LSM on the accuracy of the predictions. The plots in Fig. 5.6 show the velocity profiles for 300 rpm PBTD predicted on the basis of short-term PEPT trajectories within the range 1 10 min. Results show that even a 1 min driver trajectory is generally adequate despite significant errors in some regions of the flow. Using a 3 min driver trajectory, the agreement between prediction and experiment is good throughout the flow domain. Beyond 3 min, there is no significant improvement in prediction accuracy. This minimum driver trajectory length depends slightly on the flow conditions, in particular the speed of the impeller. It tends to increase at lower impeller speeds as less data points are acquired per unit time, and reduce at higher speeds as the data acquisition rate is higher. Tests conducted at 100 rpm showed that 3 min was still satisfactory, but at 500 rpm this could be reduced down to 2 min. Erring on the safe side, we used 5 min driver trajectories throughout the rest of this study.

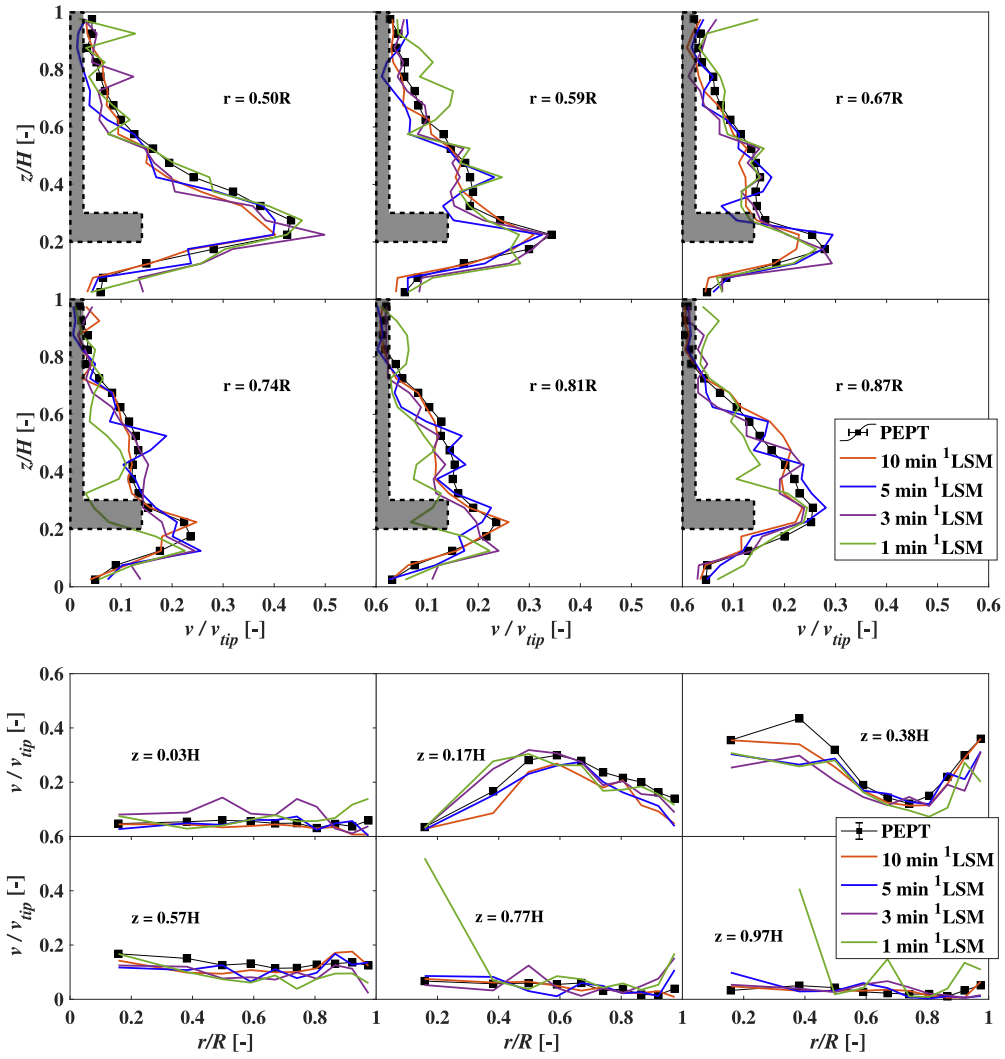


Figure 5.6: Effects of length of LSM driver trajectory on azimuthally averaged profiles of total velocity predicted: PEPT and ^1LSM compared at 300 rpm with PBTD configuration.

5.4.2 Model validation

To validate the ^1LSM and ^2LSM models, extensive PEPT experiments were conducted using the PBTD impeller running at speeds within the range 100 - 500 rpm. Experimental PEPT trajectories of 5 min length were used to drive the models (Fig. 5.2). The LSMs were used to produce 40 min long trajectories which were then compared to equivalent PEPT trajectories.

Velocity profiles

Azimuthally averaged profiles of local velocity components (v_r, v_z, v_θ) predicted by ${}^1LSM$ and ${}^2LSM$ are compared to PEPT data in Figs. 5.7-5.9 for the sample case of PBTD running at 300 rpm. Overall, both models were capable of predicting the velocity components well in all regions of the vessel across the whole range of impeller speeds used. Compared to PEPT, as observed in the vertical velocity profiles, ${}^2LSM$ tends to underpredict v_θ and v_z somewhat along the horizontal impeller plane (Fig. 5.7, Fig. 5.8). Such underpredictions are also reflected in the horizontal velocity profiles close to the impeller plane (e.g., z = 0.17H, 0.38H), but they are overall less significant in the case of v_r (Fig. 5.9). In contrast, the ${}^1LSM$ model does not suffer from these errors. It should be noted, however, that these regions contain intense turbulence and high liquid velocities and the experimental measurements themselves are subject to some uncertainty, as shown in our previous work (Pianko-Oprych et al., 2009; Liu & Barigou, 2013).

Results show that the second order model is more prone to velocity errors than the first order model. This is due to the higher order calculations (Eqs. 5.7-5.9) involved which tend to amplify any errors in the initial experimental data used to drive the model. Both models, however, are capable of predicting the velocity information with reasonable accuracy in all three directions, with ${}^1LSM$ being moderately better. Henceforth, the velocity profiles will be discussed in terms of total velocity.

Occupancy

Occupancy is defined as the fraction of the total experimental time (t_∞) a tracer particle spends in each grid cell during the experiment. This definition is subject to bias due to the density of the grid and probability of tracer presence in the cells.

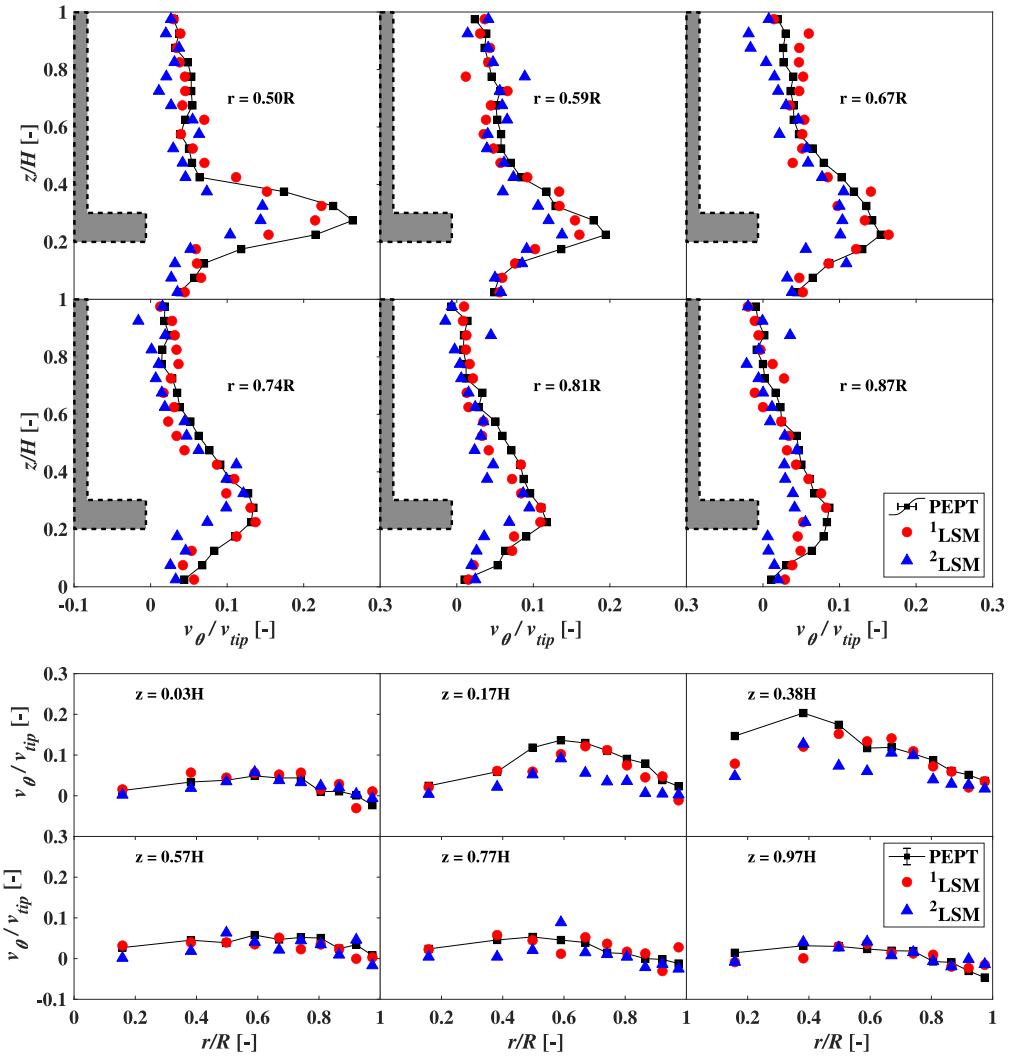


Figure 5.7: Azimuthally averaged profiles of local θ-velocity component: PEPT, ^{1}LSM and ^{2}LSM compared at 300 rpm with PBTD configuration.

Instead an ergodic time (t_E) is defined which is the time a tracer would spend in a cell assuming the flow is ergodic, thus (Guida et al., 2010a, 2010b, 2011; Liu & Barigou, 2013, 2015):

$$t_E = \frac{t_\infty}{N_c} \tag{5.13}$$

where, N_c is the total number of grid cells. Thus, the local occupancy can be defined

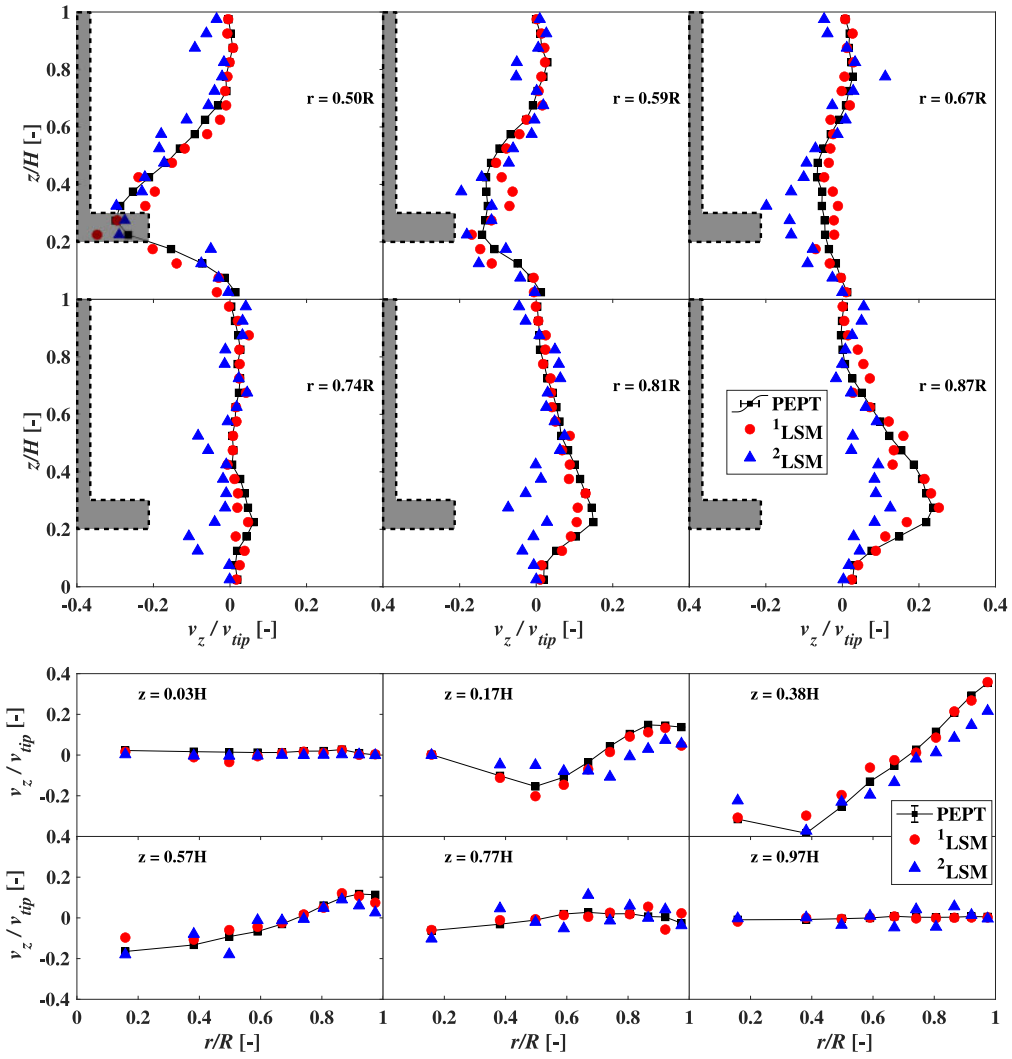


Figure 5.8: Azimuthally averaged profiles of local z-velocity component: PEPT, ${}^{1}LSM$ and ${}^{2}LSM$ compared at 300 rpm with PBTD configuration.

as:

$$O_E = \frac{\Delta t}{t_E} \tag{5.14}$$

where, Δt is the time the tracer spends inside a given cell. Azimuthally-averaged plots of radially-averaged and axially-averaged occupancy are presented in Fig. 5.10. The experimental measurements show that the local occupancy distribution is quasi-uniform, and this is well predicted by both LSM models.

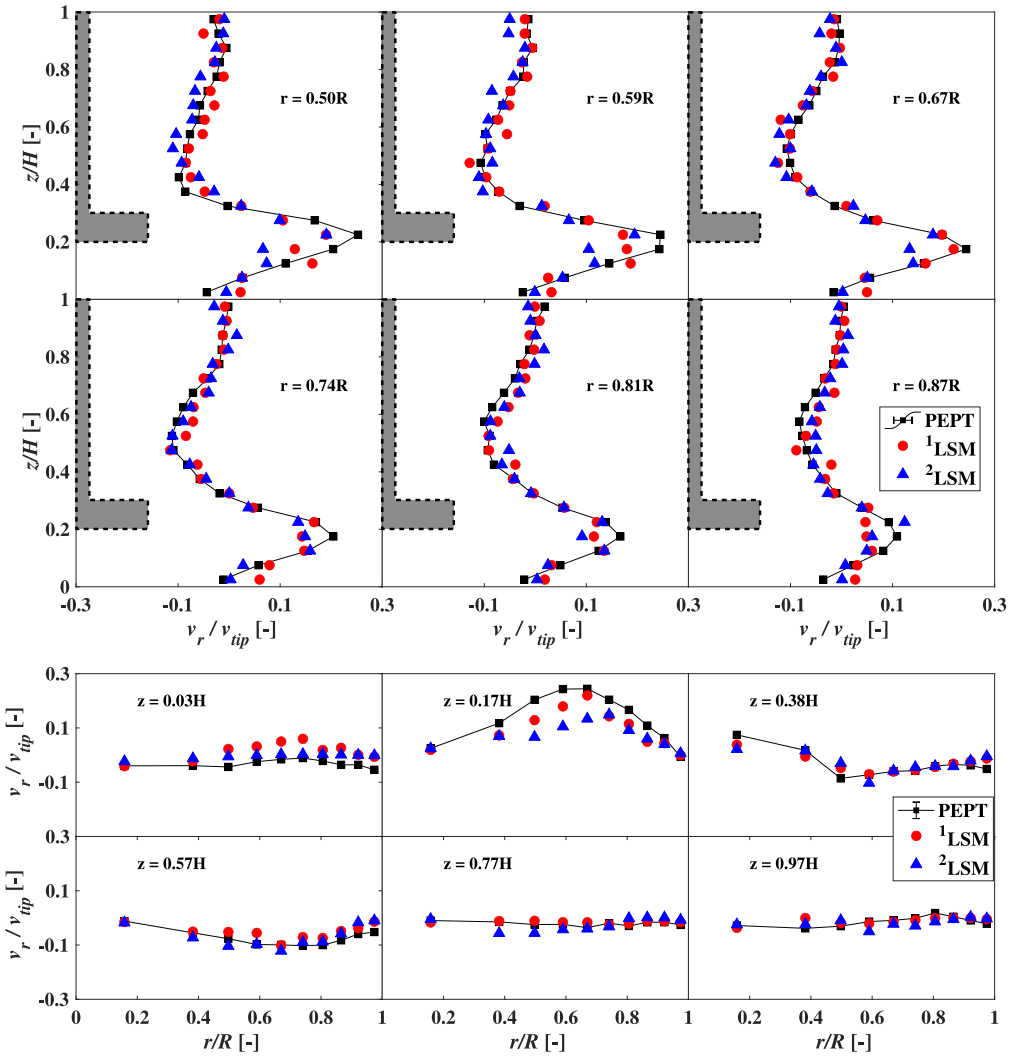


Figure 5.9: Azimuthally averaged profiles of local r-velocity component: PEPT, ^1LSM and ^2LSM compared at 300 rpm with PBTD configuration.

5.4.3 Effects of impeller configuration

In addition to the PBTD, discussed above, which is a mixed-flow 6-blade 45^o pitched-blade turbine (PBT) pumping down, we also tested the LSM models using the PBT in up-pumping mode (PBTU) as well as a radial-flow 6-blade Rushton disc turbine (RDT) for a rotational speed of 300 rpm. Between them, the flows generated by these impeller configurations represent most of the standard agitation conditions encountered in mixing vessels. Total velocity results for the PBTU, presented in

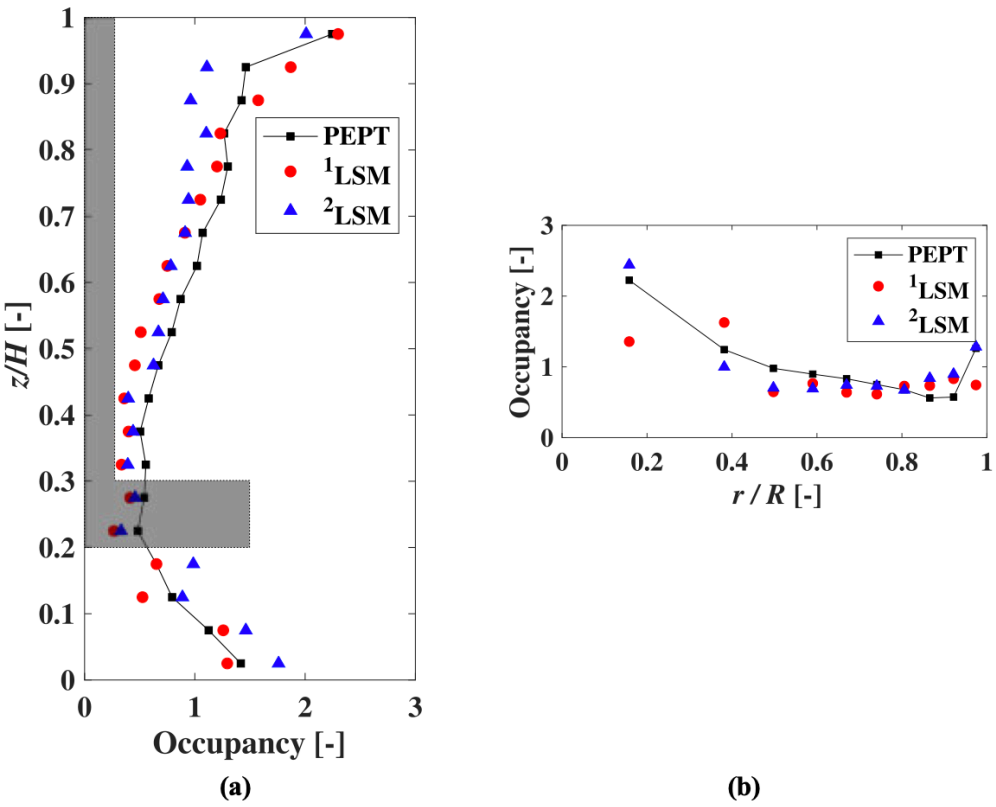


Figure 5.10: Azimuthally averaged plots of (a) radially-averaged and (b) axially-averaged occupancy: PEPT, ^{1}LSM and ^{2}LSM compared at 300 rpm with PBTD configuration.

Fig. 5.11, show that ^{2}LSM exhibits some significant underpredictions in the bottom half of the vessel below the impeller plane, especially near the bottom and the wall. ^{1}LSM exhibits only minor underpredictions in this region and overall performs moderately better than ^{2}LSM throughout the vessel.

Results for the RDT impeller are depicted in Fig. 5.12. Similar observations can be made as for the PBTD and PBTU above. Due to the radial flow nature of the RDT, the largest prediction errors occur just below and just above the impeller plane but, overall, both models perform well in the rest of the vessel. In conclusion, ^{1}LSM and ^{2}LSM are capable of predicting single-phase flow in a stirred vessel regardless of impeller configuration with generally good accuracy, with ^{1}LSM slightly surpassing ^{2}LSM. Therefore, in the rest of this study, we will focus solely on ^{1}LSM.

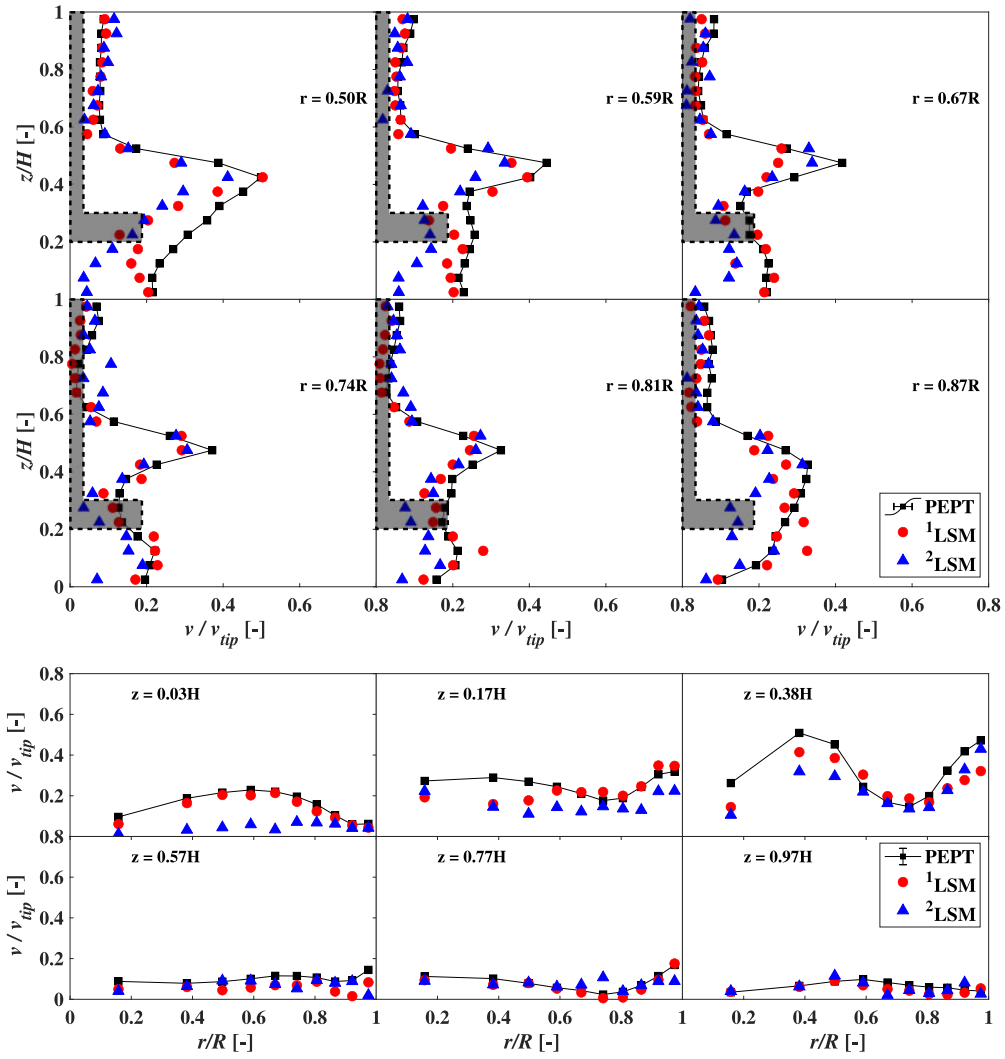


Figure 5.11: Azimuthally averaged profiles of total velocity: PEPT, ^1LSM and ^2LSM compared at 300 rpm with PBTU configuration.

5.4.4 Prediction of flow conditions outside range of experimental measurements

The data used to drive the LSM can be manipulated to predict flow conditions well outside the range of experimental measurements. For instance, velocity information from a 5 min experimental trajectory obtained at 100 rpm with PBTD was multiplied by the ratio $v_{tip,500rpm}/v_{tip,100rpm}$, and then fed to the ^1LSM to predict the long-term trajectory corresponding to 500 rpm for the same PBTD. Results presented in Fig.

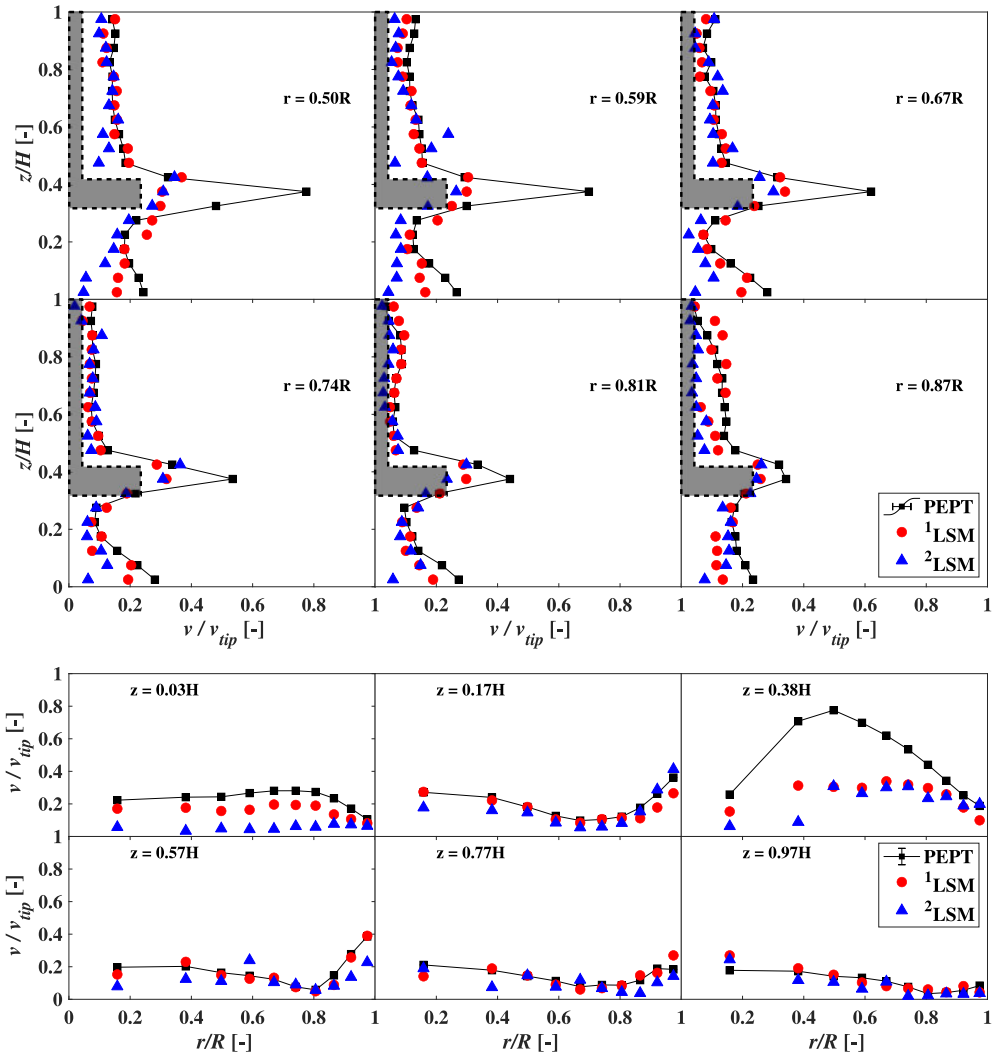


Figure 5.12: Azimuthally averaged profiles of total velocity: PEPT, ^{1}LSM and ^{2}LSM compared at 300 rpm with RDT configuration.

5.13 demonstrate a generally good agreement between predictions and experiment, the only significant errors (underestimations) being mainly confined to the bottom half of the vessel below the impeller plane. These errors may be attributed to the decorrelation times used in the LSM which were obtained from the 100 rpm experiment, resulting in a stochastic scaling which may not accurately represent the flow in the 500 rpm experiment, particularly in the high turbulence regions near the impeller. Nevertheless, the fact that the LSM can predict flow conditions far beyond the range of experimental measurements with such a level of accuracy is a significant achievement.

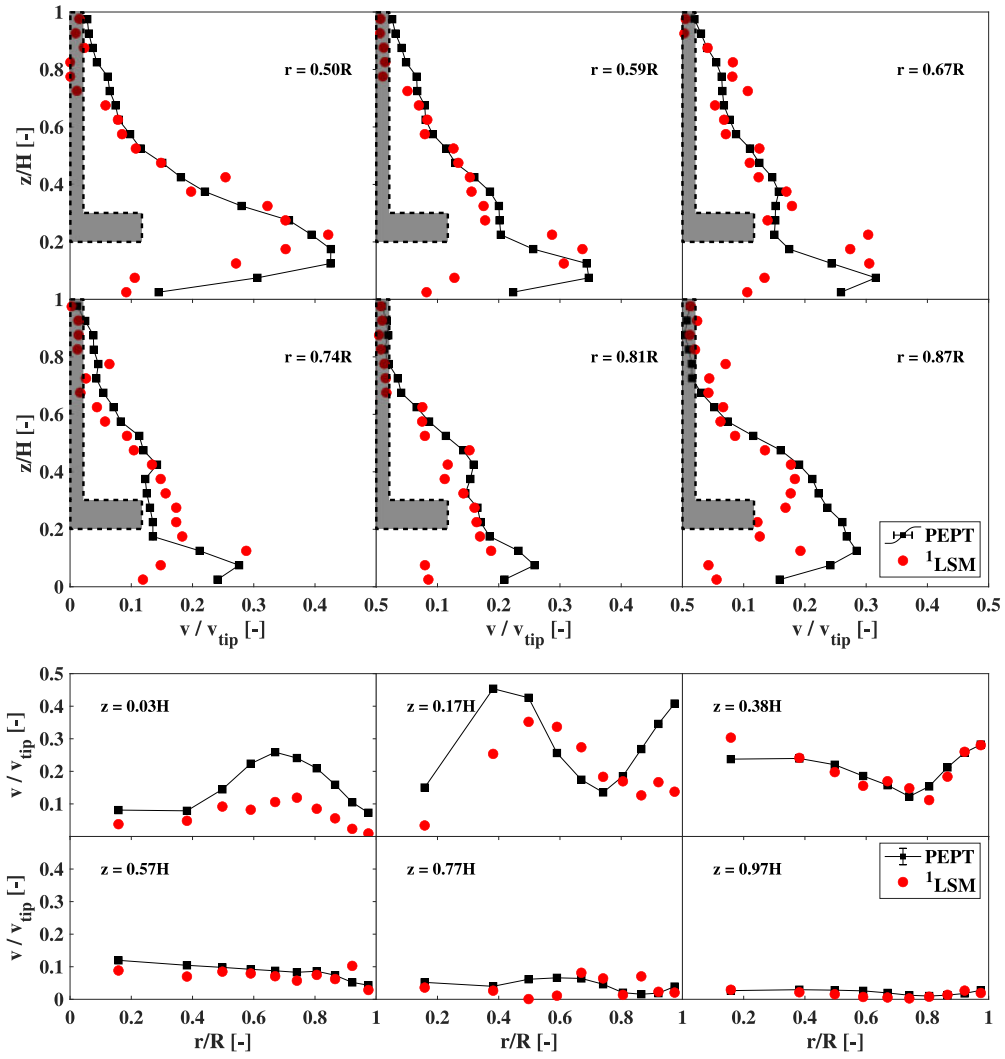


Figure 5.13: Azimuthally averaged profiles of total velocity for 500 rpm PBTD predicted on the basis of 5 min initial data from 100 rpm PBTD experiment: PEPT and 1LSM.

5.5 Conclusion

The application of a data-driven Lagrangian stochastic model based on random walk particle tracking to single-phase flow in a mechanically agitated vessel has been studied for the first time. Both first and second order models provide good predictions of local flow velocity and tracer particle occupancy, with the first order model being slightly superior. The performance of the model was studied under a range of flow

conditions including different impeller configurations and rotational speeds. The model is also capable of predicting flow well outside the range of experimental conditions, for example, using initial driver data from a lower impeller speed to predict flow at a much higher speed. The technique relies on the initial input of a small set of experimental data to drive the model. Generally, a driver trajectory on the order of 1 min length is sufficient to enable adequate prediction of long-term flow trajectories. In addition to its accuracy, the LSM approach proposed here has the added advantage of being computationally efficient compared to existing modelling techniques.

The LSM approach however, has some limitations in predictive capability. Firstly, this method is restricted by changes in geometry; a prediction for a different impeller geometry is not possible without the prerequisite velocity field and decorrelation time information, due to the distinct differences in the mean velocity field and fluctuation velocities. Secondly, significantly changing the hydrodynamic regime, i.e. a large change in impeller rotation rate, would result in larger errors for the same reasons. Therefore the main motivation for utilising the LSM method is to extend existing Lagrangian information in cases where experimental/computing time is limited.

Increasing or decreasing the vessel size is another area to investigate with the use of LSM. Theoretically, if the size of vessel changes but the hydrodynamic regime remains the same, LSM predictions should capture Lagrangian trajectories given the driver data is for the same conditions.

An area to investigate further is the use of Eulerian information as the only driver data given to the LSM. Using a Bayesian approach, the coefficients for velocity fluctuations (stochastic component) can be derived by constructing Lagrangian particle movements using an arbitary set of values, and using the velocity and occupancy comparisons in conjunction with Bayes' theorem to determine optimum model pa-

rameters. This would result in a predicted Lagrangian particle motion description from a purely Eulerian set of driver data, for example from a velocity field derived using PIV.

Nomenclature

Symbols

a	particle acceleration (m s^{-2})
B	baffle width (m)
C_f	collision factor
C_{imp}	impeller clearance (m)
D	impeller diameter (m)
dt	time step (s)
dw	Wiener process ($s^{1/2}$)
H	height of suspension (m)
N_c	total number of cells
N_r	number of cells in radial direction
N_z	number of cells in axial direction
N_θ	number of cells in azimuthal direction
O_E	local occupancy
ϕ	particle- vessel wall collision angle
Δt	time spent by tracer particle in a cell (s)
T	tank diameter (m)
T_u, T_a	velocity and acceleration decorrelation time (s)
t_E	ergodic time (s)
t_∞	total experimental time (s)
u	particle velocity (m s^{-1})

$\bar{v}$	mean particle velocity (m s^{-1})
v	total velocity (m s^{-1})
$v1, v2$	total particle velocity prior to/after collision with vessel wall (m s^{-1})
$\boldsymbol{v_i}, \boldsymbol{v_r}$	particle incident/rebound velocity vector (m s-1)
v_{cell}	local time-averaged velocity
v_{tip}	impeller tip velocity (m s^{-1})
W	impeller width (m)
x	particle position (m)

Abbreviations

CM	collision model
LSM	Lagrangian stochastic model
PBT	pitched blade turbine
PBTD	pitched blade turbine, down-pumping
PBTU	pitched blade turbine, up-pumping
PEPT	positron emission particle tracking
RDT	Rushton disc turbine
RPI	random particle injection
RWPT	random walk particle tracking

References

- Barigou, M. (2004), Particle Tracking in Opaque Mixing Systems: An Overview of the Capabilities of PET and PEPT, Chemical Engineering Research and Design 82(9), 1258-1267.

- Bergin, M. S. & Milford, J. B. (2000), Application of Bayesian Monte Carlo analysis to a Lagrangian photochemical air quality model, Atmospheric Envi-

ronment 34(5), 781-792.

- Dehling, H. G., Dechsiri, C., Gottschalk, T., Wright, P. C. & Hoffmann, A. C. (2007), A stochastic model for mixing and segregation in slugging fluidized beds, Powder Technology 171(2), 118-125.

- Farzaneh, M., Sasic, S., Almstedt, A.-E., Johnsson, F. & Pallarès, D. (2011), A novel multigrid technique for Lagrangian modeling of fuel mixing in fluidized beds, Chemical Engineering Science 66(22), 5628-5637.

- Ferrero, E. & Oettl, D. (2019), An evaluation of a Lagrangian stochastic model for the assessment of odours, Atmospheric Environment 206, 237-246.

- Gardiner, C. W. (2004), Handbook of Stochastic Methods for Physics, Chemistry, and the Natural Sciences, number 13 in Springer Series in Synergetics, 4th edition edn, Springer-Verlag, Berlin.

- Gleicher, S. C., Chamecki, M., Isard, S. A., Pan, Y. & Katul, G. G. (2014), Interpreting three-dimensional spore concentration measurements and escape fraction in a crop canopy using a coupled Eulerian-Lagrangian stochastic model, Agricultural and Forest Meteorology 194, 118-131.

- Guida, A., Nienow, A. W. & Barigou, M. (2010a), PEPT measurements of solid-liquid flow field and spatial phase distribution in concentrated monodisperse stirred suspensions, Chemical Engineering Science 65(6), 1905-1914.

- Guida, A., Nienow, A. W. & Barigou, M. (2010b), Shannon entropy for local and global description of mixing by Lagrangian particle tracking, 65(10), 2865-2883.

- Guida, A., Nienow, A. W. & Barigou, M. (2011), Mixing of dense binary suspensions: Multi-component hydrodynamics and spatial phase distribution by PEPT, American Institute of Chemical Engineers Journal 57(9), 2302-2315.

- Israelsson, P. H., Kim, Y. D. & Adams, E. E. (2006), A comparison of three Lagrangian approaches for extending near field mixing calculations, Environmental Modelling & Software 21(12), 1631-1649.

- Joshi, J. B. & Nayak, A. K. (2019), Advantages of Computational Fluid Dynamics in Nuclear Reactor Design and Safety Assessment, Elsevier.

- LaCasce, J. H. (2008), Statistics from Lagrangian observations, Progress in Oceanography 77, 1-29.

- Liu, L. & Barigou, M. (2013) Numerical modelling of velocity field and phase distribution in dense monodisperse solidliquid suspensions under different regimes of agitation: CFD and PEPT experiments, Chemical Engineering Science, 101, pp. 837850.

- Liu, L. & Barigou, M. (2015) Lagrangian particle tracking in mechanically agitated polydisperse suspensions: Multi-component hydrodynamics and spatial distribution, International Journal of Multiphase Flow, 73, pp. 8089.

- Marshall, J. S. & Sala, K. (2011), A stochastic Lagrangian approach for simulating the effect of turbulent mixing on algae growth rate in a photobioreactor, Chemical Engineering Science 66(3), 384-392.

- Matos, J., Brito, M. S. C. A., Dias, M. M., Lopes, J. C. B. & Santos, R. J. (2018), Lagrangian mixing simulation and quantification of scales, Chemical Engineering Science 192, 199-210.

- Nordam, T., Kristiansen, R., Nepstad, R. & Röhrs, J. (2019), Numerical analysis of boundary conditions in a Lagrangian particle model for vertical mixing, transport and surfacing of buoyant particles in the water column, Ocean Modelling 136, 107-119.

- Pianko-Oprych, P., Nienow, A. W. and Barigou, M. (2009) Positron emission particle tracking (PEPT) compared to particle image velocimetry (PIV) for studying the flow generated by a pitched-blade turbine in single phase and multi-phase systems, Chemical Engineering Science, 64(23), pp. 49554968. doi: 10.1016/j.ces.2009.08.003.

- Rezavand, M., Winkler, D., Sappl, J., Seiler, L., Meister, M. & Rauch, W. (2019), A fully Lagrangian computational model for the integration of mixing and biochemical reactions in anaerobic digestion, Computers & Fluids 181, 224-235.

- Ruplo, V. (2006), A Lagrangian-Based Approach for Determining Trajectories Taxonomy and Turbulence Regimes, Journal of Physical Oceanography 37, 1584-1609.

- Sadrmomtaz, A., Parker, D. & Byars, L. (2007), Modification of a medical PET scanner for PEPT studies, Nuclear Instruments and Methods in Physics Research 573(1-2), 91-94.

- Thomson, D. J. (1987), Criteria for the selection of stochastic models of particle trajectories in turbulent flows, Journal of Fluid Mechanics 180, 529-556.

Chapter 6

A data-driven stochastic model for particle-liquid flow and phase distribution in a stirred vessel

Abstract

A computationally efficient data-driven Lagrangian stochastic model has been used to study two-phase particle-liquid flow in a mechanically agitated vessel and unravel the complex behaviour of both phases. Using a small set of trajectory driver data from experimental positron emission particle tracking measurements, the stochastic model predicts the full flow field and spatial distribution of particles. The capability of first and second order models is evaluated for a range of particle concentrations. Both first and second order models provide good predictions of local phase velocities, with the latter being capable of accurately predicting particle distribution. Furthermore, the stochastic models are able to predict the two-phase flow and particle distribution outside the range of experimental conditions.

Keywords: Lagrangian trajectory, mixing, PEPT, particle-liquid flow, stirred vessel, stochastic model.

6.1 Introduction

Operations involving particle-liquid mixtures are ubiquitous in the process industries, particularly particle suspensions in mechanically agitated vessels. Deep understanding of the fluid and particle flow which is required for optimum design and operation of these vessels is still lacking, however. The flow and mixing of such suspensions have been extensively studied experimentally using mainly a global approach, and important empirical correlations have been developed such as the minimum impeller rotational speed at which solids are just suspended in a vessel (N_{js}) (Zwietering; 1958; Nienow, 1968; Brucato et al., 1997; Micale et al., 2002). In more recent years, the emergence of advanced instrumentation such as positron emission particle tracking (PEPT) and computer-automated radioactive particle tracking (CARPT) has enabled more detailed probing of these opaque systems leading to accurate measurements of local flow properties (Chen et al., 1999; Rammohan et al., 2001; Pianko-Oprych et al., 2009; Guida et al., 2010a).

Due to improvements in computational methods, research has been conducted using computational fluid dynamics (CFD) to better understand flow fields and local behaviour. The Eulerian-Eulerian two-fluid approach whereby both liquid and solid phases are treated as continua, has been applied with reasonable success (Khopkar et al., 2006; Tamburini et al., 2011; Liu & Barigou, 2013). Such an approach can give details of mean flow behaviour, however, it does not reveal the detailed flow of fluid or solid particles as this can only be fully described in Lagrangian terms. The use of Eulerian-Lagrangian CFD where only the fluid is treated as continuum and the

solid phase is treated as discrete particles has the potential to predict the full flow behaviour of solid particles and has been shown under low concentrations to give good agreement with experimental data (Brucato et al., 2002; Micale et al., 2004). It should be noted, however, that Eulerian-Lagrangian CFD approach is computationally intensive and currently not suitable for the study of dense suspensions.

Alternatively, fully Lagrangian approaches can be used to model the trajectories of solid particles. One such method known as random walk particle tracking (RWPT), has been extensively used in the analysis of dispersion and diffusion processes in porous media (Scheidegger, 1954; De Josselin de Jong, 1958). Since then, numerical codes have been developed to extend this framework to the analysis of various multiphase systems such as slug rise in fluidised beds (Dehling et al., 2007; Farzaneh et al., 2011), mixing and biochemical reactions in anaerobic digestion (Rezavand et al., 2019) and vertical transport of buoyant material in a water column (Nordam et al., 2019). The RWPT method has shown good agreement with Eulerian-Eulerian models, but it suffers from computational expense similar to Eulerian-Lagrangian CFD.

To mitigate the computational cost, hybrid methods have been developed where particles are added to a known Eulerian field using Lagrangian stochastic modelling (LSM). This approach is often used in environmental (Gleicher et al., 2014; Ferrero & Oettl, 2019) and oceanography modelling studies (Ruplo, 2006). It has also been exploited, albeit to a lesser extent, in engineering research, for example, by Matos et al. (2018) to describe the front of a fluid in a confined impinging jet reactor, and by Jalali & Borthwick (2018) to investigate particle advection near groynes in an open channel. The latter investigation led to observations of particle mixing with close agreement to analytical results for various channel and groyne combinations. A similar approach was adopted by Wu & Liang (2019) to study pollutant transport in depth-averaged flows. LSM and a Eulerian numerical model were compared to

analytical solutions, with LSM predictions showing higher accuracy due to the lack of numerical diffusion, sharp concentration gradients and solute oscillations. More recently, Yang et al. (2020) conducted comparisons of a numerical model and LSM to solve an instantaneous release of solute material into uniform straight open channel flows in shallow waters. Their extensive parametric studies showed that influence on predictions were independent of time step, but were dependant on the number of particles being simulated. Recently, we successfully applied, for the first time, a data-driven LSM to simulate turbulent single-phase liquid flow in a mechanically agitated vessel (Sheikh et al., 2022). Using a positron emission particle tracking (PEPT) technique, Eulerian velocity fields were experimentally determined along with decorrelation times for velocity and acceleration time signals to drive the LSM and predict flow behaviour.

In this study, we extend this approach to more complex two-phase particle-liquid flow systems in a mechanically agitated vessel, to unravel the complex flow behaviour of both phases. Lagrangian data obtained by tracking both phases for a short time using PEPT are used to drive the LSM and predict the long-term three-dimensional particle trajectories. LSM is studied over a wide range of particle concentrations from low (5 wt%) to high (40 wt%), and used to predict the two-phase flow for situations outside the range of experimental measurements.

6.2 Experimental

6.2.1 Mixing vessel apparatus

Particle-liquid flow and mixing was studied in a mechanically agitated vessel of diameter $T = 288$ mm and a suspension height $H = T$, as illustrated in Fig. 6.1a.

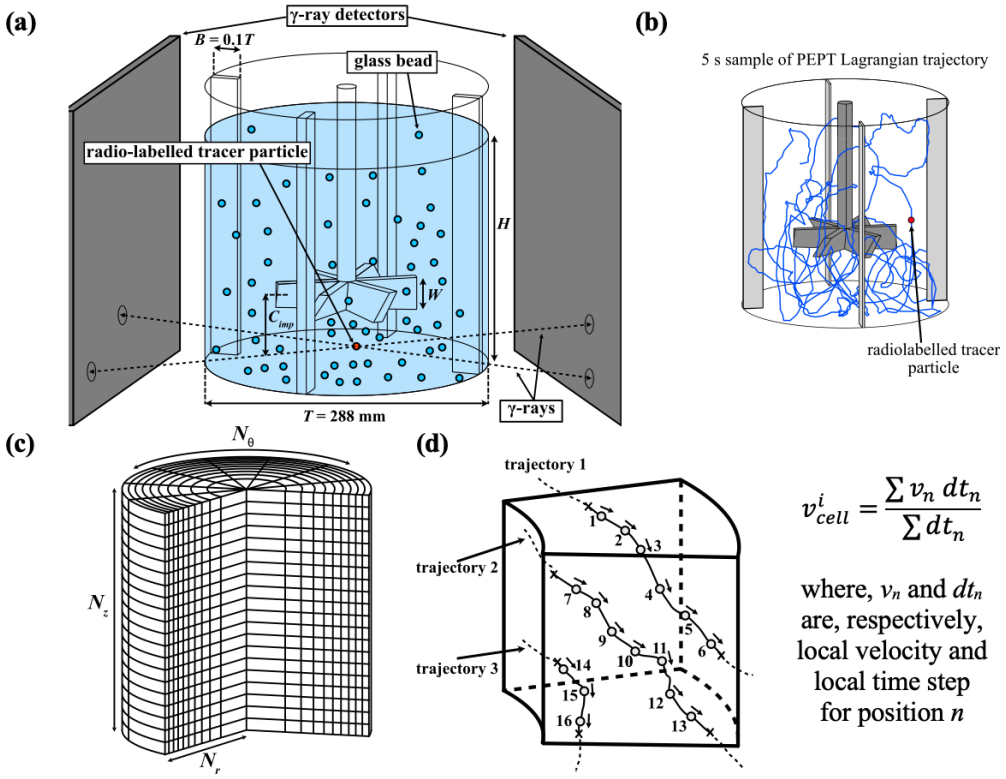


Figure 6.1: Experimental setup: (a) mixing vessel and PEPT γ-ray detectors; (b) 5 s sample of PEPT Lagrangian trajectory; (c) computational grid consisting of N_r cells in the r-direction, N_z cells in the z-direction and N_θ cells in the θ-direction; (d) method of calculation of local time-averaged velocity v_{cell} in the ith cell.

A 6-blade 45^o pitched-blade turbine was used for agitation in down-pumping mode, with a diameter $D = T/2$, impeller blade width $W = T/10$ and an impeller off-bottom clearance $C_{imp} = T/4$. The solid phase consisted of nearly monomodal nearly-spherical glass beads of 3 mm diameter, having a density of 2485 kg m-3 (Sigmund Linder, GmbH). To track particle motion, one of the representative glass particles was directly radioactively-labelled and space-time data was captured via a technique positron emission particle tracking. To track the liquid, on the other hand, a small ($\sim$ 600 μm) neutrally-buoyant resin particle radiotracer was used. Experiments were run at mean particle concentrations of 5, 10, 20 and 40 wt% (2, 5, 9 and 21 vol%, respectively) with the impeller operating at the just-suspended impeller speed, N_{js}, as described in our previous work 8.

6.2.2 Positron emission particle tracking

Long-term three-dimensional Lagrangian particle trajectories within process equipment can be obtained by using PEPT. A positron emitting tracer particle can be accurately tracked, providing three-dimensional space and time data which can, thus, be used to image flow in opaque fluids and inside opaque equipment (Barigou, 2004). The technique has a distinct advantage over other methods such as particle image velocimetry (PIV) which requires optical transparency, whilst having comparable accuracy (Pianko-Oprych et al., 2009). The PEPT technique has been extensively used to study flow and mixing in stirred vessels, and more details can be found in our earlier papers (Guida et al., 2010a, 2010b, & 2011).

6.3 Lagrangian stochastic modelling

Recently, we used LSM to successfully simulate single-phase liquid flow in a mechanically agitated vessel (Sheikh et al., 2022). In this study, LSM is used to predict three-dimensional Lagrangian particle trajectories in a solid-liquid mixing vessel. Lagrangian experimental PEPT data were used to obtain a velocity field which, along with estimated relevant decorrelation times, served as an input for the LSM model. The experimental velocity field was calculated using a defined mesh grid, where Lagrangian PEPT trajectories acquired in a stirred vessel were time-averaged in each cell, giving a local flow field for each phase of the flow, as illustrated in Fig. 6.1c-d. Then, by applying model equations, particle positions were advanced in space over a time step utilising random perturbations which are scaled according to decorrelation times. These random perturbations are defined by the Wiener process described by a Gaussian distribution with unit variance (Gardiner 2004). Decorre-

lation times for velocity and acceleration were calculated over 1 min intervals along the driver data trajectory length, and an average value is taken. Short decorrelation times indicate a quick loss in memory for the system, reflecting a high degree of stochasticity. Thereby, stochastic scaling was applied with an inverse relationship to decorrelation time. Computational cost is minimal, with simulation times being similar to that of an actual PEPT experiment, i.e. to compute a one-hour trajectory, the computational execution time of the LSM model is around one hour.

6.3.1 Model equations

Particle motion can be described using three orders of stochastic model: zeroth, first and second order, as defined by Ruplo (2006) and LaCasce (2008) in their oceanography work. The model order defines which term in calculating particle position is to be stochastically noised using the Wiener process; zeroth order noises position, first order noises velocity and second order noises acceleration. In extensive tests, the zeroth order model failed to produce accurate predictions of the two-phase particle liquid flow, thus only the first and second order models are presented here.

The first order model is defined by the following equations:

$$x_i^{t+dt} = x_i^t + dx_i^{dt} \tag{6.1}$$

$$dx_i^{dt} = (u_i^{t+dt} + \bar{U}_i)dt \tag{6.2}$$

$$u_i^{t+dt} = u_i^t + du_i^{dt} \tag{6.3}$$

$$du_i^{dt} = -\frac{u_i^t}{T_{u,i}}dt + \sqrt{\frac{2\bar{U_i}^2}{T_{u,i}}}dw^{dt} \tag{6.4}$$

where, x_i is particle position, u_i is particle velocity and $\bar{U}_i$ is mean local particle velocity in the i-direction. $T_{u,i}$ is velocity decorrelation time in the i-direction, and dw^{dt} is the Wiener process for the time step dt, which is discretised as follows:

$$dw^{dt} \approx \sqrt{dt}N(0,1) \tag{6.5}$$

where, $N(0,1)$ is a normal distribution with a mean of 0 and unit variance. In the second order model, Eq. 6.4 is replaced by the following equations:

$$du_i^{dt} = a_i^{t+dt} - \frac{u_i^t}{T_{u,i}} \tag{6.6}$$

$$a_i^{t+dt} = a_i^t + da_i^{dt} \tag{6.7}$$

$$da_i^{dt} = -\frac{a_i^t}{T_{a,i}}dt + \sqrt{2\bar{U_i}^2 \frac{T_{a,i} + T_{u,i}}{T_{a,i}T_{u,i}}}(dw^{dt})^{-1} \tag{6.8}$$

where, a_i and $T_{a,i}$ are, respectively, the local acceleration and the acceleration decorrelation time in the i-direction.

6.3.2 Model parameters

To implement LSM for particle tracking in a mixing vessel, several model parameters must be set. Firstly, an appropriate length of driver trajectory data must be selected. This is important as it defines the total amount of information supplied to the model. Using a trajectory length which is too short tends to result in significant prediction errors, as the Lagrangian driver trajectory is converted to a Eulerian velocity field and used to estimate decorrelation times. However, it turns out that in general LSM is capable of predicting long-term flow based on a short-term experimental trajectory. Tests to determine a suitable length (ranging from 1 – 10 min) of input trajectory to drive the model showed that for the two-phase flow situations considered the length of driver trajectory can be as short as 3 min. Nevertheless, a conservative driver trajectory of 5 min length was used throughout this study. Thus, using velocity and acceleration time signals obtained from the experimental PEPT trajectory, decorrelation times were estimated over 1 min intervals in for each velocity and acceleration component time signal along the 5 min trajectory, and an average value taken for each signal.

The next important step was the selection of an appropriate mesh grid defining the velocity field that achieves the highest resolution possible whilst containing enough experimental data for the length of driver data supplied. Thus, the mesh grid size

required careful consideration, as during LSM calculations if a particle encounters a cell with no velocity, i.e., no local positions from PEPT driver data, the particle will come to a halt for the rest of the simulation. A mesh of too high a density generates cells that are too small for the resolution of PEPT data, resulting in lots of zero cells containing no velocity information. On the other hand, using too low a mesh density results in a low-resolution velocity field, leading to large prediction errors. The optimum mesh density which yielded the fewest zero cells comprised of N_c = 2400 cells of equal volume: N_θ= 12 in the tangential direction, N_r = 10 in the radial direction, and N_z = 20 in the axial direction, as illustrated in Fig. 6.1c. Any zero cells encountered in converting the Lagrangian PEPT data to the Eulerian velocity field were assigned an estimated velocity value using a linear 3D grid interpolation. As verified by Yang et al. (2020), LSM predictions are independent of time step, but a time step of 5 ms was used as this matches the mean temporal resolution of experimental PEPT data and is a small enough time step to resolve particle-wall collisions with the vessel wall.

The simulated tracked particle is generally able to traverse the solid boundary of the flow field, therefore a check is implemented after each new particle position is computed. If the simulated particle is detected outside of the vessel boundary, a collision calculation is triggered to calculate a new position for the particle within the domain. Particle-wall collisions present in PEPT trajectories were analysed by comparing the ratio between tracer velocity before and after the collision. An arbitrary collision factor C_f can be defined in two ways, as follows:

$$C_f = \frac{|v_r|}{|v_i|} \tag{6.9}$$

where, v_i and v_r are, respectively, the particle-wall incident and rebound velocity vectors. Alternatively, the angle of collision with the vessel wall, ϕ, can also be taken into consideration, thus:

$$C_f = \frac{1}{tan(\phi)} \tag{6.10}$$

where, ϕ is defined as:

$$tan(\phi) = \frac{\|v_i \times v_r\|}{v_i \cdot v_r} \tag{6.11}$$

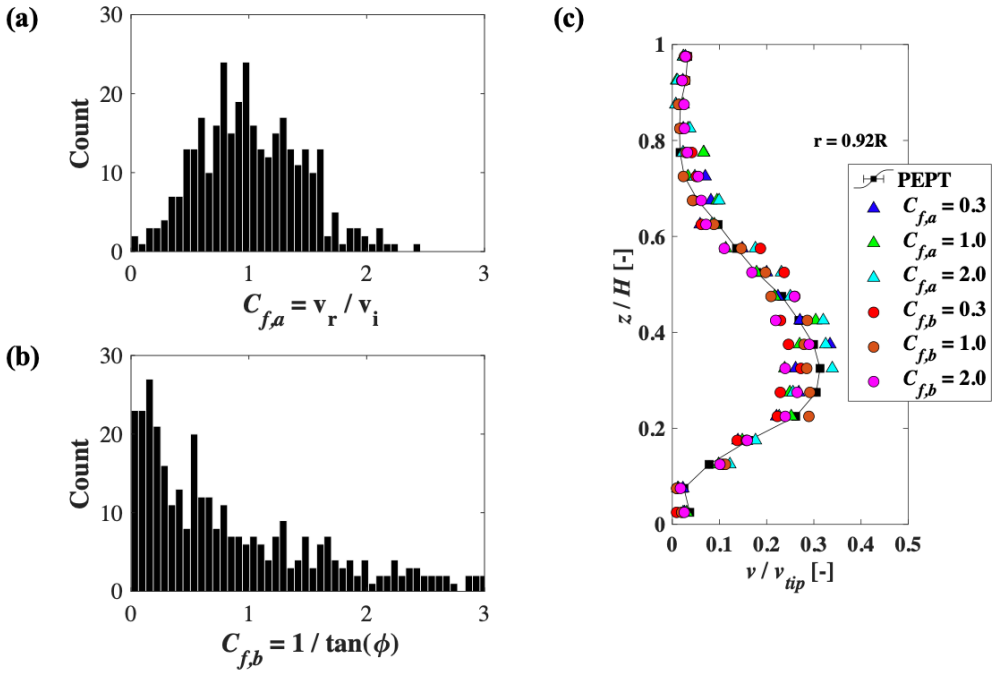


Figure 6.2: Histograms of PEPT particle-wall collision factor for experiments containing 20 wt/wt% of 3 mm glass beads: (a) $C_{f,a} = \frac{|v_r|}{|v_i|}$; (b) $C_{f,b} = \frac{1}{tan(\phi)}$; and (c) analysis of sensitivity to the definition and value of C_f adopted of LSM-predicted time-averaged velocity profiles in cells adjacent to the vessel wall.

Both definitions were used to plot distributions of C_f for typical experimental data, as depicted in Fig. 6.2. Fig. 6.2a shows a mean C_f value close to 1, indicating on average nearly perfectly elastic collisions irrespective of the particle-wall contact angle. Using the definition in Eq. 6.10, Fig. 6.2b shows a mean C_f value close to 0, i.e. $\phi \approx 90^o$, indicating, on average, almost perfectly elastic collisions. The value of C_f can also be affected by oncoming flow which may impart additional mo-

mentum to the colliding particle. Hence a sensitivity analysis where LSM-predicted trajectories using both definitions of C_f and a range of assigned arbitrary values was conducted, and the time-averaged velocity profiles in the cells adjacent to the vessel wall are compared in Fig. 6.2c. Results show that the LSM-predicted velocity is not sensitive to the definition of C_f or value adopted, hence it can be concluded that either definition can be used with no significant effects on the simulation predictions. Consequently, to minimise computational cost, Eq. 6.9 was adopted in all calculations and C_f was assigned a value of 1.

6.4 Model testing and validation

Three-dimensional Lagrangian trajectories were simulated for both the liquid and solid phase using LSM on MATLAB. Analyses were conducted for the first and second order models, denoted respectively by ${}^1LSM$ and ${}^2LSM$. The computational time for a 40 min trajectory was 30 min for ${}^1LSM$ and 60 min for ${}^2LSM$. As discussed above, the driver trajectories used were of 5 min length, providing adequate information for trajectory predictions. To evaluate model performance, the computed azimuthally averaged distributions of local velocity and particle concentration were compared to PEPT measurements in six axial (vertical) planes ranging from the tip of the impeller ($r = 0.5R$) to near the vessel wall ($r = 0.87R$). Comparison was also made in six radial (horizontal) planes ranging from near the bottom of the vessel ($z = 0.03H$) to near the free surface ($z = 0.97H$), including planes just below ($z = 0.17H$) and just above ($z = 0.38H$) the impeller. Testing and validation of ${}^1LSM$ and ${}^2LSM$ was conducted using two-phase particle-liquid PEPT measurements obtained in suspensions of 3 mm glass beads at concentrations of 5, 10, 20 and 40 wt% (2, 5, 9 and 21 vol%, respectively), in the hydrodynamic flow regime corresponding to the just-suspended impeller speed, N_{js}.

6.4.1 Velocity profiles

Velocity profiles of liquid phase

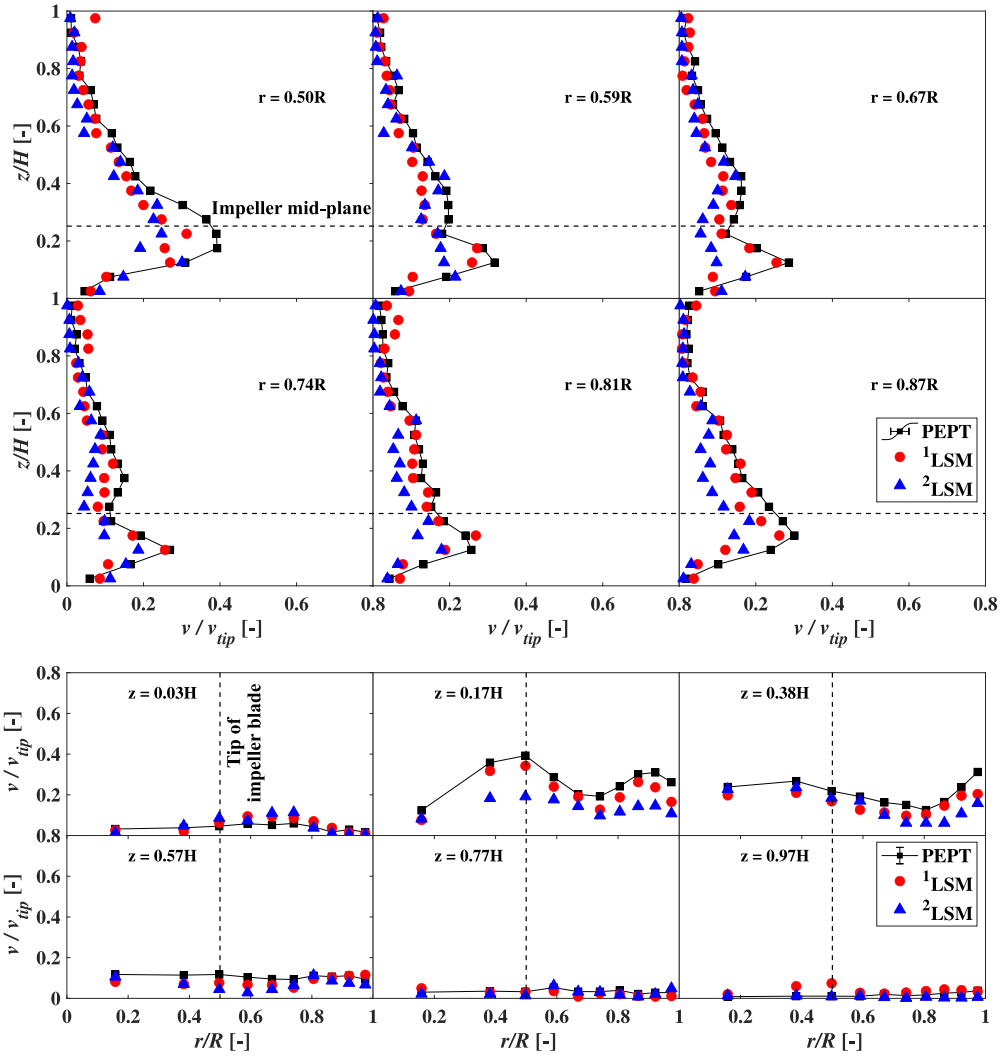


Figure 6.3: Azimuthally averaged profiles of total liquid velocity: PEPT, ^1LSM and ^2LSM compared for 40 wt% of particles.

Validation of the velocity field was performed by comparing experimental azimuthally averaged axial and radial profiles of the three velocity components (v_r, v_z, v_θ) to velocity profiles predicted by ^1LSM and ^2LSM. Predictions by ^1LSM agreed very well with experimental measurements for all velocity components. ^2LSM predicted all velocity components quite well except near the vessel wall. For illustration, the

radial and axial profiles of the total velocity which are presented in Fig. 6.3 for a typical sample case of 3 mm glass beads at 40 wt%. These results are representative of the level of prediction of both models for all cases of particle concentration studied, and show that whilst ^{2}LSM gives reasonably good predictions, ^{1}LSM is the more accurate model for simulating the liquid phase.

Velocity profiles of solid phase

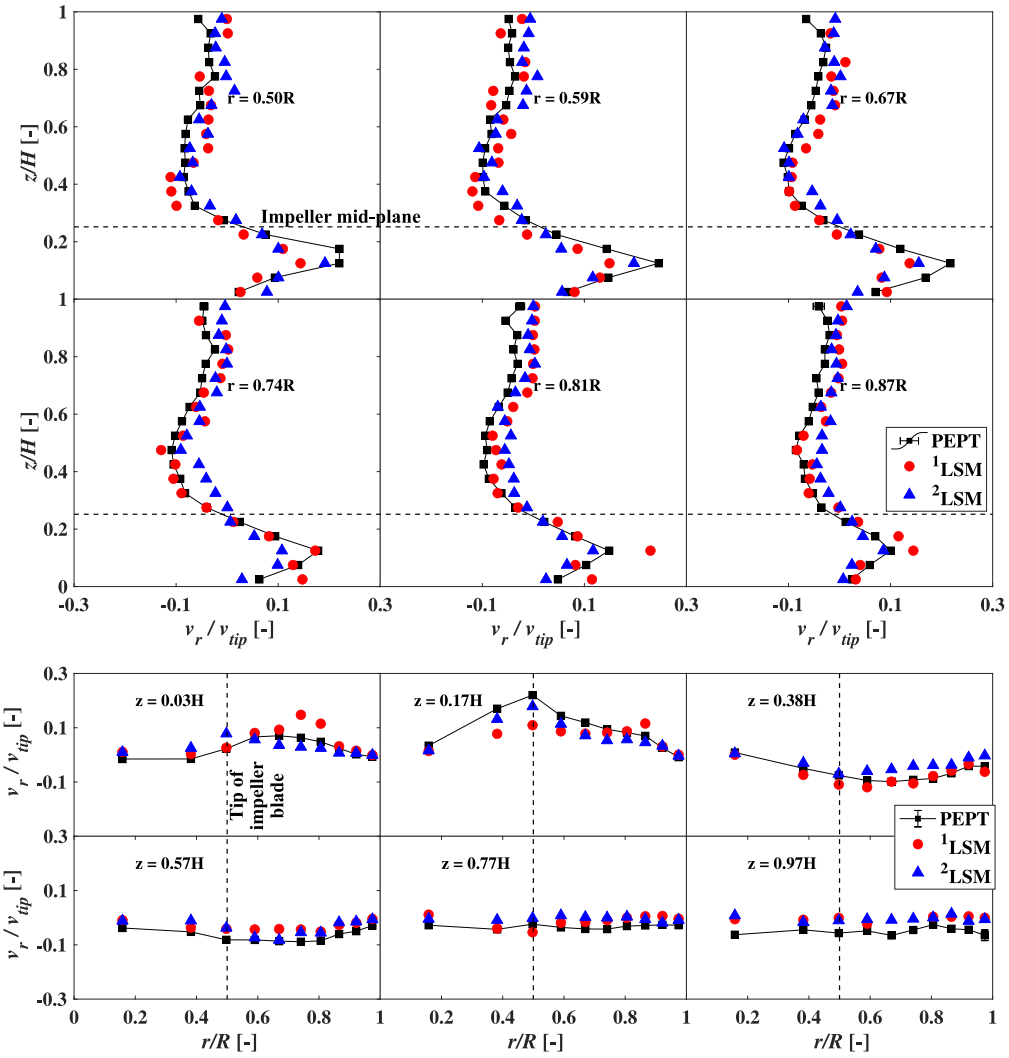


Figure 6.4: Azimuthally averaged axial and radial profiles of local solid r-velocity component: ^{1}LSM, ^{2}LSM predictions and PEPT measurements compared for 40 wt% of particles.

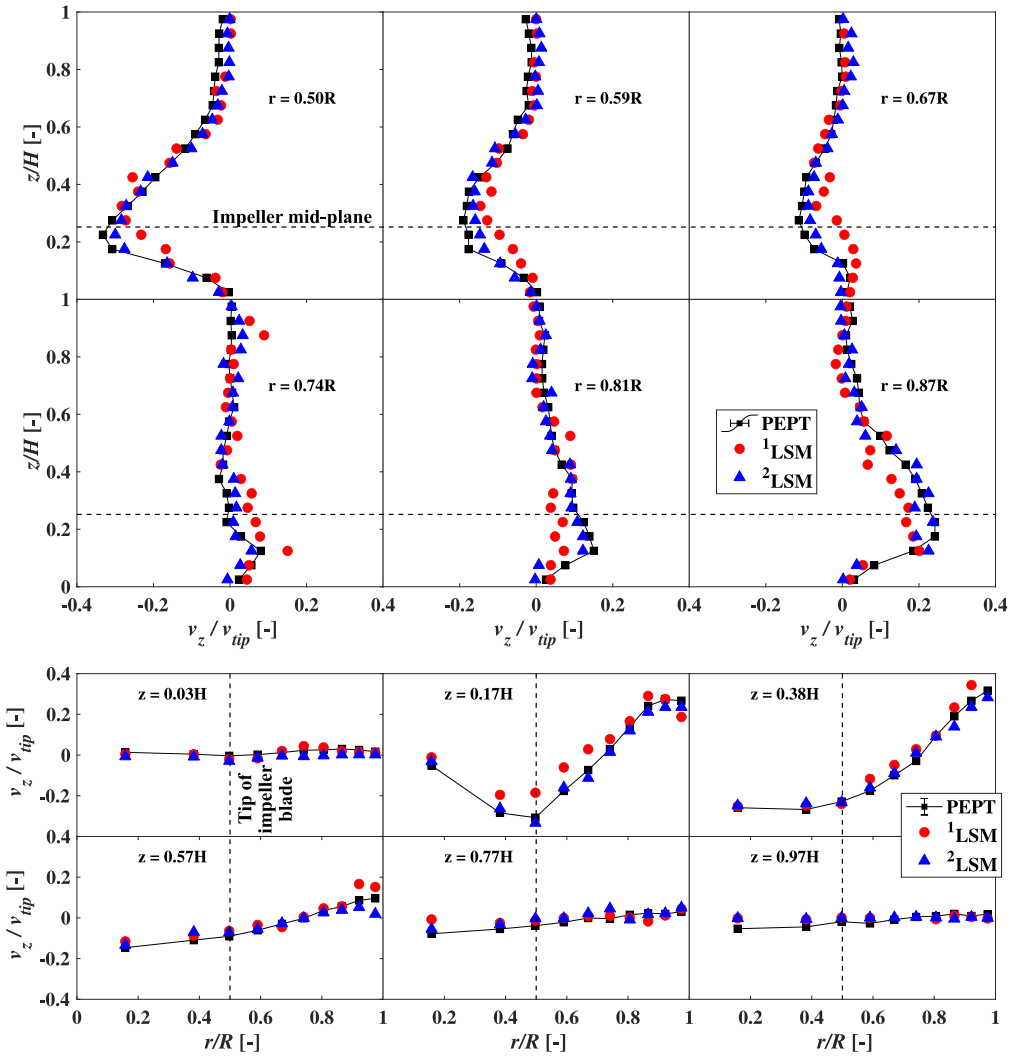


Figure 6.5: Azimuthally averaged axial and radial profiles of local solid z-velocity component: ^1LSM, ^2LSM predictions and PEPT measurements compared for 40 wt% of particles.

The azimuthally averaged radial and axial velocity profiles of the solid phase for the typical sample case of 3 mm glass beads at 40 wt% are depicted in Figs. 6.4-6.6 in the three directions (r, z, θ). Both models showed equal capability of predicting velocity components for solid phase tracking in all vessel regions. Predictions by ^2LSM show a very good agreement with experimental measurements for all velocity components. Similarly, ^1LSM predicts v_r and v_z very well, but it exhibits some local underpredictions for v_θ (Fig. 6.6), which are mainly confined to the bottom half of the vessel ($r = 0.59R0.81R$) and in the vicinity of the impeller region ($z = 0.17H$).

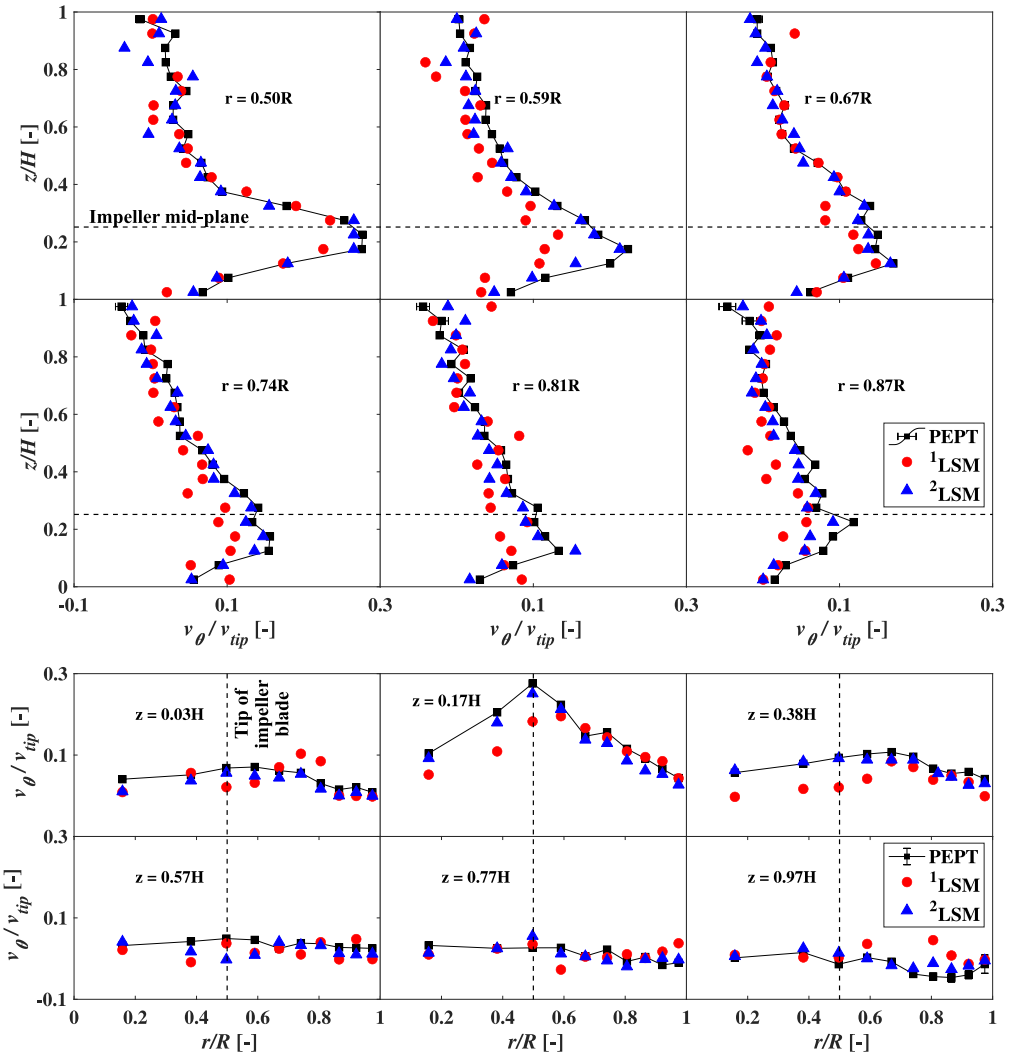


Figure 6.6: Azimuthally averaged axial and radial profiles of local solid θ-velocity component: ^1LSM, ^2LSM predictions and PEPT measurements compared for 40 wt% of particles.

Discrepancies near the impeller could also be partly attributed to a certain degree of experimental error because of the high turbulence and complex trajectories in this region (Pianko-Oprych et al., 2009; Liu & Barigou, 2013). For the case of 40 wt% of 3 mm particles, ^2LSM performs somewhat better than ^1LSM, especially in the θ direction. The discrepancies observed in Figs. 6.4-6.6 are reflected in the total velocity profiles, henceforth the capability of the two models will be evaluated in terms of total velocity.

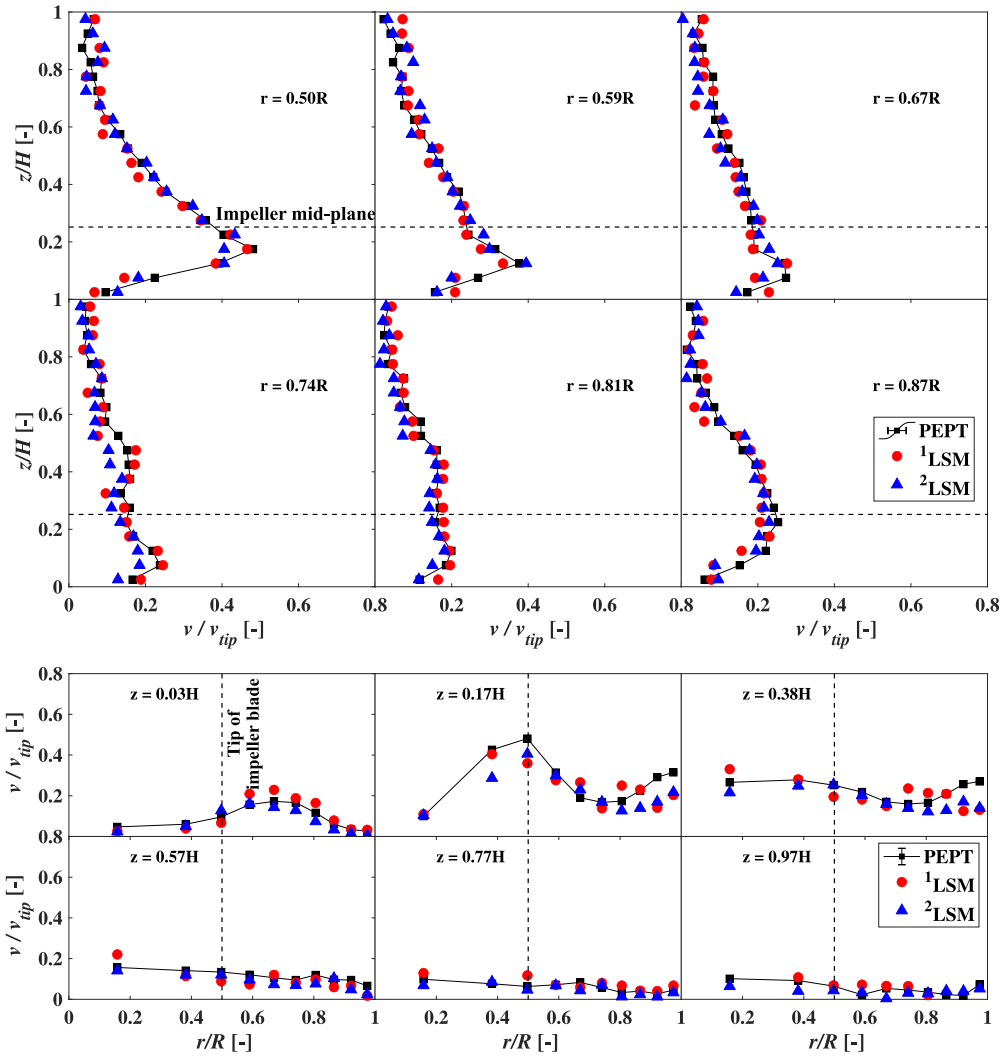


Figure 6.7: Azimuthally averaged profiles of total solid velocity: PEPT, ^{1}LSM and ^{2}LSM compared for 5 wt% of particles.

The effect of a using a much lower particle concentration (5 wt%) is represented in Fig. 6.7. Contrary to the high concentration case described above in Figs. 6.4-6.6 where ^{2}LSM performed somewhat better than ^{1}LSM, for the 5 wt% case both ^{1}LSM and ^{2}LSM show an equally very good agreement with experimental data. The improvement of ^{1}LSM occurred gradually as particle concentration was lowered from 40 wt% down to 20, 10 and 5 wt%, as depicted in Fig. 6.7. This is most likely due to particle-particle interactions in the mixing vessel being more intensive at high particle concentrations; random collision forces result in more stochastic effects on the acceleration of particles. As ^{1}LSM does not take acceleration decorrelation

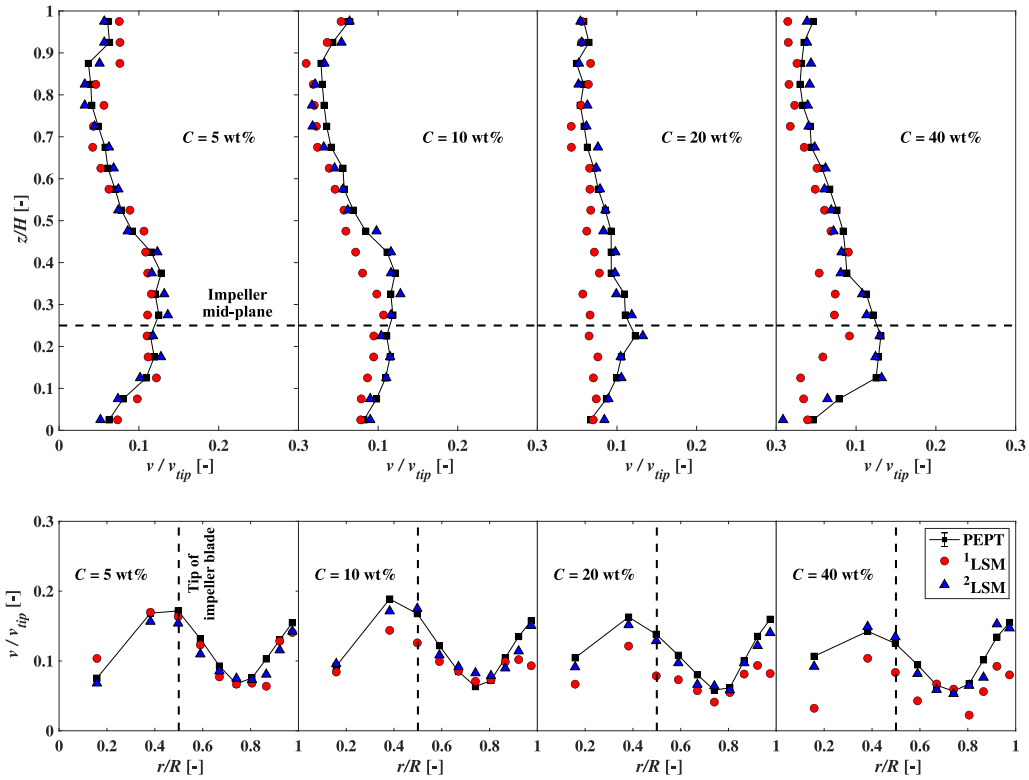


Figure 6.8: Azimuthally averaged profiles of total solid velocity: PEPT, ^{1}LSM and ^{2}LSM compared for 5, 10, 20, 40 wt% of particles.

times into account (Eq. 1-4), this effect is not captured in the trajectory simulation. In contrast, ^{2}LSM which is a second order model includes these acceleration effects. Such particle-particle interaction effects are however reduced at low concentrations so that the performance of ^{1}LSM approaches that of ^{2}LSM. Therefore, it can be concluded that whilst ^{1}LSM gives reasonable predictions of particle velocities, all results taken together indicate that ^{2}LSM overall is the more accurate model for simulating the motion of particles.

6.4.2 Spatial particle distribution

We previously established a method by which Lagrangian experimental PEPT data can be used to determine the distribution of particles in a mixing vessel, utilising the occupancy of the tracer for the duration of the experiment (Guida et al., 2010a;

Liu & Barigou, 2013). By assuming ergodicity and dividing the vessel into a grid of equal volume cells, local occupancy of the particle can be expressed as a fraction of the ergodic time (t_E), where t_E is the time which a particle would spend in a single cell and is defined as the total experimental time (t_∞) divided by number of cells, i.e., $t_E = t_\infty / N_c$. Thus, the local occupancy (O_E) can therefore be defined as:

$$O_E = \frac{\Delta t}{t_E} \tag{6.12}$$

where, Δt is the time the tracer spends inside a given cell. It can be shown that for a closed system the mean local occupancy is equal to one, and the local occupancy of a flow component in a multiphase system becomes identical to its local time-average concentration. The local occupancy can then be shown to be equal to the ratio of the local particle concentration, c, and the mean particle concentration in the vessel, C, as follows:

$$O_E = \frac{c}{C} \tag{6.13}$$

Using these definitions, the local particle distribution in the vessel can be determined from both experimental PEPT measurements and LSM predictions and compared pointwise.

The azimuthally averaged axial and radial solid phase distributions for 40 wt% of particles predicted by ${}^1LSM$ and ${}^2LSM$ are compared to the experimental profiles in Fig. 6.9. ${}^2LSM$ predicts very well throughout the vessel. ${}^1LSM$ gives a reasonably good agreement in most regions of the flow, but shows some significant underestimations in the top third of the vessel. Although any errors in the experimental driver data tend to be amplified by ${}^2LSM$, being a second order model, nevertheless results show that such a model is better at predicting particle flow due to the inclusion of acceleration decorrelation times (Eqs. 6.6-6.8).

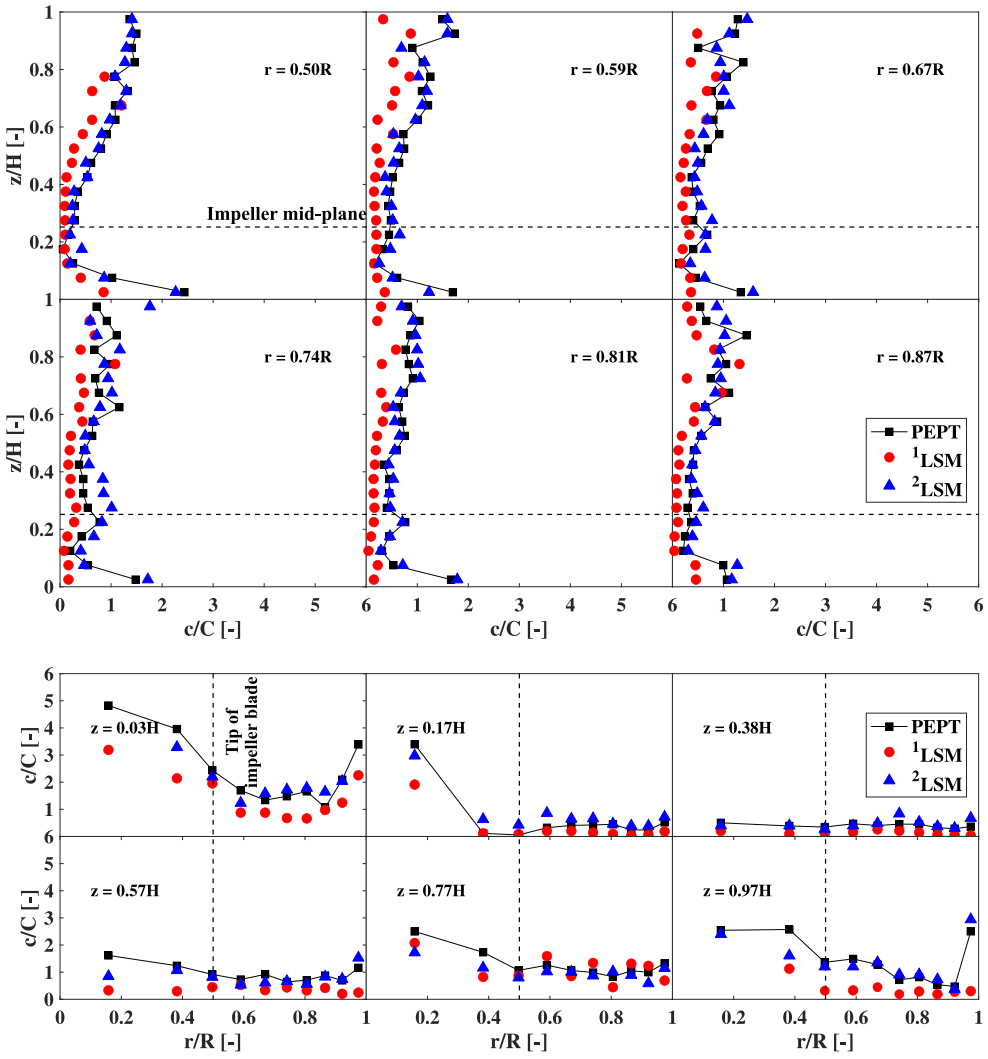


Figure 6.9: Azimuthally averaged profiles of local particle concentration: PEPT, ^{1}LSM and ^{2}LSM compared for 40 wt% of particles.

As in the case of velocity, the prediction of local particle concentration affects the degree of accuracy of ^{1}LSM. As shown in Fig. 6.10, whilst ^{2}LSM performs consistently well, ^{1}LSM clearly yields better predictions as the mean particle concentration is gradually reduced, coinciding with ^{2}LSM at the lowest concentration investigated. It is noteworthy that a stochastic model which is only driven by a small (5 min) set of experimental velocity data is not only able to accurately simulate the two-phase velocity field, but it is also able to predict the distribution of the solid phase in the vessel to such a high degree of accuracy even under the challenging conditions of a concentrated particle-liquid flow. This makes LSM a highly efficient

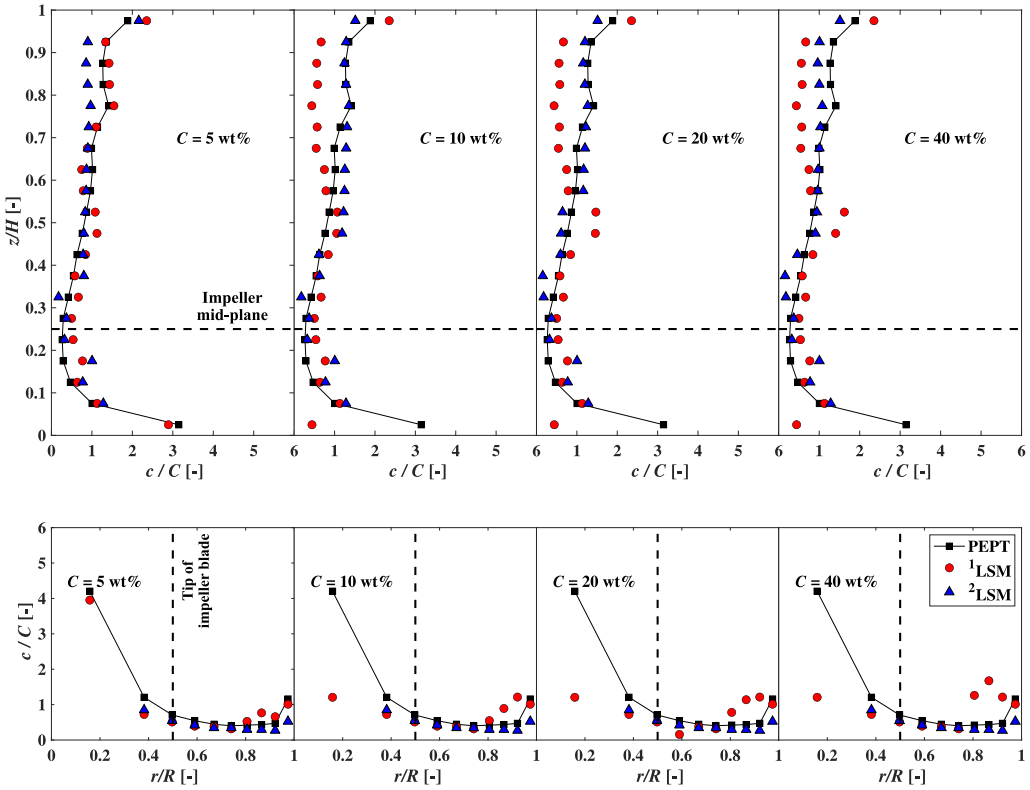


Figure 6.10: Azimuthally averaged profiles of local solid concentration: PEPT, ^1LSM and ^2LSM compared for 5, 10, 20, 40 wt% of particles.

modelling strategy.

6.4.3 Prediction of flow conditions outside range of experimental measurements

LSM can be used to predict flow conditions outside the range of experimental measurements. In other words, simulations can be extrapolated to different flow regimes can be achieved such as flow at higher impeller rotation rates or higher particle concentrations. In this study, we used a 5 min velocity data set from an experimental trajectory obtained at 490 rpm (N_{js}) in a suspension of 20 wt% particles to drive the LSM and predict the velocity field at $1.25N_{js}$, i.e., 613 rpm. This is an extrapolation from the just-suspended flow regime to an almost fully-suspended regime. The ve-

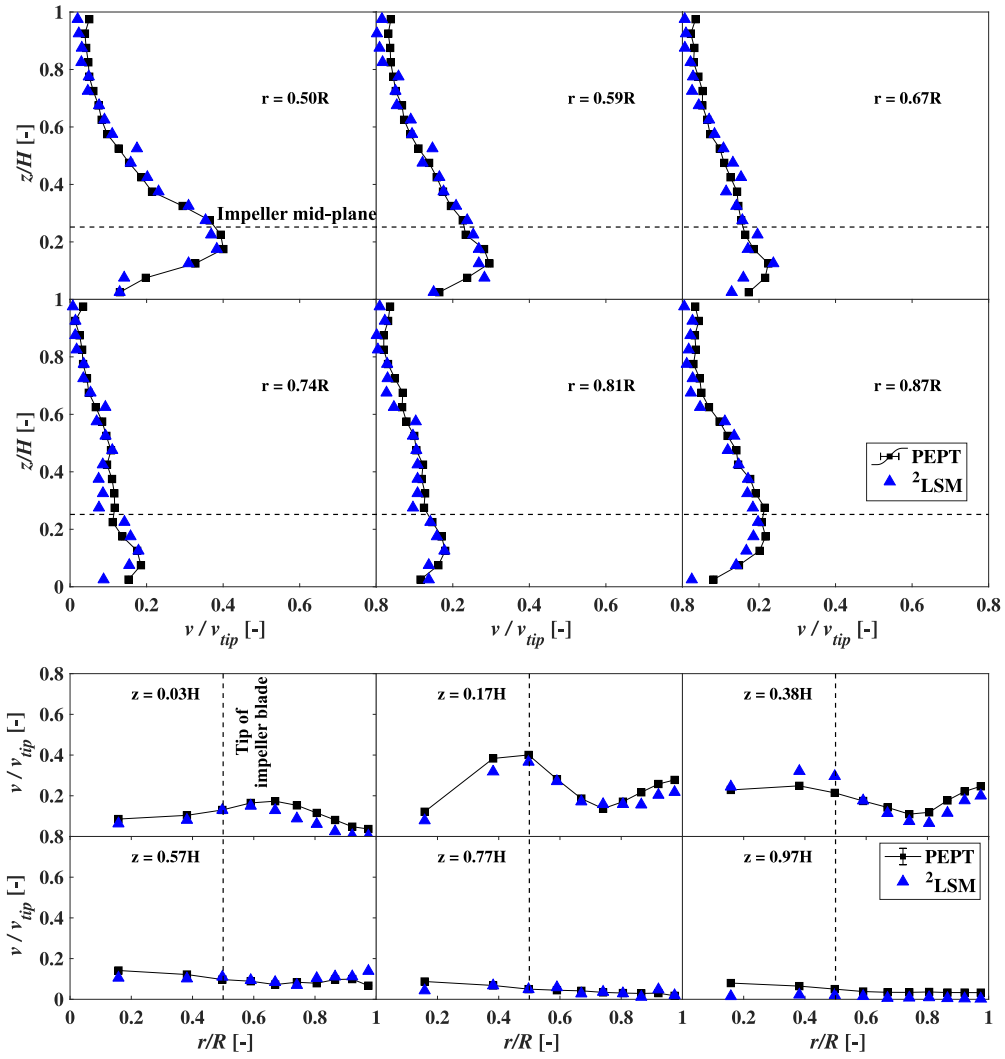


Figure 6.11: Azimuthally averaged profiles of total solid velocity: PEPT and ^2LSM compared for 20 wt% of particles at $1.25N_{js}$, where ^2LSM is driven by 5 min of velocity data at N_{js} and 20 wt% of particles.

locity data were multiplied by the ratio $v_{tip,613rpm}/v_{tip,490rpm}$, and then fed to ^2LSM to predict the long-term trajectory corresponding to 613 rpm. Total velocity results in Fig. 6.11 show predictions agree very well with the experiment, with minimal errors.

Furthermore, we used 5 min velocity driver data corresponding to 20 wt% particles at N_{js} (490 rpm) to predict the velocity field as well as the spatial distributions of particles for 40 wt% particles at N_{js} (590 rpm). The velocity data were multiplied

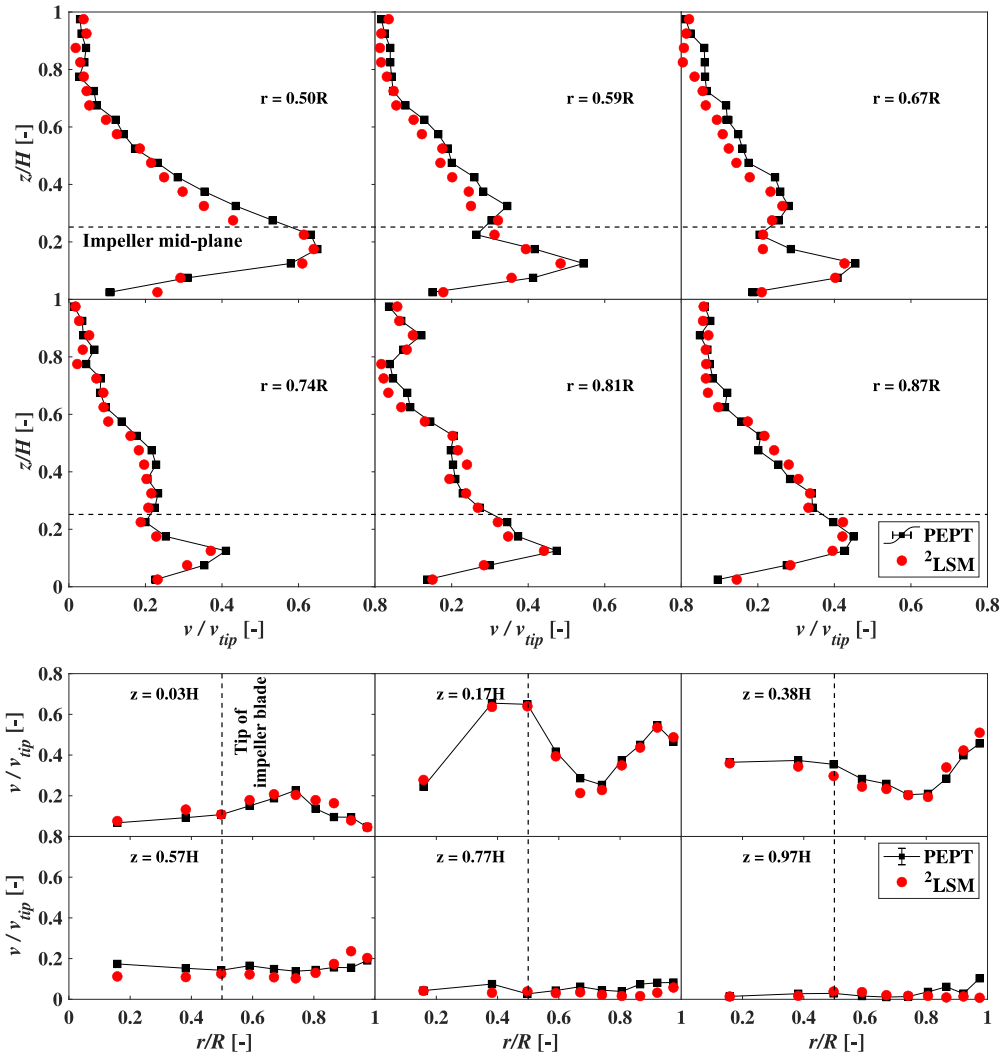


Figure 6.12: Azimuthally averaged profiles of total solid velocity: PEPT and ${}^2LSM$ compared for 40 wt% of particles at N_{js}, where ${}^2LSM$ is driven by 5 min of velocity data at N_{js} and 20 wt% of particles.

by the ratio $v_{tip,590rpm}/v_{tip,490rpm}$, and then fed to ${}^2LSM$ to predict the long-term trajectory corresponding to 40 wt% of particles. Total velocity results presented in Fig. 6.12, show very good predictions with only small errors incurred. Likewise, the predicted local concentration profiles depicted in Fig. 6.13, show good agreement with experiment. Contrary to deterministic numerical models, LSM is capable of accurately predicting particle flow and distribution at a fraction of the computational cost.

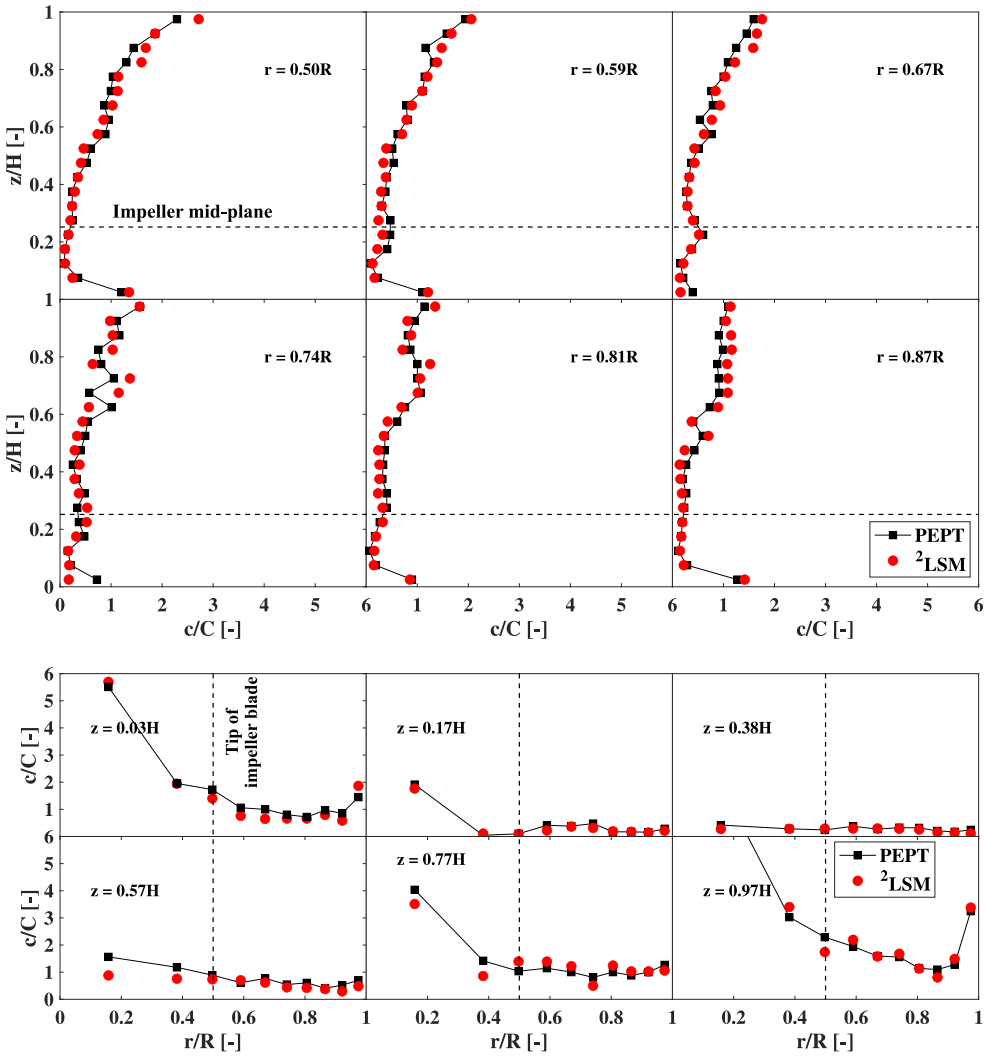


Figure 6.13: Azimuthally averaged profiles of total solid concentration: PEPT and ${}^2LSM$ compared for 40 wt% of particles at N_{js}, where ${}^2LSM$ is driven by 5 min of velocity data at N_{js} and 20 wt% of particles.

6.5 Conclusion

A data-driven Lagrangian stochastic model has been used to successfully predict two-phase particle-liquid flow in a mechanically agitated vessel. Both first and second order models provide good predictions of local phase velocity, whilst the second order model is also capable of predicting the local particle concentration. A range of particle concentrations were studied. The model can predict flow outside the range

of experimental conditions, for example, using initial driver data from a lower particle concentration experiment to predict flow and particle distribution for cases of higher mean concentrations. The LSM approach is an accurate method for predicting Lagrangian flow in multiphase mixing systems and has the advantage of being computationally efficient compared to other modelling techniques.

Limitations in using LSMs for the predictions of Lagrangian trajectories in multiphase mixing systems match those experienced in single phase cases (section 5.5), namely difficulties in predicting for new geometries and different hydrodynamic regimes. An additional limitation unique to a solid-liquid system is the properties of the solid phase, i.e. density, size, shape, etc., where these factors have a significant effect on the velocity fluctuations and in some drastic cases the mean flow field. In these cases errors in prediction would be large. As with single phase use, the best utilisation for LSM predictions is extending existing information, and predicting within the parameters of similarity such as changing particle concentration at N_{js}.

Nomenclature

Symbols

a	particle acceleration (m s^{-2})
B	baffle width (m)
C_f	collision factor
C_{imp}	impeller clearance (m)
D	impeller diameter (m)
dt	time step (s)
dw	Wiener process ($s^{1/2}$)
H	height of suspension (m)

N_c	total number of cells
N_r	number of cells in radial direction
N_z	number of cells in axial direction
N_θ	number of cells in azimuthal direction
O_E	local occupancy
r	radial position in the tank (m)
R	tank radius (m)
Δt	time spent by tracer particle in a cell (s)
T	tank diameter (m)
T_u, T_a	velocity and acceleration decorrelation time (s)
t_E	ergodic time (s)
t_∞	total experimental time (s)
u	particle velocity (m s^{-1})
$\bar{U}$	mean particle velocity (m s^{-1})
v	total velocity (m s^{-1})
$\boldsymbol{v_i}, \boldsymbol{v_r}$	particle incident/rebound velocity vector (m s-1)
v_{cell}	local time-averaged velocity
v_{tip}	impeller tip velocity (m s^{-1})
W	impeller width (m)
x	particle position (m)
z	axial position in the tank (m)

Abbreviations

LSM	Lagrangian stochastic model
^{1}LSM	first order Lagrangian stochastic model
^{1}LSM	second order Lagrangian stochastic model
PEPT	positron emission particle tracking
RWPT	random walk particle tracking

References

- Barigou, M. (2004) Particle Tracking in Opaque Mixing Systems: An Overview of the Capabilities of PET and PEPT, Chemical Engineering Research and Design, 82(9), pp. 12581267.

- Brucato, A. et al. (2002) Experimental investigation and CFD simulation of dense solid-liquid suspensions in a fully baffled mechanically stirred tank, in Proceedings of the 10th Workshop on two-phase flow predictions. Merseburg, Germany, 9-12 April, pp. 255264.

- Brucato, A., Micale, G. and Rizzuti, L. (1997) Determination of the amount of unsuspended solid particles inside stirred tanks by means of pressure measurements, Récents Progrès en Génie des Procédés, 11(52).

- Chen, J. et al. (1999) Comparative hydrodynamics study in a bubble column using computer-automated radioactive particle tracking (CARPT)/computed tomography (CT) and particle image velocimetry (PIV), Chemical Engineering Science, 54(1314).

- De Josselin de Jong, G. (1958) Longitudinal and transverse diffusion in granular deposits, Trans. Am. Geophys. Union, 39.

- Dehling, H.G. et al. (2007) A stochastic model for mixing and segregation in slugging fluidized beds, Powder Technology, 171(2), pp. 118125.

- Farzaneh, M. et al. (2011) A novel multigrid technique for Lagrangian modeling of fuel mixing in fluidized beds, Chemical Engineering Science, 66(22), pp. 56285637.

- Ferrero, E. and Oettl, D. (2019) An evaluation of a Lagrangian stochastic model for the assessment of odours, Atmospheric Environment, 206, pp.

237246.

- Gardiner, C. W. (2004), Handbook of Stochastic Methods for Physics, Chemistry, and the Natural Sciences, number 13 in Springer Series in Synergetics, 4th edition edn, Springer-Verlag, Berlin.

- Gleicher, S.C. et al. (2014) Interpreting three-dimensional spore concentration measurements and escape fraction in a crop canopy using a coupled Eulerian-Lagrangian stochastic model, Agricultural and Forest Meteorology, 194, pp. 118131.

- Guida, A., Nienow, A.W. and Barigou, M. (2010a) PEPT measurements of solid-liquid flow field and spatial phase distribution in concentrated monodisperse stirred suspensions, Chemical Engineering Science, 65(6), pp. 19051914.

- Guida, A., Nienow, A.W. and Barigou, M. (2010b) Shannon entropy for local and global description of mixing by Lagrangian particle tracking, 65(10), pp. 28652883.

- Guida, A., Nienow, A.W. and Barigou, M. (2011) Mixing of dense binary suspensions: Multi-component hydrodynamics and spatial phase distribution by PEPT, American Institute of Chemical Engineers Journal, 57(9), pp. 23022315.

- Jalali, M.M. and Borthwick, A.G.L. (2018) Tracer advection in a pair of adjacent side-wall cavities, and in a rectangular channel containing two groynes in series, Journal of Hydrodynamics, 30.

- Khopkar, A.R. et al. (2006) Computational fluid dynamics simulation of the solid suspension in a stirred slurry reactor, Industrial & Engineering Chemistry Research, 45(12).

- LaCasce, J.H. (2008) Statistics from Lagrangian observations, Progress in Oceanography, 77, pp. 129.

- Liu, L. and Barigou, M. (2013) Numerical modelling of velocity field and phase distribution in dense monodisperse solidliquid suspensions under different regimes of agitation: CFD and PEPT experiments, Chemical Engineering Science, 101, pp. 837850.

- Matos, J. et al. (2018) Lagrangian mixing simulation and quantification of scales, Chemical Engineering Science, 192, pp. 199210.

- Micale, G. et al. (2004) CFD simulation of particle suspension height in stirred vessels, Chemical Engineering Research and Design, 82.

- Micale, G., Grisafi, F. and Brucato, A. (2002) Assessment of particle suspension conditions in stirred vessels by means of pressure guage technique, Chemical Engineering Research and Design, 80(8).

- Nienow, A.W. (1968) Suspension of solid particles in turbine agitated baffled vessels, Chemical Engineering Science, 23(12).

- Nordam, T. et al. (2019) Numerical analysis of boundary conditions in a Lagrangian particle model for vertical mixing, transport and surfacing of buoyant particles in the water column, Ocean Modelling, 136, pp. 107119.

- Pianko-Oprych, P., Nienow, A.W. and Barigou, M. (2009) Positron emission particle tracking (PEPT) compared to particle image velocimetry (PIV) for studying the flow generated by a pitched-blade turbine in single phase and multi-phase systems, Chemical Engineering Science, 64(23), pp. 49554968.

- Rammohan, A.R. et al. (2001) A Lagrangian description of flows in stirred tanks via computer-automated radioactive particle tracking (CARPT), Chemical Engineering Science, 56(8).

- Rezavand, M. et al. (2019) A fully Lagrangian computational model for the

integration of mixing and biochemical reactions in anaerobic digestion, Computers & Fluids, 181, pp. 224235.

- Ruplo, V. (2006) A Lagrangian-Based Approach for Determining Trajectories Taxonomy and Turbulence Regimes, Journal of Physical Oceanography, 37, pp. 15841609.

- Scheidegger, A.E. (1954) Statistical hydrodynamics in porous media, Journal of Geophysical Research, 66.

- Sheikh, H.A., Savari, C. and Barigou, M. (2022) Lagrangian stochastic modelling of liquid flow in a mechanically agitated vessel, Chemical Engineering Science, 249.

- Tamburini, A. et al. (2011) CFD simulations of dense solid-liquid suspensions in baffled stirred tanks: Prediction of suspension curves, Chemical Engineering Journal, 178.

- Wu, X. and Liang, D. (2019) Study of pollutant transport in depth-averaged flows using random walk method, Journal of Hydrodynamics, 31.

- Yang, F. et al. (2020) On the application of the depth-averaged random walk method to solute transport simulations, Journal of Hydrodynamics, 22(1).

- Zwietering, Th.N. (1958) Suspending of solid particles in liquid by agitators, Chemical Engineering Science, 8(34), pp. 244253.

Chapter 7

Machine learning framework for construction of Lagrangian turbulent flow field in multiphase stirred vessels

Abstract

We present a novel computationally efficient machine learning (ML) framework for constructing the turbulent flow field of single-phase or multiphase particle-liquid flows in a stirred vessel by feeding a very short-term experimental trajectory. Using a supervised k-nearest neighbours regressor learning algorithm coupled with a Gaussian process, the framework predicts the mean flow and turbulent fluctuations by sharing the statistical features learned from experimental data. Its capability is evaluated by comparing the flow dynamics of predicted trajectories to extensive Lagrangian particle tracking measurements under various flow conditions. Local velocity distributions, Lagrangian statistical analysis, solid concentration distributions and phase flow numbers show very good agreement between ML-predictions and ex-

periments. Being accurate, efficient and robust, the ML framework is a powerful tool for analysing and modelling multiphase flow systems using a minimal amount of driver data input which can equally be provided from any reliable numerical simulation, thus avoiding costly experimental measurements.

Keywords: Turbulent flow; Stirred vessel; Machine learning; Lagrangian trajectory; PEPT.

7.1 Introduction

Mechanically agitated vessels operating in the turbulent regime are widely used in industry to rapidly reduce non-uniformity of phase, concentration or temperature, thus, ensuring good product physical mixing, increasing heat and mass transfer rates or enhancing chemical reaction (Paul et al., 2003; Harnby et al., 1997). Applications range from the manufacture of fine chemicals, agrichemicals, food, pharmaceuticals, consumer products and product formulation for these industries, to mining, paper and pulp, biofuels and water treatment. During mixing, various physicochemical processes might occur simultaneously and, as a result, numerous designs of stirred vessels have been developed to try and achieve these demands (Torotwa et al, 2018; Ghotli et al., 2020). The complexity of the internal processes has made the design of stirred vessels more an art than a science and the search for more effective analysis tools continues on both experimental and theoretical fronts. In particular, there is a continuous need for developing relevant predictive modelling strategies which can assist in equipment and process design.

The power of Computational fluid dynamics (CFD) to model the local flow dynamics in mixing vessels has been demonstrated in many studies, but the multiscale (spatial

and temporal) nature of turbulent flows still presents considerable challenges. With the improvements in computational power, various theoretical approaches (Aubin et al., 2004; Blazek, 2005; Ochieng et al., 2009) have been developed to model turbulent flows. Reynolds-averaged Navier-Stokes (RANS) models are the most widespread due to their relatively easy implementation and tractable computation. However, accessible RANS models tend to lack accuracy in many situations, particularly those involving more complex subscale processes. On the other hand, direct numerical simulation (DNS) which fully solves the instantaneous Navier-Stokes equations without a turbulence model, is only appliable to simple flows at low Reynolds numbers since it requires sufficient spatial and temporal resolution down to the Kolmogorov length and time scales (Gillissen et al., 2012; Blazek, 2005). As a compromise between prediction accuracy and computational cost, large eddy simulation (LES) simultaneously computes the contributions of large-scale energy-carrying and small eddy structures to momentum/energy transfer (Zadghaffari et al., 2010). It is essentially based on a spatial filtering operation that decomposes flow variables into large-scale and subscale, and how much of the latter part can be solved highly depends on the subgrid scale. Therefore, LES is computationally more expensive than RANS but much less so than DNS. In general, existing turbulence models only approximate turbulence effects and the search for improved models continues.

Recently, a variety of data-driven theoretical strategies relying on high quality driver data from experimental measurements or numerical solutions have been proposed but have not been widely exploited in the analysis and modelling of engineering fluid flow systems (Savari et al., 2021; Sheikh et al., 2022; Li et al., 2022). In particular, the recent advancements in machine learning (ML) have provided new opportunities in the field of fluid dynamics, for analysis, understanding, modelling, optimisation and control of flow systems (Brunton et al., 2020). Ling et al. (2016) applied deep learning to improve turbulence modelling in the RANS method by learning the

Reynolds stress tensor from extensive simulation data. Previously, Yarlanki et al. (2012) had utilised ML to obtain optimal parameters of existing constants in the k-model. Zhang et al. (2015) also used ML to add a new functional term (spatial-temporal modification factor) into the RANS model equation. Such efforts aim to provide or calibrate the modelling terms used in CFD predictive settings by learning potential information from high-fidelity simulations or experiment data. Other applications have included dimensionality reduction and reduced-order modelling using a ML algorithm to extract essential flow mechanisms or dominant patterns at a fraction of the normal cost for real-time flow control (Brunton and Noack, 2015). Furthermore, ML has been used in flow system identification, fault diagnosing, sensor placement and feedback control (Duriez et al., 2016; Noack, 2018), as it offers a more flexible flow control strategy than the traditional concept of precise sequence from understanding to modelling and control. Gan et al., (2020) applied variational autoencoder and generative adversarial net to produce a non-repeating circulation trajectory of flame aerosol particles that captures the statistical features obtained from experimental data. The ML technique opens new opportunities for trajectory simulation and is potentially very useful if a large number of trajectories are required which may be too difficult or costly to obtain from experimental measurements or accurate simulations. In this work, we develop a machine learning framework for constructing 3D Lagrangian flow trajectories in single-phase and multiphase particle-liquid turbulent flows inside stirred vessels. The ML methodology extracts statistical features from experimental data and, sharing the learned flow characteristics, reproduces the missing flow field. It involves a supervised learning algorithm, namely k-nearest neighbour (KNN) regression, and a Gaussian process whereby the instantaneous flow field is approximated by coupling a KNN predicted mean flow and a Gaussian distributed fluctuation. By applying the ML framework to the experimental data, a new data-driven dynamical model is established for re-tracing the long-term Lagrangian flow trajectories of each flow component to predict

its local flow dynamics over a wide range of flow conditions. Extensive experimental data acquired by PEPT are used to validate the framework in single-phase and two-phase particle-liquid flows, by considering Lagrangian statistical analysis of flow trajectories, local distributions of phase velocity and concentration as well as phase flow numbers.

7.2 Theory

7.2.1 Analysis of Lagrangian trajectory

The long-term Lagrangian trajectory provided by PEPT is defined by the three space coordinates x, y, z and time coordinate t. The Cartesian coordinates were converted into cylindrical coordinates θ, r, z, which were subsequently used to calculate the Lagrangian (instantaneous) velocity v via the time derivative of the trajectory:

$$v = v_\theta \boldsymbol{e}_\theta + v_r \boldsymbol{e}_r + v_z \boldsymbol{e}_z = r\frac{d\theta}{dt}\boldsymbol{e} + \frac{dr}{dt}\boldsymbol{e}_r + \frac{dz}{dt}\boldsymbol{e}_z \tag{7.1}$$

where, $\boldsymbol{e}_\theta$, $\boldsymbol{e}_r$ and $\boldsymbol{e}_z$ are unit vectors. The time derivative was obtained by the differencing method, for example, $\frac{d\theta}{dt}$ is approximated by the ratio $\frac{\theta_{i+1}-\theta_i}{t_{i+1}-t_i}$. Subsequently, the Eulerian (mean) velocity $\bar{v}$ fields were calculated from the Lagrangian data points using a pre-defined cylindrical mesh with equal-volume cells, as illustrated in Fig. 7.1 (c, d). According to the RANS concept, the exact solution of the instantaneous Navier-Stokes equations is decomposed into the mean (ensemble-average) and fluctuating components. Thus, the local fluctuating velocity can be written as:

$$v_i^{'} = v_i - \bar{v}_i \tag{7.2}$$

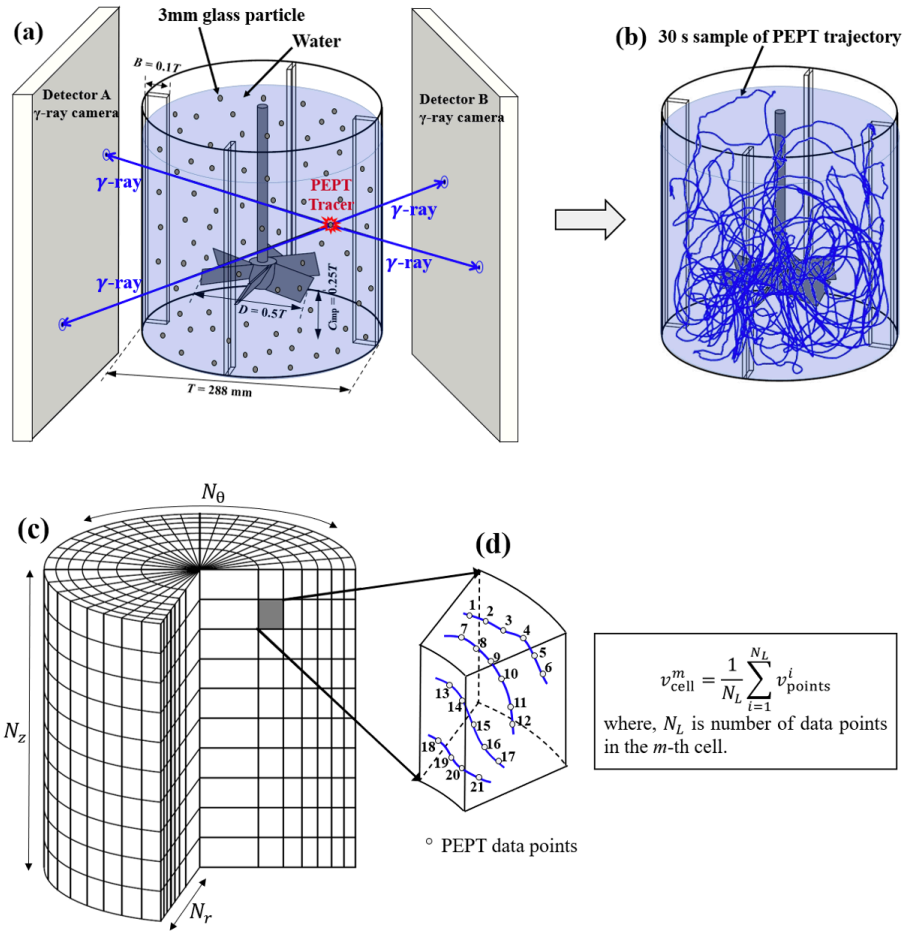


Figure 7.1: Experimental set up and grid for Lagrangian data analysis: (a) stirred vessel inside the field of view of PEPT camera; (b) 30 s sample of PEPT Lagrangian trajectory; (c) grid of equal-volume cells used for Lagrangian data analysis; (d) local velocity calculation in each cell.

where, v_i, $\bar{v}_i$ and $v_i^{'}$ are, respectively, the instantaneous, mean and fluctuating velocities in the i-direction. Thus, a new Lagrangian data array $[t, r, z, \theta, v_r, v_z, v_\theta, v_r^{'}, v_z^{'}, v_\theta^{'}]$ was generated. In previous works (Krogstad and Davidson, 2011; Morsy and Yang, 2021), the local fluctuating velocity in fully turbulent flows in stirred vessels was characterised as a reasonably Gaussian probability distribution function (PDF) which is approximately invariant throughout the whole flow field (Batchelor, 1953). Accordingly, as shown in Fig. 7.2, the global fluctuating velocity components $v_r^{'}, v_z^{'}, v_\theta^{'}$ were analysed in the whole vessel and were well-fitted by a Gaussian dis-

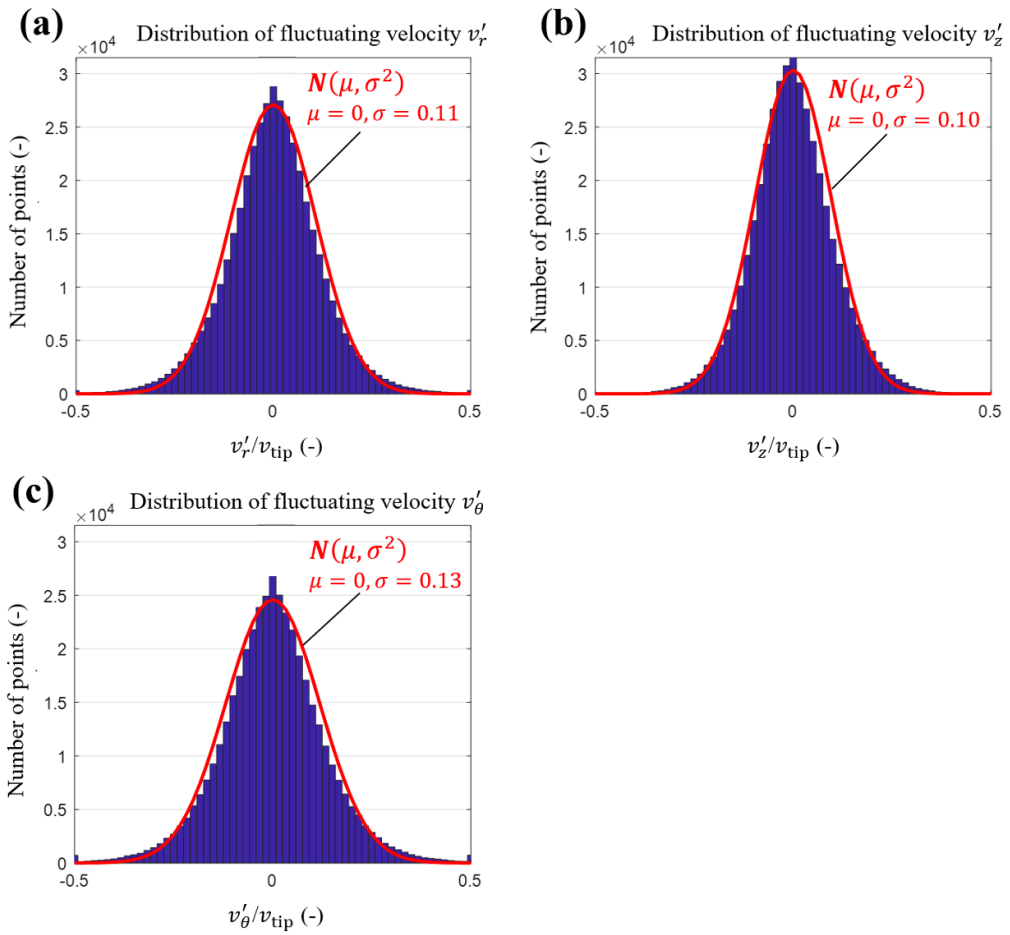


Figure 7.2: Typical distribution of global fluctuating velocity components in single-phase flow: (a) radial, (b) axial and (c) tangential directions; PBTD; $N = 500$ rpm.

tribution:

$$v_i^{'} \sim N(\mu_i, \sigma_i^2) \tag{7.3}$$

where, μ_i and σ_i are the mean and standard deviation of fluctuating velocity in the i-direction, respectively.

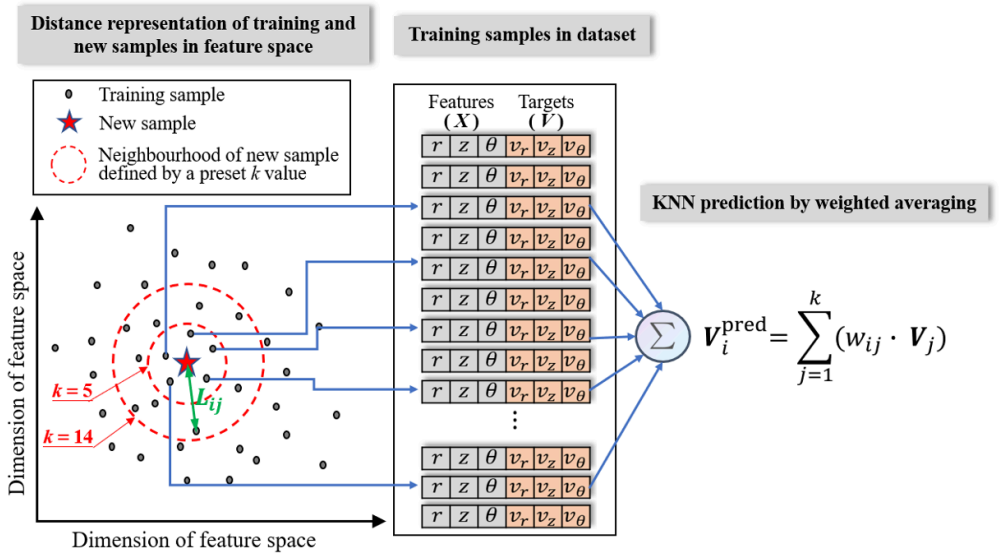


Figure 7.3: Concept of KNN regression.

7.2.2 K-nearest neighbours regressor

In recent years, ML has attracted increasing interest since it can be used to support computational fluid dynamics, for example, by optimizing simulation parameters or improving closure models (Brunton, 2020). KNN is one of the simplest supervised ML algorithms, which caches all available samples and predicts the target of new samples based on a similarity measure e.g., distance representation in the feature space. Due to its ease of interpretation and low computational cost, KNN regression has been widely used in many areas, such as banking systems, intelligent agriculture and commercial product recommendation (Brunton, 2020). In this work, the KNN model was applied to learn the mean flow from a very short-term Lagrangian trajectory obtained from experimental measurements in a stirred vessel, and was then used to predict the full flow dynamics in the whole vessel. Fig. 7.3 shows the principle of KNN regressor, which firstly transforms the training data into a fast-indexing data structure, then finds a preset number (k) of training samples which are the closest neighbour to the new sample and gives a new target by the weighted average

of training targets, thus:

$$\boldsymbol{V}_i^{pred} = \sum_{j=1}^{k} w_{ij} \cdot \boldsymbol{V}_j \tag{7.4}$$

where, $\boldsymbol{V}_j$ and $\boldsymbol{V}_i^{pred}$ are, respectively, the target of the j-th training sample and the new predicted target, which here correspond to the trained instantaneous and predicted mean velocity components. w_{ij} is a weight function which can be a uniform weight or a distance weight. The distance weight is based on the inverse of the distance in the feature space, $\boldsymbol{X}$, between the new i-th sample and the training j-th sample. $\boldsymbol{X}$ here represents the 3D coordinates of the Lagrangian trajectory.

In order to weaken the multiple features spanning effect caused by the varying degrees of magnitude and units in the feature space, feature scaling is necessary to avoid the algorithm being biased towards one feature. Thus, normalisation is used as a scaling technique to shift and rescale all the feature values between 0 and 1:

$$\boldsymbol{X}^{'} = \frac{\boldsymbol{X} - \boldsymbol{X}_{min}}{\boldsymbol{X}_{max} - \boldsymbol{X}_{min}} \tag{7.5}$$

where, $\boldsymbol{X}$ and $\boldsymbol{X}^{'}$ are the original and normalised feature spaces, respectively. The aforementioned distance used to measure feature similarity between two samples is defined by:

$$L_p(\boldsymbol{X}_i, \boldsymbol{X}_j) = (\sum_{l=1}^{n} \left| X_i^{(l)} - X_j^{(l)} \right|^p)^{\frac{1}{p}} \tag{7.6}$$

where, $X_i^{(l)}$ is the l-th dimensional feature of the i-th sample. p is a constant for different types of distance function, which was set as $l = 3$ and $p = 2$ for normalised Euclidean distance in three-dimensional feature space (Pedregosa et al, 2011). The optimal size of the neighbourhood, i.e., k value (see Fig. 7.3), is highly dependent on the size of training data set and can be determined using a cross-validation method

which minimises the root mean square error (RMSE) of the KNN regressor. It should be noted that too large a k value will cause under-fitting, although it suppresses the effects of noise, while too small a k value will result in over-fitting and will increase the sensitivity of noisy data.

7.2.3 Lagrangian trajectory construction using ML

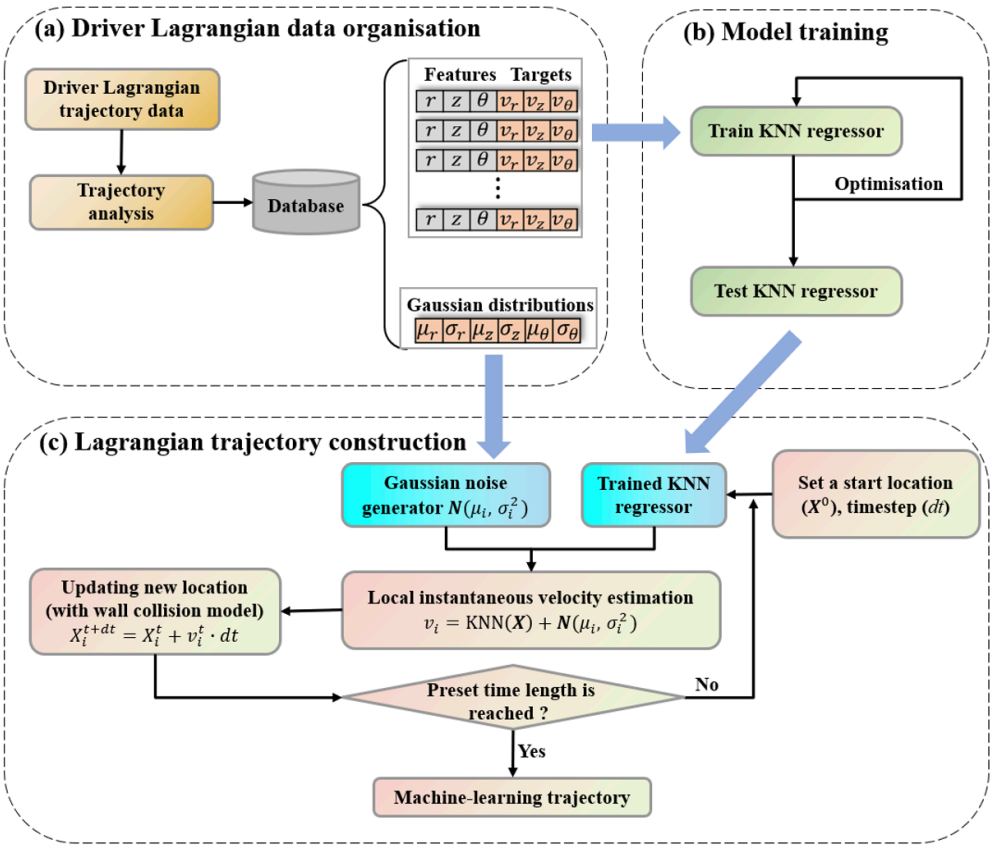


Figure 7.4: Workflow of ML framework for Lagrangian trajectory construction in a stirred vessel.

As shown in Fig. 7.4, we have developed a ML framework to construct a new representative trajectory containing the flow dynamics of a stirred vessel, based on learning the flow field encoded in the input driver Lagrangian trajectory data. The framework strategy is similar to the concept of Reynolds averaging, where the instantaneous flow field is approximated by coupling a KNN-predicted mean flow

and a Gaussian distributed fluctuation. The workflow consists of three main units: (a) organisation of input driver Lagrangian trajectory data; (b) model training; and (c) Lagrangian trajectory construction, which are discussed in detail below.

Driver Lagrangian trajectory data organisation

As described in Section 7.2.1, a new Lagrangian data array containing time, location, instantaneous and fluctuating velocities is obtained from an experimental PEPT trajectory. The locations are used to create a feature space $\boldsymbol{X} = [r, z, \theta]$, while the instantaneous velocity is used to produce a target space $\boldsymbol{V} = [v_r, v_z, v_\theta]$. The new Lagrangian data array is converted into a time-varying vector field and stored in the database for feeding the KNN regressor. Each vector represents a data sample consisting of feature and target data (Fig. 7.4a). The turbulence fluctuations are analysed by fitting the approximated Gaussian distributions of the fluctuating velocity components $[v_r^{'}, v_z^{'}, v_\theta^{'}]$ in the whole vessel, as discussed above (Fig. 7.2). The extracted Gaussian variables $[\mu_r, \sigma_r, \mu_z, \sigma_z, \mu_\theta, \sigma_\theta]$ are subsequently stored in the database for feeding the Gaussian noise generator.

Model training

The KNN model training process (Fig. 7.4b) is illustrated in greater detail in Fig. 7.5. The training was implemented using the pipeline function from the scikit-learn library (Pedregosa et al, 2011), with the aim of obtaining the optimal hyperparameters (w, k) for the KNN model via the *GridSearchCv* algorithm. When the organised driver data are loaded from the database, the normalisation Eq. 7.5 is applied to perform feature scaling. The scaled data are subsequently split into a training dataset (85%) and a test dataset (15%). A pipeline is then created to run

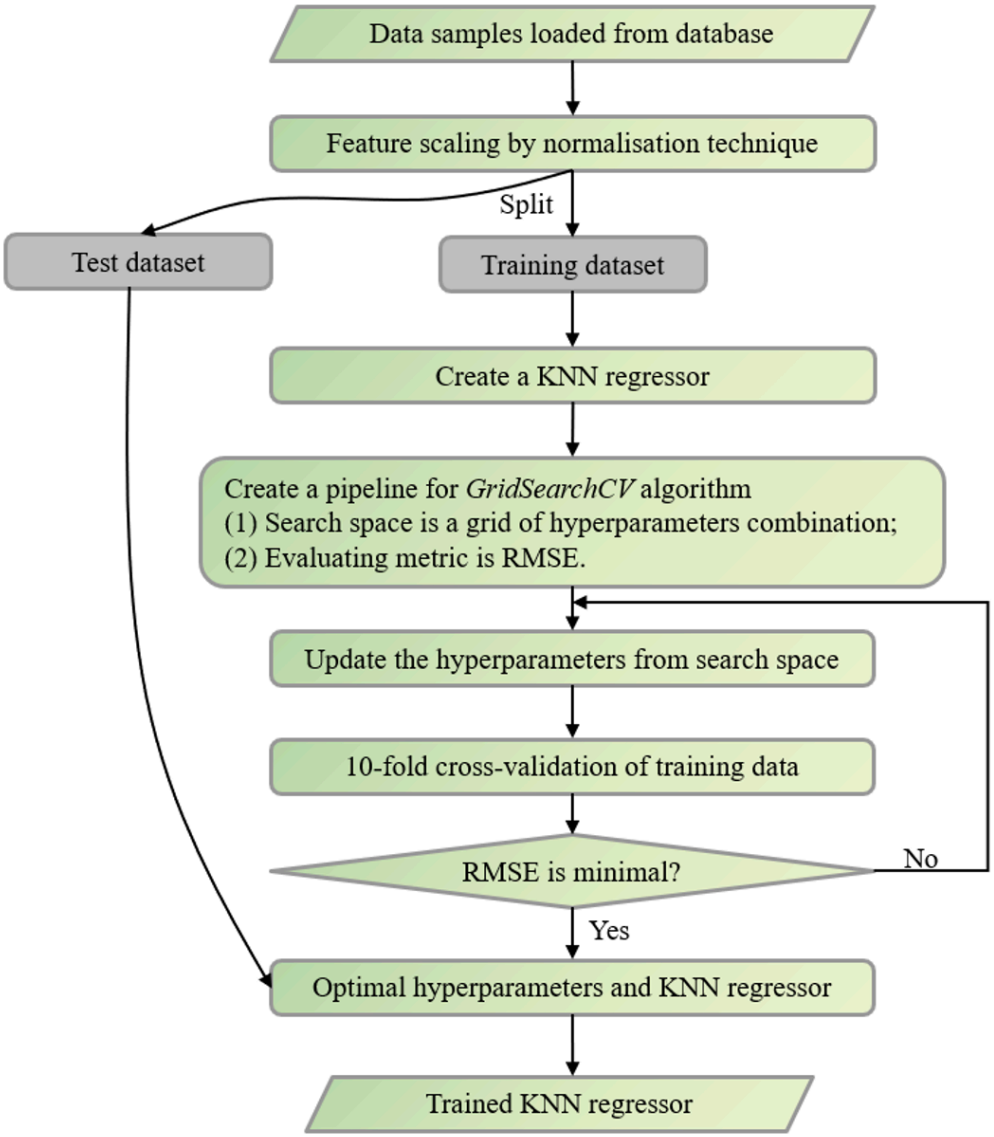


Figure 7.5: Flowchart of KNN model training.

the grid search algorithm over the hyperparameter space, where the combination of the weight function type (uniform or distance) and k value is defined as the search space. The RMSE is used as an evaluation metric for model performance and the KNN regressor is an estimator of the search algorithm. At each step of the hyperparameters search, the KNN regressor is trained and its performance is independently validated by the 10-fold cross-validation technique using the training dataset (Wong and Yeh, 2019). The optimal hyperparameters and KNN regressor are determined by searching for the minimum RMSE, and the KNN regressor is subsequently tested

using the test dataset to recheck the model performance.

Lagrangian trajectory construction

The Lagrangian construction process is schematically illustrated in Fig. 7.4c. By setting a start location for a seed tracer, a local mean velocity is predicted by the trained KNN regressor and a local fluctuating velocity is produced from the Gaussian noise generator. Thus, the local instantaneous velocity is estimated by:

$$v_i^{'} = v_i - \bar{v_i} = KNN(\boldsymbol{X}) + \boldsymbol{N}(\mu_i, \sigma_i^2) \tag{7.7}$$

The Lagrangian trajectory is constructed by advancing the seed tracer through the local instantaneous velocity field, where the location of seed tracer is updated at each time step by:

$$\boldsymbol{X}_i^{t+dt} = \boldsymbol{X}_i^t + \boldsymbol{v}_i^t \cdot dt \tag{7.8}$$

where, $\boldsymbol{X}_i^t$ and $\boldsymbol{X}_i^{t+dt}$ are, respectively, the tracer locations in the i-th direction at time t and $t+dt$. The instantaneous velocity of the tracer is estimated by Eq. 7.7 and its location is updated by Eq. 7.8 repeatedly until the sought trajectory time length is reached. Thus, a new representative ML-constructed trajectory is produced, which contains the same statistical flow characteristics as the input driver flow data.

Model training

Uncertainties in tracer location near the vessel wall may occasionally cause the tracer location $\boldsymbol{X}_i^{t+dt}$ to fall outside of the flow field boundary. If not restricted, such events could cause the tracer to wander outside the flow field for long periods of time, thus,

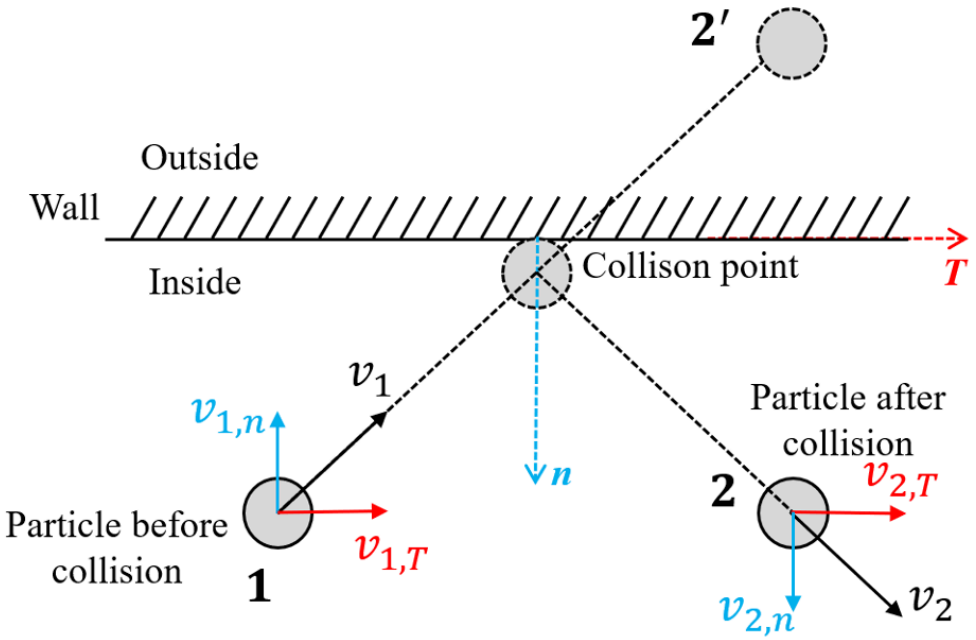


Figure 7.6: Illustration of wall collision model.

wasting computational effort and imparting framework efficiency. To circumvent such a problem, a wall collision model was implemented, as illustrated in Fig. 7.6, whereby, the tracer velocities before and after collision are related thus:

$$e_n = \frac{v_{2,n}}{v_{1,n}}$$

$$e_n = \frac{v_{2,T}}{v_{1,T}} \tag{7.9}$$

where, $v_{1,n}, v_{1,T}, v_{2,n}$ and $v_{2,T}$ are the tracer velocities in the normal and tangential direction before and after collision, respectively. The e_n and e_T are the restitution coefficients in the normal and tangential direction, respectively, which are within the range 0 to 1. A sensitivity test of restitution coefficients was performed over a wide range, and results showed that ML predictions were not sensitive to the adopted values. Hence, in this work, the restitution coefficients e_n and e_T were assigned a value of 1.0, indicating the collision is perfectly elastic (Sheikh et al., 2022).

7.3 Experimental

7.3.1 Stirred vessels

Experiments including single-phase and particle-liquid turbulent flows were performed in a flat-based stirred vessel of standard configuration, having diameter $T =$ 288 mm and four equidistant wall baffles of width $0.1T$, as illustrated in Fig. 7.1a. The height of liquid or suspension in the vessel was set at $H = T$ and was agitated by a 6-blade 45^o pitched-turbine (PBT) of diameter $D = 0.5T$ and width $0.1T$, set at an off-bottom clearance $C_{imp} = 0.25T$. The continuous phase was water with added salt (NaCl), and the solid phase consisted of nearly-monomodal and spherical glass beads of diameter 3 mm and density 2485 kg/m3. The single-phase flow tests were run at impeller rotational speeds in the range 100 - 500 rpm corresponding to turbulent impeller Reynolds numbers ($Re_{imp} = ND^2/\mu$) $\geq$ 0.4Œ105. The particle-liquid flow experiments used mean solid concentrations of 5, 10, 20 and 40 wt% corresponding to 2.5, 5.2, 10.4 and 23.6 vol%, respectively, and were run at the just-suspended impeller speed, N_{js}, determined according to the well-known Zwietering criterion (Zwietering, 1958). These experiments were operated in the down-pumping (PBTD) and up-pumping (PBTU) modes. The experimental conditions are listed in Table 7.1.

7.3.2 Positron emission particle tracking

PEPT is a non-invasive flow measurement technique which uses a representative positron-emitting particle tracer to track the motion of a carrier liquid or dispersed solid phase, thus, providing 3D long-term Lagrangian trajectories for all phases and

Table 7.1: Experimental flow conditions.

Flow system	Solid concentration (wt%)	(vol%)	*N or Njs (s-1)* PBTD	PBTU	Impeller Reynolds number Re_{imp} ($\times 10^5$) PBTD	PBTU
Single-phase	0	0	1.67 (100 rpm)	1.67 (100 rpm)	0.40	0.40
			2.50 (150 rpm)	2.50 (150 rpm)	0.60	0.60
			4.33 (260 rpm)	4.33 (260 rpm)	1.03	1.03
			5.00 (300 rpm)	5.00 (300 rpm)	1.19	1.19
			5.50 (330 rpm)	5.50 (330 rpm)	1.31	1.31
			6.67 (400 rpm)	6.67 (400 rpm)	1.59	1.59
			8.33 (500 rpm)	8.33 (500 rpm)	1.98	1.98
Particle-liquid	5.2	2.5	6.00 (360rpm)	6.25 (375rpm)	1.43	1.49
	10.6	5.2	6.83 (410rpm)	6.75 (405rpm)	1.63	1.61
	20.0	10.4	8.17 (490rpm)	7.83 (470rpm)	1.94	1.87
	40.0	23.6	9.83 (590rpm)	9.67 (580rpm)	2.34	2.31

components of the flow (Barigou, 2004). PEPT has an accuracy comparable to that of leading optical techniques such as PIV and LDV, but has the unique advantage of imaging opaque flows and within opaque equipment (Pianko-Oprych et al., 2009). PEPT has been extensively used to investigate single-phase and multiphase flows in mixing vessels and in pipes (Barigou, 2004; 2009; Eesa et al., 2008; Guida et al., 2010ab; 2012; Li et al., 2022; Savari et al., 2021; 2022; Sheikh et al., 2022; Yang et al., 2022). In this work, a representative 3 mm radio-labelled glass particle was used to track the solid phase, and a tiny 600 μm neutrally-buoyant radio-labelled resin particle tracer was used to track the liquid phase (water whose density was adjusted to the resin density of 1150 kg/m3 by adding NaCl). The long-term Lagrangian PEPT trajectory of each phase was independently recorded for 40 min to acquire sufficient data points in all regions of the vessel, and a 30 s sample is shown in Fig. 7.1b.

7.4 Results and discussion

The proposed ML framework used to construct the long-term 3D Lagrangian trajectories of single-phase and particle-liquid turbulent flows in a stirred vessel, was set up and executed in Jupyter Notebook with Python 3 kernal. The typical com-

putation time for a simulated ML trajectory with a time length of 40 min and a time step of 5 ms is $\sim$ 2 hr. The computation time can be reduced several times by parallel running of the script or by using multiple tracers initiated at different start locations of the flow to generate multiple shorter trajectories which together will provide the same Lagrangian information as one long-term trajectory. For example, 10 tracers yielding 10 trajectories of 6 min length are equivalent to one tracer producing one trajectory of 60 min length. In any case, however, the computation expense is orders of magnitude smaller compared to most of the conventional numerical simulations of turbulent flows. To evaluate the performance of the proposed framework, the optimal parameters were firstly determined, then the ML-computed trajectories were compared with extensive PEPT measurements using local velocity distributions, Lagrangian statistical analysis, particle phase distributions and phase flow numbers.

7.4.1 Framework validation and evaluation

Hyperparameter tuning of KNN regressor

As discussed above, optimal performance of the KNN regressor was achieved when the best hyperparameters, i.e., weight function w and k value, determined in the training process were used. Here, the model performance was evaluated by the RMSE and coefficient of determination R2, defined as:

$$RMSE = \sqrt{\frac{\sum_j^n \left| v_j - v_j^{pred} \right|^2}{n}}$$

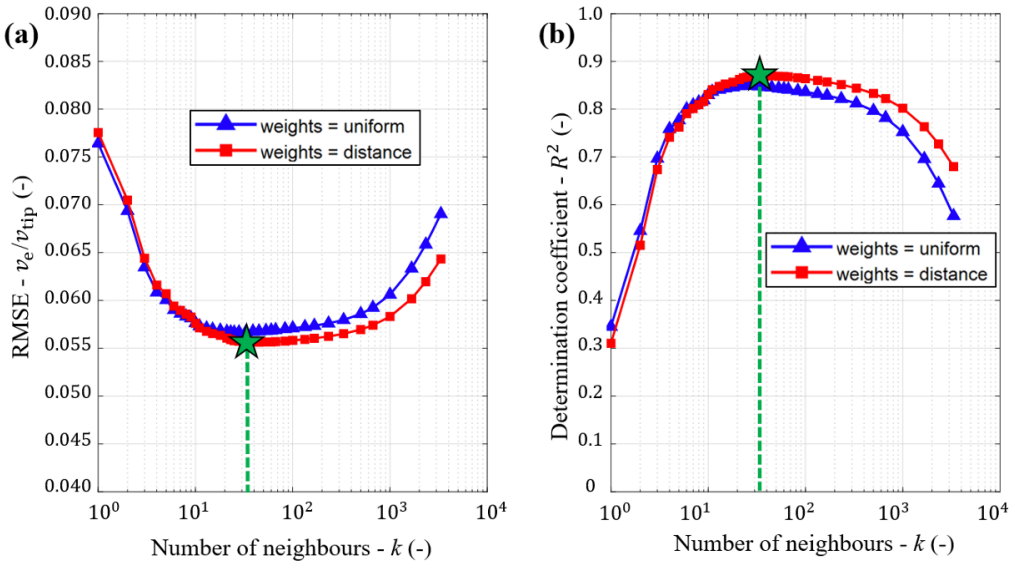


Figure 7.7: Effects of number of neighbours and weight function type on (a) root mean square error (RMSE), and (b) determination coefficient for a 2 min PEPT trajectory (23706 training samples) of single-phase flow: PBTD; $N = 500$ rpm.

$$R^2 = 1 - \frac{\sum_j^n (v_j - v_j^{pred})^2}{(\sum_j^n (v_j - \bar{v_j})^2} \tag{7.10}$$

where, n is the number of training data samples; v_j is the actual local velocity of the j-th sample; and v_j^{pred} is the corresponding prediction of local velocity. A perfect KNN regressor should achieve a very small RMSE $\rightarrow 0$ and a large $R^2 \rightarrow 1$, while $R^2 \rightarrow 0$ means the KNN regressor predicts poorly. The effects of number of neighbours and weight function types on the RMSE and R^2 values are exhibited in Fig. 7.7. As the number of neighbours, k, increases, the performance of the KNN regressor gradually improves reaching an optimum point beyond which it deteriorates. Regardless of the k value, the distance weight function worked slightly better than the uniform weight function and was adopted. The optimal hyperparameters need to be determined for each set of driver data input even if such data sets belong to the same trajectory but are of different size. For example, using a 2 min PEPT trajectory of single-phase flow with 500 rpm as the training dataset (23706 samples), the

KNN regressor with distance weight function and $k = 33$ achieved the best model performance; however, using 5 min of PEPT data for training would require $k = 61$.

Effects of training dataset size

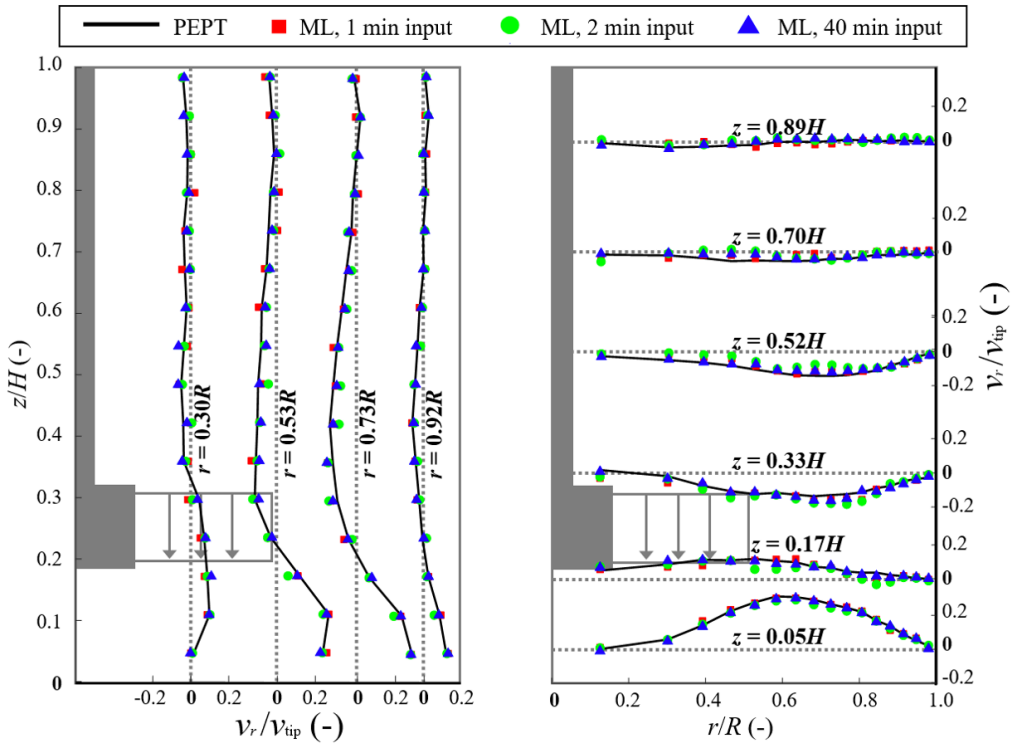


Figure 7.8: Effects of training dataset size on azimuthally-averaged vertical and horizontal profiles of r-velocity component PEPT and ML compared in single-phase liquid flow: PBTD; $N = 500$ rpm.

Considering the interpolation nature of the KNN regressor, it has a potential advantage to produce a long-term Lagrangian trajectory from a very short-term trajectory. In order to investigate the effects of the size of the dataset used to train the model, the framework was tested using input PEPT trajectories of various lengths, e.g., 1, 2, 5, 10 and 40 min (full-length trajectory) corresponding to single-phase liquid flow with a PBTD impeller running at 500 rpm. A detailed quantitative comparison of azimuthally-averaged profiles of local velocity components (v_r, v_z, v_θ) and total velocity was performed in different vertical and horizontal planes, as shown in Figs.

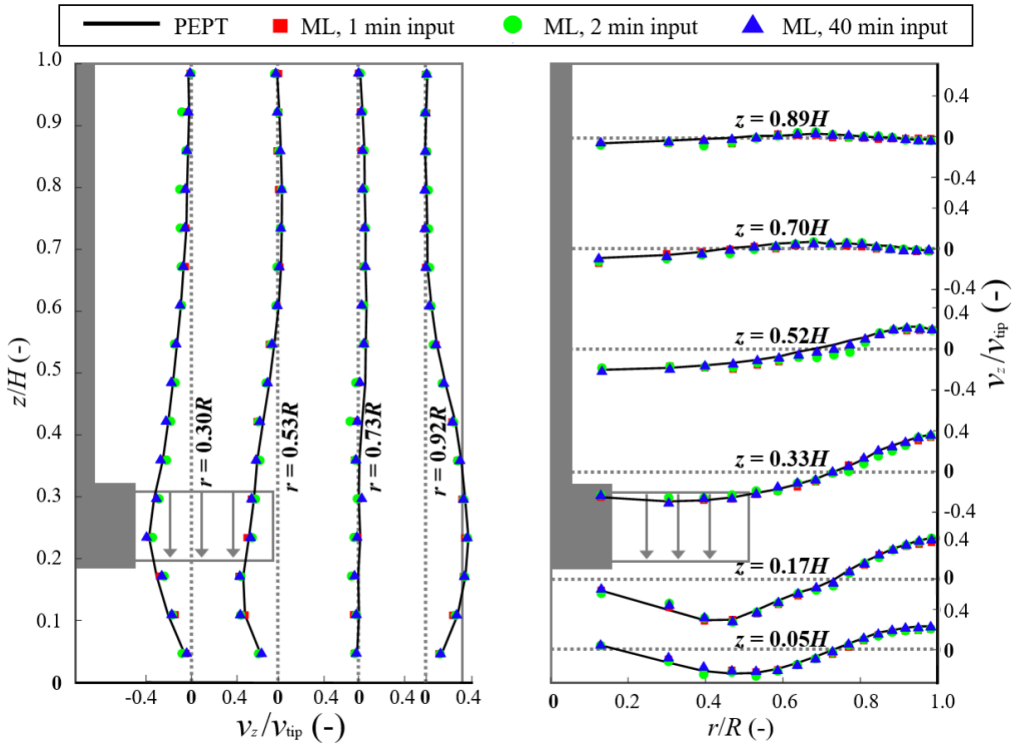


Figure 7.9: Effects of training dataset size on azimuthally-averaged vertical and horizontal profiles of z-velocity component PEPT and ML compared in single-phase liquid flow: PBTD; $N = 500$ rpm.

7.8-7.11. The vertical planes examined were within the impeller region ($r = 0.3R$), at the tip of the impeller ($r = 0.53R$), approximately halfway between the impeller tip and vessel wall ($r = 0.73R$), and near the wall of the vessel ($r = 0.92R$). The horizontal planes were near the bottom of the vessel ($z = 0.05H$), just below the impeller ($z = 0.17H$), just above the impeller ($z = 0.33H$), and 3 other equidistant planes from approximately the mid-height position to near the free surface ($z = 0.52H \sim 0.89H$).

Results in Figs. 7.8-7.11 show that using the full-length trajectory (40 min) as input predicts the exact details of the flow without any loss in accuracy. This is an important step in the validation of the framework as it shows that it is completely faithful in reproducing the characteristics of the flow contained in the input data. Using a training dataset of 1 min trajectory input is sufficient to give generally very

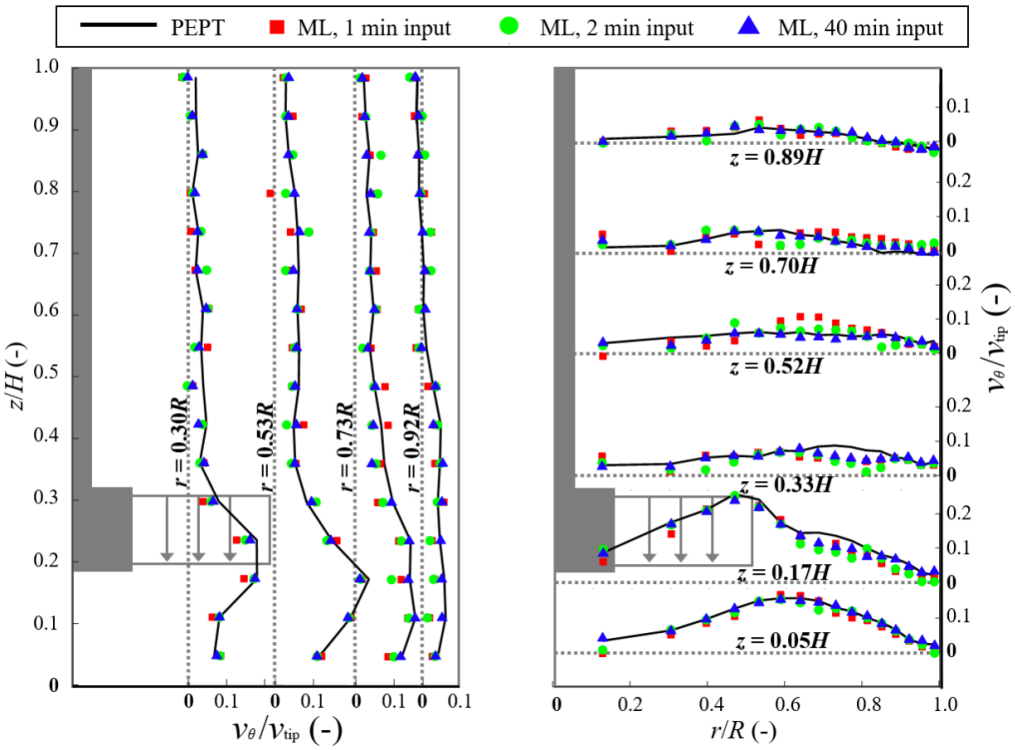


Figure 7.10: Effects of training dataset size on azimuthally-averaged vertical and horizontal profiles of θ-velocity component PEPT and ML compared in single-phase liquid flow: PBTD; N = 500 rpm.

good predictions, although some slight errors exist in the θ-velocity component in some regions. However, 2 min of trajectory input achieves a nearly perfect agreement between the entire ML-predicted flow field and PEPT measurements, i.e., the full-length trajectory can be faithfully produced using only 2 min of data input. The accuracy of the predictions is reflected in all three velocity components and, consequently, also in the total velocity. Note that henceforth, in order to keep the number of figures to a manageable level, we will only present comparison plots of total velocity.

The validation of the framework used more extensive PEPT measurements pertaining to various flow conditions (see Table 7.1: PBTU and PBTD running at N = 100-500 rpm). Sample results are included in Supplementary Material. As illustrated in Figs. 7.16 and 7.17, 1 min of driver data is still sufficient for the prediction

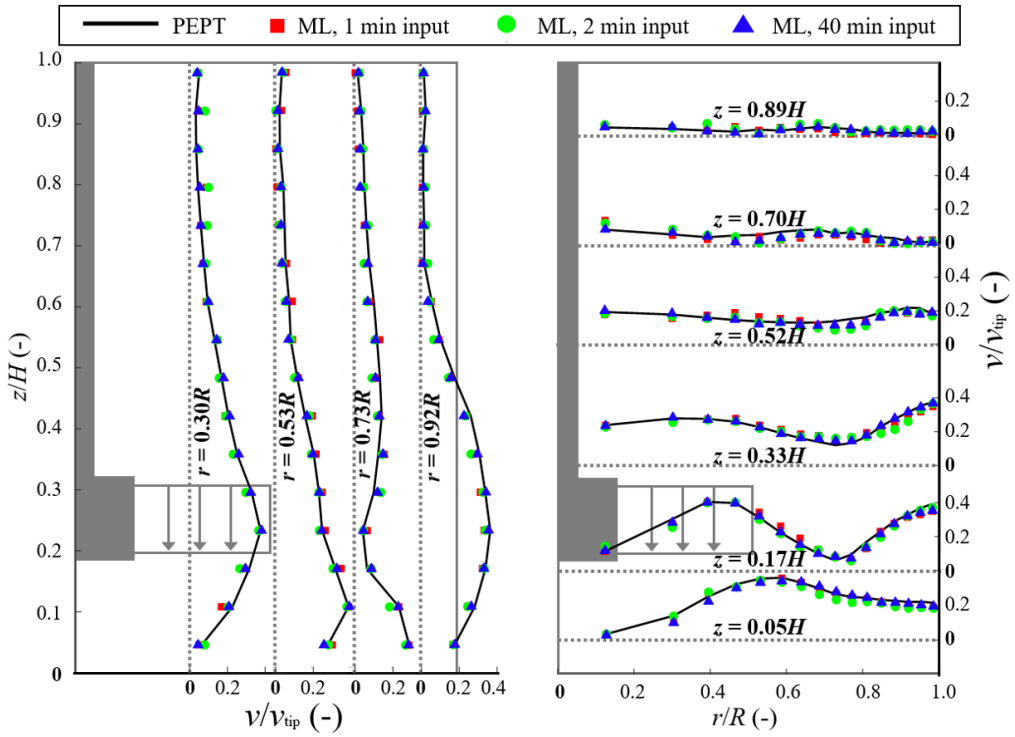


Figure 7.11: Effects of training dataset size on azimuthally-averaged vertical and horizontal profiles of total velocity PEPT and ML compared in single-phase liquid flow: PBTD; $N = 500$ rpm.

of flow at other higher impeller speeds, e.g., 330 rpm, while 100 rpm needs at least 2 min of input data. This means that the minimum size of input dataset is slightly dependent on the flow conditions, including impeller speed, vessel configuration, liquid properties. Due to the fact that at lower agitation speeds the tracer requires a longer time to be able to visit most of the regions in the flow domain, the minimum size of input data is expected to be larger for lower speeds. For a robust performance, we henceforth adopted training datasets of 5 min PEPT trajectory for the rest of this work. It should be noted that numerical trajectories from any reliable numerical simulation can equally be used to drive the proposed ML framework. This is potentially very useful for the analysis, design and optimisation of industrial processes since the direct determination of long-term trajectories is usually a costly task in practice.

Lagrangian statistical analysis

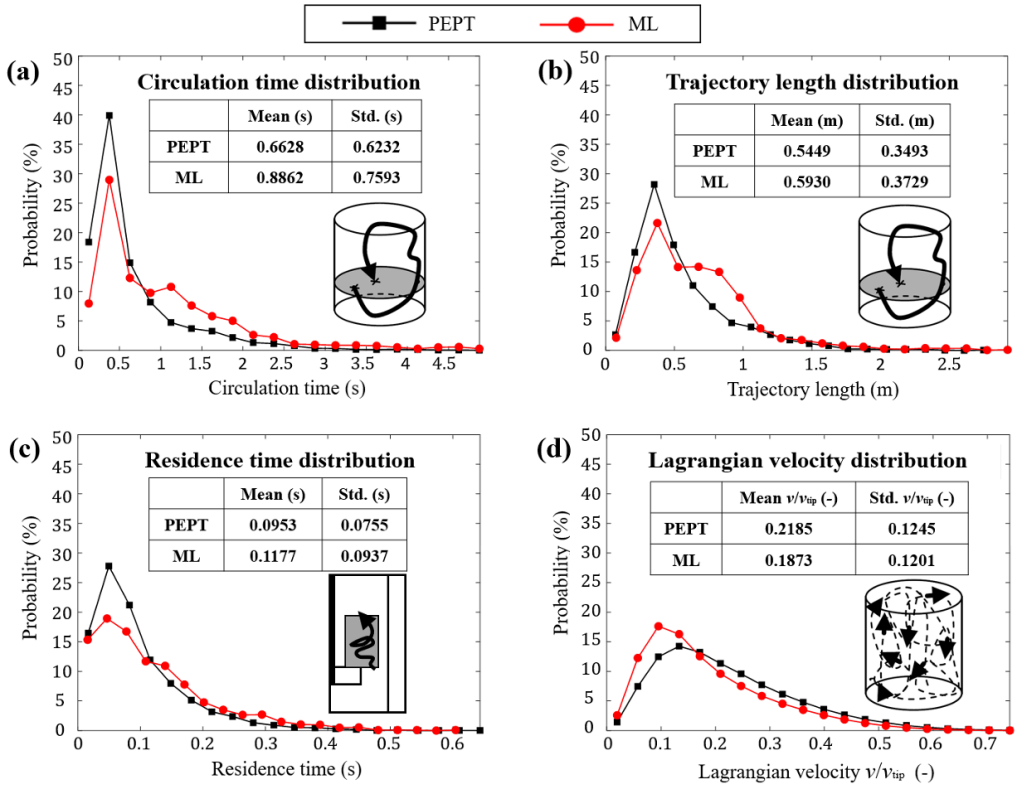


Figure 7.12: Probability distributions of (a) circulation time, (b) circulation trajectory length, (c) residence time and (d) Lagrangian total velocity PEPT and ML compared in single-phase liquid flow: PBTD; $N = 500$ rpm.

As discussed above, the proposed ML framework can be effectively used to construct the flow field using a small set of Lagrangian data (5min). Further statistical analysis was performed to compare ML simulations and PEPT measurements in terms of circulation time, circulation trajectory length, residence time and Lagrangian total velocity. The circulation time is defined as the time from when a Lagrangian tracer leaves the impeller discharge plane ($z = 0.2H$) until it returns to it. The circulation trajectory length is the length of the path that the tracer follows during the circulation time (Villermaux, 1996). Thus, a long-term continuous flow trajectory can be segmented into a set of circulation trajectories (Fig. 7.12a-b). Using a cylindrical cell in the tank with dimensions of $0.3R < r < 0.7R$ and $0.3H < z < 0.7H$, a residence time can be defined as the time that a tracer spends in that cell in each visit

(Fig. 7.12c). Moreover, the Lagrangian total velocity at each tracer location can be calculated using Eq. 7.1, as shown in Fig. 7.12d. The probability distributions of circulation time, circulation trajectory length, residence time and Lagrangian total velocity are depicted in Fig. 7.12. There is a good agreement between the ML-predicted and experimentally determined probability distributions, which reflects the accuracy of the ML framework.

7.4.2 Prediction of particle-liquid flows

The ML framework was extended to the study of particle-liquid flows with various solid loadings at the just suspended regime. Driver datasets of 5 min PEPT liquid and solid phase trajectories were utilised to produce the corresponding long-term (40 min) trajectories of both phases.

Local velocity distributions of liquid and solid phases

The azimuthally-averaged profiles of local total velocity for the liquid and solid phases are presented in Figs. 7.13 and 7.14 for a sample case of 20 wt% solids agitated by a PBTD impeller. Predictions by the ML framework are in very good agreement with PEPT measurements for both phases, albeit there are some minor underpredictions in solid velocity in the vicinity of the impeller and near the bottom of the vessel. Such small errors may actually stem from the measurements due to the high level of particle-impeller and particle-wall collisions. The prediction capability of the framework was equally good for other combinations of solid loading (5 - 40 wt%) and impeller configuration, some of which are presented in Supplementary Material (Figs. 7.18-7.20).

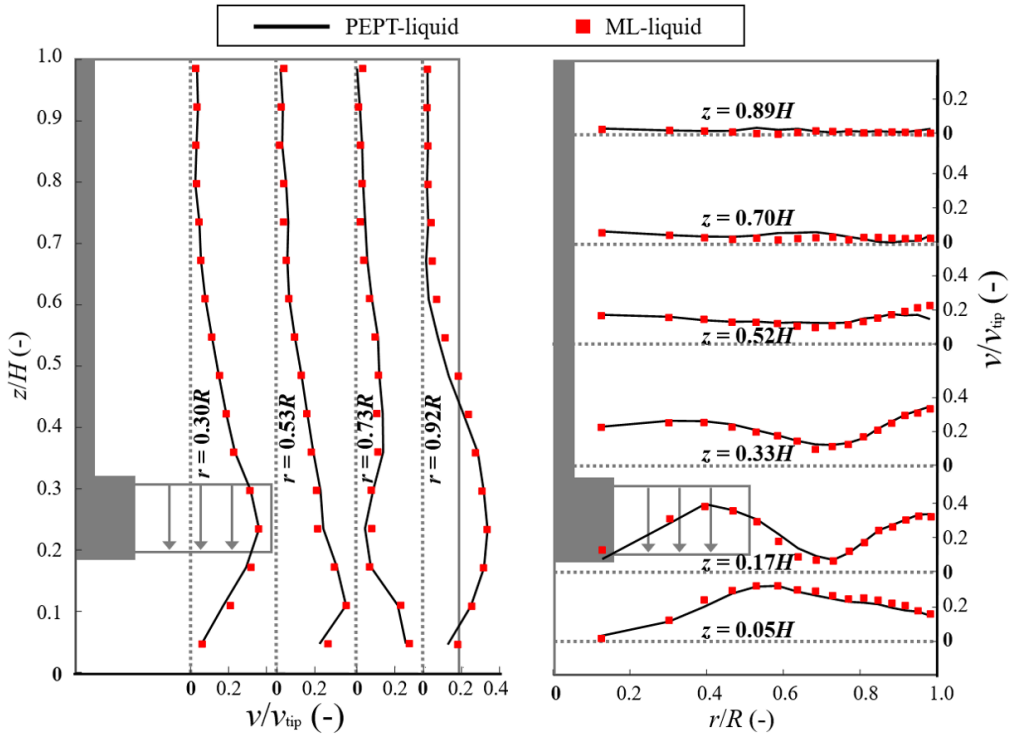


Figure 7.13: Azimuthally-averaged vertical and horizontal profiles of total liquid velocity PEPT and ML compared in 20 wt% particle-liquid flow: PBTD; N_{js} = 490 rpm.

Spatial particle concentration distribution

Local solid phase concentration can be inferred from the Lagrangian PEPT trajectory using the local occupancy map of a particle tracer in the particle-liquid flow (Guida et al., 2009, 2012; Jadhav and Barigou, 2022). The local occupancy is traditionally defined as the time a tracer spends in each cell during the experiment, divided by the total experimental runtime (t_∞). The local occupancy calculated from this definition is strongly dependent on the mesh grid density used, and it tends to zero as the number of cells increases. According to the concept of ergodicity and using a mesh with equal-volume cells, the ergodic time which is defined as $t_E = t_\infty/N_c$, where N_c is the total number of cells ($N_c = N_\theta \times N_r \times N_z$), can be used to circumvent this mesh grid-dependence. Thus, the local occupancy (O_E) can be

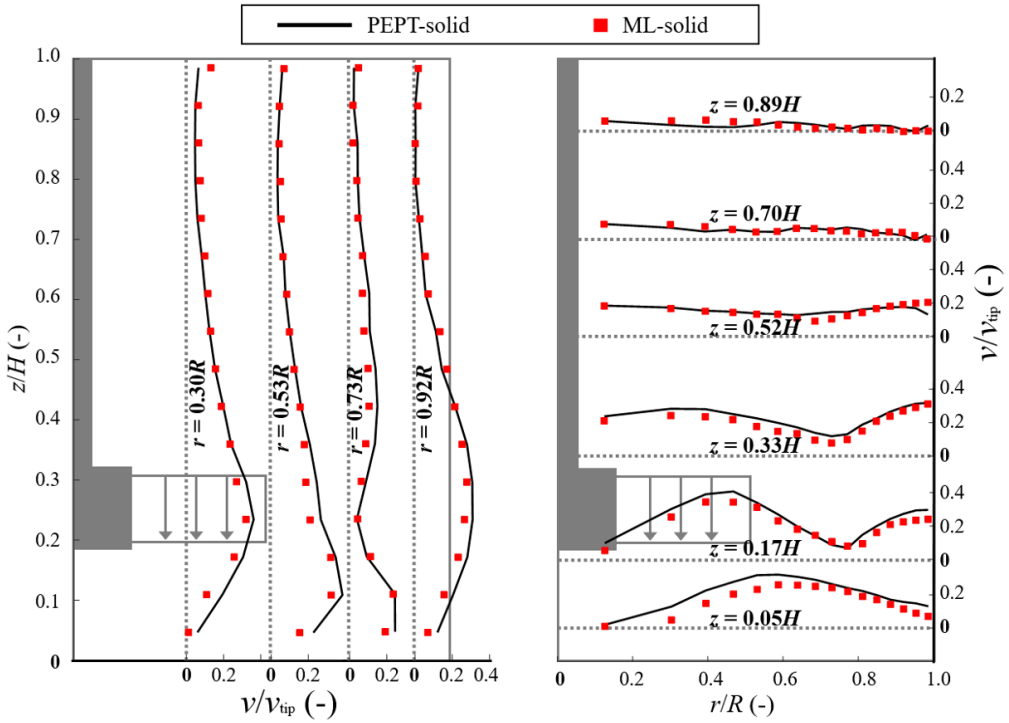


Figure 7.14: Azimuthally-averaged vertical and horizontal profiles of total particle velocity PEPT and ML compared in 20 wt% particle-liquid flow: PBTD; N_{js} = 490 rpm.

defined as:

$$O_E = \frac{\Delta t}{t_E} \tag{7.11}$$

where, Δt is the total time the PEPT tracer spends in each cell during the experiment. We have previously demonstrated that the local occupancy is equal to the local volume concentration fraction (Guida et al., 2009, 2012), thus:

$$O_E = \frac{c}{C_v} \tag{7.12}$$

where, c and C_v are the local and mean particle volume concentration, respectively. This approach was applied to the PEPT-measured and ML-predicted trajectories, and the spatial solid phase distribution of the sample case of 20 wt% suspension is presented in Fig. 7.15. The ML framework overall predicts the spatial particle

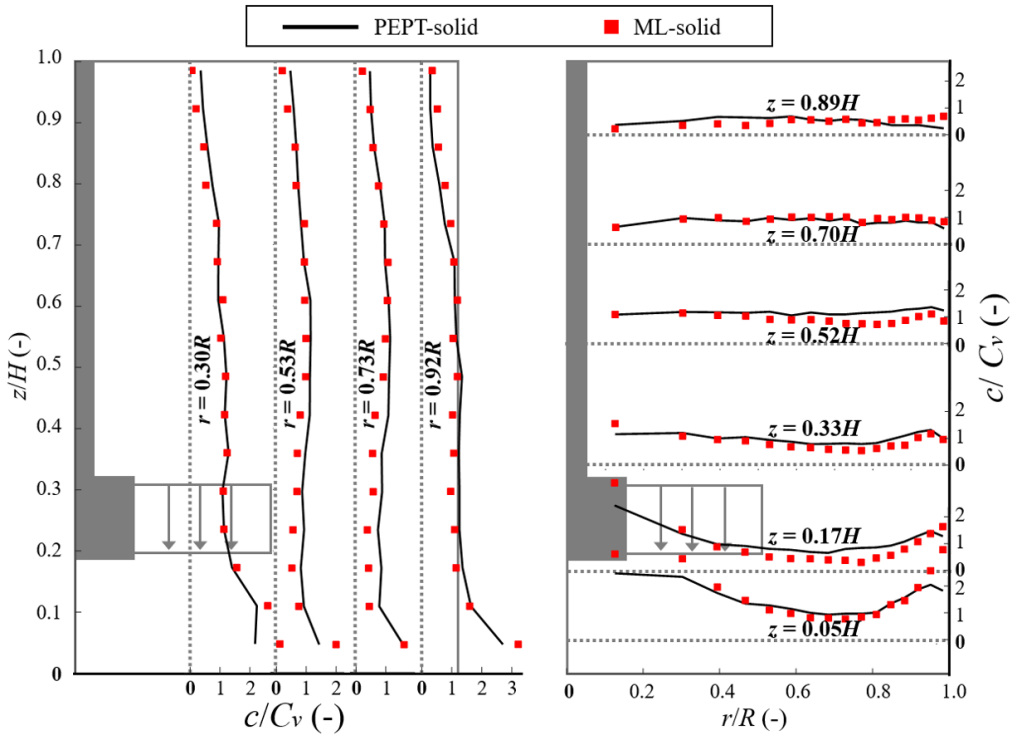


Figure 7.15: Azimuthally-averaged vertical and horizontal profiles of solid phase distribution PEPT and ML compared in 20 wt% particle-liquid flow: PBTD; N_{js} = 490 rpm.

distribution very well throughout the entire vessel volume, with only some minor discrepancies.

Phase flow number

The flow number, Fl, is a dimensionless parameter used to evaluate the impeller pumping effectiveness and is generally defined as the normalised volumetric discharge flow rate Q/ND^3, and can be readily extended to multiphase flow systems (Guida et al., 2010a). For particle-liquid flow, the volumetric discharge flowrate of the solid phase ($Q^{(S)}$) and that of the liquid phase ($Q^{(L)}$) are separately calculated by integrating the axial local velocity weighted by the local phase concentration over the impeller discharge plane, i.e., the lower edge of the PBTD ($z = 0.2H$) and the upper edge of the PBTU ($z = 0.3H$). Thus, the liquid-phase flow number is

Table 7.2: Experimental and ML-predicted phase flow numbers for particle-liquid flows.

Impeller	Solid concentration (wt%)	(vol%)	*N(rpm)*	$Fl^{(S)}_{PEPT}$	$Fl^{(S)}_{ML}$	$Fl^{(L)}_{PEPT}$	$Fl^{(L)}_{ML}$	Fl_{PEPT}	Fl_{ML}	$\frac{Fl_{ML}-Fl_{PEPT}}{Fl_{PEPT}} \times 100\%$
PBTD	5.2	2.5	360	0.021	0.027	0.846	0.866	0.867	0.893	3.0
	10.6	5.2	410	0.048	0.043	0.832	0.840	0.880	0.883	0.3
	20.0	10.4	490	0.139	0.091	0.636	0.749	0.775	0.840	8.4
	40.0	23.6	590	0.165	0.173	0.556	0.589	0.721	0.762	5.7
PBTU	5.2	2.5	375	0.021	0.024	0.819	0.729	0.840	0.753	-10.3
	10.6	5.2	405	0.043	0.043	0.788	0.749	0.831	0.792	-4.7
	20.0	10.4	470	0.121	0.083	0.546	0.555	0.667	0.638	-4.3
	40.0	23.6	580	0.175	0.163	0.322	0.352	0.497	0.515	3.6

expressed as:

$$Fl^L = \frac{Q^L}{ND^3} = \frac{1}{ND^3} \cdot \int (1-c) v_z^{(L)} dS \tag{7.13}$$

and the solid-phase flow number is expressed by:

$$Fl^S = \frac{Q^S}{ND^3} = \frac{1}{ND^3} \cdot \int c v_z^{(S)} dS \tag{7.14}$$

where, c and $(1-c)$ are the local solid and liquid volume concentration, respectively. Thus, the total flow number for the particle-liquid flow is:

$$Fl^L = \frac{Q^L}{ND^3} = \frac{Q^{(L)} + Q^{(S)}}{ND^3} = Fl^{(L)} + Fl^{(S)} \tag{7.15}$$

The flow numbers estimated from PEPT and ML are compared in Table 7.2. There is a very good agreement on liquid, solid and total flow numbers. The discrepancies are mostly less than $\pm 5\%$.

7.5 Conclusions

A computationally efficient machine learning (ML) framework has been successfully developed and thoroughly validated for constructing 3D long-term trajectories of

single-phase and multiphase turbulent flows in a stirred vessel. The framework uses the Lagrangian information contained in a very short-term experimental trajectory as driver data. The use of KNN regression in conjunction with a Gaussian process efficiently generates a long-term ML trajectory that has the same statistical features as the real flow. Validation was achieved by comparing ML-predicted trajectories to PEPT-measured trajectories using the characteristics of extensive flow systems inferred from local velocity distributions, Lagrangian statistical analysis, particle concentration distributions and phase flow numbers. Results overall showed excellent agreement and confirmed the accuracy and robustness of the proposed ML framework for predicting single-phase and two-phase particle-liquid turbulent flows under a wide range of flow conditions.

Generally, a 2 min long trajectory length is sufficient to drive the framework and the computation cost is orders of magnitude less than conventional turbulence simulations. The efficiency and accuracy of the framework make it a powerful tool for the analysis and modelling of flow systems using only a small set of experimental data input, and has great potential for assisting in the design and optimisation of industrial processes. In addition, the small driver dataset can equally be provided from any reliable numerical simulation e.g., LES, DNS, thus avoiding costly experimental measurements.

A typical concern of using such models is the need for training using large datasets for accurate predictions, which can result in excessive time and computational expense. If this were to be the case, the argument for using such a tool diminishes as more accurate deterministic models could be used in its place. For this framework, however, the relatively small amount of data needed for accurate prediction makes the model an efficient method in comparison to more complex calculations such as SPH. Although training is required for each case, the time and cost of calculations is minute compared to alternative methods, which can be potentially very usedul

for the analysis, design, and optimisation of industrial processes since the direct determination of long-term trajectories is usually a costly task in practice.

Similar to Lagrangian Stochastic Models (LSM, section 5 – 6), utilising the data driven ML models is limited to the provided data set, restricting the predictive capability to those within parameters of similarity, where hydrodynamics and flow profiles are similar. The advantage of a ML framework, however, is the ability to introduce additional input parameters for the regressor. Theoretically, this leads to correlations between different experiments, which in turn can be used to predict flow behaviour given a trend between conditions. In order to evaluate this capability, however, a larger set of experimental data is required to determine the minimum necessary data sets for accurate prediction for various parameter changes.

7.6 Supplementary material

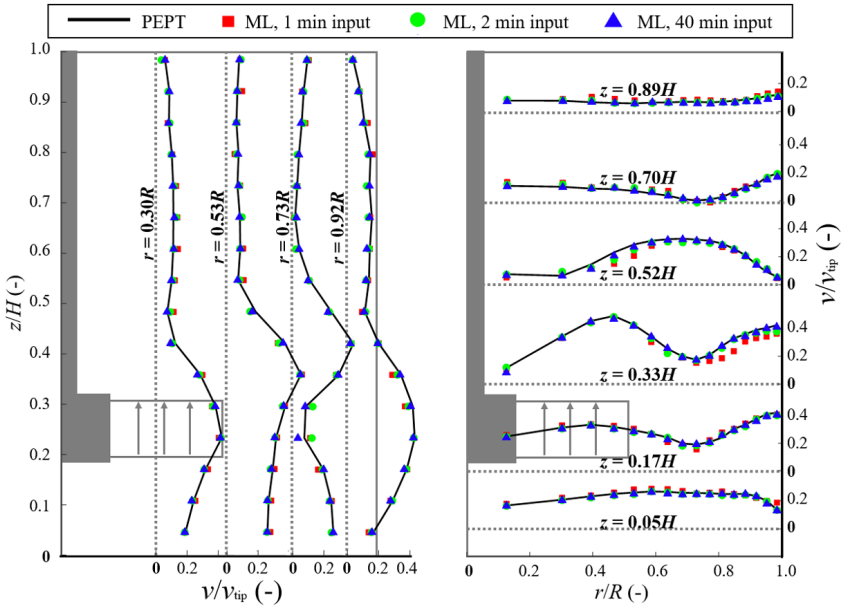


Figure 7.16: Effects of training dataset size on azimuthally-averaged vertical and horizontal profiles of total velocity PEPT and ML compared in single-phase liquid flow: PBTU; $N = 330$ rpm.

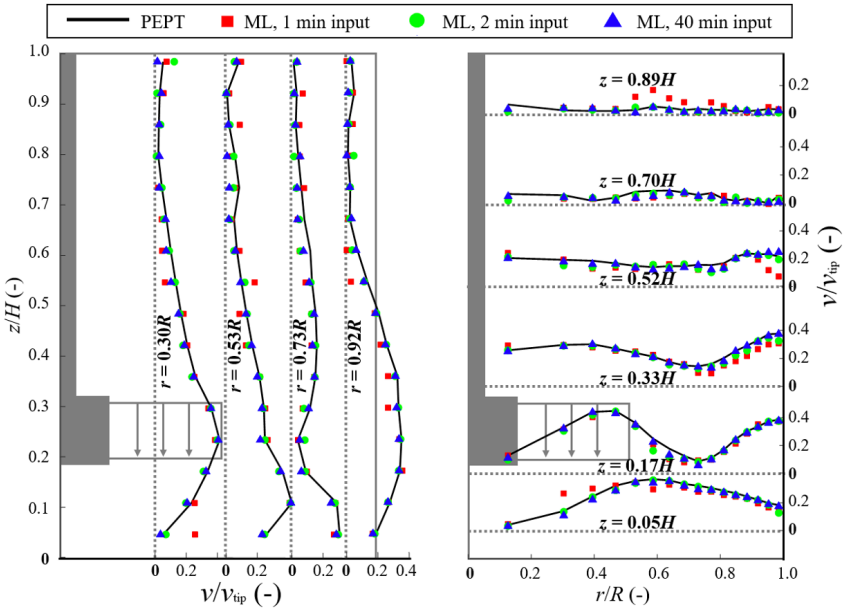


Figure 7.17: Effects of training dataset size on azimuthally-averaged vertical and horizontal profiles of total velocity PEPT and ML compared in single-phase liquid flow: PBTD; $N = 100$ rpm.

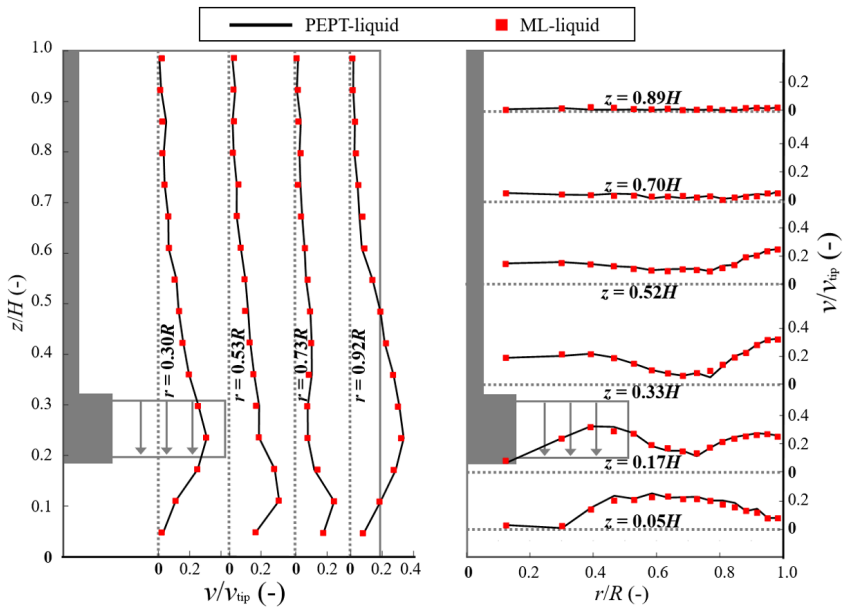


Figure 7.18: Azimuthally-averaged vertical and horizontal profiles of total liquid velocity PEPT and ML compared in 40 wt% particle-liquid flow: PBTD; $N_{js} = 590$ rpm.

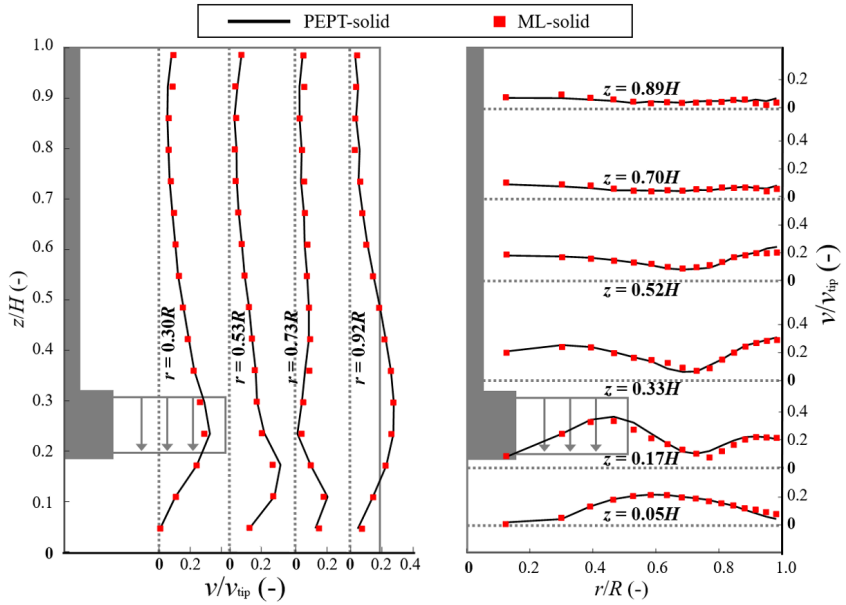


Figure 7.19: Azimuthally-averaged vertical and horizontal profiles of total particle velocity PEPT and ML compared in 40 wt% particle-liquid flow: PBTD; N_{js} = 590 rpm.

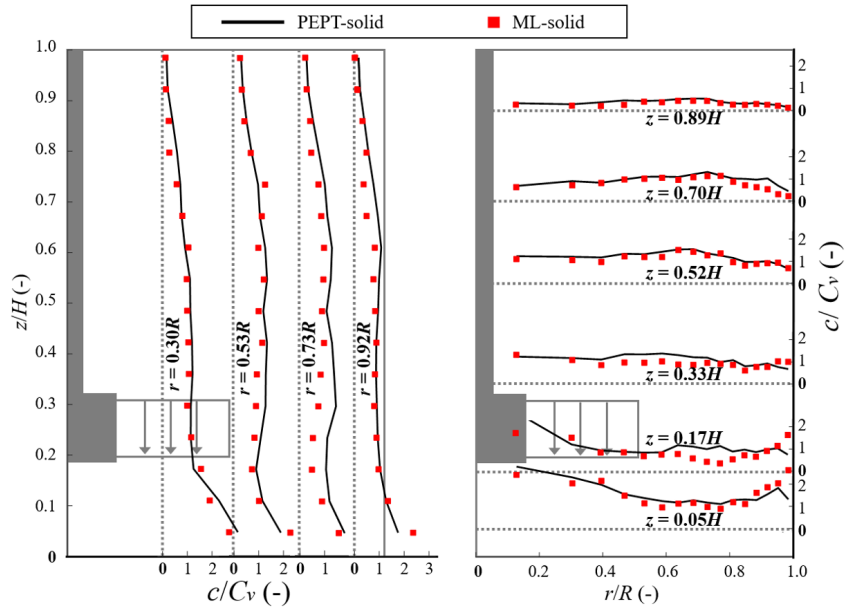


Figure 7.20: Azimuthally-averaged vertical and horizontal profiles of solid phase distribution PEPT and ML compared in 40 wt% particle-liquid flow: PBTD; N_{js} = 590 rpm.

Nomenclature

Symbols

c	Local volume particle concentration (%)
C_{imp}	Impeller off-bottom clearance (m)
C_m	Mean solid mass concentration (%)
C_v	Mean solid volume concentration (%)
D	Impeller diameter (m)
dt	Time-step of machine learning trajectory (s)
$\boldsymbol{e}_n, \boldsymbol{e}_T$	Restitution coefficients at normal and tangential direction (-)
$\boldsymbol{e}_\theta, \boldsymbol{e}_r, \boldsymbol{e}_z$	Unit vectors of cylindrical coordinate system (-)
Fl	Flow number of particle-liquid flow (-)
$Fl^{(L)}$	Liquid-phase flow number (-)
$Fl^{(S)}$	Solid-phase flow number (-)
H	Liquid/suspension height in the vessel (m)
k	Number of training samples used in KNN regressor (-)
L_p	Distance between two samples in feature space (m)
N	Impeller rotational speeds (s-1)
$\boldsymbol{N}(\mu, \sigma^2)$	Gaussian distribution with mean value and standard derivation (-)
N_c	Number of equal-volume cells of cylindrical mesh system (-)
N_{js}	Just-suspended impeller rotational speed
N_θ, N_r, N_z	Number of cells in azimuthal, radial and axial directions (-)
O_E	Local occupancy (-)
Q	Volumetric discharge flow rate (m3/s)
r	Radial coordinate (m)
R	Vessel radius (m)
Re_{imp}	Impeller Reynolds number (-)
t	Time (s)

Δt	Cumulative time of tracer spent in each cell (s)
t_E	Ergodic time (s)
t_∞	Total experimental runtime (-)
T	Vessel diameter (m)
v	Lagrangian velocity (m/s)
$v^{'}$	Fluctuating velocity (m/s)
$\bar{v}$	Mean velocity (m/s)
v_θ, v_r, v_z	Lagrangian velocity components (m/s)
$v_\theta^{'}, v_r^{'}, v_z^{'}$	Fluctuating velocity components (m/s)
$v_{1,n}, v_{1,T}$	Velocities in the normal and tangential direction before collision (m/s)
$v_{2,n}, v_{2,T}$	Velocities in the normal and tangential direction after collision (m/s)
v_{tip}	Impeller tip velocity (m/s)
$\boldsymbol{V}$	Target of training sample (m/s)
$\boldsymbol{V}^{pred}$	New predicted target (m/s)
w	Weight function of KNN regressor (-)
$\boldsymbol{X}$	Feature space of KNN regressor (m)
$\boldsymbol{X}^{'}$	Normalised features of KNN regressor (-)
$\boldsymbol{X}_i^t$	i-th coordinate of ML trajectory at time t (m)
x, y, z	Cartesian coordinates (m)
Greek Symbols	
θ	Azimuthal coordinates of cylindrical system (rad)
μ	Mean normalised fluctuating velocity (m/s)
σ	Standard deviation of normalised fluctuating velocity (m/s)
Abbreviations	
CFD	Computational fluid dynamics
DNS	Direct numerical simulation
KNN	k-nearest neighbours

LES	Large eddy simulation
LVD	Lagrangian velocity distribution
ML	Machine learning
PBT	Pitched blade turbine
PBTD	Down-pumping PBT
PBTU	Up-pumping PBT
PDF	Probability distribution function
PEPT	Positron emission particle tracking
RANS	Reynolds-averaged Navier-Stokes
RMSE	Root mean square error
RTD	Residence time distribution

References

- Aubin, J., Fletcher, D.F. and Xuereb, C., 2004. Modeling turbulent flow in stirred tanks with CFD: the influence of the modeling approach, turbulence model and numerical scheme. Experimental thermal and fluid science, 28(5), 431-445.

- Barigou, M., 2004. Particle Tracking in Opaque Mixing Systems: An Overview of the Capabilities of PET and PEPT. Chemical Engineering Research and Design 82, 1258-1267.

- Barigou, M., Chiti, F., Pianko-Oprych, P., Guida, A., Adams, L., Fan, X., Parker, D., Nienow, A., 2009. Using Positron Emission Particle Tracking (PEPT) to Study Mixing in Stirred Vessels: Validation and Tackling Unsolved Problems in Opaque Systems. Journal of chemical engineering of Japan. 42,

839-846.

- Batchelor, G.K., 1953. The theory of homogeneous turbulence. Cambridge university press.

- Blazek, J., 2015. Computational fluid dynamics: principles and applications. Butterworth-Heinemann.

- Brunton, S.L. and Noack, B.R., 2015. Closed-loop turbulence control: Progress and challenges. Applied Mechanics Reviews, 67(5).

- Brunton, S.L., Noack, B.R. and Koumoutsakos, P., 2020. Machine learning for fluid mechanics. Annual review of fluid mechanics, 52, 477-508.

- Duriez, T., Brunton, S.L. and Noack, B.R., 2017. Machine learning control-taming nonlinear dynamics and turbulence. 116. Switzerland: Springer International Publishing.

- Eesa, M. and Barigou, M., 2008. Horizontal laminar flow of coarse nearly-neutrally buoyant particles in non-Newtonian conveying fluids: CFD and PEPT experiments compared. International Journal of Multiphase Flow, 34(11), 997-1007.

- Fangary, Y.S., Barigou, M., Seville, J.P.K., Parker, D., 2002. A Langrangian Study of Solids Suspension in a Stirred Vessel by Positron Emission Particle Tracking (PEPT). Chemical Engineering & Technology 25, 521-528.

- Gan, J., Liu, P. and Chakrabarty, R.K., 2020. Deep learning enabled Lagrangian particle trajectory simulation. Journal of Aerosol Science, 139, 105468.

- Ghotli, R.A., Shafeeyan, M.S., Abbasi, M.R., Raman, A.A.A. and Ibrahim, S., 2020. Macromixing study for various designs of impellers in a stirred vessel. Chemical Engineering and Processing-Process Intensification, 148, 107794.

- Gillissen, J.J.J. and Van den Akker, H.E.A., 2012. Direct numerical simulation of the turbulent flow in a baffled tank driven by a Rushton turbine. AIChE Journal, 58(12), 3878-3890.

- Guida, A., Nienow, A.W. and Barigou, M., 2010a. PEPT measurements of solidliquid flow field and spatial phase distribution in concentrated monodisperse stirred suspensions. Chemical Engineering Science, 65(6), 1905-1914.

- Guida, A., Nienow, A.W. and Barigou, M., 2010b. Shannon entropy for local and global description of mixing by Lagrangian particle tracking. Chemical engineering science, 65(10), 2865-2883.

- Guida, A., Nienow, A., Barigou, M., 2012. Lagrangian Tools for the Analysis of Mixing in Single-Phase and Multiphase Flow Systems. AIChE Journal 58.

- Harnby, N., Edwards, M.F., Nienow, A.W., 1997. Mixing in the process industries. Butterworth-Heinemann.

- Jadhav, A.J. and Barigou, M., 2022. Eulerian-Lagrangian Modelling of Turbulent Two-Phase Particle-Liquid Flow in a Stirred Vessel: CFD and Experiments Compared. International Journal of Multiphase Flow, 155, 104191.

- Krogstad, P.Å. and Davidson, P., 2011. Freely decaying, homogeneous turbulence generated by multi-scale grids. Journal of fluid mechanics, 680, 417-434.

- Li, K., Savari, C. and Barigou, M., 2022. Computation of Lagrangian coherent structures from experimental fluid trajectory measurements in a mechanically agitated vessel. Chemical Engineering Science, 254, 117598.

- Ling, J., Kurzawski, A. and Templeton, J., 2016. Reynolds averaged turbulence modelling using deep neural networks with embedded invariance. Journal of Fluid Mechanics, 807, 155-166.

- Morsy, M.E. and Yang, J., 2021. Numerical and experimental study on turbulence statistics in a large fan-stirred combustion vessel. Experiments in Fluids, 62(5), 1-20.

- Noack, B.R., 2017. Closed-loop turbulence control-from human to machine learning (and retour). In Symposium on Fluid-Structure-Sound Interactions and Control. 23-32. Springer, Singapore.

- Ochieng, A., Onyango, M. and Kiriamiti, K., 2009. Experimental measurement and computational fluid dynamics simulation of mixing in a stirred tank: a review. South African Journal of Science, 105(11), 421-426.

- Paul, E.L., Atiemo-Obeng, V.A., Kresta, S.M., 2003. Handbook of Industrial Mixing. John Wiley & Sons, Inc.

- Pedregosa, F., Varoquaux, G., Gramfort, A., Michel, V., Thirion, B., Grisel, O., Blondel, M., Prettenhofer, P., Weiss, R., Dubourg, V. and Vanderplas, J., 2011. Scikit-learn: Machine learning in Python. the Journal of machine Learning research, 12, 2825-2830.

- Pianko-Oprych, P., Nienow, A., Barigou, M., 2009. Positron Emission Particle Tracking (PEPT) Compared to Particle Image Velocimetry (PIV) for Studying the Flow Generated by a Pitched-Blade Turbine in Single Phase and Multi-Phase Systems. Chemical Engineering Science 64, 4955-4968.

- Savari, C., Sheikh, H.A. and Barigou, M., 2021. Lagrangian Recurrence Tracking: A Novel Approach for Description of Mixing in Liquid and ParticleLiquid Flows. Industrial & Engineering Chemistry Research, 60(50), 18501-18512.

- Savari, C., Li, K. and Barigou, M., 2022. Multiscale wavelet analysis of 3D Lagrangian trajectories in a mechanically agitated vessel. Chemical Engineering Science, 260, 117844.

- Sheikh, H.A., Savari, C. and Barigou, M., 2022. Lagrangian stochastic modelling of liquid flow in a mechanically agitated vessel. Chemical Engineering Science, 249, 117318.

- Torotwa, I. and Ji, C., 2018. A study of the mixing performance of different impeller designs in stirred vessels using computational fluid dynamics. Designs, 2(1), 10.

- Villermaux, J., 1996. Trajectory length distribution (TLD), a novel concept to characterize mixing in flow systems. Chemical engineering science, 51(10), 1939-1946.

- Wong, T.T. and Yeh, P.Y., 2019. Reliable accuracy estimates from k-fold cross validation. IEEE Transactions on Knowledge and Data Engineering, 32(8), 1586-1594.

- Yang, Z., Savari, C. and Barigou, M., 2022. Numerical and Experimental Investigations of Horizontal Turbulent ParticleLiquid Pipe Flow. Industrial & Engineering Chemistry Research, 61(32), 1204012051.

- Yarlanki, S., Rajendran, B. and Hamann, H., 2012. Estimation of turbulence closure coefficients for data centers using machine learning algorithms. In 13th IEEE InterSociety Conference on Thermal and Thermomechanical Phenomena in Electronic Systems, 38-42.

- Zadghaffari, R., Moghaddas, J.S. and Revstedt, J., 2010. Large-eddy simulation of turbulent flow in a stirred tank driven by a Rushton turbine. Computers & Fluids, 39(7), 1183-1190.

- Zhang, Z.J. and Duraisamy, K., 2015. Machine learning methods for data-driven turbulence modeling. In 22nd AIAA computational fluid dynamics conference, 2460.

- Zwietering, T.N., 1958. Suspending of solid particles in liquid by agitators. Chemical engineering science, 8(3-4), 244-253.

Chapter 8

Predicting three-dimensional flow in stirred vessels using neural networks

8.1 Introduction

Neural networks, which are inspired by the structure and function of the human brain, have been widely used in various fields for modelling and prediction tasks. In the context of mixing vessels, neural networks have been utilised to model and predict the dynamic behaviour of mixing processes, as well as to control mixing systems.

One type of neural network that has been applied to mixing vessels is the artificial neural network (ANN). ANNs are composed of interconnected processing units, called neurons, that are organized in layers. ANNs have been used for a variety of tasks in mixing systems, including the prediction of mixing time (Zhang et al., 2017), modeling of mixing intensity (Li et al., 2018), and optimization of mixing processes (Wang et al., 2019).

Another type of neural network that has been applied to mixing vessels is the long short-term memory (LSTM) network. LSTM networks are a type of recurrent neural network (RNN) that are capable of learning long-term dependencies in sequential data. In a study by Li et al. (2019), an LSTM-based control system was developed for a stirred tank reactor to maintain a constant output concentration. The authors found that the LSTM-based control system was able to achieve a higher control accuracy and faster response time compared to a traditional PID (proportional-integral-derivative) controller.

In addition to ANNs and LSTM networks, other types of neural networks, such as convolutional neural networks (CNNs) and self-organising maps (SOMs), have also been applied to mixing vessels. For example, in a study by Chen et al. (2018), a CNN was used to identify and classify mixing patterns in a stirred tank reactor. The authors found that the CNN was able to accurately classify the mixing patterns with a high accuracy rate.

Overall, neural networks have been shown to be effective in modelling and predicting the dynamic behaviour of mixing processes in mixing vessels, as well as in controlling mixing systems. These networks have the potential to improve the efficiency and effectiveness of mixing systems in various industries.

Neural networks are machine learning models that consist of multiple layers of interconnected nodes, or "neurons," that are used to model complex relationships and patterns in data. Neural networks are trained by adjusting the weights and biases of the neurons based on the inputs and outputs of the network, and have the ability to learn and adapt to new data. Neural networks have been applied to a wide range of applications, including the prediction and control of fluid flow and transport processes.

One area where neural networks have been applied to the study of solid-liquid flow is in the modelling and simulation of solid-liquid systems. Neural networks have been used to model the rheology and flow behaviour of suspensions and emulsions, and to predict the flow properties of complex fluids. For example, Lee et al. (2006) used a neural network to model the viscosity of aqueous suspensions of clay particles, and found that the neural network was able to accurately predict the viscosity over a wide range of concentrations and shear rates.

In addition to the modelling and simulation of solid-liquid flow, neural networks have also been used to control and optimise solid-liquid systems. For example, Ghasemi et al. (2013) used a neural network-based controller to optimise the flow rate and mixing performance of a stirred tank reactor, and found that the controller was able to improve the mixing efficiency and reduce the residence time of the system.

Another area where neural networks have been applied to the study of solid-liquid flow is in the measurement and analysis of particle movement and transport. Neural networks have been used to analyze particle image velocimetry (PIV) data to study the flow of suspensions and emulsions, and to investigate the mixing and segregation of particles in stirred tanks and fluidized bed reactors. For example, Wang et al. (2018) used a neural network to analyze PIV data to study the particle transport and mixing in pipes, and found that the neural network was able to accurately predict the particle movement and transport in the system.

In summary, neural networks have been applied to the study of solid-liquid flow in several areas, including the modelling and simulation of solid-liquid systems, the control and optimisation of solid-liquid systems, and the measurement and analysis of particle movement and transport. Neural networks have demonstrated the ability to accurately predict and analyse the flow and transport behaviour of solid-liquid systems, and have the potential to inform the design and optimisation of mixing and

transport processes.

8.1.1 Recurrent networks

Recurrent neural networks (RNNs) are a type of machine learning model that are well-suited for tasks that involve sequential or time-dependent data. RNNs are designed to handle data with a temporal dimension, and are able to model complex dependencies between data points that occur over time. This makes RNNs particularly useful for tasks such as time series prediction, language modeling, and speech recognition. In chemical engineering, RNNs have been applied to a wide range of tasks, including the modeling and simulation of chemical reactions and processes, the prediction of physical and chemical properties of materials, and the control and optimization of chemical systems. For example, RNNs have been used to model the behavior of dynamic systems, such as chemical reactors, and to predict the properties of complex fluids. One advantage of using RNNs in chemical engineering is that they are able to capture temporal dependencies in data, which is important in many chemical systems where the behavior of the system may depend on the history of the system. RNNs are also able to handle large and complex datasets, and can learn and adapt to new data. However, there are also some limitations to the use of RNNs in chemical engineering. One limitation is that RNNs can be sensitive to the quality and relevance of the data, and may not perform well if the data is noisy or not representative of the system being studied. Another limitation is that RNNs may require a large amount of data for training and optimization, which can be a challenge in situations where data is scarce or difficult to obtain. In addition to the applications mentioned above, RNNs have also been used for tasks such as the prediction of chemical kinetics, the control of batch processes, and the identification of patterns in chemical data. RNNs have the ability to model complex

dependencies between variables, and have been found to be particularly effective for tasks that involve time-series data or sequential data. One of the key features of RNNs is their ability to retain information from past time steps, which allows them to model dependencies between data points that occur over time. This is achieved through the use of hidden states, which are internal representations of the network that are updated at each time step based on the input and previous hidden state. The hidden states allow RNNs to capture temporal dependencies in data, and are an important factor in the ability of RNNs to learn and adapt to new data. There are several different types of RNNs, each with their own properties and characteristics. Some common types of RNNs include: Vanilla RNNs: Vanilla RNNs are the simplest type of RNN, and consist of a single layer of neurons that are connected in a cyclic manner. Vanilla RNNs have the ability to retain information from past time steps, but are limited in their ability to model long-term dependencies. Long Short-Term Memory (LSTM) networks: LSTM networks are a type of RNN that have been designed to address the issue of long-term dependencies. LSTMs have additional components called gates, which are used to control the flow of information through the network and allow the network to retain relevant information for longer periods of time. Gated Recurrent Units (GRUs): GRUs are another type of RNN that have been designed to address the issue of long-term dependencies. GRUs have a similar structure to LSTMs, but have fewer parameters and are generally easier to train.

8.1.2 Long short-term memory networks

Long Short-Term Memory (LSTM) networks are a type of recurrent neural network (RNN) that have been successful in a wide range of applications, including natural language processing, speech recognition, and machine translation (Hochreiter &

Schmidhuber, 1997). LSTMs are able to process long sequences of data, making them particularly well-suited for tasks that involve long-term dependencies.

One key advantage of LSTMs is their ability to remember information for extended periods of time. Unlike traditional RNNs, which have difficulty retaining information for more than a few time steps, LSTMs are able to store and access information from much further back in the input sequence (Hochreiter & Schmidhuber, 1997). This is achieved through the use of gates, which control the flow of information into and out of the LSTM's memory cells.

The gates in an LSTM consist of input, output, and forget gates, which control the flow of information into, out of, and within the memory cells, respectively (Gers et al., 2000). The input gate determines which information from the input sequence is stored in the memory cells, while the output gate determines which information from the memory cells is passed on to the next time step (Gers et al., 2000). The forget gate determines which information from the previous time step is retained in the memory cells (Gers et al., 2000).

Another key feature of LSTMs is their ability to process input sequences of varying lengths. Traditional RNNs require fixed-length input sequences, but LSTMs can handle input sequences of varying lengths by using special "forget" gates to reset the memory cells (Gers et al., 2000). This makes LSTMs more flexible and easier to train, as they do not require the input sequences to be padded or truncated to a fixed length.

One application of LSTM networks in mixing vessels is in the prediction of mixing time, which is an important parameter in the design and optimization of mixing systems. In a study by Zhang et al. (2017), an LSTM network was used to predict the mixing time of a T-shaped mixing vessel under different operating conditions.

The authors found that the LSTM network was able to accurately predict the mixing time with a mean absolute error of less than 1%.

Another application of LSTM networks in mixing vessels is in the control of mixing processes. In a study by Li et al. (2019), an LSTM-based control system was developed for a stirred tank reactor to maintain a constant output concentration. The authors found that the LSTM-based control system was able to achieve a higher control accuracy and faster response time compared to a traditional PID (proportional-integral-derivative) controller.

In addition to mixing time prediction and control, LSTM networks have also been used for the modelling and prediction of other mixing-related quantities, such as mixing intensity and mixing uniformity. For example, in a study by Li et al. (2018), an LSTM network was used to predict the mixing intensity of a stirred tank reactor under different operating conditions. The authors found that the LSTM network was able to accurately predict the mixing intensity with a mean absolute error of less than 5%.

In summary, LSTM networks have been shown to be effective in the modelling and prediction of dynamic mixing processes in mixing vessels. These networks have been applied to a variety of tasks, including the prediction of mixing time, control of mixing processes, and prediction of mixing-related quantities. Overall, the use of LSTM networks has the potential to improve the efficiency and effectiveness of mixing systems in various industries.

8.2 Neural network theory

For many engineering applications, traditional non-linear regression or cluster based algorithms are used to model and predict various systems. These techniques involve finding correlations between input parameters and output results. Modelling systems with multiple interconnected input parameters can be a challenge using these straightforward techniques, where theoretical governing equations are either unobtainable or require extensive computation to solve numerically. For these challenges, neural networks provide an alternative methodology to link inputs to their respective outputs.

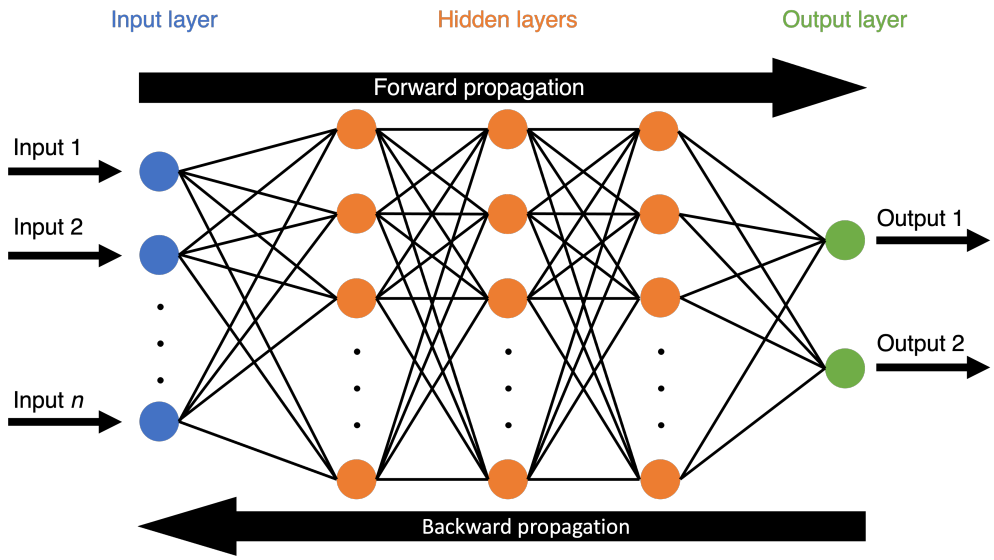


Figure 8.1: Diagram of a neural network.

These networks consist of processing nodes, or neurons, which are interlinked via connections of variable weighting. Neurons are separated into layers, of which there are three types; an input layer, an output layer and hidden layers (fig. 8.1). Each layer may contain one or more neurons, and the number of hidden layers is typically a related to the complexity of the model required. Input nodes match the number of independent variables and similarly, the output layer will contain the same number of nodes as outputs required from the model. To determine the network structure and

hyperparameters, a pre-defined set of data containing inputs and their respective outputs are required. This data set is separated into a training set and a test set, where the former is used to train the network to apply appropriate interlink weighting and the latter is used to evaluate the trained network's predictive accuracy. By conducting this methodology for a matrix of networks of various structures, a trained network with highest accuracy can be found and tested further, providing a predictive model independent of theoretical descriptions and regression correlations.

Along with the network structure, the method by which data "flows" through the network can be one of two methods; feed forward and recurrent. Feed forward networks are mostly suitable for learning patterns in data which are time independent. Recurrent networks are used for time-series data, for a system in which time cannot be ignored. Neural networks are machine learning models that are inspired by the structure and function of the human brain. Neural networks are composed of layers of interconnected neurons, or nodes, which process and transmit information through weighted connections. Neural networks are trained to perform a specific task by adjusting the weights of the connections between the nodes, based on a set of input and output data.

There are two main types of neural networks: feedforward neural networks and recurrent neural networks. Feedforward neural networks are characterised by a one-way flow of information, with the output of each layer serving as the input to the next layer. Recurrent neural networks, on the other hand, have feedback connections that allow the network to process sequential data, such as time series or natural language.

The training process for neural networks involves several steps:

1. Data preparation: The first step in training a neural network is to prepare the training data. This involves selecting a dataset that is relevant to the task

at hand and preprocessing the data to make it suitable for training the network. Preprocessing steps may include cleaning and formatting the data, splitting the data into training and validation sets, and normalising or standardising the data.

2. Model selection: The next step is to select a neural network model that is appropriate for the task. There are various types of neural network models, such as feedforward neural networks, convolutional neural networks, and long short-term memory networks, each of which is suited to different types of tasks. The choice of model will depend on the complexity of the task, the size and structure of the dataset, and the resources available for training the network.

3. Model architecture: Once the model has been selected, the next step is to design the architecture of the network. This involves specifying the number of layers and the number of nodes in each layer, as well as the type of activation function to be used at each layer. The activation function determines the output of the node, based on the input and the weights of the connections. The choice of activation function will depend on the task and the requirements of the network.

4. Weight initialisation: The next step is to initialise the weights of the connections between the nodes. This can be done randomly or using a predetermined set of weights. The choice of initialisation method will depend on the task and the characteristics of the dataset.

5. Training the model: The next step is to train the model on the training data. This involves feeding the input data through the network, comparing the output of the network with the desired output, and adjusting the weights of the connections based on the error between the predicted and desired outputs. This process is repeated for each data sample in the training set, and the weights are updated based on the average error across the entire training set.

6. Validation: Once the model has been trained on the training data, it is tested on the validation data to evaluate its performance. The validation data is used to assess the generalisation of the model, or its ability to perform well on unseen data.

7. Model tuning: If the model performs poorly on the validation data, it may be necessary to tune the model by adjusting the architecture or the parameters of the network, such as the number of layers, the number of nodes in each layer, or the learning rate. The learning rate determines the speed at which the weights are updated during training, and can have a significant impact on the performance of the model.

8. Testing: Once the model has been trained and validated, it is tested on the test data to evaluate its performance. The test data is used to assess the final performance of the model, and provides an estimate of how the model will perform on unseen data in the future.

9. Deployment: If the model performs well on the test data, it can be deployed for use in the real world. This involves integrating the model into a system or application, and testing it in a real-world setting to ensure that it performs as expected.

In summary, training a neural network involves preparing the data, selecting and designing a model, initialising the weights, training the model on the training data, evaluating the model on the validation data, and fine-tuning the model as needed. Once the model has been trained and validated, it can be tested and deployed for use in the real world.

8.2.1 Data pre-processing

Data pre-processing is an important step in the training of neural networks, as it involves the preparation and cleaning of the data that will be used to train the network. Data pre-processing is necessary to ensure that the data is in a suitable format for training, and to remove any noise or errors that may affect the performance of the network.

There are several steps that may be involved in data pre-processing, including:

- Data cleaning: Data cleaning involves the removal of any errors or inconsistencies in the data, such as missing values or duplicate records. This is important to ensure that the data is reliable and accurate, and that it does not contain any errors that may affect the performance of the network.

- Data transformation: Data transformation involves the modification of the data in order to make it more suitable for training. This may involve scaling the data to a specific range, applying transformations such as logarithmic or exponential functions, or encoding categorical variables. Data transformation is important to ensure that the data is in a format that is suitable for the network, and to prevent issues such as bias or overfitting.

- Data splitting: Data splitting involves the separation of the data into different sets for training, validation, and testing. The training set is used to train the network, the validation set is used to evaluate the performance of the network during training, and the testing set is used to evaluate the performance of the network after training. Data splitting is important to ensure that the network is not overfitted to the training data, and that the performance of the network can be accurately evaluated.

- Data augmentation: Data augmentation involves the creation of additional data by modifying or transforming the existing data. This can be useful when the amount of available data is limited, as it allows the network to learn from a larger number of examples. Data augmentation may involve techniques such as adding noise to the data, rotating or scaling the data, or applying filters.

Data pre-processing is an important step in the training of neural networks, and involves the preparation and cleaning of the data to ensure that it is in a suitable format for training. Data pre-processing may involve steps such as data cleaning, data transformation, data splitting, and data augmentation, and is important to ensure that the network is able to learn and adapt effectively.

8.2.2 Activation functions

Nodes in a neural network will process inputs and, depending on importance to the prediction, will activate and produce an output. This importance is governed by an internal transfer function, called an activation function, which derives an output from inputs fed to the node. The summed weighted inputs to the node are transformed by the activation function as an output to the next layer in the network, adding non-linearity for the purpose of prediction. There are a number of activation functions available for use in neural networks, each differentiable for determining weighting during training back-propagation. Typically, all nodes in hidden layers will utilise the same activation function. Determining the correct activation function for a neural network requires testing of models and evaluating errors in prediction, however output nodes will have activation functions based on the type of prediction:

- Sigmoid for binary classification or multilabel classification

- Softmax for multiclass classification
- Linear for regression

Neural network activation functions are mathematical functions that are used to introduce non-linearity into the output of a neural network. Activation functions are applied to the output of each node in a neural network, and determine the output of the node based on the input and the weights of the connections. Activation functions are an important component of neural networks, as they allow the network to model complex relationships and to learn more sophisticated patterns in the data (Glorot & Bengio, 2010).

There are various types of activation functions, each with its own set of characteristics and advantages. Some commonly used activation functions include (Klambauer et al., 2017):

1. Sigmoid function: The sigmoid function is a smooth, S-shaped curve that maps the input to the range of 0 to 1. It is defined by the equation:

$f(x) = \frac{1}{1+e^{-x}}$

where x is the input and $f(x)$ is the output. The sigmoid function has the advantage of producing outputs that are easy to interpret as probabilities, but it can suffer from the vanishing gradient problem, which can slow down the learning process.

2. Hyperbolic tangent function: The hyperbolic tangent function, or tanh function, is a smooth, S-shaped curve that maps the input to the range of -1 to 1. It is defined by the equation:

$f(x) = \frac{e^{x}-e^{-x}}{e^{x}+e^{-x}}$

The tanh function has the advantage of producing outputs that are centred around zero, which can help to stabilise the learning process. However, it can also suffer from the vanishing gradient problem.

3. Rectified linear unit function: The rectified linear unit function, or ReLU function, is a piecewise linear function that maps the input to the range of 0 to infinity. It is defined by the equation:

$f(x) = max(0, x)$

The ReLU function has the advantage of being computationally efficient and producing outputs that are easy to interpret as binary activations. However, it can suffer from the problem of dying ReLUs, which occur when the output of a ReLU node becomes zero and the weights of the node are not updated during training.

4. Leaky ReLU function: The leaky ReLU function is a variant of the ReLU function that allows a small negative slope for negative input values. It is defined by the equation:

$f(x) = max(ax, x)$

where a is a small constant, typically 0.01. The leaky ReLU function has the advantage of addressing the problem of dying ReLUs, but it can still suffer from the vanishing gradient problem for large negative input values.

5. Exponential linear unit function: The exponential linear unit function, or ELU function, is a smooth function that maps the input to the range of -1 to infinity. It is defined by the equation:

$f(x) = a(e^x - 1)$ if $x \leq 0$, $f(x) = x$ if $x > 0$

where a is a small constant, typically 1. The ELU function has the advantage of producing outputs that are centered around zero, which can help to stabilize the learning process. It also has the advantage of avoiding the vanishing gradient problem, as the derivative of the function approaches 1 for large positive input values.

6. Softmax function: The softmax function is a generalisation of the sigmoid function that is used to produce a probability distribution over a set of classes. It is defined by the equation:

$$f(x_i) = \frac{e^{x_i}}{\sum_j^k e^{x_j}}$$

where x_i is the input of the i-th node and $f(x_i)$ is the output. The softmax function has the advantage of producing outputs that are easy to interpret as probabilities, but it can be computationally expensive to compute, especially for large datasets.

7. Swish function: The swish function is a smooth, S-shaped curve that maps the input to the range of 0 to infinity. It is defined by the equation:

$$f(x) = x \cdot sigmoid(x)$$

The swish function has the advantage of producing outputs that are centered around zero, which can help to stabilize the learning process. It also has the advantage of avoiding the vanishing gradient problem, as the derivative of the function approaches 1 for large positive input values (Ramachandran et al., 2017).

In addition to the activation functions listed above, there are many other activation functions that have been proposed and used in neural network models. The choice of activation function will depend on the specific requirements of the task and the characteristics of the data. Some factors to consider when selecting an acti-

vation function include the convergence rate, the robustness, and the computational complexity of the function.

Neural network activation functions are mathematical functions that are used to introduce non-linearity into the output of a neural network. Activation functions are an important component of neural networks, as they allow the network to model complex relationships and to learn more sophisticated patterns in the data. There are various types of activation functions, each with its own set of characteristics and advantages, and the choice of activation function will depend on the specific requirements of the task and the characteristics of the data.

8.2.3 Hyperparameters

The process of training a neural network involves the optimization of a loss function, which measures the difference between the predicted outputs of the network and the actual outputs.

There are several factors that can influence the performance and efficiency of a neural network, including the architecture of the network, the type of activation function used, and the training algorithm. In addition to these factors, there are several hyperparameters that can also affect the performance of a neural network. Hyperparameters are parameters that are not learned by the network during training, but rather are set by the user. Examples of hyperparameters include the learning rate, the number of epochs, and the batch size (Bishop, 1995; Goodfellow et al., 2016; Chollet & Allaire, 2018).

1. Learning rate: The learning rate is a hyperparameter that controls the step size of the optimization algorithm during training. It determines the amount by

which the weights and biases of the neurons are adjusted at each iteration. A larger learning rate can lead to faster convergence, but it can also lead to unstable training and overshooting the optimal solution. A smaller learning rate can lead to slower convergence, but it can also provide a more stable and accurate solution.

2. Number of epochs: The number of epochs is a hyperparameter that determines the number of times the training algorithm will iterate over the entire training dataset. A larger number of epochs can lead to better model performance, but it can also increase the training time and the risk of overfitting.

3. Batch size: The batch size is a hyperparameter that determines the number of training examples that are processed by the training algorithm at each iteration. A larger batch size can lead to faster convergence and a more stable optimization process, but it can also require more memory and computational resources. A smaller batch size can lead to slower convergence and a less stable optimization process, but it can also allow for a more flexible and adaptable model.

4. Activation function: The activation function is a hyperparameter that determines the type of function that is used to introduce non-linearity into the output of a neural network. Different types of activation functions, such as sigmoid, tanh, and ReLU, have different characteristics and can affect the performance and efficiency of the network. The choice of activation function will depend on the specific requirements of the task and the characteristics of the data.

Neural network hyperparameters are parameters that are not learned by the network during training, but rather are set by the user. Hyperparameters, such as the learning rate, the number of epochs, the batch size, and the activation function, can significantly influence the performance and efficiency of a neural network. The optimal values of the hyperparameters will depend on the specific requirements of the

task and the characteristics of the data, and can be determined through a process known as hyperparameter tuning (Geron, 2019).

8.2.4 Data propagation

Training neural networks involves passing data through a constructed architecture and using algorithms to minimise errors to provide optimal weighting on each node. Input data fed into the network into the input layer is passed into the hidden layers, where weighting and activation functions operate, passing information to subsequent hidden layers until finally calculating a prediction in the output layer. This transfer of data is known as forward-propagation. During training, forward-propagation is used to calculate a prediction for a training set of data, where the outputs are known. The weightings in the network can then be tuned using algorithms such as stochastic gradient descent, minimising the error between data and prediction. This procedure is known as back-propagation. Iterating through this process allows for optimal weighting through the layers thereby resulting in a trained network for the given architecture. Once the network is trained, normal operation of the network to provide predictions is executed using forward-propagation; input information is passed through the layers where weightings are optimised resulting in a prediction more accurate than that calculated prior to training. Neural networks are initialised with uniform weighting on all nodes, and are trained using data where outputs for given inputs are known. A portion of training data is input to the network and forward-propagated through the network to give a resulting output prediction. This output is compared with the known output for the training data using a loss function:

$$L(y, \hat{y}) = 1/m \sum_{n=1}^{m} (y_i - \hat{y}_i)^2$$

where y is the known output, and $\hat{y}$ is the model output. Minimising the loss function

for a neural network results in a weights that provide the most accurate prediction for the architecture.

8.2.5 Network training and optimisers

Neural network optimisers are algorithms that are used to adjust the weights and biases of the neurons in a neural network in order to minimise the error between the predicted outputs of the network and the true outputs. Optimisation is an important step in the training of neural networks, as it allows the network to learn and adapt to new data. There are several different types of optimisers that are commonly used in neural networks, each with their own properties and characteristics. Some common optimisers include (Goodfellow et al., 2016; Chollet & Allaire, 2018; Geron, 2019):

- Stochastic gradient descent (SGD): SGD is a simple and widely-used optimization algorithm that is based on the gradient descent method. It updates the weights and biases of the network by taking the derivative of the loss function with respect to each parameter, and moving in the opposite direction of the gradient. SGD is defined as:

$$w_i = w_i - \eta \frac{\partial L}{\partial w_i}$$
$$b_i = b_i - \eta \frac{\partial L}{\partial b_i}$$

  where w_i and b_i are the weights and biases of the network, L is the loss function, and η is the learning rate. The learning rate determines the size of the steps that are taken during optimization, and is a hyperparameter that must be set manually.

- Momentum: Momentum is an optimization algorithm that is based on SGD, but incorporates a momentum term that helps to smooth the optimization

process. The momentum term is defined as:

$$v_i = \gamma v_i + \eta \frac{\partial L}{\partial w_i}$$
$$w_i = w_i - v_i$$

where v_i is the momentum term, γ is the momentum hyperparameter, and the other variables are as defined above. The momentum term helps to smooth the optimization process by adding a fraction of the previous update to the current update.

- Adagrad: Adagrad is an optimization algorithm that adapts the learning rate of the network based on the past gradients of the parameters. It updates the weights and biases of the network using the following equations:

$$g_i = g_i + \left(\frac{\partial L}{\partial w_i}\right)^2$$
$$w_i = w_i - \frac{\eta \frac{\partial L}{\partial w_i}}{\sqrt{g_i + \epsilon}}$$

where g_i is a running sum of the squares of the gradients, ϵ is a small constant to prevent division by zero, and the other variables are as defined above. Adagrad has the advantage of adapting the learning rate to the properties of the data, but may require more computation and storage than other optimisers.

- Adam: Adam is an optimization algorithm that combines the ideas of momentum and Adagrad. It updates the weights and biases of the network using the

following equations:

$$
\begin{aligned}
m_i &= \beta_1 m_i + (1 - \beta_1) \frac{\partial L}{\partial w_i} \\
v_i &= \beta_2 v_i + (1 - \beta_2) \left(\frac{\partial L}{\partial w_i} \right)^2 \\
m_i &= \frac{m_i}{1 - \beta_1^t} \\
v_i &= \frac{v_i}{1 - \beta_2^t} \\
w_i &= w_i - \frac{\eta m_i}{\sqrt{v_i} + \epsilon}
\end{aligned}
$$

where m_i and v_i are the momentum and Adagrad terms, respectively, β_1 and β_2 are hyperparameters, and t is the iteration number. Adam has he advantage of being able to adapt the learning rate to the properties of the data, while also incorporating a momentum term to smooth the optimization process. It has been found to work well for a wide range of tasks and is a popular choice for many neural network applications.

Neural network optimisers are algorithms that are used to adjust the weights and biases of the network in order to minimise the error between the predicted outputs and the true outputs. There are several different types of optimisers that are commonly used in neural networks, including SGD, momentum, Adagrad, and Adam. The choice of optimiser can impact the performance and efficiency of the network, and it is important to carefully select the appropriate optimiser for the task at hand, taking into consideration the characteristics of the data and the specific requirements of the problem.

8.3 Experimental

8.3.1 Mixing vessel

The flow and mixing of a single-phase water system was investigated using a mixing vessel with a diameter of 288 mm and a liquid height of 288 mm. The agitation was achieved using a down pumping 6-blade turbine with a 45 degree pitch and a diameter of 144 mm. The impeller had a blade width of 28.8 mm, a baffle width of 28.8 mm, and an impeller clearance of 72 mm. A radioactively labelled resin tracer particle was used to track the flow, which was made neutrally buoyant by adding salt to the water to match its density. The experiments were conducted at different impeller rotational speeds ranging from 100 to 500 rpm to determine the long-term trajectory of the liquid in each case.

8.3.2 Positron emission particle tracking

Positron emission particle tracking (PEPT) can be used to obtain three-dimensional Lagrangian particle trajectories within process equipment. This technique involves accurately tracking a positron emitting tracer particle, which provides three-dimensional space and time data that can be used to visualize the flow of opaque fluids and inside opaque equipment (Barigou, 2004). The PEPT technique has been widely used to study flow and mixing in stirred vessels, and more information can be found in previous papers (Guida et al., 2010a, 2010b, and 2011).

8.4 Network setup

8.4.1 Data preparation

Using neural networks for prediction requires defined parameters as inputs and desired outputs. Lagrangian flow paths obtained via PEPT consisted of time-series spatial coordinates in three dimensions at irregular time intervals. For feed-forward networks (FFN) predictions are time-dependent, therefore, inputs to the models were defined as the tracer spacial coordinate at a given time stamp. Three FFN networks were investigated, predicting next position, current velocity and current acceleration from current position, respectively. Although time information is not stored in the network, outputs are defined by the time interval between data points. Therefore, an interpolating algorithm was applied to the dataset to give regular time intervals (1 ms), then velocity and acceleration for each position was calculated. Training data was compiled into sample rows with columns for inputs (x_0, y_0, z_0 coordinate) and respective outputs: next coordinate position (x_1, y_1, z_1) for variant A, current velocity ($\dot{x_0}, \dot{y_0}, \dot{z_0}$) for variant B, and current acceleration ($\ddot{x_0}, \ddot{y_0}, \ddot{z_0}$) for variant C. To mitigate bias between features, all variables were scaled to a range [0,1] using equation 8.1:

$$x_{scaled} = \frac{x - x_{min}}{x_{max} - x_{min}} \tag{8.1}$$

where minimum and maximum variables were vessel geometry boundaries, $\pm v_{tip}$, and $\pm a_{max}$ for position, velocity and acceleration respectively.

The network setup procedure for recurrent networks followed a similar methodology to feed-forward networks, with the minor alteration to data preparation; data was

stored as a three-dimensional array, where dimension one and two were samples of features and responses, and the third dimension was time. In other words, the data arrays matched the data arrays used for feed-forward networks, but also included the data for the previous time steps in subsequent arrays appended in a third dimension. This allowed for the recurrent networks to have access to information at the current time step and the previous time steps simultaneously. In this study, in addition to the FFN models, a vanilla RNN and a LSTM network were assessed in their capability of predicting flow in the stirred vessel.

Once model architecture and training was completed, each model was used to construct a predicted Lagrangian flow trajectory. Each model was given an initial position as a starting input and used to calculate the respective output parameter. Then, the subsequent position was determined (without further calculation for model A) by integrating to give the model tracer position after one time interval. This position was then re-input to the models and the process was repeated, resulting in model Lagrangian trajectories with a duration of 60 min.

8.4.2 Network architecture

Neural networks are used to make complex predictions by learning a non-linear relationship between inputs and outputs provided by a set of training data. Networks consist of three main parts, or layers, which contain nodes linked between layers with weighted connections:

- Input layer - each node in the input layer receives input information, otherwise known as features, and pass it forward to the next layer. An input layer, therefore has the same number of nodes as independent variables for the problem.

- Hidden layers - a neural network may contain one or more hidden layers, each with numerous nodes. Generally, the number of nodes per layer is constant. Nodes in the hidden layers are responsible for learning the relationship between independent variables and dependent variables (features and responses), by adjusting the weights of node connections.

- Output layer - a prediction of all output responses are stored in the output layer, which consists of the same number of nodes as dependent variables.

When a network is called to make a prediction, input features enter the input layer nodes, pass into the hidden layers with their appropriate weighting where the prediction is computed, then passed to the output layer as a final result. This is known as forward propagation.

Constructing a suitable network architecture for each model requires testing of multiple architectural hyperparameters, namely: number of nodes in each hidden layer, number of hidden layers, and activation functions. A dropout probability of 0.5 was used for all cases to mitigate overfitting. A selected portion of randomised experimental consisting of 100 RPM and 500 RPM data was separated into a 70% for training and 30% for testing. To determine the optimal structure, a matrix of network architectures were trained using the training data, then used to make predictions for the test data. As the real experimental responses were known, the test predictions were compared and a root mean square error calculated for each set of predictions. Training was conducted using the Adam optimiser, a version of stochastic gradient descent with an adaptable learning rate. Results are summarised in table 8.1.

Neural networks are susceptible to overfitting, particularly when presented with smaller training datasets. An attempt to mitigate this effect is achieved by utilising

Table 8.1: Neural network architectures

Network	**Activation function**	**Hidden layers**	**Nodes per layer**
FFN A	ReLU	3	35
FFN B	ReLU	4	24
FFN C	ReLU	2	20
RNN A	ReLU	3	35
RNN B	ReLU	3	30
RNN C	ReLU	3	45
LSTM A	LSTM	5	35
LSTM B	LSTM	6	25
LSTM C	LSTM	6	18

dropout, a method by which random nodes are "dropped" during the training procedure. This regularisation procedure approximates training a large number of neural networks with varying architectures in parallel, forcing non-dropped nodes within the hidden layers to activate and have weightings adjusted accordingly. The dropout hyperparameter defines the probability at which outputs of each hidden layer are retained, being a value between [0,1]. Dropout is only utilised during training, and not present when making predictions with the network. Dropout was included at 0.5, reducing RMSE by in some cases by 12% during training.

Training procedure

For the neural network to "learn" the relationship between features and responses for a problem, it must first undergo an iterative training procedure, which when converged to a stable error, produces a network with node link weightings optimised for predictions. This iterative procedure uses a combination of forward-propagation and back-propagation of data through the network where weights are adjusted after each full propagation of training data, or epoch, until a desired number of epochs are reached. Adjustments to weightings can also be made using batched training data, where multiple adjustments are made per epoch.

In this study, we used the Adam optimiser for the training procedure of each network, a well known and efficient back-propagation algorithm based on gradient descent (section 8.2.5).

Number of epochs and batch size for each optimised network were evaluated by assessing the RMSE after training with varied numbers of epochs and batch size. Reducing the batch size per epoch increased training time significantly therefore a size of 1000 data points was chosen. Similarly, increasing the number of epochs resulted in more computing time, however after 125 epochs no significant reduction in prediction was seen. Therefore 150 epochs was chosen as an optimum for accuracy and computational time, erring on the conservative side.

8.5 Results and discussion

8.5.1 Evaluation method

The neural networks were used to construct 40 min long Lagrangian flow trajectories, mimicking an experimental result normally obtained via the PEPT technique. Each network was trained on 3 min of experimental data ($\approx$ 18,000 data points) matching the desired prediction output. This short driver data is not sufficient to infer Eulerian parameters from experimental data, therefore the objective of the neural networks was to provide an extended trajectory with sufficient information. As comparing Lagrangian trajectories in a semi-chaotic system like-for-like is not achievable, Eulerian metrics for both the experimental and predicted trajectories were calculated and compared. These were namely the Eulerian velocity profile and tracer occupancy in the stirred vessel.

Both parameters were calculated by defining a grid of equal-volume cells for the vessel, with 15 cells in the r direction and 30 cells in the z direction, taking an average in the azimuthal (θ) direction. Velocity for each tracer position in the trajectory was calculated by taking the displacement to the next position and dividing by the difference in time stamp. For each cell in the grid, a time-averaged velocity for all the tracer positions present were calculated to give an Eulerian map of mean velocity for the system.

Occupancy of each cell was calculated by determining the total time the tracer spent in each cell and dividing by the ergodic time, i.e. the total experimental time divided by the number of cells in the grid.

Furthermore, probability density functions for detections in each dimension were computed for comparison by taking histograms of tracer positions. Bins in the r- and z-directions had a width of 2 mm, and bins in the θ-direction had a width of 5^o.

8.5.2 Velocity profiles

Three variants of each network were tested, predicting position (variant A), velocity (variant B), and acceleration (variant C). Each network with its variants was used to construct Lagrangian flow trajectories and compared to the existing experimental data. Figure 8.2 shows velocity magnitudes for the height of the stirred vessel at each radial cell, comparing variants of the FFN network against experimental data. Radial cell centroid location for each graph (from top left to bottom right) are as follows: 0.13, 0.31, 0.41, 0.48, 0.55, 0.60, 0.66, 0.71, 0.75, 0.80, 0.84, 0.88, 0.91, 0.95, 0.98 r/R. Figure 8.2 shows large deviations in velocity from trajectories constructed using FFN A and FFN C. Although predictions during the training phase for both variants provided low errors, these minor deviations propagate into

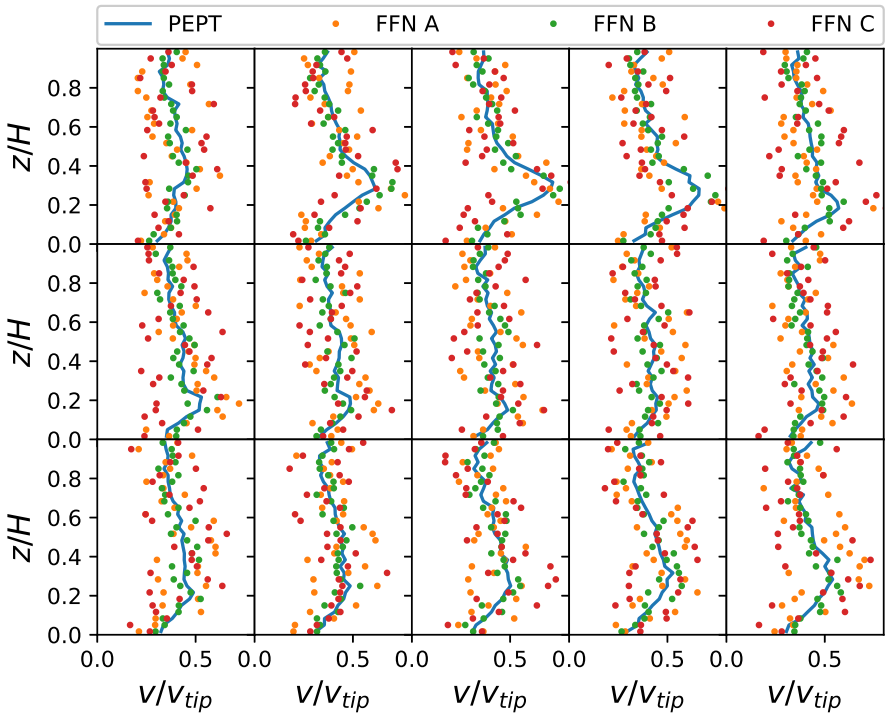


Figure 8.2: Velocity magnitude profiles comparing FFN predictions with experimental data at 100 RPM

larger changes when the Lagrangian trajectory is constructed. FFN B provides a closer representation of flow than the other variants, with far less deviation. Similar results are observed at a higher rotation rate (figure 8.3), with more differences between model variants. FFN A results in the poorest predictions, with FFN C capable of predicting flow at the top regions of the vessel. Again, FFN B results in the closest predictions to experimental data. Errors occur mostly in areas of high velocity, where flow is most likely to be more chaotic and therefore less predictable.

Similar tests were conducted using variants of the RNN and LSTM networks, as shown in figures 8.4 & 8.5. Results from RNN predictions show good agreement with experimental data particularly in the top region of the vessel, where all three variants show small deviations. Larger errors are observed where velocity is higher, however these errors are minor in comparison to FFNs. Smallest errors are observed

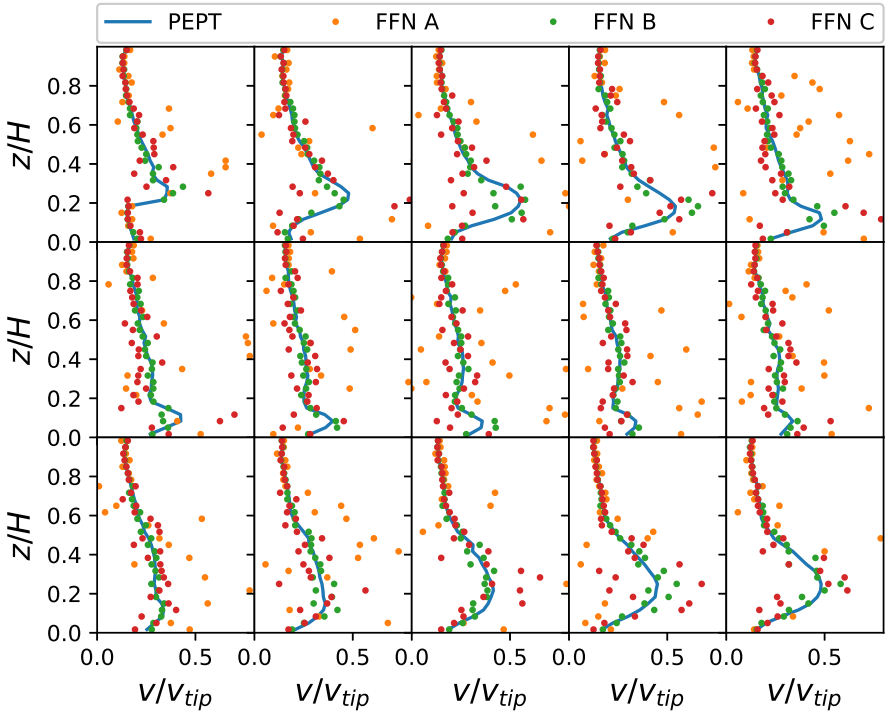


Figure 8.3: Velocity magnitude profiles comparing FFN predictions with experimental data at 500 RPM

with the trajectory constructed by RNN B, indicating velocity predictions are close to reality.

LSTM predictions (figure 8.5) show very similar results, with the majority of flow being predicted to good accuracy. Largest deviations are again observed in regions of high velocity, with LSTM B producing the most accurate tracer trajectory.

Figure 8.6 shows the velocity profiles resulting from trajectories constructed from B variants of each network in comparison to experimental data. Results show indistinguishable performance; each network when predicting velocity from position gives minimal error and subsequent trajectories are close to those found experimentally. Results shown henceforth focus on the B variants of each of the networks.

Figure 8.7 shows azimuthally averaged velocity maps comparing PEPT data to results obtained from constructed trajectories. As above, each model captures the

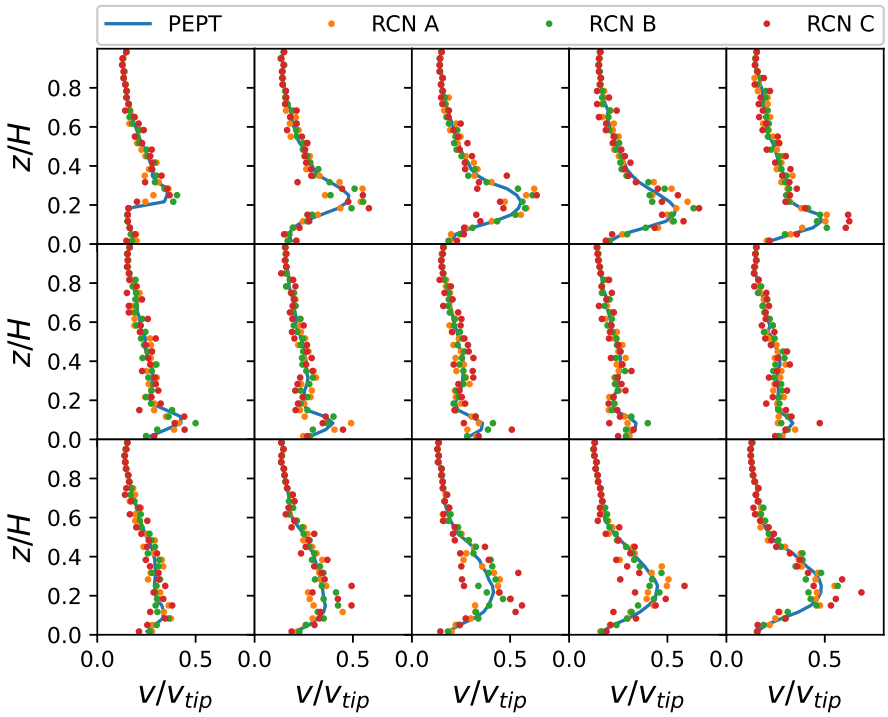


Figure 8.4: Velocity magnitude profiles comparing RNN predictions with experimental data at 500 RPM

flow profile with good accuracy. Figures 8.7c, 8.7f and 8.7i show the percentage error in velocity for each cell in the vessel, with dark regions indicating high error. As inferred previously, areas of high velocity incur the highest errors, as regions surrounding the impeller region and vessel boundary are darker in all cases than areas at the top of the vessel. Errors are largest with FFN B, less so with RNN B and the least with LSTM B. Peak errors are observed as 23%, 20% and 9% for FFN B, RNN B and LSTM B, respectively. Figures shown are limited to 10% error to maintain a contrast for lower errors to be observed.

8.5.3 Occupancy

Lagrangian trajectories constructed from the neural networks and their variants were also evaluated to compare occupancy to experimental data. Figure 8.8 shows errors

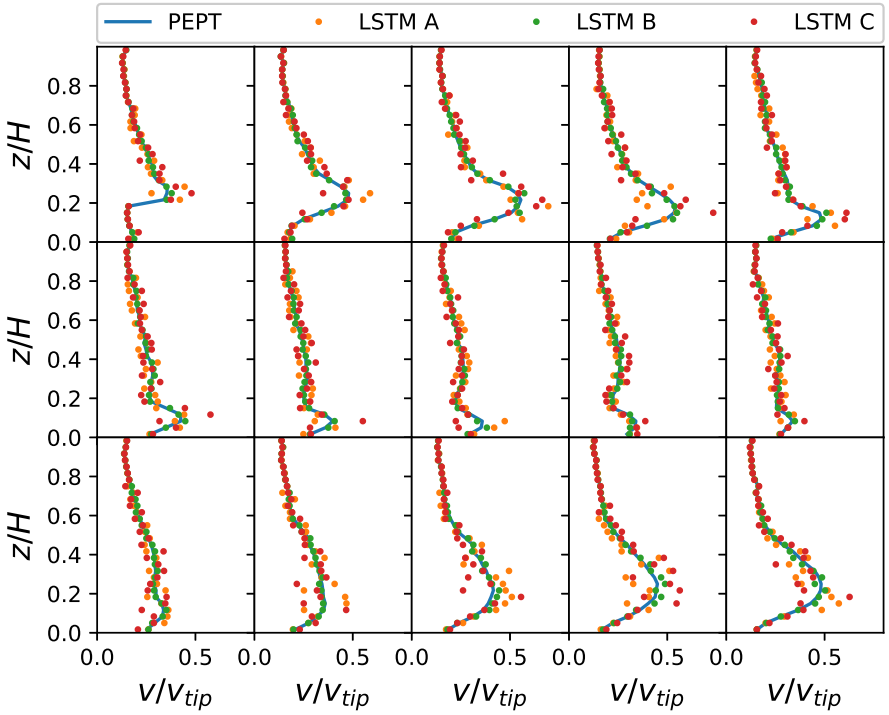


Figure 8.5: Velocity magnitude profiles comparing LSTM predictions with experimental data at 500 RPM

in occupancy for each network in comparison to experimental data at 100 RPM and 500 RPM. As with velocity errors, FFN B shows the highest errors, with lower values observed with RNN B and LSTM B. Conversely to velocity, however, errors are distributed throughout the vessel, and do not necessarily occur where occupancy is high experimentally. Percentage errors in occupancy are higher than velocity, with FFN B peaking at 31%, RNN B peaking at 32% and LSTM B peaking at 11%. This would suggest although velocity predictions are accurate, the small errors in magnitude for each direction cause the computed particle to deviate from the expected trajectory enough to result in a different occupancy map. This, however, is uniform across the vessel and not concentrated in any particular region, therefore a result of a systematic error rather than caused due to any flow dynamics.

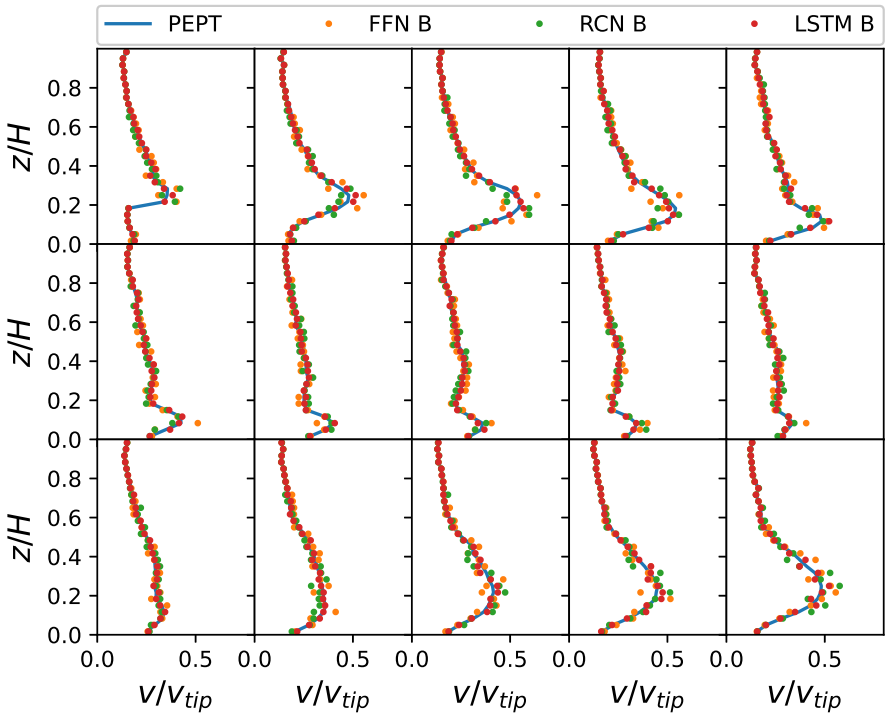
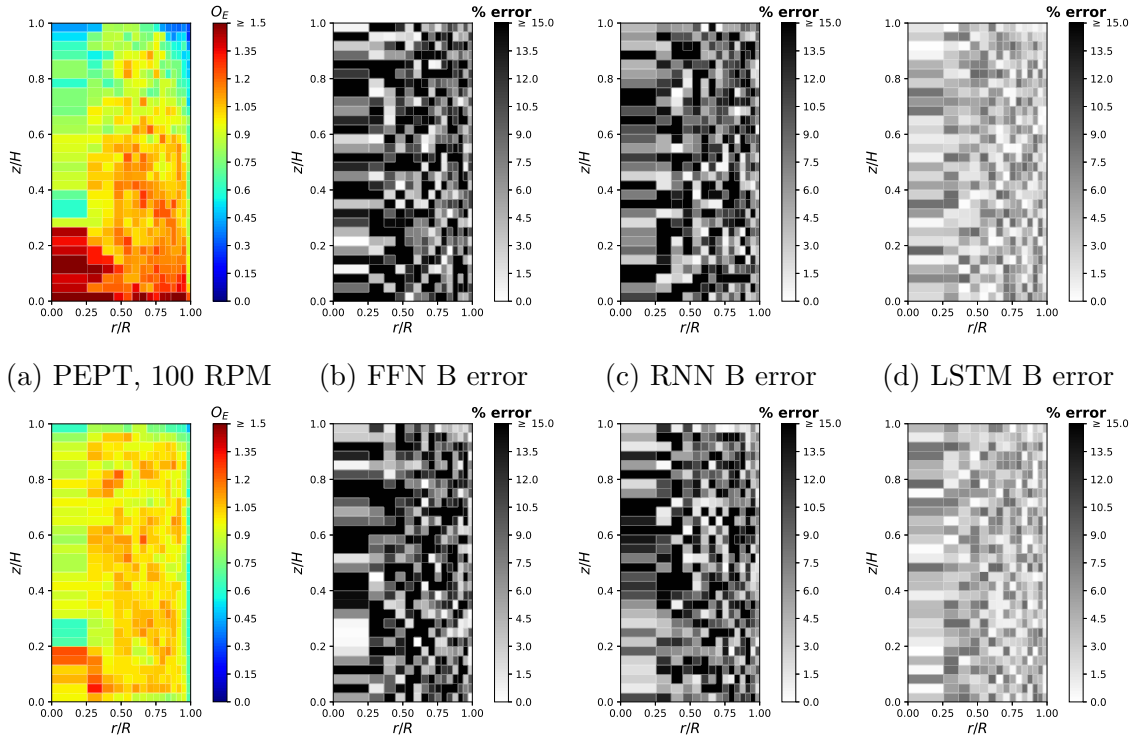


Figure 8.6: Velocity magnitude profiles comparing FFN, RNN and LSTM predictions with experimental data at 500 RPM

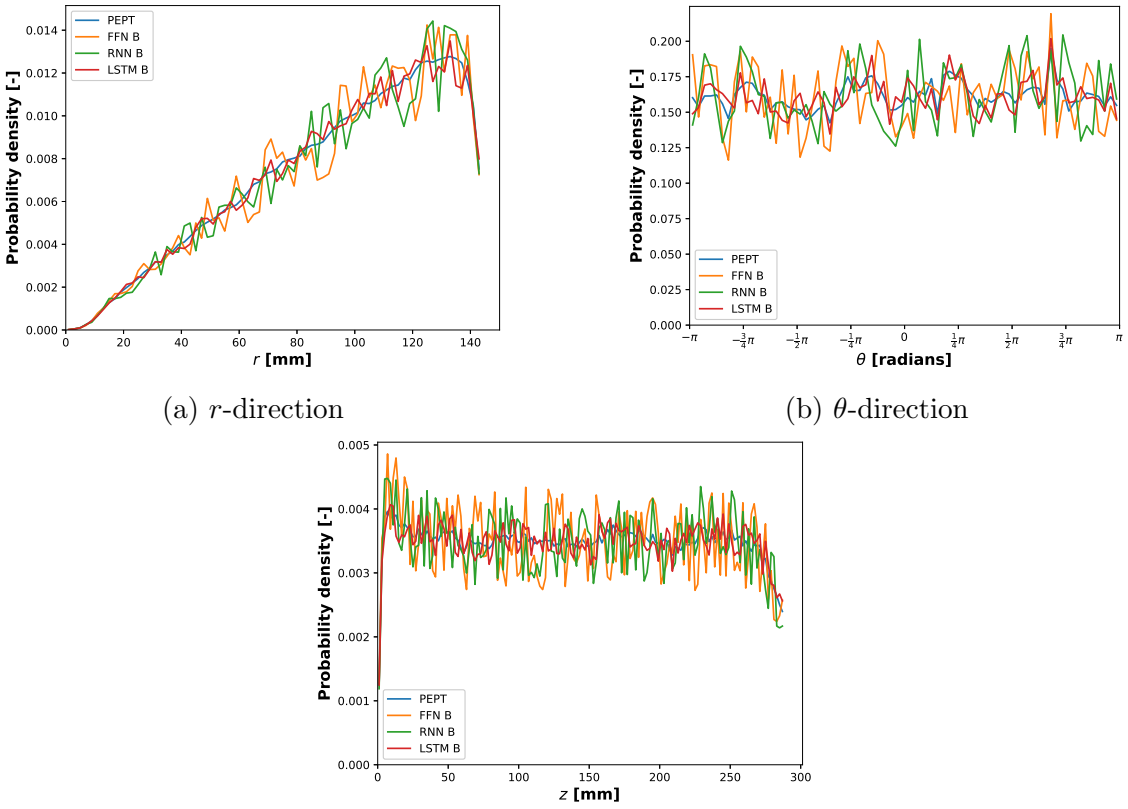


(a) PEPT, 100 RPM (b) FFN B error (c) RNN B error (d) LSTM B error

(e) PEPT, 500 RPM (f) FFN B error (g) RNN B error (h) LSTM B error

Figure 8.8: Azimuthally averaged occupancy comparison for FFN, RNN and LSTM predictions with experimental data

The uniform error in occupancy can also be observed when computing probability density functions for each of the models. Figure 8.9 shows the largest deviation from experimental probability in each direction occurs with FFN B, with a similar profile observed with RNN B. Again, LSTM B shows the smallest deviation in spatial location error.



(a) r-direction

(b) θ-direction

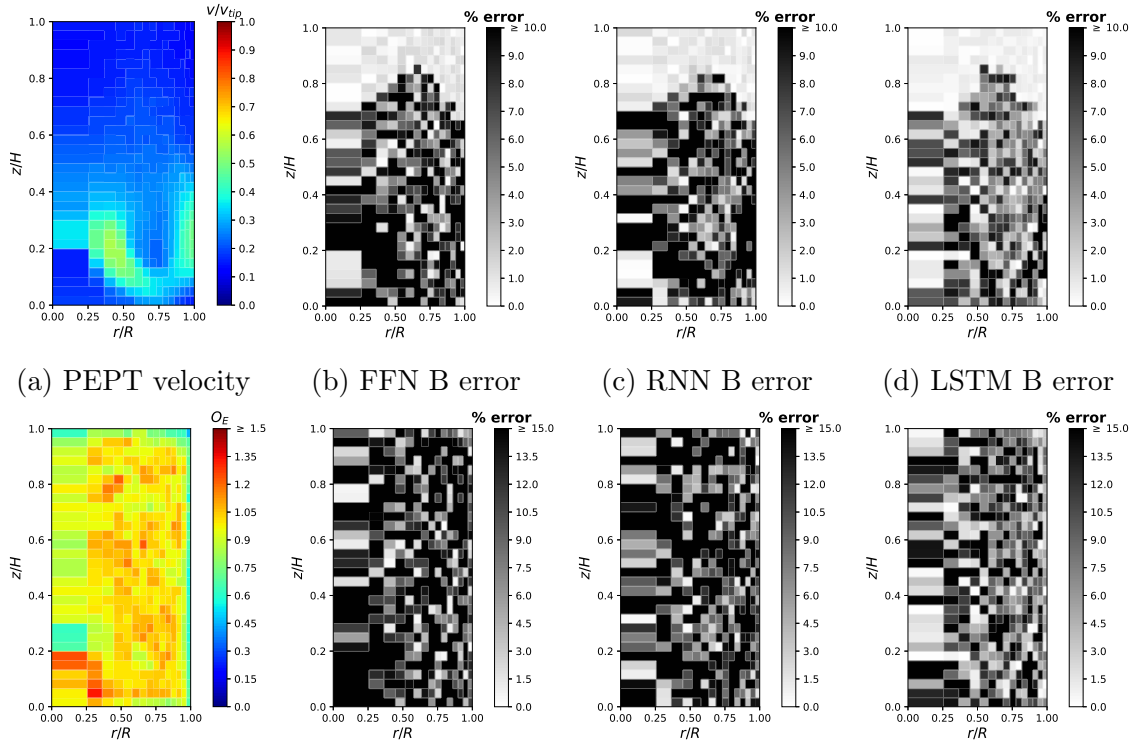
(c) z-direction

Figure 8.9: Probability density functions for FFN B, RNN B and LSTM B compared to 500 RPM experimental data

8.5.4 Predicting flow for conditions outside of training data

The models described were also used to predict trajectories for flow conditions outside of the training data supplied. Training data consisted of 10 min trajectories from experimental data of 100 RPM and 300 RPM, used to predict the flow of a tracer in a vessel with the same impeller rotating at 500 RPM. In order to make

these predictions, an additional input node was used to accommodate for the RPM value for each data point. The other architectural and training hyperparameters were unchanged for each model.



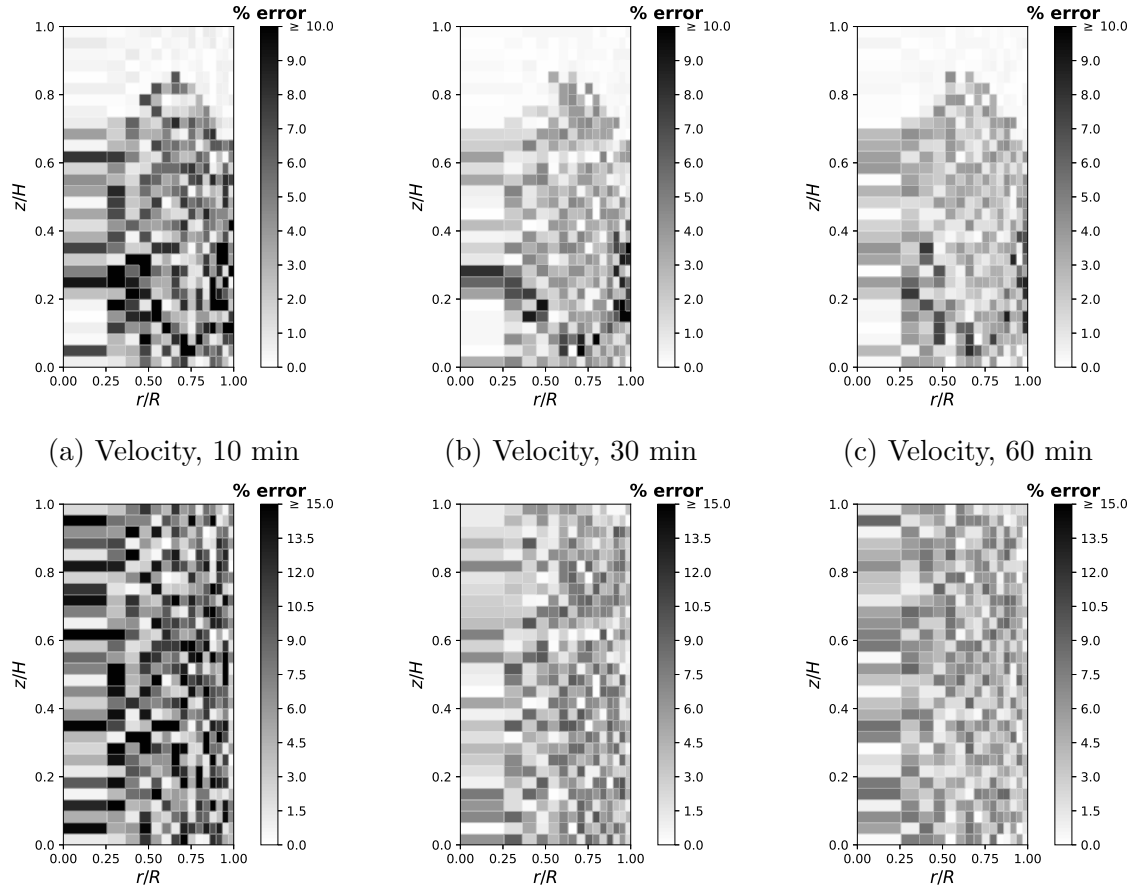
(a) PEPT velocity (b) FFN B error (c) RNN B error (d) LSTM B error

(e) PEPT occupancy (f) FFN B error (g) RNN B error (h) LSTM B error

Figure 8.10: Velocity and occupancy errors for predictions outside of training conditions

Figure 8.10 shows the velocity and occupancy errors for each of the networks predicting flow at 500 RPM. As shown, errors in predicting outside of training conditions are larger than those observed when predicting long term trajectories. Trends observed are similar however, velocity errors mostly occur in high velocity zones and occupancy errors are mostly uniform across the vessel for all networks. Velocity errors peak at 32%, 30% and 19% for FFN B, RNN B, and LSTM B, respectively. Similarly, occupancy errors peak at 38%, 38% and 18% for FFN B, RNN B, and LSTM B, respectively. This would suggest information from the training data is sufficient to make a rough prediction of flow at a higher rotation rate, however the

depth of information is not enough to result in a more accurate trajectory. This can be improved, however, by including more information during training, as shown by the LSTM predictions in figure 8.11



(a) Velocity, 10 min (b) Velocity, 30 min (c) Velocity, 60 min

(d) Occupancy, 10 min (e) Occupancy, 30 min (f) Occupancy, 60 min

Figure 8.11: Effect of training data length on LSTM B predictions for 500 RPM

By increasing the length of training data used, the errors in prediction can be reduced significantly; peak velocity errors of 19%, 10%, and 9%, and peak occupancy errors of 18%, 13% and 13% for 10, 30 and 60 min of training data, respectively, are observed. The difference in errors when increasing time from 10 min to 30 min is a substantial difference, and improves the predictions significantly. Doubling this training time to 60 min does not however, double the performance. A reduction in errors is observed, however this is a minor change, particularly for occupancy.

8.6 Conclusion

In conclusion, the results of this study show that neural networks can be used to accurately predict the flow patterns in solid-liquid mixing vessels. The performance of the feed-forward neural networks (FFN) was found to be poorer compared to the recurrent neural networks (RNN) and long short-term memory (LSTM) networks, with the B variant of each type of network producing the most accurate results. The highest errors were observed in regions of high velocity, with peak errors of 23%, 20% and 9% for FFN B, RNN B and LSTM B, respectively. The errors in occupancy were found to be higher than the errors in velocity, with peak errors of 31%, 32% and 11% for FFN B, RNN B and LSTM B, respectively. Overall, the LSTM B network performed the best in terms of both velocity and occupancy prediction, with the lowest errors among the three types of neural networks. These results suggest that neural networks, and in particular LSTM networks, have the potential to be useful tools for the modelling and simulation of solid-liquid mixing processes. Furthermore, LSTM networks are capable of predicting flow outside of the training set, and therefore are not only a tool for extending Lagrangian information available, but also can be used to predict flow under new condtions. Accuracy of these predictive calculations is determined by the length of the training information; using more data typically increases accuracy.

Limitations of using such models is the sensitivity to the training information, making the models not as generalisable as traditional deterministic methods. In the case of Lagrangian trajectories, predictions are limited to the same time step as provided in the training data, and all training data must have a constant time step. In order to run a calculation with a different time step, the entire model must be trained again which can be a costly exercise. However, computations for the stirred vessel system using the neural networks were significantly more efficient than what would

be required for the equivalent CFD calculation; the neural network calculations completed within an hour using simpler hardware (4x2GHz cores, 8GB RAM). Overall such hardware and efficiency is preferable in an industrial setting, where accurate estimations are required without the need for commitment to long periods of time and expensive hardware.

Future work could involve the use of more advanced neural network architectures, such as convolutional neural networks or transformers, to improve the performance of the networks for this specific task. In addition, the use of different training algorithms, such as reinforcement learning or unsupervised learning, could also be explored to further improve the accuracy of the predictions.

Overall, the results of this study demonstrate the potential of neural networks for the modelling and simulation of solid-liquid mixing processes, and highlight the importance of carefully selecting the type of neural network and the training parameters for optimal performance.

References

- Bishop, C. M. (1995). Neural networks for pattern recognition. Oxford University Press.

- Chen, X., Li, Y., & Lu, J. (2018). Mixing pattern identification and classification in a stirred tank reactor using convolutional neural network. Chemical Engineering Research and Design, 135, 356-365.

- Chollet, F., & Allaire, J. (2018). Deep learning with R. Manning Publications Co.

- Geron, A. (2019). Hands-on machine learning with Scikit-Learn, Keras, and TensorFlow: concepts, tools, and techniques to build intelligent systems. O'Reilly Media, Inc.

- Ghasemi, A., Shahriari, A., & Mohseni, M. (2013). Neural network based control of a stirred tank reactor. Chemical Engineering Science, 89, 280-289.

- Glorot, X., & Bengio, Y. (2010). Understanding the difficulty of training deep feedforward neural networks. In Proceedings of the thirteenth international conference on artificial intelligence and statistics (pp. 249-256).

- Goodfellow, I., Bengio, Y., & Courville, A. (2016). Deep learning. MIT press.

- Klambauer, G., Unterthiner, T., Mayr, A., & Hochreiter, S. (2017). Self-normalizing neural networks. In Advances in neural information processing systems (pp. 971-980).

- Lee, J., Kim, J., & Kim, K. (2006). Viscosity modeling of aqueous clay suspensions using artificial neural network. Journal of Colloid and Interface Science, 299(1), 121-128.

- Li, Y., Lu, J., & Chen, X. (2018). Prediction of mixing intensity in a stirred tank reactor using long short-term memory network. Chemical Engineering Research and Design, 134, 1-10.

- Li, Y., Lu, J., & Chen, X. (2019). LSTM-based control of a stirred tank reactor using model predictive control. Chemical Engineering Research and Design, 146, 559-568

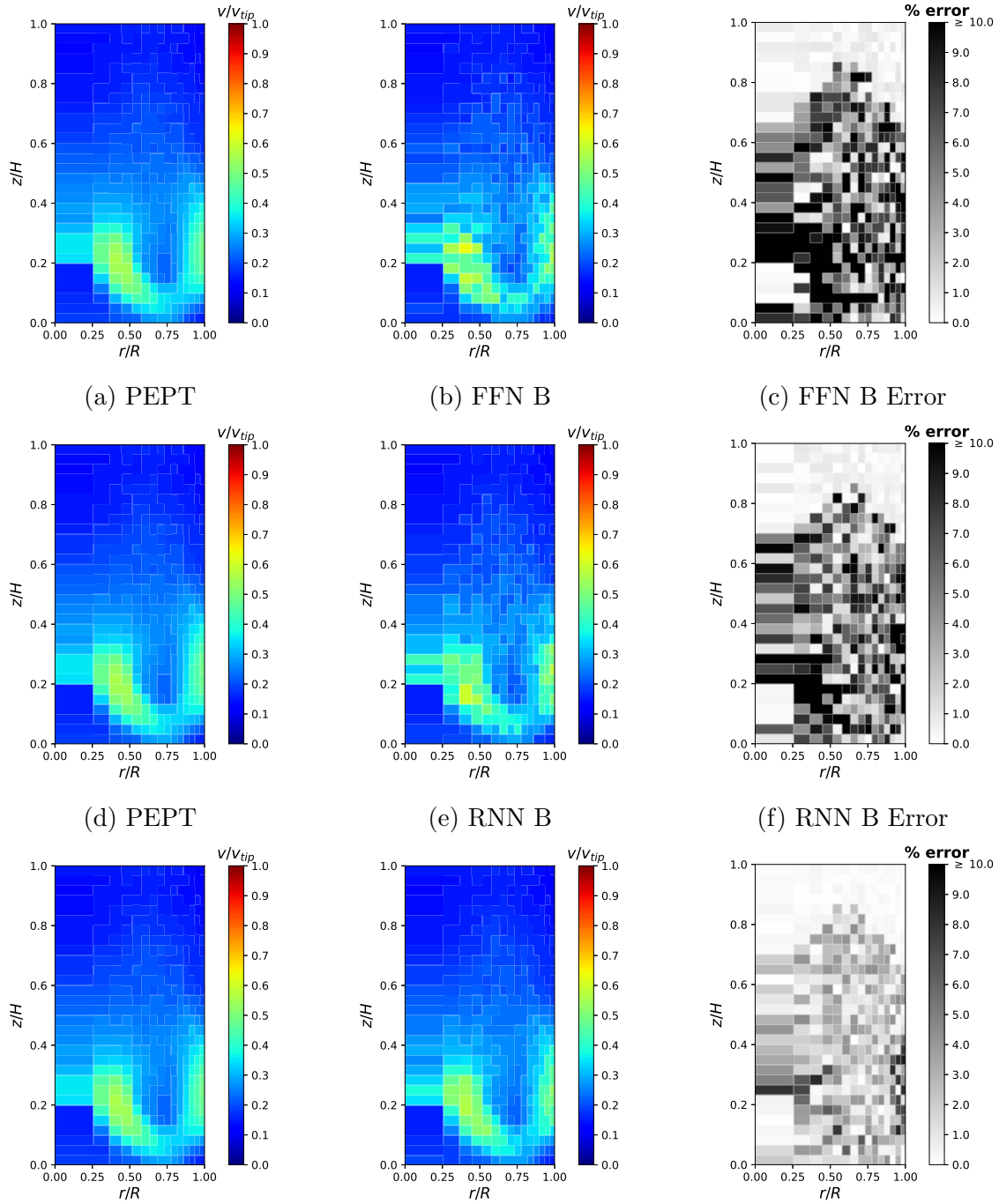
- Ramachandran, P., Zoph, B., & Le, Q. V. (2017). Swish: A self-gated activation function. arXiv preprint arXiv:1710.05941.

- Wang, J., Lu, J., & Chen, X. (2019). Optimization of mixing processes in stirred tanks using artificial neural network and particle swarm optimization.

Chemical Engineering Research and Design, 142, 452-461.

- Wang, Y., Li, J., Li, X., Li, C., & Ni, Y. (2018). Particle transport and mixing in pipes using positron emission particle tracking (PEPT). Chemical Engineering Science, 179, 95-104.

- Zhang, X., Lu, J., & Chen, X. (2017). Prediction of mixing time in a T-shaped mixing vessel using long short-term memory network. Chemical Engineering Research and Design, 121, 456-465.



(a) PEPT (b) FFN B (c) FFN B Error

(d) PEPT (e) RNN B (f) RNN B Error

(g) PEPT (h) LSTM B (i) LSTM B Error

Figure 8.7: Azimuthally averaged velocity magnitude comparison for FFN, RNN and LSTM predictions with experimental data at 500 RPM

Chapter 9

General conclusions and recommendations

Solid motion in pipeline and stirred vessel slurry flows is intrinsically Lagrangian, and although Eulerian information is important, Lagrangian analysis is required for a complete description. The Lagrangian approach presented in this work has been used to investigate solid-liquid flow in horizontal pipes, and to develop data-driven models to extend and predict Lagrangian motion of tracer particles in stirred vessels.

9.1 PEPT

The PEPT technique has shown to be an accurate and repeatable methodology for opaque solid-liquid flows, which would be otherwise difficult to measure and evaluate using other experimental methods. Furthermore, the technique provided Lagrangian three-dimensional trajectories with high spatial and temporal resolution, a unique result compared to other methods.

Although spatial and temporal accuracy are adequate for the purposes of this study, improvements can be made to increase the resolution to capture more detail such as turbulence and eddies. In order for this to be achievable, a few factors must be improved. Firstly, the size of tracer particle must be smaller, in the order of magnitude of the Kolmogorov length scales. Smaller tracers are a challenge due to the ability to hold enough radioactivity for detection in the camera systems, however current research at King's College London aims to use surface labelling techniques to activate particles as small as 1 μm. Secondly, the base accuracy of the camera systems must be improved, which is a restriction due to the size of photomultipliers blocks implemented. Further work at the University of Birmingham for the superPEPT and microPEPT camera facilities aims to address the hardware limitations to enable higher temporal and spatial resolution.

9.2 Solid-liquid pipe flow

The primary aim of the first stage of work presented was to develop a suitable experimental methodology to obtain a Lagrangian description of solid-liquid pipe flows. The construction of the flow apparatus in conjunction with the positron emission particle tracking technique was a successful methodology in providing detail in good spatial and temporal resolution for the Lagrangian flow data.

This cutting-edge method delivered distinctive and precise Lagrangian flow data within opaque flows. Thus, it offers up new avenues for addressing a number of difficult issues that have up to now gone neglected or unresolved due to a lack of appropriate measurement techniques in the flow of opaque single-phase and concentrated multi-phase systems. For example, at high solid loadings the Lagrangian trajectories could provide three-dimensional granular velocity and occupancy detail which would

be otherwise impossible with optical techniques. Lagrangian multi-phase data analysis has also made it possible to provide in-depth Eulerian descriptions, including the whole 3D velocity field, local occupancy, and spatial distribution of each phase component.

An important tool was developed for the analysis of experimental PEPT data. After post-processing the raw data using the Birmingham Method (section 2.3.2), a computational code for extracting valuable Eulerian information was required. The code was developed based on a set of subroutines with various algorithms designed to gradually analyse the original Lagrangian information and save significant intermediate outputs. The code has been written with intrinsic flexibility due to the diversity of experimental systems that may be investigated, allowing key-parameters to be adjusted and individual subroutines to be activated or deactivated as needed.

Another important development for the study of solid particles, particularly for investigations into the flow of food solids, was the establishment of a methodology for mass fabricating spherical calcium alginate particles. Using a custom manifold, adjustable needles, and a peristaltic pump setup, a large number of nearly identical spherical particles could be manufactured for the requirement of the experiments. Furthermore, the methodology developed for activating these alginate particles using a radiolabelled ion exchange resin particle encapsulated with a calcium alginate particle gave near perfect results, with no radioactive leaching.

In conclusion, the study demonstrated that increasing solid concentration in a pipe has a small effect on the liquid flow profile, but a more significant effect on the solid flow profile. The velocity of the solid particles was found to be higher at the top of the pipe, and there were significant reductions in velocity in the bottom section of the pipe. These findings can provide valuable insights into solid-liquid flow and mixing in pipes, and the effect of solids on the flow field.

Based on the results of this study, it is recommended that further research be conducted to explore the effects of different solid concentrations on flow and mixing in pipes. This could include studying a wider range of solid concentrations and particle sizes, as well as examining the effects of different pipe diameters and flow rates.

In terms of future work, it would also be interesting to investigate the effects of other factors on solid-liquid flow and mixing in pipes, such as the presence of surfactants or the use of different types of solid particles. Overall, this research has the potential to provide valuable insights into the behaviour of solid-liquid systems in pipes and other flow systems.

9.3 Modelling of solid-liquid flow in mixing vessels

The use of data-driven Lagrangian stochastic models and machine learning techniques has been shown to be an effective way of predicting the flow patterns in single-phase and multiphase systems in mechanically agitated vessels. Both the Lagrangian stochastic models and the machine learning frameworks were found to be highly accurate, with the ability to predict flow patterns outside the range of experimental conditions. In addition, both approaches have the advantage of being computationally efficient, requiring only a small set of experimental data as input and producing results much faster than conventional turbulence simulations. These findings demonstrate the potential of these approaches for assisting in the design and optimization of industrial processes and have great potential for further application in the analysis and modelling of flow systems.

Based on the results of this study, it is recommended that further research be conducted to explore the use of data-driven Lagrangian stochastic models and machine

learning techniques for predicting flow patterns in other types of systems, such as pipes and reactors. It would also be interesting to investigate the use of these approaches for studying other types of multiphase systems, such as gas-liquid or solid-gas systems.

In terms of future work, it would be useful to examine the sensitivity of the models and frameworks to different types of experimental data and to different flow conditions. It would also be valuable to study the performance of these approaches when applied to more complex systems, such as those with more than two phases or those with more complex flow patterns. Overall, this research has the potential to provide valuable insights into the behaviour of complex flow systems and to improve our understanding of flow patterns in mechanically agitated vessels.

The results of this study show that neural networks, particularly recurrent and long short-term memory networks, can be effectively used to predict flow patterns in solid-liquid mixing vessels. While the feed-forward neural networks performed poorly, the recurrent and long short-term memory networks demonstrated good accuracy, with the latter performing the best overall. The highest errors were observed in regions of high velocity, with errors in occupancy being generally higher than errors in velocity. These findings suggest that neural networks have the potential to be useful tools for the modelling and simulation of solid-liquid mixing processes.

Based on the results of this study, it is recommended that further research be conducted to explore the use of advanced neural network architectures, such as convolutional neural networks or transformers, to improve the performance of the networks for this specific task. In addition, the use of different training algorithms, such as reinforcement learning or unsupervised learning, could be explored to further improve the accuracy of the predictions.

In terms of future work, it would be valuable to test the performance of these neural networks on a larger dataset, as the use of a larger training dataset may improve the accuracy of the predictions. It would also be interesting to examine the performance of these networks when applied to other types of flow systems, such as pipes or reactors. Overall, this research has the potential to provide valuable insights into the behaviour of complex flow systems and to improve our understanding of flow patterns in solid-liquid mixing vessels.

The data-driven models presented in this work show increasing applicability to predicting Lagrangian trajectories outside their respective provided data sets. Namely, the LSM has the poorest ability of predicting outside of the given data of the modelling methods, which is improved upon by the ML methods. The best performer is the LSTM neural network, the most complex of the methods, but also the most capable of being generalisable for other flows. Nonetheless, these methods are computationally efficient in comparison to deterministic CFD methods, making them useful tools for industrial settings where accurate estimations can be made quickly on less expensive hardware for optimising designs and processes.